Nottingham Geospatial Institute

VALIDATING THE SUBSAR TECHNIQUE FOR BURIED FEATURE DETECTION USING SATELLITE SAR DATA

By

AHMED DHAHIR ATHAB

Thesis submitted to the University of Nottingham for the degree of

Doctor of Philosophy

September 2018

Abstract

This thesis has tested the validity of the SubSAR technique for subsurface feature detection on a field-scale experiment using Synthetic Aperture Radar (SAR) satellite data. Most of the current SAR subsurface imaging approaches are based on analysing the amplitude component of the SAR images only, which is not sufficient by itself to determine whether an imaged object lies on the earth's surface or it is beneath the surface. Thus, the current approaches usually require an additional source of information (e.g., optical imagery) to help interpret SAR images for subsurface feature detection.

A recent approach for subsurface detection, called SubSAR, utilises the amplitude information of the SAR image, as well as the DInSAR phase history, proved to be a promising method for discriminating between surface and buried features without requiring additional source of information. However, this method has only demonstrated in the lab.

The overall aim of this thesis it to validate the SubSAR technique for application to satellite SAR data. Therefore, a field-scale experiment was designed, which extends the lab experiments into the field. This involves creating a set of radar point targets and covering them with a layer of sand to simulate buried targets.

A set of measurements are then undertaken to test the validity and the quality of the experiment, involving the analysis of the radiometric and interferometric phase stability of the point targets. This is required to ensure that any change in the measured phase and backscatter is due to the variations in the water content of the covering sand and not the instability of the radar point targets (the Corner Reflectors CRs). Lastly, the SubSAR experiment itself is then implemented by monitoring the effect of the covering sand's moisture content on the incident signal, including both the backscatter and the DInSAR phase.

Results of the experiments suggested that it is possible to apply the SubSAR technique for subsurface feature detection from satellite SAR data. It is also found that the information obtained from the SAR data only can be used to detect buried features, without the need to an additional source of information, such as the soil moisture. This is very important in real life applications, such as pipeline and landmines detection, where soil moisture measurements are probably unavailable.

Dedication

To my lovely family

Acknowledgements

Firstly, I would like to express my special appreciation and thanks to my supervisors Dr Andrew Sowter, Prof Stuart Marsh and Dr Stephen Grebby for their continuous support of my Ph.D study, and for their patience, motivation and immense knowledge. I could not have imagined better supervisors and I would like to thank you for encouraging my research and allowing me to grow as a research scientist. Your advice on my research, as well as my career have been priceless.

This study was funded by the Iraqi Ministry of Higher Education and Scientific Research (MOHSR) through its Cultural Attaché in London. Much gratitude goes to the University of Baghdad – Surveying Engineering Department for giving me the permission to undertake this research.

I take this opportunity to thank the staff of the Nottingham Geospatial Institute, who were always equipped with kind words of encouragement and advice during my study. I highly appreciate the technical support and resources provided by the University of Nottingham through training courses and the facilities made available for comfort and study. My sincere thanks also go to Mr. Mike Davies from the School of Bioscience (Bunny farm manager) and Mr. Thomas Ryder (the Beeman), who allowed me to work at Bunny farm and helped during the installation of the CRs. Without their precious support it would not have been possible to conduct this research.

I am also grateful to Mr Peter Meadows, from BAE Systems Applied Intelligence Laboratories, for his guidance and help in calibrating Sentinel-1 images and on corner reflector detection.

I would like to thank my friend David Gee, a fellow doctoral student, for his feedback, cooperation and of course friendship.

The Sentinel-1 data used in this thesis were provided by the European Space Agency (ESA) through the Sentinel Scientific Data Hub. I would like to thank Geomatic Ventures Limited for access to their software, Punnet, which was used to process Sentinel-1 images.

A special thanks to my family. Words cannot express how grateful I am to my beloved wife Basima Haider, who has spent sleepless nights with me and has always supported me spiritually during the entire period of my PhD study. I would like to thank my mother, father and sisters for all the sacrifices you have made on my behalf. Your prayer for me is what has sustained me thus far.

Publications and conferences

Publications:

- Sowter, A., Amat, M.B.C., Cigna, F., Marsh, S., Athab, A. and Alshammari, L., 2016. Mexico City land subsidence in 2014–2015 with Sentinel-1 IW TOPS: Results using the Intermittent SBAS (ISBAS) technique. *International Journal of Applied Earth Observation and Geoinformation*, *52*, pp.230-242.

- Sowter, A., Athab, A., Novellino, A., Grebby, S. and Gee, D., 2018. Supporting energy regulation by monitoring land motion on a regional and national scale: A case study of Scotland. *Proceedings of the Institution of Mechanical Engineers, Part A: Journal of Power and Energy*, *232*(1), pp.85-99.

- Marshall, C., Large, D.J., Athab, A., Evers, S.L., Sowter, A., Marsh, S. and Sjögersten, S., 2018. Monitoring tropical peat related settlement using ISBAS InSAR, Kuala Lumpur International Airport (KLIA). *Engineering Geology*, *244*, pp.57-65.

Conferences

Conference name/sponsor	Date	Place	Participation
Seismology from Space- Geodetic observations and early warning of earthquakes	May 2014	London, UK	Poster
RSPSoc Annual Conference	September 2016	Nottingham, UK	Oral presentation
Fringe 2017	June 2017	Helsinki, Finland	Oral presentation

Table of content

List of Tables

List of Figures

List of Acronyms and Abbreviations

CR	Corner Reflector
DEM	Digital Elevation Model
DN	Digital Number
ESA	European Space Agency
EU	European Union
GPR	Ground Penetrating Radar
InSAR	Interferometric Synthetic Aperture Radar
IRF	Impulse Response Function
IW	Interferometric Wide
LOS	Line-of-Sight
LUT	Look-Up Table
NBMI	Normalized backscatter moisture index

PPS	Pulses Per Second
PRF	Pulse Repetition Frequency
RADAR	Radio Detection and Ranging
RCS	Radar Cross Section
RID	Radar Imaging Depth
SAR	Synthetic Aperture Radar
SInSAR	Differential InSAR
SIR	Shuttle Imaging Radar
SLAR	Side Looking Airborne Radar
SLC	Single-Look Complex
SNR	signal to noise ratio
SRTM	Shuttle Radar Topographic Mission
SCR	Signal-to-Clutter Ratio
SubSAR	Sub-surface Synthetic Aperture Radar

Chapter 1: Introduction

1.1 Research background

Remote sensing is the process of obtaining information about objects or features without being in direct contact with them. Obtaining information remotely relies upon knowing how electromagnetic radiation interacts with the object or features of interest. For a spaceborne or airborne platform, the remote sensing process consists of several stages, beginning with emission of electromagnetic energy from either a natural (e.g., the sun) or artificial source (e.g., a laser or radio source). This energy propagates through the atmosphere towards the surface and then interacts with visible terrain features. These features respond to the electromagnetic energy in different ways, e.g., it can be reflected, transmitted, or scattered, depending on a combination of the wavelength of the energy and the feature's physical characteristics. Consequently, the proportion of energy reflected by the surface will contain information about the variation in the terrain features. The reflected energy is then retransmitted through the atmosphere and back to the sensor. The sensor records the received energy and uses it to generate a digital image depicting the variations in the illuminated surface (Lillesand et al. 2014).

Remote sensing has many benefits, such as wide area coverage for regional applications. The repetitive capability for the sensor platform offers temporal monitoring and analysis for agricultural and environmental monitoring. Different sensors offer a range of data at different scales with different resolutions. Remote sensing has many applications in geography, hydrology, oceanography, and geology. Remote sensing is also successfully used in reconnaissance surveying, military intelligence and for commercial and economic planning.

A significant limitation of remote sensing is that the object under consideration may be buried under some medium, such as soil, therefore obscuring the line of sight between the sensor and object. This overlying medium may impede electromagnetic radiation with specific wavelengths (e.g., visible light) so that no energy is reflected by buried objects to the sensor, and hence, it will not be imaged or detected using optical remote sensing techniques. On the other hand, microwave radiation, which is utilised in radar remote sensing, has a longer wavelength than visible light and has the potential to pass through unconsolidated material on the immediate Earth surface (Ulaby et al. 1982). As they do so, microwave signals are still subject to a number of effects; namely, surface scattering, such as specular reflection or diffuse backscatter, and volume scattering (i.e., subsurface scattering) (Schaber et al. 1986). Nonetheless, under certain conditions, microwave signals are capable of detecting buried features.

Current microwave subsurface imaging techniques typically involve using a sensor that is in direct contact with the surface, such as Ground Penetrating Radar (GPR). The GPR technique provides high resolution subsurface information that is widely used in urban planning, civil engineering, buried manmade object detection, geological surveying and archaeological site explorations, etc (Merrill 1990). However, as it is ground-based, its main limitation is that each measurement provides only limited coverage of an area, so large surveys are impractical and costly in terms of resources. Additionally, GPR cannot be used in areas with difficult access, such as mountainous areas or those with buried landmines. It is possible that these limitations could be overcome by using spaceborne microwave remote sensing systems.

An example of such a system is Synthetic Aperture Radar (SAR), which is an active system operating in the microwave domain with a wavelength on the order of few centimetres. Since longer wavelengths can penetrate deeper into dielectric materials (Ulaby et al. 1981), in contrast to visible light, SAR can essentially be used to see through dust, fog and even clouds. This makes SAR a valuable earth observation technique for studying regions with persistent cloud cover (e.g., tropical regions), while its active nature means it is can be used to acquire data irrespective of the solar illumination conditions (Elachi et al. 1982, Curlander and McDonough 1991, Lillesand et al. 2014). Another unique characteristic of SAR is that it is a coherent system. This means that the system records both the amplitude of the reflected signal as well as the phase information, which is related to the target to sensor distance. Therefore, the information provided by the imaging SAR for each ground resolution is a function of the distance between the radar antenna and the imaged terrain and the terrain characteristics (Zebker and Goldstein 1986).

The capabilities of microwave signals to penetrate soils has well been documented through laboratory experiments (Bussey 1960, Geiger and Williams 1972, Ulaby et al. 1978, Hallikainen et al. 1985). The first ever subsurface imaging discovery from space was reported by McCauley et al. (1982). They discovered some lineaments in the Shuttle Imaging Radar (SIR-A) SAR images over the Selima Sand Dunes region, located on the border of Libya, Sudan, and Egypt. These linear features were neither visible in the optical images of Landsat or in the field. Further field investigations confirmed that these features represent previously unknown, hidden paleo-drainage channels buried under the desert sands (McCauley et al. 1982). Other studies used the available SAR images in the early spaceborne SAR systems and yet they made remarkable findings. These researches were mainly reliant on the visual analysis of the SAR images which, for the L-Band signals, had the ability to directly penetrate the soil to a specific depth and the return could be interpreted as a subsurface feature return. However, this technique for subsurface imaging from space has some restrictions and limitations that make it a challenging task. These difficulties can be summarized as follows:

1- The covering medium often restrains the subsurface imaging process by either absorbing, scattering, or attenuating the incoming electromagnetic signals, preventing the signals from reaching the buried target. A successful subsurface imaging task is only made possible when sufficient energy is reflected back from the buried object to the sensor.

2- The penetration capability depends on both the signal properties, i.e. wavelength, and the medium's physical properties, primarily, structure and moisture content. This means that specific conditions should be met, such as using signals with long wavelengths, and the covering medium should be homogeneous and dry, for a successful subsurface imaging task

3- The Radar Imaging Depth (RID) is the distance at which the signal is attenuated by a specific factor and yet returns sufficient energy for the subsurface imaging task. Subsurface imaging is not possible if the object is buried at a distance deeper than the RID in a highly absorbing medium.

4. Data interpretation: The backscattered signal from the surface and the subsurface features are all recorded in the SAR image. Making the separation of the subsurface object information from the surface features is a challenging task. Additional information would be required for the interpretation such as data from optical remote sensing, or even field investigations.

5. The water content of the medium, i.e., soil moisture, controls how the signal will propagate through the medium, and affects both the amplitude of the backscattered signal, as well as the phase. Early subsurface imaging techniques depended on qualitative analysis for the SAR amplitude images, which typically lack the efficiency to discriminate between the surface and subsurface

reflections and ignore an important component of the SAR image which is the phase.

New approaches are clearly required in order to improve the limited capability of spaceborne SAR for mapping or detecting buried features. In an attempt to address this, Morrison et al. (2013) developed a scheme, called SubSAR, for discriminating between surface and subsurface features. In a laboratory experiment, Morrison et al., (2013) buried a radar target under a layer of sand, whose moisture content was precisely measured, and monitored the behaviour of both the phase and the amplitude of the buried target while the sand water content was gradually reduced (dried) with time. They reported a positive correlation between the phase trend and the change in the soil moisture, as well as a negative correlation between the backscatter and the moisture content change. They suggested that if the backscatter from an object increases while the moisture content of the surface decreases at the same time, this could be an indicator of a buried target signature, this is contrary to the general rule of thumb of SAR images that suggests radar backscatter increases as the surface soil moisture is increased (Geiger and Williams 1972, Hoekstra and Delaney 1974, Wang et al. 1978, Hallikainen et al. 1985).

Although the SubSAR scheme appears to provide a more effective means of detecting buried features, it has only been implemented in a controlled laboratory environment. Its application to spaceborne SAR for buried feature detection remains to be realised.

1.2 Aim and research questions

The overall aim of this thesis is therefore to assess the application of the SubSAR scheme for buried feature detection using satellite SAR data. This will be explored by addressing the following specific research questions:

1- Is it possible to use SubSAR to detect objects buried under a layer of sand using satellite SAR data?

2- What is the effect of the covering layer's moisture content on the satellite SAR signal?

3- What is the maximum soil moisture content that allows a measurable SAR signal to still be detected from the buried target?

1.3 Objectives

The following objectives have been defined in order to answer the above research questions and achieve the overall aim of this thesis:

1- Design and implement a field-scale equivalent of the SubSAR laboratory experiment, for the first time, which uses a network of corner reflectors mimicking buried features during the satellite SAR overpass.

2- Test the quality and the validity of the experiment (radiometric stability, phase stability and accuracy). This is required to ensure that any change in the measured phase and backscatter is due to the variations in the soil moisture and not related to the stability of the CRs

3- Investigate the variations of both the backscatter and the phase of the buried features while the water content of the sand layer is precisely monitored, to be able to derive a relationship between these two factors and the amount of the water content change

1.4 Novelty and importance of the research

This thesis reports on a novel series of experiments that were designed to test the validity of using SubSAR for subsurface imaging using satellite SAR data. So far, the SubSAR principle was only identified in laboratory experiments. In this thesis, an experiment was designed to validate the SubSAR technique, utilising a network of radar corner reflectors (CRs), in such a way that the only changing parameter is the water content of the covering sand. The effects of the soil moisture on the SAR signal is investigated, and the maximum soil moisture at which subsurface imaging is still possible for a 1cm thickness layer of sand is calculated.

To the author's knowledge, no previous work has been implemented in a way that it was able to simulate a buried target and quantitatively analyse the data from SAR satellites. This approach can be extended to study other parameters that affect buried target detection, such as SAR frequency and the type of covering materials. This approach could also be used to calibrate SAR systems for detecting buried targets.

Answering these questions will help to establish the constraints under which the SubSAR technique can be used for buried feature detection from a spaceborne SAR imagery. Ultimately, understanding these constraints may then help in to moving a step closer to the development of enhanced techniques that are readily able to exploit satellite SAR data for effective subsurface imaging. This would consequently have important implications for applications such as mapping buried oil and gas pipelines, archaeological explorations, and the detection of buried objects like landmines.

1.5 Thesis overview

This thesis is organized into seven chapters. The current chapter (Chapter One) has presented an introduction to the research problem and defined the aims and objectives of the research undertaken. Chapter Two provides the general background to the concept of radar, including a summary of the development of radar techniques from their initial conception, through to the most advanced SAR techniques. The necessary theory of the interaction of the microwave signals with the soil medium is discussed in Chapter Three, along with an extensive review of the use of microwave remote sensing for buried feature detection. Chapter Four details the experiment that has been designed and implemented to determine the validity of the SubSAR technique for subsurface feature detection using spaceborne SAR data. This focusses on the design and implementation of the field-scale experiment that involves deploying corner reflectors during the satellite overpasses. The results of the experiment are presented and discussed in Chapter Five with respect to the individual objectives. Chapter Six discusses the various challenges that could influence the performance of the SubSAR scheme. This involves the use of simulations to help to understand how SubSAR could be applied in real-world scenarios. Lastly, in Chapter Seven, the main conclusions of the research are summarised, and recommendations for future work are made.

Chapter 2: Radar Background

2.1 Introduction

Radio Detection and Ranging (i.e., radar) is a technique that uses electromagnetic waves for the detection and locating of objects. The principle of radar commences with a microwave signal, or pulse, being emitted by a transmitter in a specific direction at the speed of light. If an object intercepts the transmitted pulse, the signal will scatter in different directions depending on the object's properties. The radar receiver can detect that object if it measures the reflected signal or 'echo'. Moreover, measuring the time difference between the transmitted pulse and the received echo also enables the distance between the radar and the target to be calculated (Moore and Thomann 1971). Radar was originally developed in the early 20th century for ship detection and was later adopted for military defence applications to detect enemy targets, such as aircraft, tanks and ships. In the 1950s, radar was developed to produce images for the earth's surface, which included the introduction of the concept of Side Looking Airborne Radar (SLAR). The imaging radar system has many advantages over optical imaging systems (i.e., aerial images). For example, imaging radar is an active system in that it provides its own source of energy to illuminate targets, meaning that it can be operated day and night without any dependency on solar radiation. Additionally, microwave radiation has the capability to penetrate clouds, fog and dust, and so radar can be operated in all weather conditions. Recent imaging radars used Doppler frequency shift techniques to produce high-resolution imagery, which is an important remote sensing tool that has a variety of applications (Ulaby et al. 1981). This chapter provides the technical basis for radar systems in general, paying particular attention to imaging radars. The chapter concludes by describing radar interferometry – an advanced application of radar images.

2.2 Brief History

In the 1880s, a German physicist called Heinrich Rudolf Hertz designed an experiment to prove the Maxwell mathematical theory of electromagnetic waves. Hertz built an oscillator to generate electromagnetic signals and a simple receiver, made from a looped wire, to receive these signals. He also discovered that these signals can be reflected by electric conductors and can be focused by using concave reflectors. This was the first ever transmit-receive device to be created (Hertz 1893). In April 1904, Christian Hülsmeyer, a German inventor, was awarded a patent for his 'telemobiloscope' device; a system which is able to detect distant metallic objects using microwaves. It had a transmitter and a receiver, and used an antenna to transmit 40-50 cm wavelength microwave pulses in a specified direction (Hulsmeyer 1904). The primary application of this device was as an anti-collision system for ships, which was later developed to be used for military purposes during the first and second world wars.

Radar usage evolved from a simple range detection device into an advanced imaging system with the invention of Side-Looking Airborne Radar (SLAR) during World War II (Franz Leberl et al. 1976). The SLAR system overcame many limitations associated with optical remote sensing systems; notably, it could penetrate clouds and operate day and night and in all weather conditions. However, it was limited in terms of ground resolution, particularly the azimuth resolution, which is directly proportional to the antenna size. In 1951, Carl Wiley, developed a technique to improve the azimuth resolution of the radar image by synthesising a very large antenna from a physically short antenna and the motion of the platform (Atwood 1952). Wiley called this method Doppler beam sharpening. The SAR technique improves the azimuth resolution from a few kilometres for SLAR systems to a few metres, and is independent of the platform altitude, making it most suitable for spaceborne platforms.

The first use of spaceborne radar for science applications began with the launch of the SEASAT satellite in 1978 (Jordan 1980). This was an experimental Earth Observation mission by NASA/JPL hosting the first ever spaceborne SAR system. SEASAT was mainly oriented for ocean applications, providing information on diverse ocean phenomena, such as wave heights, length and direction, near-surface temperatures and wind speed and direction, sea ice and rainfall. The ocean data provided by SEASAT during its 106 day-lifetime was more than that collected by ships in over 100 years. Subsequent spaceborne radar missions included the Shuttle Imaging Radar missions (A and B) (Elachi 1982), and the Cosmos experiments of the Soviet Union in the 1980s. However, it was not until the 1990s that spaceborne SAR missions intensified with the launch of many SAR satellites from space agencies around the world, such as ERS-1 and ERS-2 from ESA, JERS-1 from the Japanese space agency and Radarsat-1 from the Canadian space agency (Lillesand et al. 2014). Table 2.1 below summarize the many spaceborne SAR missions from SEASAT to the most recent Sentinel-1 mission.

Table 2.1: Spaceborne SAR missions

Mission	Institution/Country	Operation	Frequency Band (polarization)	Spatial resolution (Range, Azimuth) (m)
SEASAT	NASA/ USA	June 27, 1978	L (HH)	25 × 25
SIR-A	NASA/ USA	November 1981 – 2 days	L (HH)	40 × 40
SIR-B	NASA / USA	October 05, 1985 – 8.3 days	L (HH)	25 × 25
Kosmos-1870	Russia	July 1987 -	S (HH)	25 × 25
Almaz-1a	Russia	March 1991	S (HH)	13
SIR-C/X	NASA-JPL/USA, DLR/ Germany ASI/Italy	April 19, 1994 - October 11, 1994	L, C, (quad) X (VV)	

ERS-1	ESA/Europe	1992 - 2000	C (VV)	20 × 4
JERS-1	JAXA/Japan	1992 - 1998	L (HH)	18 × 18
ERS-2	ESA/Europe	1995 - 2011	C (VV)	
SRTM	NASA/JPL/ USA DLR/ Germany ASI/Italy	Feb. 2000	C (HH + VV) X (VV)	30 × 30
ENVISAT	ESA/Europe	2002 - 2012	C (dual)	20 × 4
RadarSAT-1	CSA/Canada	1995 - 2013	C (HH)	20 × 5
RadarSAT-2	CSA/Canada	2007 – Present	C (quad)	20 × 5
ALOS/PalSAR	JAXA/Japan	2006 - 2011	L (quad)	10 × 5
ALOS-2	JAXA/Japan	2014 - Present	L	7 × 7
KOMPSat-5	KARI/ Korea	2014 - Present	X (dual)	3 × 3
TerraSAR-X(TSX)	DLR-Astrium/ Germany	2007 - present	X (quad)	3 × 3
TanDEM-X	DLR-Astrium/ Germany	2010 - Present	X (quad)	
COSMO-Skymed (CSk) – 1/4	ASI-Mid/Italy	2007 - 2010 - Present	X (dual)	3 × 3
RISAT-1	ISPO/ India	2012 - Present	C (quad)	
Sentinel-1	ESA/Europe	2014 - Present	C (dual)	4 × 20

2.3 Radar principles

Radar is based on the general principle of transmitting microwave signals and receiving echoes from targets encountered within the path of the signal. The received echoes indicate the presence of targets, and are used to determine the target's distance and characteristics (Skolnik 1962). The simplest forms of a radar consist of a radio transmitter, a radio receiver, an antenna to transmit and receive the signals, and a display unit (Fig 2.1). The radio transmitter generates a radio wave which is then emitted by the antenna in a specific direction. The signal will travel through the medium (e.g., atmosphere) in the line of sight direction and, if a target lies within the field of view of the emitted pulse, the signal will scatter or reflect off that target. If the radar receiver detects energy reflected from that target, then a signal will be indicated on the display unit. To avoid interference between the transmitted and the received signals, the radar emits the signal as pulses while the receiver is switched off during the transmission, after which it is switched on. Once the pulse is emitted by the radar, the echo will take some time before it returns to the radar (Stimson 1983).

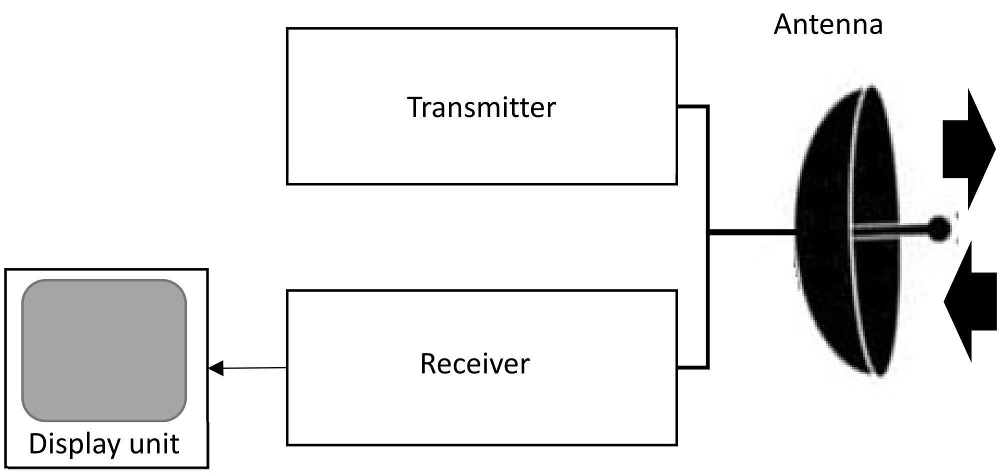

Figure 2.2: Simple Radar configuration

The pulse transmits at the speed of light, and the time lapse between the signal transmission and reception is proportional to the antenna–target distance (i.e., range). The rate at which the pulses are transmitted per second is called the Pulse Repetition Frequency (PRF) (Fig 2.2), which is designed to enable the radar to detect echoes from the designed range (Merrill 2001).

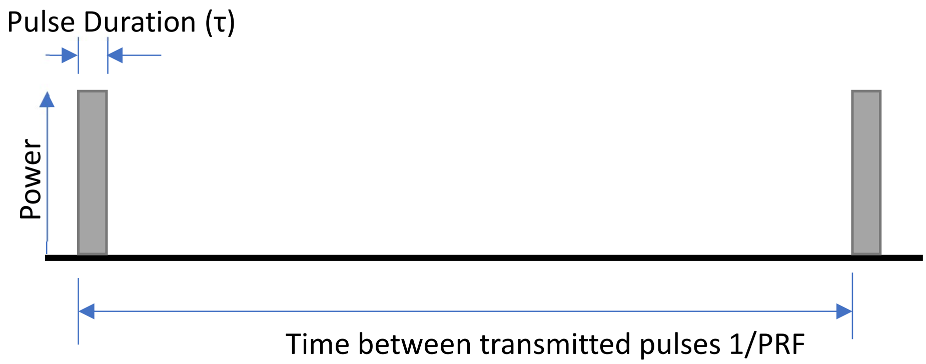

Figure 2.3: Radar transmits pulses at discrete intervals to prevent interference with returning echoes

Different types of radar systems have been developed for specific applications. For example, ground-based radars are mainly used for the detecting, locating, and tracking of aircraft. Ships use radars for navigation in order to avoid collisions with other ships and to detect shorelines. Airborne radars are used for locating other aircraft and ground targets, and also successfully used for ground mapping (further details later in this chapter), and many other different applications (Stimson 1983). Regardless of the type and application, there are some key conditions for successful target detection. First, the target has to be within the radar line of sight, so that the radar can receive an echo from the target. Additionally, the reflected signal should be strong enough that the radar system can differentiate it from the invariable background noise (often referred to as clutter) that is simultaneously received by the system. The ability to detect an echo is ultimately governed by a fundamental equation known as the Radar Equation.

2.4 The radar equation

Consider an ideal isotropic antenna that emits a microwave signal. The energy will be uniformly transmitted in all directions. If a target with a surface area of A_σ is located at distance (R) from the isotropic antenna (Fig 2.3), then the amount of the energy received by that target, known as the target power density (P_σ) or the power per unit area (in units of W m^{-2}), can simply be calculated as the product of the target area and the transmitted energy (P_t), divided by the surface area of a sphere whose radius is the distance from the isotropic antenna, R, (Skolnik 1990);

$$P_\sigma = \frac{P_t\, A_\sigma}{4\pi\, R^2} \qquad (2.1)$$

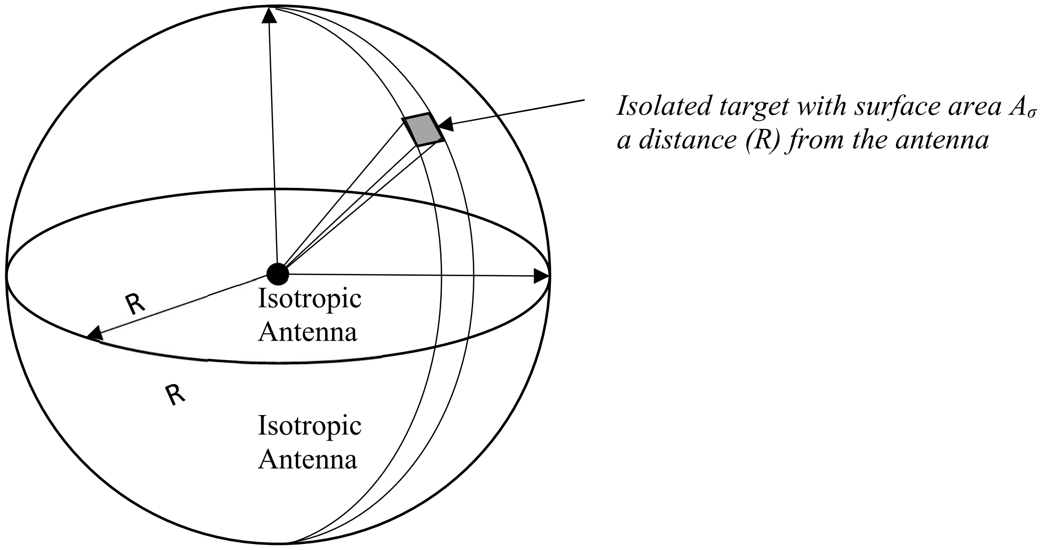

Figure 2.4: Isotropic antenna transmits energy to all directions

As the distance from the transmitter (R) increases, the surface area of the sphere also increases, the power density received by the target at that distance is naturally reduced by the expansion and is proportional to $1/R^2$, which is known as signal path loss.

To overcome this, radar systems utilise a more efficient way to transmit the energy by using a directional antenna to channel most of the transmitted power in a specific direction. The antenna efficiency in focussing energy in a specific direction is called the gain, G_t. For a directional antenna (Fig. 2.4), the power density received by an isolated target whose surface area is A_σ, can be calculated as:

$$P_\sigma = \frac{P_t\, G_t\, A_\sigma}{4\pi\, R^2} \qquad (2.2)$$

Equation 2.2 indicates that targets with larger surface area (A_σ) will usually receive more energy than smaller targets. Furthermore, targets closer to the emitter will receive more energy than identical targets that are at a further distance from the emitter.

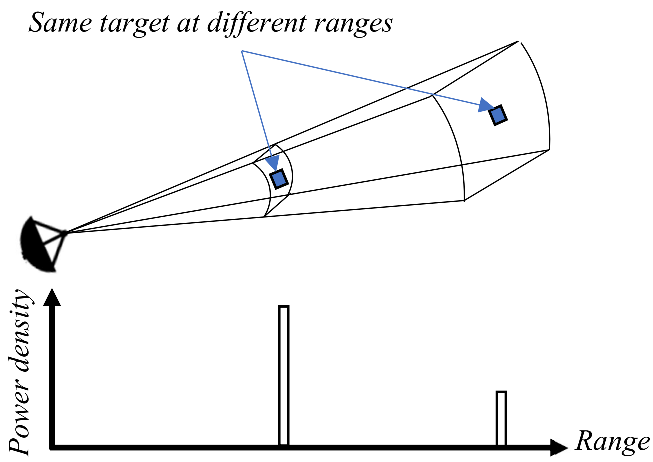

Figure 2.4: Radar using directional antenna to direct its energy into a specific direction

Compared to a target located the same distance from an isotropic antenna, the power density will now be greater due to the antenna gain. This is because the same amount of energy is now focused in a specific direction, rather than distributed in all directions. The amount of energy received by the target is also inversely proportional to the range. As previously mentioned, a target can only be detected if it reflects a sufficient proportion of energy back to the radar. If we assume an ideal point target where all the incident energy is reflected back to the radar antenna without any losses, then the amount of the energy that will be received by the antenna is given by:

$$P_r = \frac{P_\sigma A_e}{4\pi R^2} \tag{2.3}$$

Where P_r is the intensity of the received power by the radar antenna (receiver), and A_e is the effective area of the radar antenna. This is the same equation as the power density from point transmitter but in reverse form, where the energy source this time is the point target. Substituting Eq. 2.3 in Eq. 2.2 yields:

$$P_r = \frac{G_t P_t A_\sigma}{4\pi R^2} \frac{A_e}{4\pi R^2} = \frac{G_t P_t A_\sigma A_e}{(4\pi)^2 R^4} \tag{2.4}$$

The effective area of the antenna that receives the reflected energy is given by:

$$A_e = \frac{G_t \lambda^2}{4\pi} \tag{2.5}$$

Thus, the received power by the radar antenna is:

$$P_r = \frac{G_t \, P_t \, A_\sigma}{(4\pi)^2 \, R^4} \frac{G_t \lambda^2}{4\pi} = \frac{G_t^2 \, \lambda^2 \, P_t \, A_\sigma}{64\pi^3 \, R^4} \tag{2.6}$$

The target area A_σ for an ideal reflector is its radar cross section (RCS), which has units of area and is denoted as the symbol, σ. Substituting this into Eq. 2.6 gives:

$$P_r = \frac{G_t^2 \, \lambda^2 \, P_t \, \sigma}{64\pi^3 \, R^4} \tag{2.7}$$

This formula (Eq. 2.7) is known as the Radar Equation for a point target. As illustrated above, the radar equation is a mathematical representation of the signal propagation from the source (e.g., the radar antenna), to the target, and back to the radar receiver antenna. It can be used to estimate the received power from a point target whose RCS is known, or, conversely, can be used to estimate the RCS of targets based on the intensity of the received power. It can also be used to adjust the radar measurements by deriving a correction factor from the measurements of a target with known scattering parameters, in a process called radiometric calibration, as well as in calculating the maximum radar detection range. (King 1949).

2.5 Imaging Radar

The ability to measure the intensity of the echo and relate it to the target RCS, as well as the radar ranging and locating capabilities, enabled the development of a new imaging system in the 1950s. Using an airborne radar system, the distribution of objects along the range direction, along with the received echoes intensities, can be mapped into a single profile or strip (Fig. 2.5). With the motion of the aircraft, different strips of the terrain are sequentially mapped. These recorded range profiles are then stacked together to produce a pictorial representation of the terrain (Fig. 2.6) that represents the distribution of objects in two dimensions (i.e., the radar range and the aircraft flight path), as well as information about the objects characteristics, such as the RCS. The imaging radar has many advantages over optical remote sensing systems.

Being an active system means that it can operate independently of the sunlight. Adding this benefit to the capability of the microwave signal to penetrate cloud cover, this benefit remote sensing in regions with persistent cloud cover, especially tropical regions, and the Polar regions which suffer from lack of solar illumination for half of the year. Using microwaves as an imaging tool provides the opportunity to study specific physical properties of targets (i.e. scatterers) that are not possible using other types of electromagnetic radiation (e.g., optical, infrared). It is these factors that have encouraged the development of the imaging SAR satellite missions (Hanssen 2001).

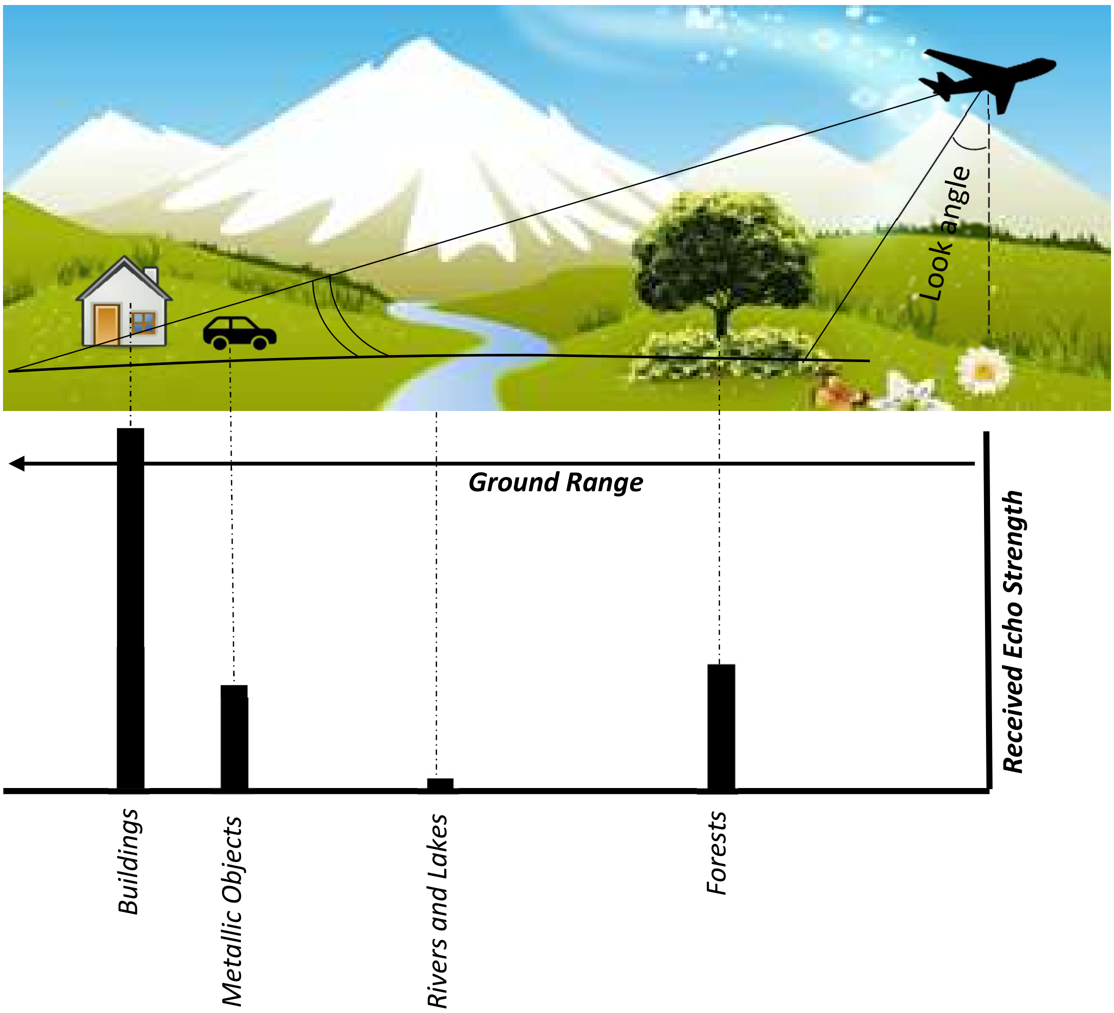

Figure 2.5: Radar Range Imaging

The imaging radar transmits microwave pulses from its antenna obliquely towards the ground, usually at right angle to the direction in which the platform is travelling. A two dimensional image is created by measuring parallel range lines across the moving platform (Carver et al. 1985).

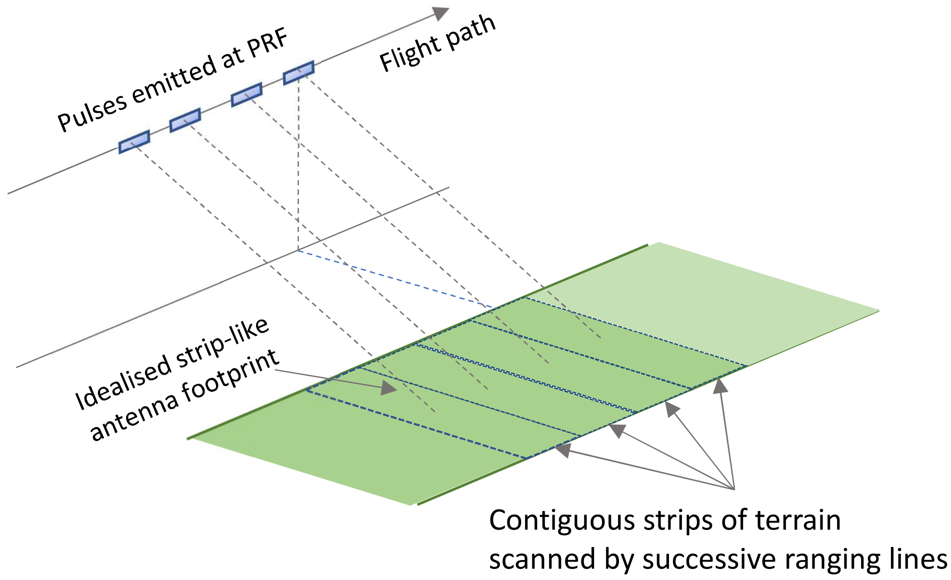

Figure 2.6: Continuous strips imaging to form the image

The PRF typically ranges from a few hundred pulses per second (PPS) for airborne systems to few thousand PPS for spaceborne imaging systems. As with classic radars, the imaging system also measures both the time delay between the transmitted and received signal, and the magnitude of the backscattered signal. From the radar equation, the magnitude of the backscattered signal depends on the target's RCS and is represented as different brightness levels in the image; the stronger the returned signal, the brighter the object appears in the image. For each scanned range line or profile, echoes from objects at different ranges will arrive at different time delays, enabling the image range geometry to be constructed. The first received signals will correspond to reflections from targets closer to the radar (near range) as the two-way travel is less than that for objects in the far range. Fig 2.7 below is an example of a SLAR amplitude image where the two dimensions of this image are the azimuth coordinates. The two types of imaging radars, Real Aperture Radar and Synthetic Aperture Radar (SAR), are described below.

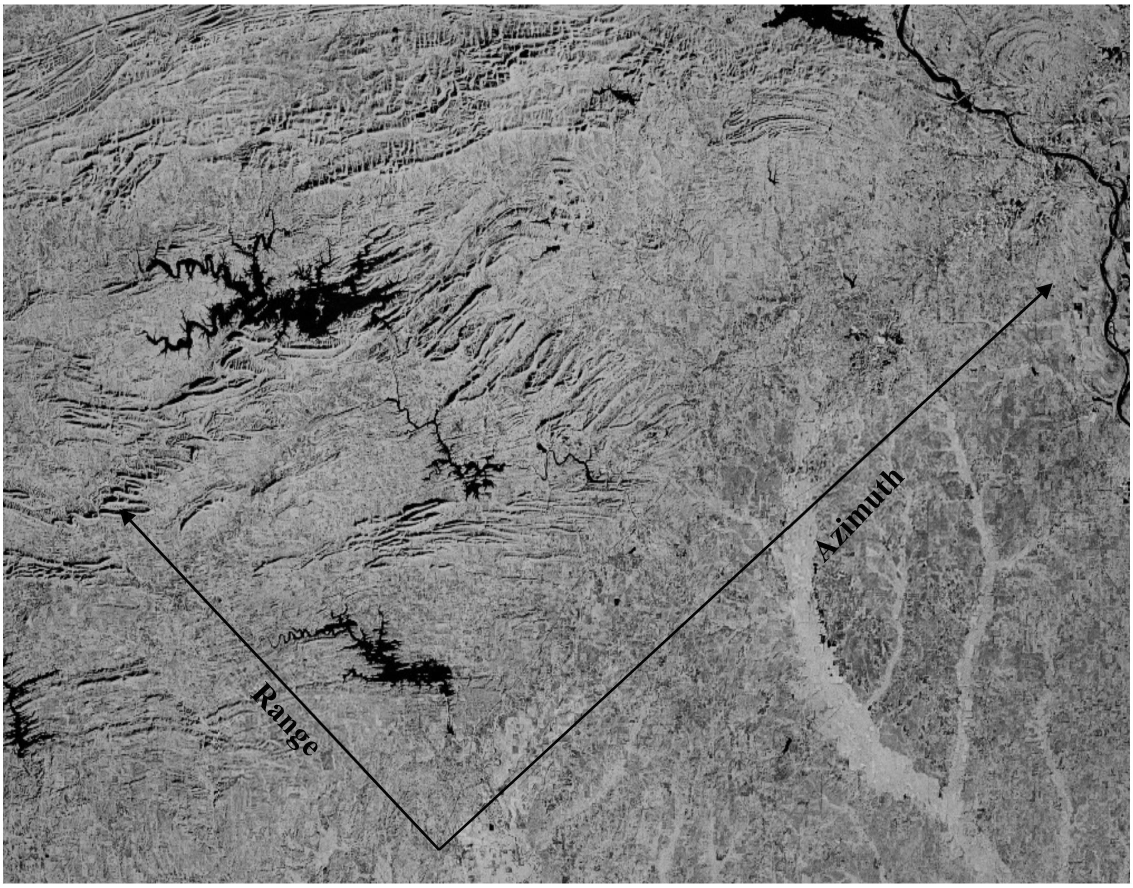

Figure 2.7: SLAR image over Little Rock, Arkansas, USA. Acquisition date: November 1st 1984, X-band HH. (Source: Freely downloaded from USGS Earth Explorer: https://earthexplorer.usgs.gov/)

2.5.1 Real Aperture Radar

Real Aperture Radar is the first type of imaging radar, which is commonly known as Side Looking Airborne Radar (SLAR). A typical SLAR system includes an antenna that is affixed to a moving platform, usually an aircraft, orientated parallel to the flight path (Fig 2.6). As the platform moves, the SLAR antenna emits microwave pulses obliquely in a direction perpendicular to the flight path, called the range direction. The angle between the radar beam and the aircraft nadir is called the look angle. The size of the illuminated area by each pulse in the azimuth direction is determined by the azimuth beamwidth (β) of the radar beam, which is equal to the ratio of the wavelength to antenna length. The size of the illuminated area in the range direction (the swath width) is determined by the elevation beamwidth and is the ratio of the wavelength to the antenna width. Together with the look angle, the elevation beamwidth determines the footprint of the radar pulse, which is the imaged area on the ground. Detailed SLAR geometry can be observed in Fig. 2.8. Since the radar platform is moving while it is scanning, microwaves emitted at a known PRF will image slightly different strips of the ground (Franz Leberl et al. 1976). Emitted microwave signals are scattered by the different objects (scatterers) and some of the scattered energy will return to the radar antenna (backscatter). The backscattered signal received by the radar antenna is then amplified and detected by the receiver. The amplitude of the detected signal is directly proportional to the magnitude of the received signal at any instant. As the radar antenna moves forward while the platform is moving, the radar pulse beam is also moved to new terrain positions. Succeeding pulses scan adjacent terrain strips resulting in a two-dimensional map of the terrain reflectivity, or in other words, a microwave photograph for the earth's surface (Stimson 1983).

2.5.1.1 Spatial resolution

The spatial resolution of an imaging radar can be defined as the shortest distance between two objects which the radar can distinguish as two separate targets (Cutrona et al. 1961). A SLAR system can only resolve the ground objects if it receives separate echoes from each object. Two different types of spatial resolution for the radar system are the range and the azimuth resolution, each of which has its own geometrical characteristics (Fig. 2.8).

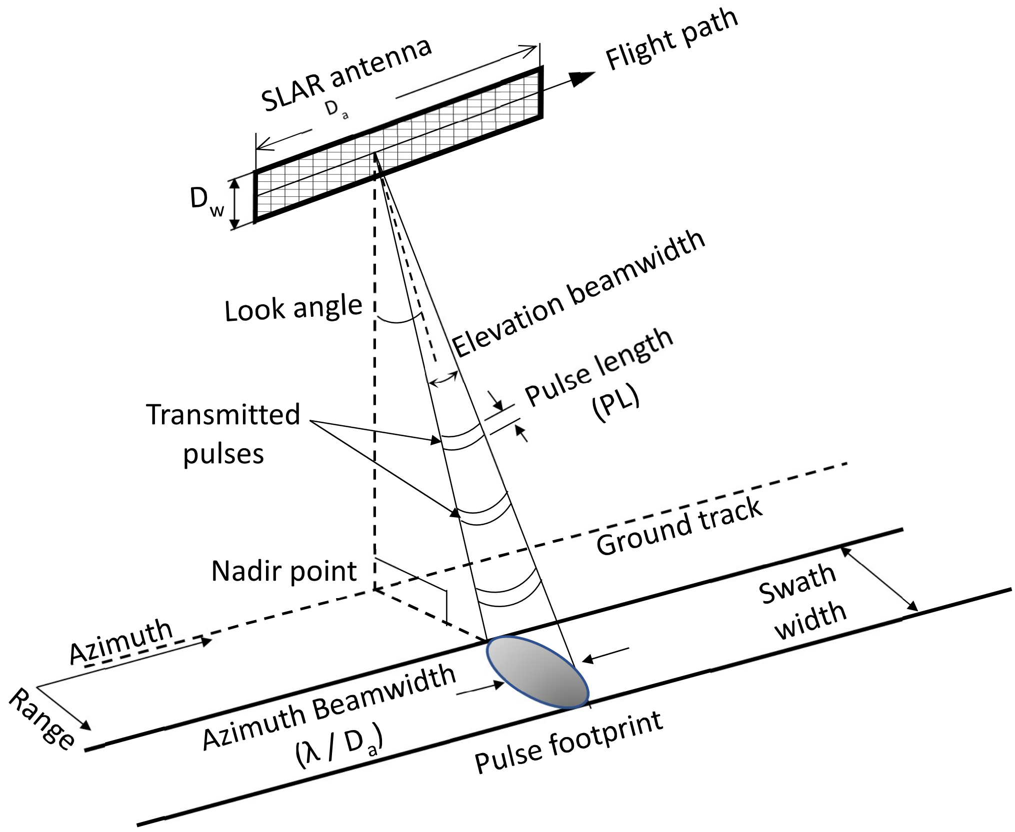

Figure 2.8: Geometry of SLAR system

2.5.1.1.1 Range resolution

Range resolution is the ability of the radar system to resolve objects in the range direction. Two objects in the range direction can only be imaged as separate objects if the separation distance between them is more than half the pulse length. This concept is illustrated in Figure 2.9. The SLAR emits a pulse that has a length (*PL*) determined by the pulse duration, which illuminates a footprint on the ground. If two objects (A and B) are separated in the slant range direction by a distance less than half the pulse length (*PL*/2), then the return signals from these two objects will overlap and they will consequently appear as a single object that extends from A to B (Stimson 1983).

However, if the distance between these two objects is more than $PL/2$, the backscatter from these objects will be received separately and therefore recorded by the radar system as two separate objects. From this principle, the range resolution can be improved by using short pulses (i.e. decreasing the term $PL/2$). However, if the pulse is shortened, the magnitude must be increased to keep the same total energy level in the pulse in order to improve the signal to noise (SNR) ratio. Such systems that are able to transmit short pulses at high energy are very difficult to build. For this reason, most radar systems use chirp signals, which is a pulse compression technique by frequency modulation. Instead of using short pulses, a long pulse is transmitted with the modulated frequency which after processing yields the same results as short pulses (see Section 2.6 for more details).

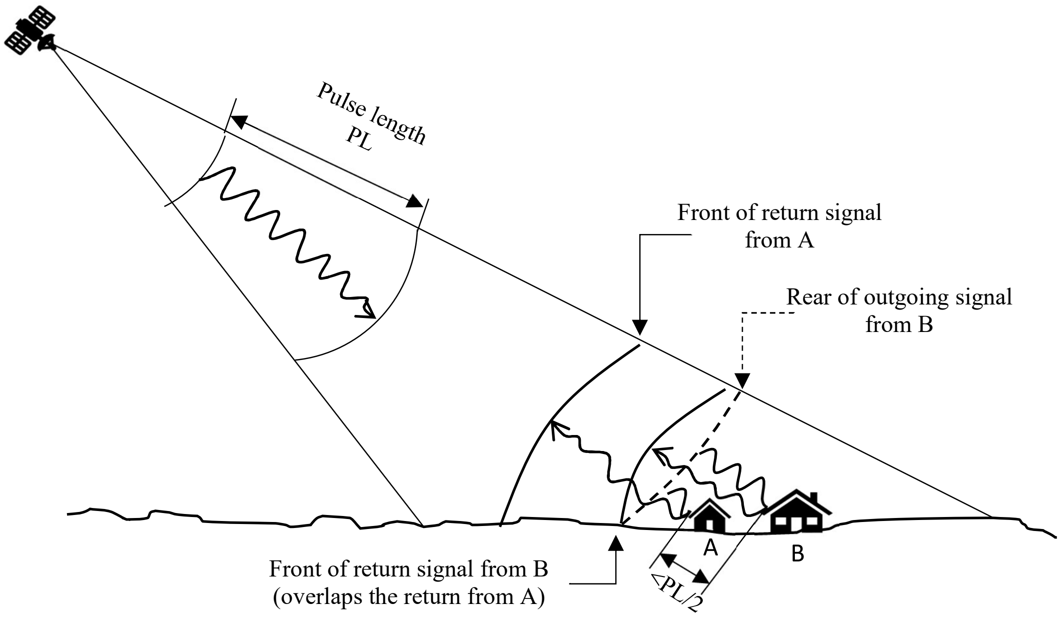

Figure 2.9 Range resolution of SLAR system

2.5.1.1.2 Azimuth resolution

Azimuth resolution is the ability of the radar system to resolve objects in the azimuth direction. In order for two objects with the same range distance from the SLAR system to be imaged as two separated targets in the azimuth direction, their echoes should be received separately by the radar (Curlander 1982).This means that objects need to be imaged in two different pulses, as objects at the same range will appear as a single object if they are illuminated by the same pulse. The minimum distance between any two objects in the azimuth direction has to be at least the size of the illuminated area which is given by the azimuth beamwidth (β) and the range (R). The azimuth resolution (Az_{res}) depends on the beamwidth, antenna length and the wavelength. From Fig. 2.10 below, the radar azimuth beamwidth (β) is determined by the length of the antenna (D_a) and the wavelength (λ).

$$\beta = \frac{\lambda}{D_a} \tag{2.9}$$

$$Az_{res} = \beta R = \frac{\lambda R}{D} \tag{2.10}$$

The azimuth resolution varies with range, where the finest azimuth resolution (*L1* in Figure 2.10) can be obtained in the near range (*R1*), while in the far range (*R2*) the azimuth resolution will be relatively coarse (*L2*).

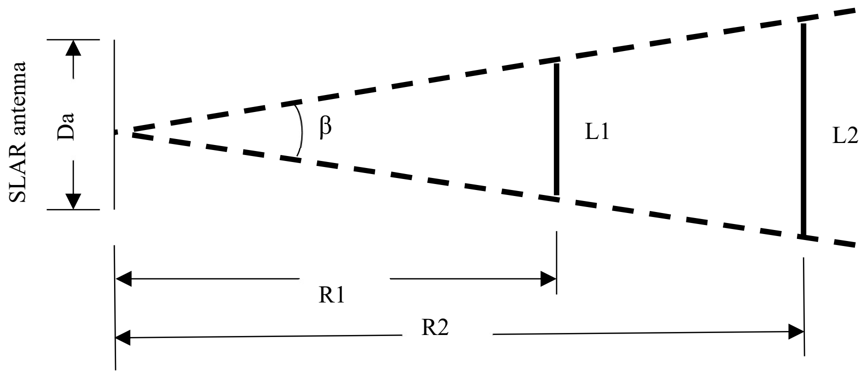

Figure 2.10. Illustration of the azimuth resolution of SLAR imaging radar

From Eq. 2.10 it is apparent that the azimuth resolution can be improved by using a finer beamwidth, which in turn requires a longer antenna or a shorter microwave wavelength (Griffiths et al. 2014). However, both are impractical, as short wavelengths are highly affected by the atmosphere and the size of the antenna is limited by the ability of the platform (airborne or spaceborne) to hold such antenna.

2.5.2 Synthetic Aperture Radar

With improvements in the SLAR azimuth resolution limited by factors that are physically impractical (i.e. increasing the antenna size or sending high energy short pulses), an alternative approach to imaging radar was required. In 1951, Carl Wiley from Goodyear Aircraft Corporation developed a technique to improve the azimuth resolution of a radar image by synthesising a very large antenna from a physically short antenna and the moving platform. This made it possible to resolve the reflection received from two fixed targets along the flight direction, separated by a specific distance, by analysing the frequency of the along track spectrum. Wiley called this method Doppler beam sharpening (Atwood 1952). The frequency of the received echoes from a stationary target are shifted due to the platform motion. Wiley explains the Doppler shift with a simple example, as follows. If two points are located at slightly different viewing angles from the radar, then at any instant these two points will have different speeds relative to the radar location along their motion vectors. Thus, the reflected signals from these two points will have two distinct Doppler frequency shifts (Brown and Porcello 1969). SAR can measure these shifts and use them to resolve the targets in the azimuth direction. The principle of the SAR technique depends on the along track radar motion and a modified signal processing technique. In Fig 2.11 the radar is moving along the flight path in a straight line. The radar receives echo signals from the point target provided that it is within the footprint of the illuminating beam.

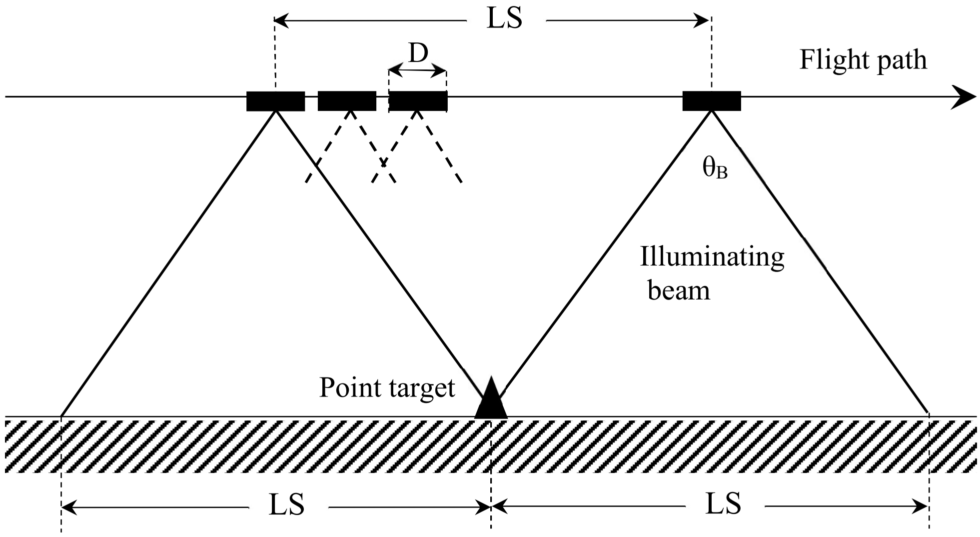

Figure 2.11: Formation of the synthetic antenna

The width of the illuminated area (*LS*) is the same as the path length at which the radar receives the echo signals from that point target, and can be calculated as:

$$LS = R\ \theta_B \tag{2.11}$$

Where θ_B is the beam width of the antenna, which is defined as the signal wavelength divided by the antenna length (real aperture) in radians.

$$\theta_B(rad) = \sim \frac{\lambda}{D} \tag{2.12}$$

All signals received from the target are coherently recorded (i.e., both the amplitude and the phase are recorded) and used to synthesize a linear array of antennas (an extended antenna) (Elachi 1987). The synthesized beam width ($\theta_{synthetic}$) corresponds to the length of the synthetic array (*Ls*) in Fig 2.11, which is equivalent to the ground distance at which the target is in the radar beam field of view during the satellite overpass. The azimuth resolution can then be calculated as:

$$AZ_{res} = R\ \theta_{synthetic} \tag{2.13}$$

Where $\theta_{synthetic}$ is synthetic aperture horizontal beam width, and is half the real aperture (D):

$$\theta_{syntheti} = \frac{\lambda}{2\,D} \tag{2.14}$$

Thus, the azimuth resolution could be expressed as:

$$AZ_{res} = \frac{\lambda\,R}{2\,D} \tag{2.15}$$

In summary, the real antenna is transformed into an array of successive antennas that can be linked together mathematically in the data post-processing stage (Merrill 1990).

2.6 SAR image characteristics

As explained above, a SAR image is a two-dimensional representation of the ground surface scattering, where the horizontal dimension represents the range of the scene and the vertical dimension of the image represents the azimuth direction of the radar platform (Elachi et al., 1982). The amplitude and the phase of the received signals for each pixel are encoded in each pixel as complex numbers (Curlander and McDonough 1991).The main component of the phase is related to the slant range distance between the radar antenna and the target, while the amplitude represents the intensity of the received backscattered signal. The amplitude information can be displayed as a greyscale image – appearing similar to aerial photographs or optical satellite images – while the phase information of a single SAR image has no immediate meaning as each pixel contains an apparently random number (Gabriel and Goldstein 1988). In the following sub-sections, information about the key aspects of a SAR image is provided. This includes a description of the amplitude and phase components of a pixel, along with geometrical distortions affecting SAR images.

2.6.1 Amplitude

The amplitude component of a SAR image pixel value is a measure of that individual pixel's brightness and is a direct representation of the amount of backscattered energy received from the corresponding area. The backscatter depends mainly on the physical and electrical properties of the surface or object, as well as the radar system characteristics. Physical properties include the surface roughness, slope, and inhomogeneities and the electrical properties relate mainly to the dielectric constant of the surface. The SAR system properties are represented by the wavelength, the incidence angle and the polarizations (Elachi et al. 1982). Brighter pixels in a SAR image generally represent areas with objects characterized with large RCS, such as urban areas and exposed rocks. In contrast, smooth surfaces like rivers and lake surfaces tend to reflect the incident energy away from its source and thus appear darker in the SAR image because less backscattered energy is recorded for that part of the scene. As mentioned above, the pixel value – also known as the Digital Number (DN) – can be used to visualize the SAR images as greyscale images, which are useful for qualitative analyses. However, to analyse a target or surface, or perform a comparison between multi-temporal or multi-sensor SAR images, it is compulsory to convert the amplitude into a meaningful physical quantity. This can include the normalized radar cross-section or backscatter coefficient, measured in decibel/m^2 and having values ranging between -40 dB for very dark areas to +5 dB for bright areas (Ferretti et al. 2007). The process of converting the amplitude into these quantities is known as radiometric calibration.

2.6.2 Phase

The phase of each pixel is a measure of the slant-range distance from the radar antenna to the ground targets, and the scattering component of the phase shift due to the signal reflection from the surface. The scattering component can be eliminated between two SAR images over the same area if all the scatterers within the resolution cell preserved their characteristics between the two acquisitions (Goldstein et al. 1988). The phase (ϕ) can be expressed as:

$$\phi_{pixel} = 2.\frac{2\pi R_{pixel}}{\lambda} + \phi_{scatt,pixel} \quad \text{(radiance)} \qquad (2.16)$$

Where R is the slant range to the pixel, λ is the wavelength and $\phi_{scatt,pixel}$ is the scattering component of that pixel. The factor of 2 denotes the two-way distance between the antenna and the target. The actual path length between the resolution cell and the SAR antenna is unknown and the total integer number of wavelengths is also unknown. Instead, the radar can only measure and record a fraction of the wavelength of the returned signal in the range of - π to + π (modulo 2 π) (Goldstein et al. 1988).

The SAR image resolution cell is in the order of a few metres, which is much larger than the SAR wavelength (few centimetres). Each image cell corresponds to an area of the terrain that potentially contains hundreds of scatterers that all contribute to the measured phase of that cell. These scatterers have variable ranges from the radar antenna, and therefore a variable number of cycles from the antenna to the target and back to the antenna again. The overall phase of the image pixel is the coherent summation of all these elementary scatterers and therefore, the pixel phase of a single image seemingly appears random and of no meaning on its own (Massonnet and Feigl, 1998; Zebker and Villasenor 1992).

2.6.3 Geometric distortions

A radar image is typically affected by three types of geometrical distortions that are associated with the side-looking geometry of the radar and the fact that the radar is ranging-based system. The geometrical distortions manifested in the radar image are foreshortening, layover and shadow, which are created by the terrain relief and in some cases, tall buildings (Lewis and Macdonald 1970).

2.6.3.1 Foreshortening

Foreshortening occurs when a topographic feature (e.g. the side of the hill) faces the look direction of the incidence microwave pulses (MacDonald and Lewis 1976). The hill slope labelled 'AB' in Figure 2.12 is facing the radar look direction, with the base (labelled A) and the summit (B) having approximately the same slant range distances. Consequently, the echo from the base and the summit will be detected by the sensor at the same time, despite the actual ground range distance between them. This is a common phenomenon in mountainous regions and results in a compressed appearance of the terrain in the range direction, particularly from fore slopes that face the direction of the incident radar pulses. This can be compensated for by geocoding the image, provided that a suitable digital elevation model (DEM) is available.

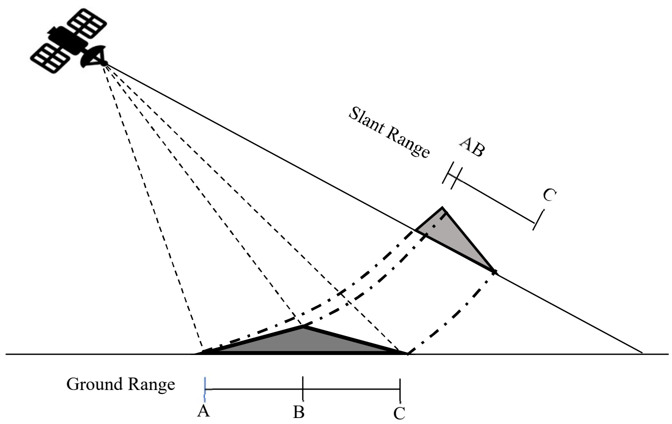

Figure 2.12 Foreshortening

2.6.3.2 Layover

Layover is a geometrical distortion in the SAR images that occurs when the slant range to the summit of a hill is less than the slant range to the base (Holtzman et al. 1978). Therefore, the return from the summit (B) in Fig. 2.13 will reach the sensor sooner than the return from the base (A), causing the features to appear in the incorrect locations within the image. This distortion is an extreme case of foreshortening and cannot be compensated for.

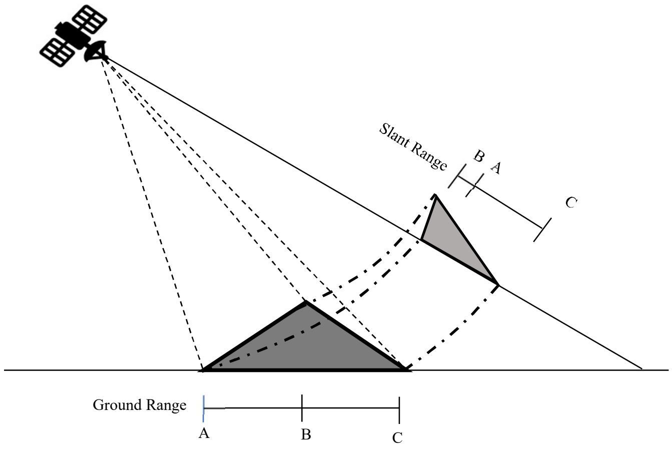

Figure 2.13 Layover

2.6.3.3 Shadow

In mountainous regions, a radar beam will not be able to measure everything within its footprint if the signal is obstructed by a relief feature. For example, in Figure 2.14, the slope labelled BC is not illuminated by the radar beam because is not oriented in the look direction of the incident radar beam. Therefore, this slope is essentially in the shadow of the slope labelled AB and will appear dark in the SAR image because it has a low brightness value.

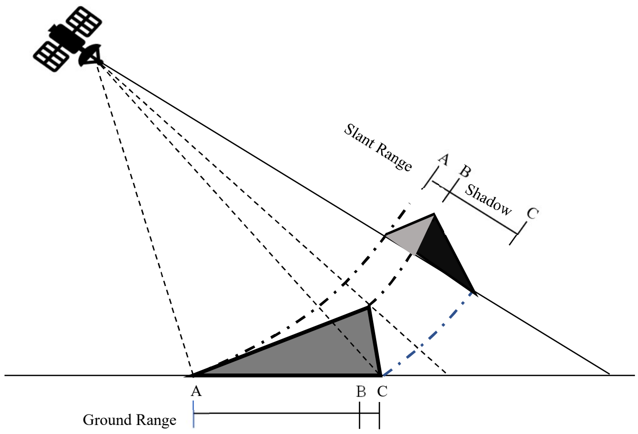

Figure 2.14 Shadow

2.6.4 Image speckle

Radar images commonly contain a random pattern of bright and dark pixels that produces a “salt-and-pepper” effect known as speckle. Fig. 2.15 provides an example of speckle observed in SAR images. Zooming into a small area of the image clearly shows the level of noise that the images can suffer from. This image artefact is associated with constructive and destructive interference of backscattered signals. A single resolution cell usually contains many objects, or scatterers, that are randomly organized within the resolution cell. Each of these scatterers will backscatter the incident signal in specific way depending on its physical and electrical properties. The radar receives echoes from all these individual scatterers and coherently combines them all into a single value. Combining multiple signals together will result in constructive and destructive interference between these signals. Constructive interference, Fig 2.16 A, occurs where the return signals in a cell are in phase with each other, resulting in the amplification of the overall intensity to produce a bright pixel in the image. On the other hand, if the returning signals from within a single resolution cell are in opposite phases (i.e. one signal is at its wave cycle peak and the other one is at a trough) as in Fig. 2.16 B, these signals will cancel out and reduce the intensity of the combined signal to generate a dark pixel (Frost et al. 1982). The combination of constructive and the destructive interferences within the scene gives the radar image its grainy appearance. Speckle can be reduced, but not eliminated, by using image processing techniques, of which the most widely used is the multi-looking technique. This involves averaging several pixels from the same image to produce a smooth image. The number of images used in the averaging process is called the number of ‘looks’ (Goodman 1976).

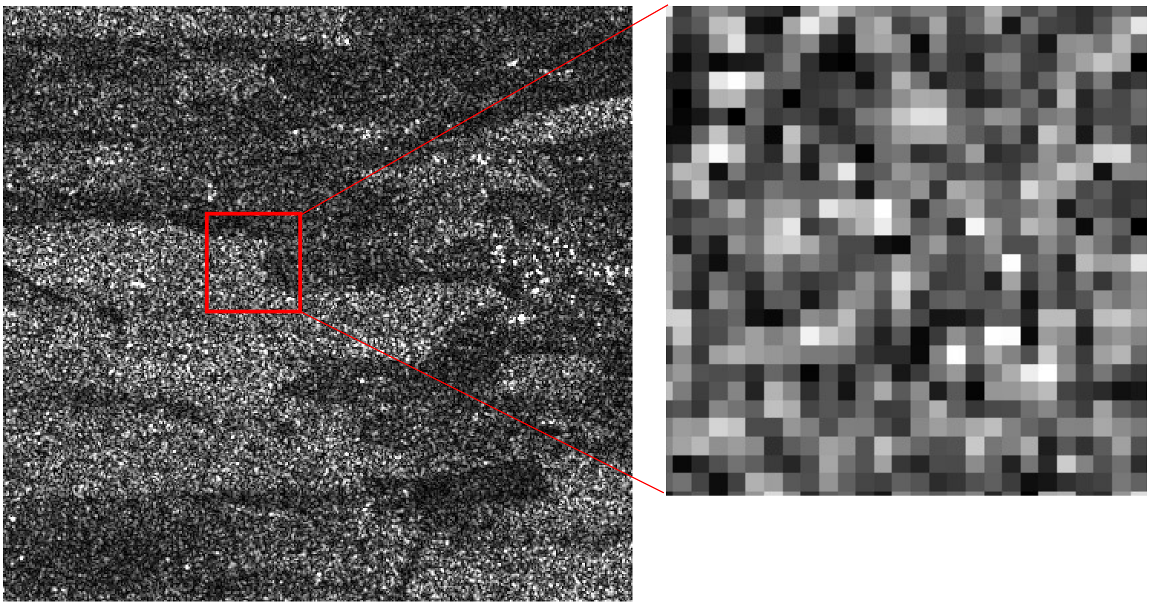

Figure 2.15: Speckle noise in SAR images

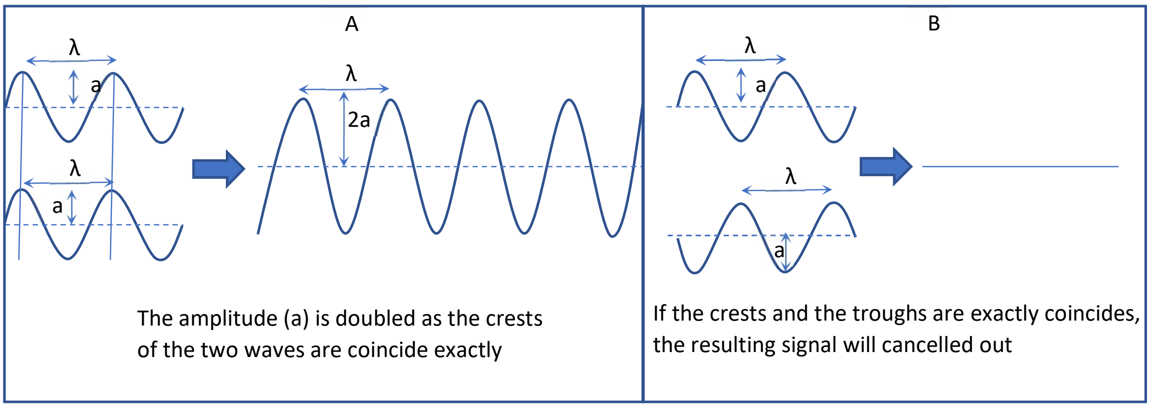

Figure 2.16: Two-wave superposition results in (A) constructive interference when they are in phase, or (B) destructive interference when they are out of phase

2.7 SAR Interferometry

SAR Interferometry (InSAR) is one of the most important, rigorous and robust remote sensing techniques that utilises SAR data to obtain high accuracy measurements of Earth's geophysical parameters, such as surface topography (Graham 1974) and ground displacement (Gabriel et al. 1989).

As mentioned in the previous sections, the SAR image is a matrix of complex numbers, where the phase of each pixel is related to the sensor-to-target distance. This distance consists of an integer number of whole wavelengths, plus a fraction of a wavelength. The radar receiver only detects and record that fraction of the wavelength, which is observable as phase shift between the sent and received signals, Fig. 2.17.

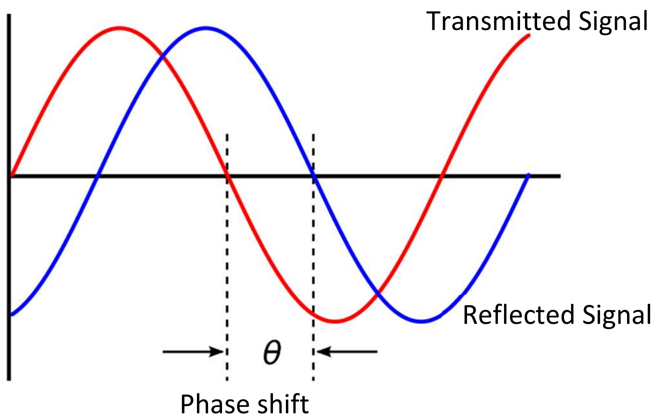

Fig. 2.17 The phase shift between the transmitted and reflected signals

The observed phase shift (ϕ) of pixel P is a combination of four components:

$$\Phi(P) = \varphi + \frac{4\pi}{\lambda} r + \alpha + \nu \tag{2.17}$$

Where:

φ: is the phase contribution due to the location of the elementary scatterers within the resolution cell of pixel *P*.

4πr/λ: is the geometric contribution where r is the radar antenna to the target distance. This is the most important phase contribution for any InSAR analysis.

α: represents the atmospheric effects on the radar signal. Water vapour and fog, as well as the free particles in the atmosphere, affect the propagation speed of the radar signal.

ν: is the noise, mostly thermal noise.

Therefore, the phase of a single SAR image is of no practical use, as it is impossible to separate the different phase contribution from the above sources. The phase of a SAR image is only known modulo-2π, all wrapped phase values appear to be completely uncorrelated for adjacent pixels.

SAR interferometry aims to use the SAR image phase observations as a sensitive tool for topographic mapping, and deformation monitoring. Instead of using a single SAR image, SAR interferometry measures the phase differences between two SAR acquisitions over the same area. The phase difference between two well aligned SAR images is illustrated in an interferogram. The interferogram is an interference mode of the phase differences, appearing like fringes, that contains important information about the relative geometry of the two satellite positions and the terrain (Zebker and Goldstein 1986, Massonnet and Feigl 1998). The phase difference of pixel P from two well-aligned SAR images can be presented as:

$$\Delta\Phi(P) = \Delta\varphi + \frac{4\pi}{\lambda}\Delta r + \Delta\alpha + \Delta\nu \qquad (2.18)$$

The interferogram is an image of the phase differences ($\Delta\phi$) of all pixels. Mathematically, the interferogram can be generated by multiplying the phase of the first image, namely the master image, by the complex conjugate of the second image, the slave:

$$I = Z_m Z_s^* \qquad (2.19)$$

Where:

Z_m is the phase of the master image, and Z_s is the phase of the slave image, the star represents the complex conjugate of the slave.

There are two types of interferometry, depending on the image acquisition method (Fig. 2.18). The platform could host two SAR antennas which image the earth simultaneously from slightly different look angles, such as the case of airborne SAR missions or the Shuttle Radar Topographic Mission (SRTM). This acquisition geometry is known as single-pass interferometry, where the separation distance between the two antennas (baseline) is fixed and precisely measured. The other acquisition geometry involves single SAR antenna hosted by the platform. The platform can repeat its track precisely at regular time periods, such as the case of orbiting spaceborne SAR systems. This is known as repeat-pass interferometry, where the two SAR images are acquired at two different times from slightly different orbital positions and the baseline is variable between any two acquisitions (Evans et al. 1992).

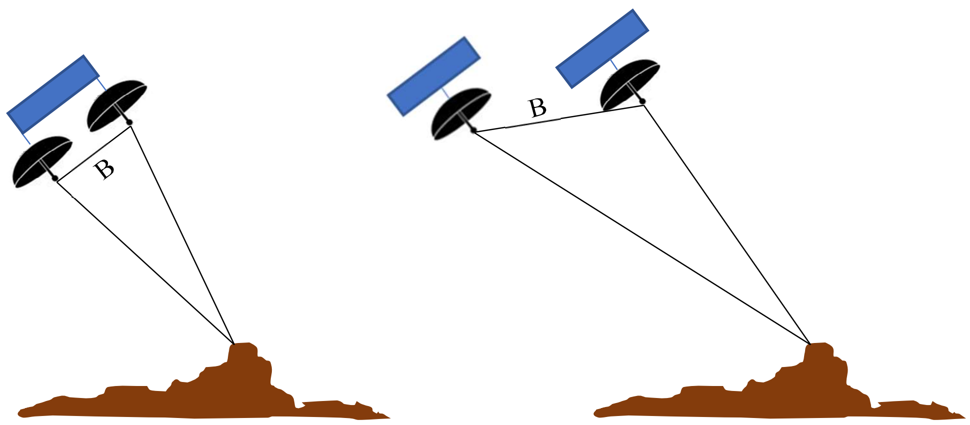

Figure 2.17: Geometry of SAR Interferometry. Left: single-pass case, two SAR systems acquired simultaneous images from different look angles at the same time. Right, repeat-pass case, two SAR systems acquired from different look angles at different times. In both cases, the distance between the two antennas (B) is known as the baseline.

Repeat-pass interferometry has some drawbacks compared to the single pass method, which can make its application more difficult. First, the separation distance between the two satellite passes (the baseline) can only be calculated form the orbital information of the satellite orbits, and not direct measurements. Secondly, the change in the atmosphere between the two passes can significantly cause delays to the signal phase which will generate errors in the interferometry (Gabriel and Goldstein 1988). Another possible drawback to repeat-pass interferometry is that the content of the scene between the two passes might change, which will cause decorrelation between the two observations (Zebker et al. 1994). This decorrelation appears as noise in the interferogram. Repeat-pass interferometry is widely applicable with spaceborne SAR systems, as the satellite can repeat similar cycles every time it orbits. In contrast, with aircraft it is very difficult to repeat similar passes and therefore, it is an impractical and challenging task to use airborne SAR systems for interferometry (Massonnet and Feigl

1998). Thus airborne repeat-pass interferometry is not a viable method for DEM mapping (Gray and Farris-Manning 1993).

Conversely, in single-pass interferometry the same platform holds two antennas, separated by a fixed distance (baseline), enabling simultaneous imaging of the earth from two slightly different look angles (Zebker and Goldstein 1986). This acquisition geometry could overcome the limitations of the repeat-pass interferometry of the baseline as it is fixed and precisely measured, and the atmospheric effects are neglected as the two images are acquired simultaneously. Finally, simultaneous imaging for the scene means that no decorrelation occurs between the images, thus this method is widely used for topographic mapping. This technique was successfully applied to the spaceborne SAR mission of the Shuttle Radar Topographic Mapping mission (SRTM) in February 2000. During its 11 day mission, the SRTM acquired data to generate a digital elevation model (DEM) of the landmass between latitudes 60° North and 56° South, using single-pass interferometer at 30 m resolution and 15 m vertical accuracy (Farr and Kobrick 2000). This is one of the most successful missions that demonstrates the capability of InSAR as a tool for topographic mapping. However, if the scene is changed (displaced), such as is often the case for earthquakes, this technique cannot be used to detect ground displacement as the two images are acquired at the same time and no change can be detected. In such circumstances, two-pass InSAR can detect the change in topography between two scenes, which makes it more applicable for topographic change detection or surface deformation studies.

2.7.1 InSAR Configuration

Each pixel in the SAR image is processed in Single-Look Complex (SLC) format, which contains information about the phase and the scattering properties within the pixel. To understand the interferometric phase, consider the target (*P*) in Fig 2.18 that is being observed by two SAR images acquired from different positions (t_1 and t_2). The range (distance) from t_1 is R1 and from t_2 is R2. The viewing angle of that point is slightly different between the two satellite positions. The separation distance between the two satellites is known as the baseline (B), and its projection to the line-of-sight (LOS) is the perpendicular baseline ($B_{\perp}$). Eq. 2.20 represents the phase (ϕ) of P from a single SAR image (Li and Goldstein 1990), which is directly related to the two-way distance travelled by the signal; from the sensor to the target and back to the sensor again:

$$\phi_1 = 2.\frac{2\pi R_1}{\lambda} + \phi_{scatt,1} \tag{2.20}$$

And the phase of P from the second image is given by Eq. 2.21:

$$\phi_2 = 2.\frac{2\pi R_2}{\lambda} + \phi_{scatt,2} \tag{2.21}$$

When viewed from two satellites, there will be slightly different distances between the two SAR positions and the target. SAR interferometry utilizes the phase information of each pixel to calculate the difference in range measurements (ΔR) made during the acquisitions. The contribution of the pixel scattering component (ϕ_{scatt}) is unknown, thus, the phase values from a single SAR image have no practical meaning. If we assume that the target is unchanged between the two acquisitions and remains correlated (i.e., no temporal decorrelation) – such as the case of single-pass interferometry – these scattering components would be cancelled out by differencing the two equations above:

$$\Phi_{scatt,1} = \Phi_{scatt,2} \tag{2.22}$$

$$\phi_{int}\ (\Delta\phi) = \phi_2 - \phi_1 = \frac{4\pi}{\lambda}\ (R_2 - R_1) \tag{2.23}$$

Which is only related to the geometrical contribution to the phase (ΔR), or the topography. ΔR is usually much larger than the wavelength (λ). Therefore, the measured phase of a single point ($\Delta\phi$) has an ambiguity of many wavelengths (cycles). Thus, the interferometric phase of a single point has no practical use. On the other hand, variation in the travel path ($R_2 - R_1$) of adjacent pixels (just few metres apart) is much smaller than the wavelength. As a consequence, the variation in the interferometric phase of adjacent pixels ($\Delta\phi$) is not ambiguous. The interferogram is a map of $\Delta\phi$ over an extended area, which contains information about the geometry of the two satellite SAR images and appears as a series of fringes where each fringe is a full phase cycle (2π) (Ferretti 2014). The interferogram is a highly accurate map of the phase difference over the terrain which can be used to map the surface topography for every pixel in the interferogram. This technique was successfully used to produce a high-resolution DEM from airborne SAR imagery (Zebker and Goldstein 1986), and a global DEM mapping from the SRTM mission (Farr et al., 2000).

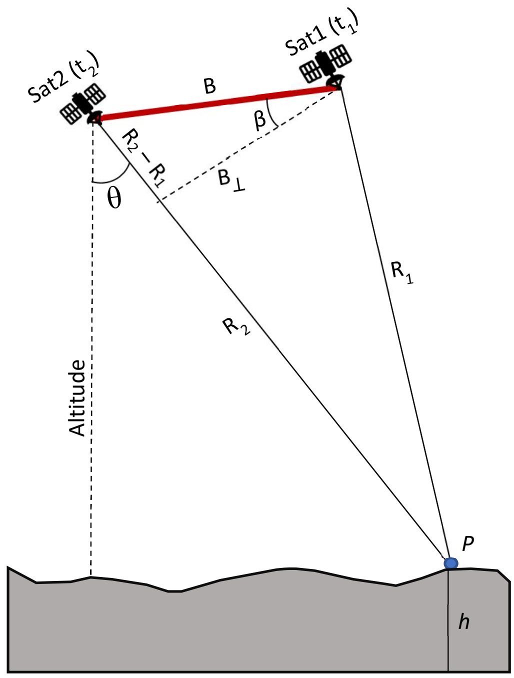

Figure 2.18: The principles of SAR interferometry. Sat1 and Sat 2, are the two satellite positions, R1 and R2 are the distance to Sat1 and Sat2, respectively. B spatial baseline, B⊥ perpendicular baseline, θ look angel, β angle between absolute and perpendicular baseline, ΔR distance difference between the two ranges, and h height of object on surface

2.7.2 Differential Interferometry

Differential InSAR (DInSAR) is an advanced type of SAR interferometry that can detect surface displacement to a very high degree of accuracy. It is a change detection technique that aims to quantify the relative movements in the scene's scatterers between two SAR observations (Gabriel et al. 1989). DInSAR is based on modelling and removing the topographic phase signature from the interferogram to isolate the phase change associated with surface deformation.

If the target P is displaced between the two SAR acquisitions by a distance (d) in the radar line of sight (Fig 2.22), then the equations above will become:

$$\phi_1 = \frac{4\pi\, R_1}{\lambda} + \phi_{scatt,1} \tag{2.24}$$

$$\phi_2 = \frac{4\pi\, (R_2 + d)}{\lambda} + \phi_{scatt,2} \tag{2.25}$$

$$\Delta\phi = \phi_2 - \phi_1 = \frac{4\pi}{\lambda}\,(R_2 - R_1) + \frac{4\pi}{\lambda}\, d \tag{2.26}$$

The InSAR phase component, $\frac{4\pi}{\lambda}\,(R_2 - R_1)$, is related to the topography and can be simulated and removed from Eq. 2.26 using knowledge of the orbital information for the two satellite positions and a digital elevation model for the area of interest. Removing the topographic phase component of Eq. 2.26 will leave the phase component associated with the displacement of the target. It is the process of removing the topography component from the interferometric phase that differential interferometry refers to. However, the computed phase difference is not entirely related to the scene displacement, but it is also combined with other sources of phase difference, such as the atmospheric effects, errors due to the DEM used in the simulation process, and a noise term which is related to the decorrelation in the scattering components between the two scenes.

$$\Delta\phi_{diff} = \frac{4\pi}{\lambda}\, d + \varphi_{atmo} + \varphi_{topo} + \varphi_{noise} \tag{2.27}$$

Where φ_{atmo} is the atmospheric phase delay, φ_{topo} is the errors associated with the used DEM in the simulation process, and φ_{noise} is the error due to the correlation between the two images. DInSAR is a powerful tool for surface deformation detection and monitoring over large areas (Massonnet et al. 1993, Massonnet and Feigl 1998). The DInSAR measurements are also modulo 2π and so phase unwrapping is required to calculate the relative displacement between the pixels.

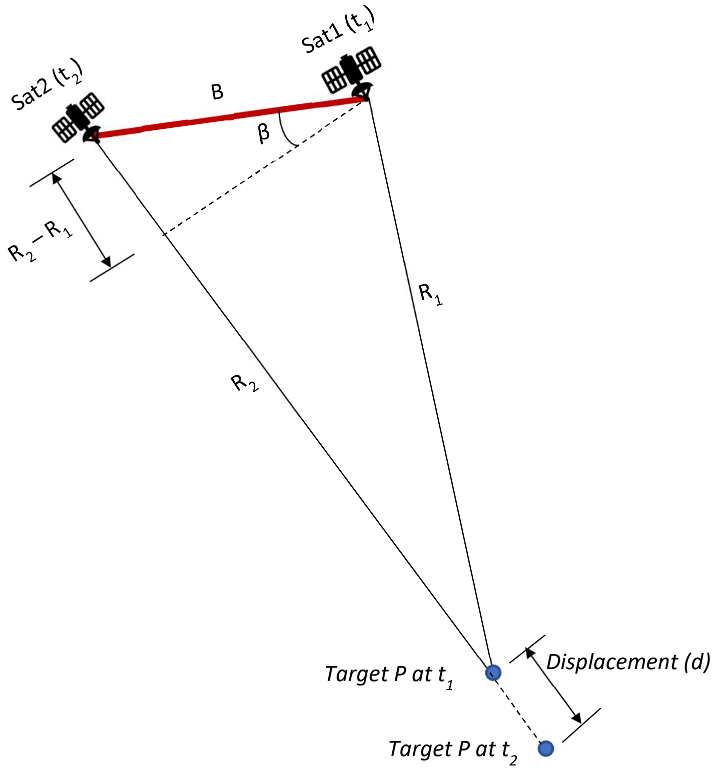

Figure2.19: Displacement in the second observation

2.7.3 Decorrelation in SAR Interferometry

Physical change in the target (or surface) that occur between the two SAR acquisitions is known as temporal decorrelation, which is a complex function of the change in the radar signal reflectivity of the surface between the two acquisitions. The interferometric phase equation assumes that the location and the nature of all the elementary scatterers within the resolution cell remain static between the two SAR acquisitions. This is so the scattering component can be eliminated when generating the interferogram. Two conditions need to be met for this assumption to be valid (Zebker & Villasenor, 1992):

1- The acquisition geometry between the two SAR images should be identical;
2- All the elementary scatterers within the resolution cell remain unchanged between the two SAR acquisitions, or in other words, the speckle pattern between the two images should be the same.

If one of the above two conditions is not satisfied, the phase difference (and the interferogram) of that resolution cell will contain noise. The level of noise depends on the level of similarity between the two images. Similarity, or the coherence, can be measured by the correlation coefficient (γ) between the two SAR images (s_1 and s_2), and can be computed as follow:

$$\gamma = \frac{|\langle s_1 s_2^* \rangle|}{\sqrt{\langle s_1 s_2^* \rangle \langle s_1 s_2^* \rangle}} , \quad 0 \leq \gamma \leq 1 \qquad (2.28)$$

Where the two SAR images (s_1 and s_2) are observing the same area from slightly different locations and acquired at two different times. The star symbol (*) refers to the complex conjugate product. The angled brackets are the ensemble averaging. If all scatterers remain static in terms of their positional and physical characteristics between the two images, the coherence will tend to the maximum value of 1. If the scene is completely changed between the two images (i.e. temporally decorrelated), then no correlation between the images exists and the coherence is 0. Changing the positional or physical properties of the scatterers will cause the coherence to decrease. If some scatterers within the cell kept their positional characteristics, then the coherence could be any value between 0 and 1. Generally, urban areas, exposed rocks and soil have higher coherence than vegetated areas as the physical change over vegetated areas tends to be higher in the time scale of the two images (Zebker and Villasenor 1992).

2.8 The interferometric processing procedure

Owing to its capabilities, the advanced DInSAR technique is widely used for the detection and monitoring of the Earth's surface motion over wide areas with sub-centimetre accuracy. The general steps of the interferometric processing chain include co-registration, interferogram formation, and phase unwrapping. Fig 2.21 below represents a typical flowchart for the DInSAR processing chain (Hanssen, 2001).

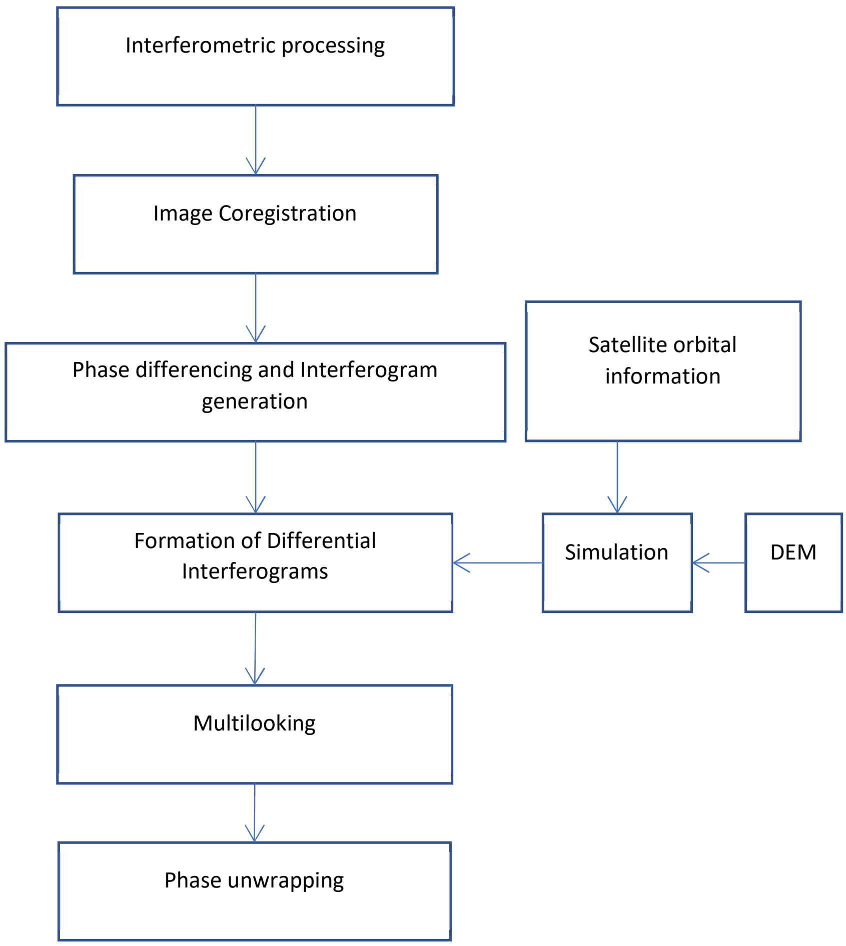

Figure 2.21: Flowchart of Interferometric processing steps

2.8.1 Co-registration

Although a satellite has a repeat-pass geometry, it cannot precisely repeat the exact same orbital location with each pass. That means the start azimuth time and the stop azimuth time of the two images are not the same and the look angles will be different, and so the scattering mechanism from the surface will also different. This results in two images that have difference in the coverage area, the rotation, and backscattering values. However, SAR interferometry is a very precise processing technique and requires the geometry of the two SAR images to be exactly the same. Therefore, the two SAR images must be co-registered to within subpixel accuracy (Ferretti et al. 2007). The image co-registration process aims to transform the location of each pixel from the second image (slave) to the corresponding locations of the first image (master) to sub-pixel accuracy (Just and Bamler 1994).

2.8.2 Interferogram formation

The resulting images after the co-registration process are two complex matrices that are identical in size. The interferogram is the phase difference between two well aligned images, and is the product of multiplying the first co-registered image by the corresponding complex conjugate of the second image on a pixel by pixel basis:

$$\emptyset_{i,j} = S_{1_{i,j}} . S^{*}_{2_{i,j}} \tag{2.29}$$

Where $\Phi_{i,j}$ is the interferometric phase of pixel i,j, S_1 and S_2 are the master and slave images respectively, and * is the complex conjugate. The resulting interferogram is a complex matrix where its phase is the difference of the two input images and its amplitude is their product.

2.8.3 Multilooking

Speckle noise is commonly observed in all coherent imaging systems, i.e., radar imagery, which degrade the quality of the data. Eventually, it will exist in the interferogram due to the speckle characteristics of the two SAR images used to create the interferogram. To reduce the noise in the interferogram, a procedure called multilooking is applied to increase the image Signal to Noise ratio (SNR) as well as improving the accuracy of the phase unwrapping process (Goldstien et al. 1988). This involves spatially averaging several adjacent pixels (looks) into one pixel. Multilooking is usually performed simultaneously with the complex multiplication for interferogram creation by applying a range-azimuth ratio. Although multilooking process will degrade the image resolution by increasing the pixel size, it greatly improves the interpretability of the interferogram as well as the pixel statistics (Lee et al., 1994). The mean of the multilooked image will remain same as the original image, and the standard deviation will be decreased. SNR corresponds to the ratio between the mean and the standard deviation; therefore, the SNR will be increased. The coherence defined in eq. 2.28 can be calculated for each pixel in the complex interferogram. Coherence is a measure for the interferometric phase accuracy. The absolute value of the coherence is a function of SNR (Foster and Guinzy, 1967; Zebker and Villasenor, 1992; Bamler and Just, 1993):

$$|\gamma| = \frac{SNR}{SNR+1} \qquad (2.30)$$

As the multilooking improve the SNR, the coherence is improved as well and therefore make the phase unwrapping simpler, more robust, and more efficient. Multilooking is a widely used approach for mitigating the speckle in the SAR images, but it reduces the spatial resolution of the image (De Leeuw and De Carvalho 2009). The size of the neighbourhood included in the averaging is called the multilooking window that will yield square pixels, rather than rectangle ones.

2.8.4 Phase Unwrapping

The resulting differential interferogram is wrapped, where the pixel values are modulo 2π. The phase difference across the interferogram will contain one or more 2π jumps. To determine the phase difference across the image, an integer number of 2π jumps has to be detected and mathematically removed. The wrapped phase in Fig 2.23 has several 2π jumps. In order to retrieve any useful information from the phase, these phase jumps need to be calculated and removed for any analysis. This process is called phase unwrapping and the resulting 'unwrapped' phase is a continuous phase image that is free of any 2π jump. Fig. 2.22 is an illustration of an optimal case for a 1-dimensional phase where the modulo phase has no noise and thus, no discontinuities between the adjacent points. The phase unwrapping is one of the most difficult tasks in the DInSAR processing chain. This is because, in the real data scenario, the wrapped phase contains some level of noise, which makes the detection of the 2pi jumps very difficult. There are two main approaches for phase unwrapping; the residua-based algorithm by Goldstein et al. (1988) and the least squares algorithm by Zebker and Lu (1998). In contrast to the 1D example above, the phase is unwrapped in two directions (2 dimensions). The gradient is computed between adjacent pixels and integrated over a given path from a starting point (i.e. the reference point). Thus, all the phase values of the unwrapped interferogram are relative to a selected reference point (Ghiglia and Pritt 1998).

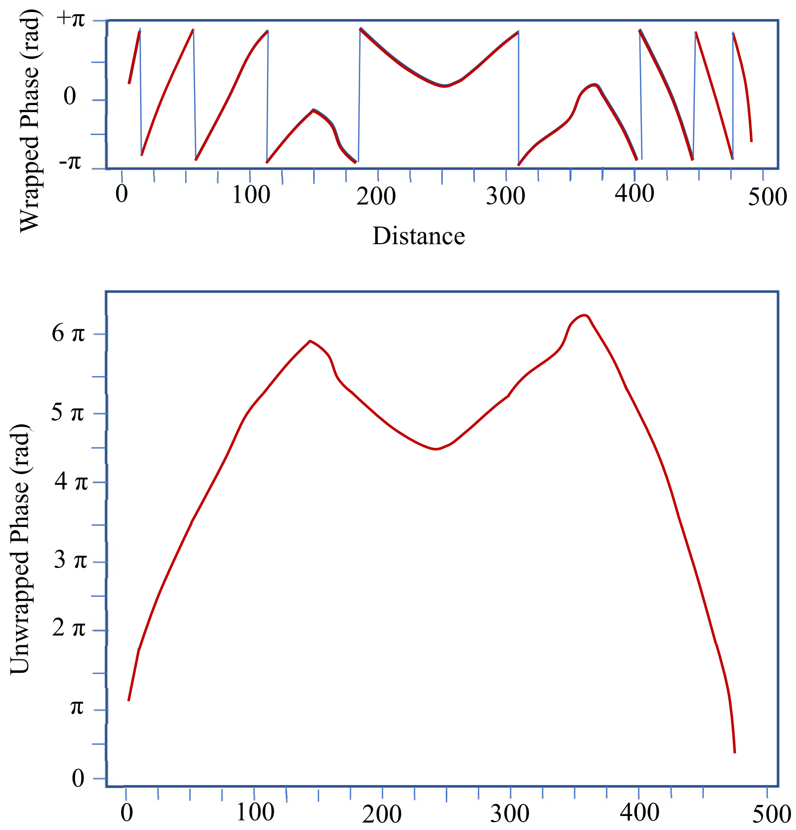

Figure 2.22: The first image is the wrapped phase of the interferogram where the values range between -πi and +π (Modulo 2π). The second image is the unwrapped phase of the interferogram

Fig. 2.23 summarizes the general steps of the InSAR processing chain in a graphical representation. Starting from two co-registered SAR images, the interferogram is generated by differencing the phase of these images. To remove the topographic phase component from this interferogram (the first term in Eq. 2.21), a DEM for the same area is used, along with the precise ephemeris data for the satellite, to simulate an interferogram that represents the topography of the study area. Subtracting the simulated interferogram from the interferogram generated above, results in a differential interferogram whose signal is a combination of the four components in Eq. 2.22. This differential interferogram must then be unwrapped to get the continuous phase image of that area, as discussed above.

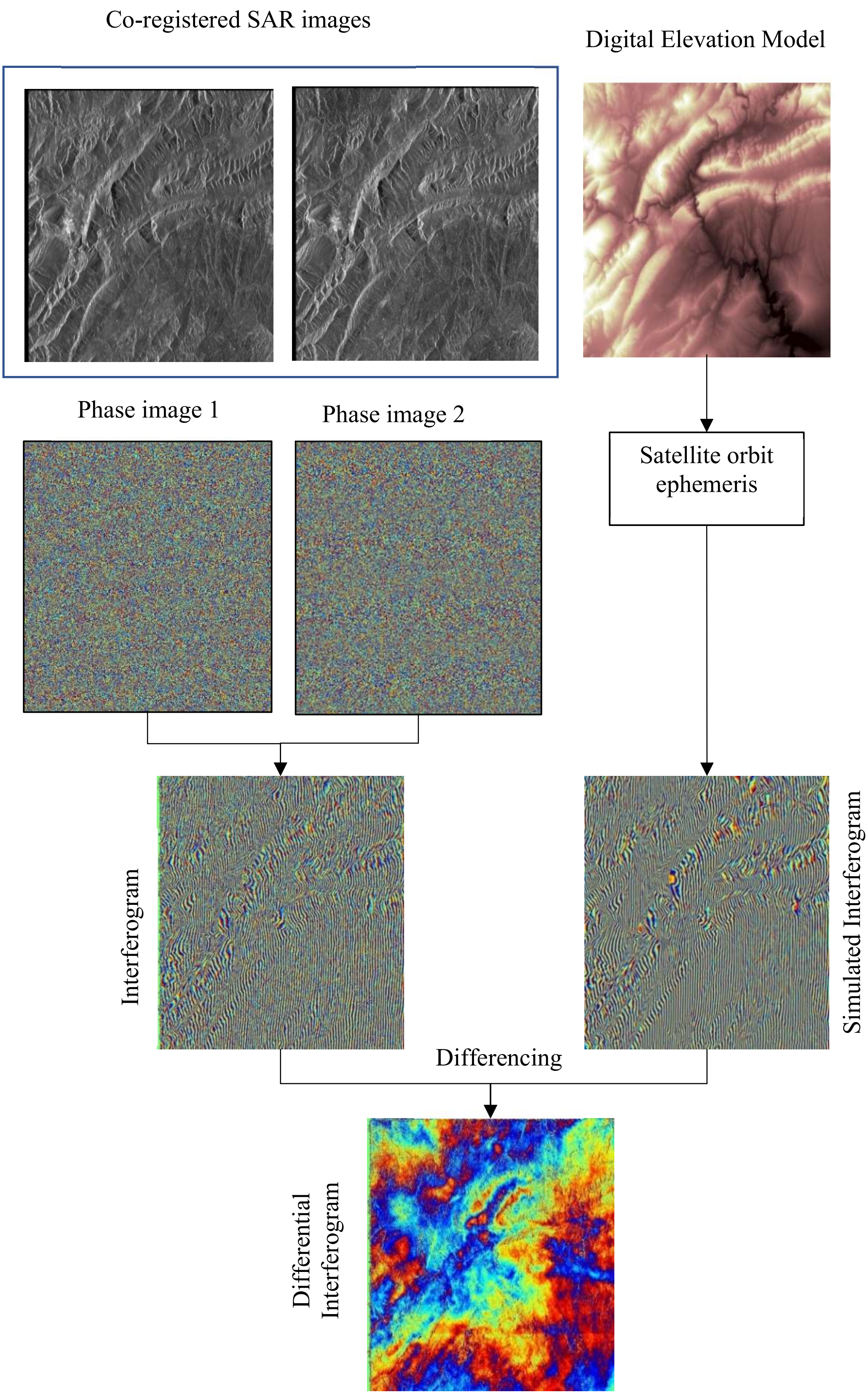

Figure 2.23: Differential Interferometry processing results

2.9 Summary

This chapter has introduced the main aspects of radar, beginning with a summary of the development of the Side-Looking Airborne Radar (SLAR), through to Synthetic Aperture Radar and how this enabled the spatial resolution to improve from a few km for SLAR to a few metres with the application of advanced signal compression and processing technique. The structure of the SAR image is explained and how the coherent systems record both the amplitude and phase of the measured resolution cell. The phase information is utilised in the SAR interferometry for digital elevation model production. Also, the advanced differential SAR interferometry (DInSAR) is introduced briefly and some examples are given about using the DInSAR for ground deformation monitoring. The next chapter will introduce the physics of microwave signal interaction with different mediums, with a particular focus on soils. This will also show how the water content of the soil affects the signal interaction mechanism, which in turn affects the penetration capability of the signal. Examples of the early subsurface signal penetration studies will be reviewed, summarising how SAR imagery is utilised for soil moisture estimation, depending on the variation in the scene amplitude. Finally, the SubSAR approach will be introduced, which is a robust, laboratory experiment that utilises both the amplitude and the phase to detect buried targets from the SAR images.

Chapter 3: Subsurface Imaging by SAR

3.1 Introduction

As explained in Chapter Two, Synthetic Aperture Radar (SAR) is an advanced radar sensor that uses a Doppler sharpening technique to produce high resolution radar images for topographic mapping and ground deformation monitoring. One of the greatest benefits of utilising microwave signals is their ability to penetrate different media, such as the soil surface, to provide information about objects beneath the surface medium; this is the basis of subsurface imaging. Although the SAR sensor can produce high resolution two-dimensional images of the earth's surface, it has very limited capability in locating objects in the vertical direction. As a result, it is extremely challenging to discriminate between surface and subsurface features from the SAR image. Most of the current SAR subsurface imaging approaches are based on analysing the amplitude component of the SAR images only, which is not sufficient by itself to determine whether an imaged object lies on the earth's surface or it is beneath the surface. Thus, the current approaches usually require an additional source of information (e.g., optical imagery) to help interpret SAR images for subsurface feature detection. However, recent approaches that utilise both the phase and the amplitude information contained within a SAR image seem to be more robust in subsurface imaging, in that they do not require any additional sources of information to interpret the results.

This Chapter begins by discussing the physics of microwave signal propagation in different media. Understanding the soil's interaction with the microwave signal is key for successful implementation of subsurface imaging. Subsequently, a review of previous examples of subsurface imaging from space will be presented to establish the possibilities and limitations associated with ordinary subsurface imaging approaches. At the end of this Chapter, a newly proposed robust method for more effective subsurface feature detection is introduced, which is based on analysing both the amplitude and the differential phase of the signal.

3.2 Microwave Signal Propagation

To describe the propagation of an electromagnetic wave in a uniform medium, two important physical terms need to be defined; the relative permittivity and refractive index. The permittivity of a medium is its resistance to an electromagnetic field, also known as absolute permittivity (ε). The ratio of the absolute permittivity of a medium to that of the vacuum (ε_o) is known as the relative permittivity, or the dielectric constant (ε_r) of the medium (Bussey 1960):

$$\varepsilon_r = \frac{\varepsilon}{\varepsilon_o} \tag{3.1}$$

For reference, the dielectric constant of air is considered unity, unless the air has a very high moisture content.

A microwave signal (wavelengths between 0.001 – 1 m), travels in free space (vacuum) at the speed of light (3 x 10^8 m/sec). When it encounters a medium with different relative permittivity, the speed of light changes by a factor known as the refractive index (Orfanidis 2002). This is the ratio of the speed of light in the free space (c) to the speed of light in that medium (c_m), normally referred to as n:

$$n = \frac{c}{c_m} \tag{3.2}$$

The refractive index is a dimensionless quantity that describes how the electromagnetic radiation propagates through different media. Its definition in Eq. 3.2 implies that the refractive index of the vacuum is 1. The refractive index is a function of the dielectric constant of the medium (Orfanidis 2002):

$$n = \sqrt{\varepsilon_r} \tag{3.3}$$

When an electromagnetic wave travels from one medium of refractive index (n_1) to another medium of refractive index (n_2), the signal will partially be reflected and partially transmitted at the interface between them. This is illustrated in Fig. 3.1, which depicts an incident wave (E^i) striking the plane interface between two media. Part of the incident signal is reflected (E^r) oppositely to the incident direction, where the reflection angle (θ_r) is equal to the incident angle (θ_i). The other part of the signal is transmitted through the second medium and is refracted by an angle, θ_t, due to the change in speed. The magnitude of the reflected signal can be characterised by the fraction of the reflected energy (R) (Orfanidis 2002):

$$R=|\rho^2| \tag{3.4}$$

where ρ is known as Fresnel reflection coefficient of the two media interface. It describes the effectiveness of that surface to reflect the electromagnetic energy.

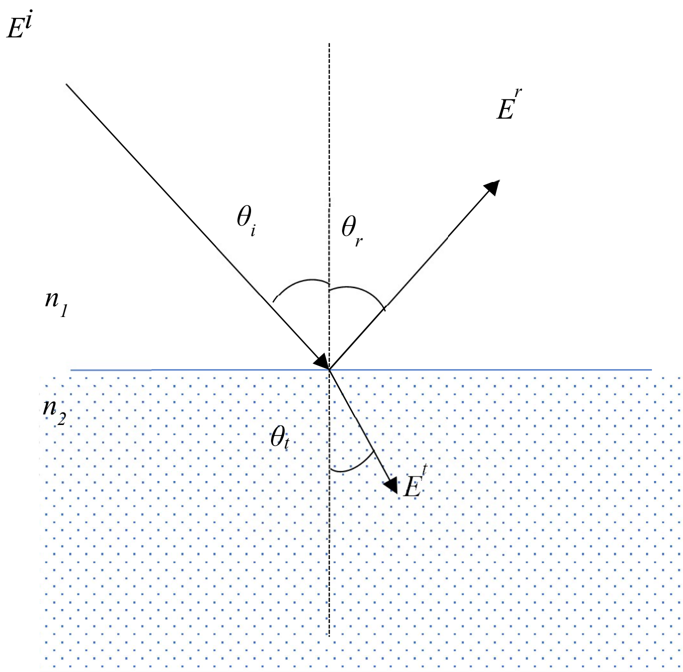

Figure 3.1: Definition of reflection and transmission components of the incident electromagnetic wave

For a non-normal incident angle, which is applicable to the SAR imaging systems, the Fresnel reflection coefficient (ρ) is given by:

$$\rho = \frac{1-\sqrt{\varepsilon_r}}{1+\sqrt{\varepsilon_r}} \tag{3.5}$$

The remaining component of the incident wave that is transmitted through the medium (i.e., penetrates the surface and travels through the medium) can be simply calculated in accordance with the energy conservation law. This states that the sum of the reflected (R) and transmitted (T) energy should be equal to the incident energy:

$$R + T = 1 \tag{3.6}$$

The transmission power is given as:

$$T = 1 - R \tag{3.7}$$

Therefore, the magnitude of the reflected and transmitted energy from a dielectric medium both depend on the dielectric constant of that medium.

From Eq. 3.4, 3.5 and 3.7, the relationship between the dielectric constant of a medium and the fraction of the reflected and transmitted energy from that medium can be derived (Fig 3.2). This figure represents the theoretical diagram where it is assumed all the incident energy is either being reflected or transmitted, and no absorption occurs in this type of medium. As seen in Fig 3.2, the magnitude of the reflected energy is positively correlated with the dielectric constant of the medium. On the contrary, the magnitude of the transmitted signal is inversely related to the dielectric constant. In most cases, however, the medium absorbs the signal energy, resulting in reduction in the transmitted power (attenuation). The medium's atoms absorb the energy of the wave photons and this energy is transformed into an internal energy by the absorber (thermal energy).

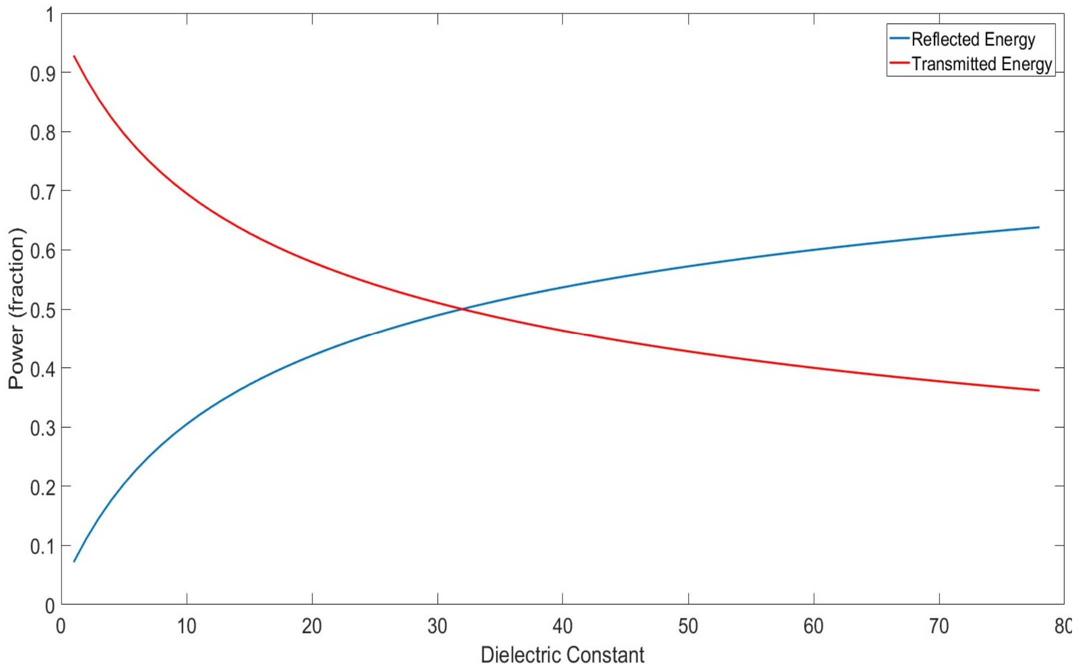

Figure 3.2: The relationship between the dielectric constant with the magnitude of the reflected and transmitted energy

3.3 Common scattering mechanisms

As explained above, when the microwave signal travels from one medium to another (i.e. from air to the Earth's surface), the signal will experience reflection off, and transmission into, the medium interface. The radar system can only directly measure the amount of reflected energy that returns to the receiver, which according to the Radar Equation (Chapter 2), will be weaker than the transmitted signal. Two types of reflections occur between the electromagnetic wave and natural media; surface and volume effects (Fig. 3.3). Each of them has different forms and specifications, as will be explained in the following sub-sections.

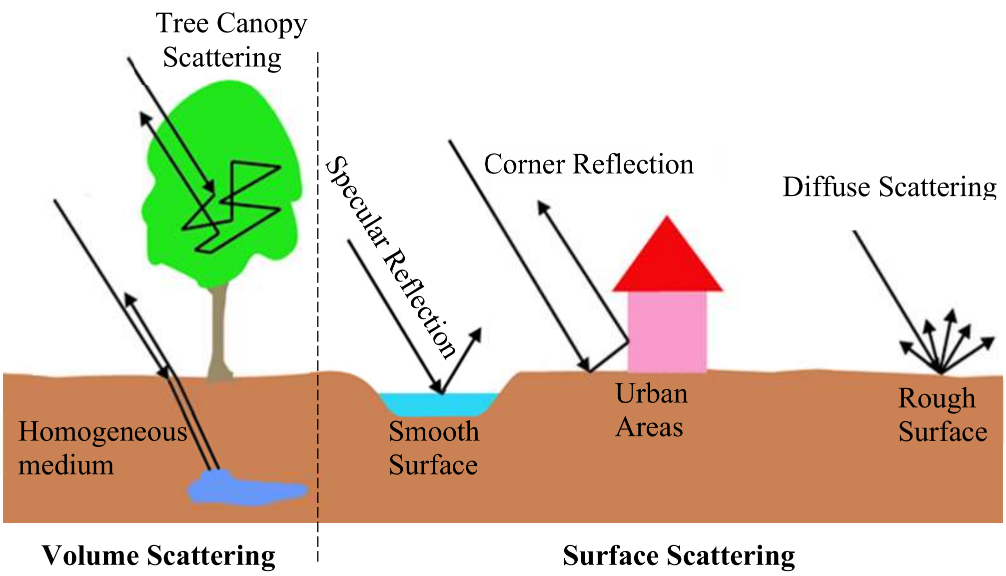

Figure 3.3: Common scattering mechanisms

3.3.1 Surface Scattering

Surface scattering takes place only at the interface between two inhomogeneous media, where the electromagnetic wave is incident from one of them to the other. The magnitude of the reflected energy is related to the ratio of their relative dielectric constant of the medium (as explained in section 3.2), while the scattering direction depends on the surface roughness, as shown in Fig 3.4. Surface roughness is determined by the local variations of the surface height (Δh) profile with respect to a mean reference plane. The surface is considered rough if the following condition is satisfied:

$$\Delta h > \frac{\lambda}{8\,\mathrm{co}} \tag{3.8}$$

where λ is the signal wavelength and θ is the local incident angle. Eq. 3.8 shows that the classification of surface roughness depends on the signal wavelength, where the same surface is considered smooth at longer wavelengths (e.g., L-band, ~23 cm) but rough at shorter wavelengths (X-band ~3cm).

Specular reflection occurs at a perfectly smooth surface, reflecting the incidence signal away from its source (Fig. 3.4a) at an angle equal, but opposite, to the incidence angle. For active microwave remote sensing, this scattering mechanism is not very useful as the reflected signal will be directed away from the source (the radar) and hence, there will be no return to the radar if viewed from a non-nadir angle. A calm lake surface is an example of a smooth surface, where the water surface acts like a mirror to the radar signal and thus appears dark in the SAR image.

For non-smooth surfaces, the incident wave will scatter in different directions. Fig. 3.4b and 3.4c below depicts how the roughness of the surface affects the direction of the reflected energy. For a slightly rough surface, the component of the specular reflection is lower than that of a smooth surface, but still sizeable compared to the backscattered component. Whereas for very rough surfaces, scattering will occur in all directions, which increases the magnitude of the backscattered signal component to the radar.

According to the Fresnel reflection coefficient (Eq. 3.5), if the dielectric constant of dry soil is 4.0, for example, then the Fresnel reflection coefficient would be approximately 0.33. Thus, the power of the reflected signal is approximately 0.11, meaning that the amount of the reflected power is only 11% of the incident power. On the other hand, water has a dielectric constant of ~80. The reflected power density from water surface is therefore about 64% of the incident energy, which is significantly higher than the dry soil reflection. Since there is a sizeable difference between the dielectric constant of the dry soil and water, it can be concluded that adding water to dry soil will increase its dielectric constant, which in turn increases its reflected power density.

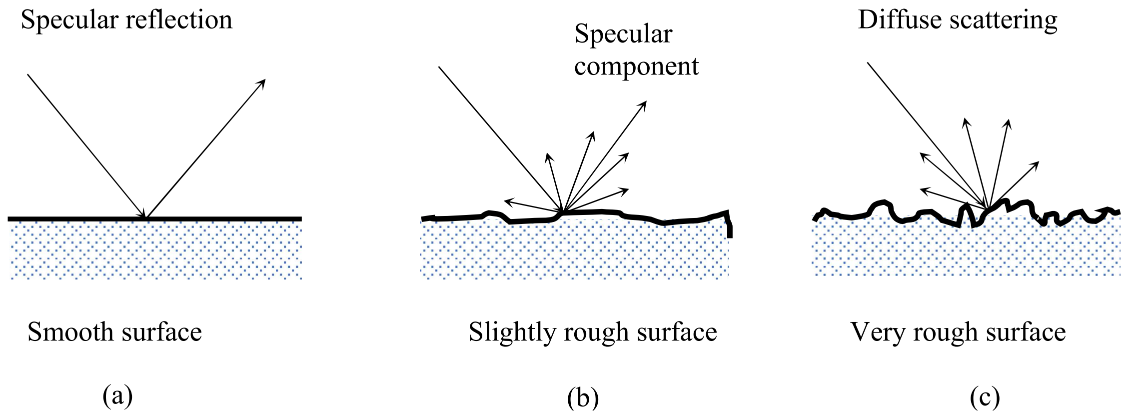

Figure 3.4: Microwave reflection from different surface roughness

Consequently, the power density reflected from soil surface (the radar reflectivity) is a function of its water content, so wet soils with a given roughness should appear brighter than dry soils of the same roughness. Moreover, unlike a smooth water surface, non-smooth water surfaces will appear significantly brighter than soil surfaces in a SAR image.

Another type of surface scattering occurs when the signal hits hard targets, which is known as corner reflection. When the signal hits a hard target, such as building wall or a road, which are relatively smooth surfaces, the signal will reflect off these surfaces. If the reflected signal then bounces off another hard target and is redirected to the SAR antenna, this results in a stronger returned signal and the area appears as very bright region in the image. An obvious example of this is for a building wall and the ground surface. Together, these two orthogonal surfaces represent a typical dihedral reflector, which strongly reflects the radar pulse directly back to the radar antenna. Corner reflection, or double bounce, represents the main scattering mechanism in the urban areas. This is the reason that most urban areas appear very bright in the SAR images and can be easily identified from other landscape features (see area 5 in Fig 3.5)

3.3.2 Volume Scattering

Surface scattering, which occurs at the interface between two media, represents the reflected fraction of the incident (E^r) depicted in Fig 3.1. The other fraction of the incident signal will cross the two media interface and travel beyond the surface of the second medium (E^t). In such a case, the radar signal follows more than one path before some energy is scattered towards the radar antenna (see Fig. 3.3). Such a scattering mechanism is referred to as volume scattering. Volume scattering often occurs in vegetated and forest areas. Here, the tree canopy contains many elementary scatterers that together backscatter energy to the radar. The radar pulse is scattered by the leaves and branches at different heights of the canopy making the vegetated area appearing as a brighter pixel than a smooth surface. Furthermore, the microwave signal is scattered wherever there is a discontinuity in the dielectric constant. For the case of tree canopies, the dielectric constant of leaves is higher than the surrounding air due to the high-water content in the leaf structure. As there is a complex distribution of leaves in the tree canopy, there is no identifiable single dominant scatterer. The amount of the backscatter is independent of the incidence angle and thus the forest canopies appear the same regardless of the viewing angle.

The other form of volume scattering is known as subsurface scattering, which is the principle of subsurface imaging depicted in Fig. 3.3. The microwave signal has the ability to cross the media interface and propagate within the second medium. If the medium is homogenous (i.e., there is no dielectric discontinuities) and infinite in size, the signal will continue propagating through the medium and the power of the signal will be reduced by two factors. The first one is the gradual absorption by the medium particles, in which the signal will transform into internal energy. The other attenuation source is the path length loss, in which the signal strength is attenuated by the natural expansion of the wave front, which is significant for the spaceborne system. On the other hand, if the medium contains an object with a different dielectric constant, the signal will be scattered off that target in different directions, producing a measurable backscattered component. The most obvious example of the subsurface scattering scenario is an object buried in a soil medium, and it this type of scattering that can be exploited for subsurface imaging using SAR.

Fig. 3.5 shows a Sentinel-1 image in which a variety of scattering mechanisms can be identified from different parts of the landscape. Area 1 in the centre of the image is a small pond within an agricultural land. The water surface is smooth, and a specular reflection dominates so it appears dark due to an absence of backscatter. Volume scattering from tree canopy can be seen in area 2, and scattering from rough surface (cultivated land) in area 3. Corner reflection mechanisms are represented by area 4 (isolated corner reflector) and area 5 (urban area).

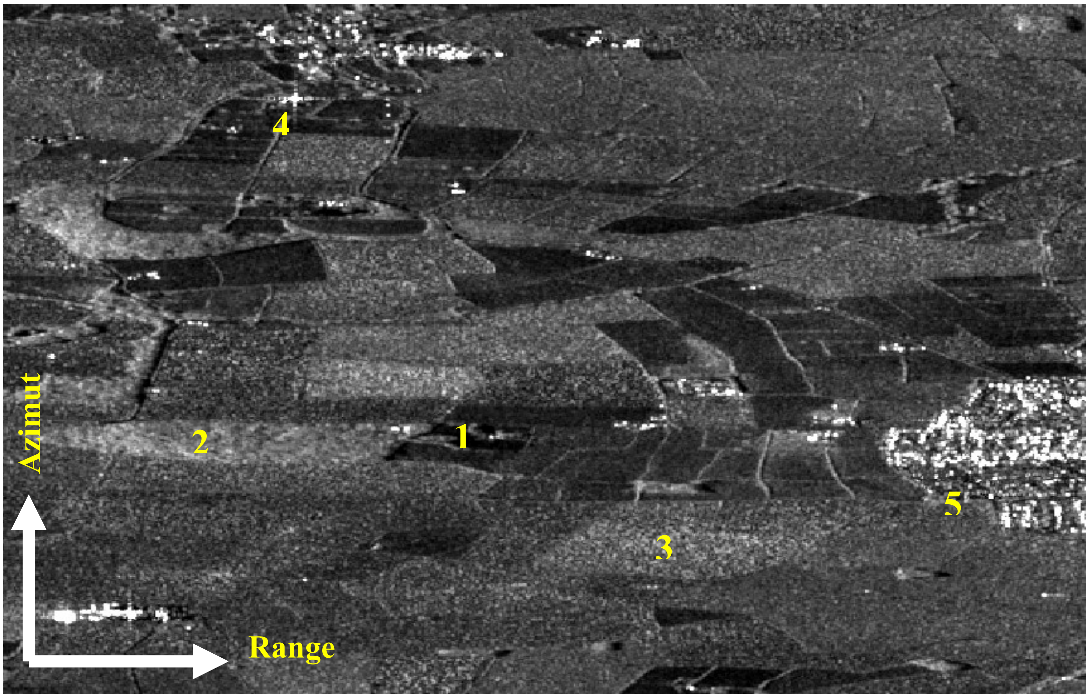

Figure 3.5: Sentinel-1 image showing different scattering mechanisms. 1) is a smooth surface which appears dark in the image, 2) Volume scattering from a tree canopy, 3) rough surface scattering represented by a cultivated agricultural field, 4) Point target Scatterer (corner reflector), 5) corner reflection from urban area.

3.4 Soil Medium

The soil medium is a vital part of the environment. It is the natural habitat for a wide range of organisms and, without soil, life would be very difficult on earth, if not impossible. Soil is the interface between the atmosphere and the earth's surface, and it controls the flow and storage of water (in the form of rivers, lakes, aquifers, and moisture) and gases (such as carbon dioxide and oxygen) (Lal 1990). Soils are also a natural record of human activities both in the past and in the present. They are part of the human cultural heritage, responsible for helping to preserve buried archaeological remains. The soil medium is a mixture of variable natural particles like minerals and organic matter, that vary in size from the smallest clay particles to large gravels. Soil is also composed of air voids, water, and organisms, and is considered to be a very complex natural system to support life on earth. It generally exists as a thin layer that covers of the Earth's surface. The shape and the size of the complex aggregates in the soil defines its structure (Lockhart and Wiseman 2012).

Electromagnetically, the soil medium is a mixture of four components; soil particles, air voids and water in two forms; free and bound water (Fig. 3.6). The presence of water in soil is a measure of its moisture, which can be represented as volumetric water content or percentage. Soil moisture plays an important role in the existence of life and greatly influences the soil dynamic properties, which is well known as the major factor affecting the soil relative permittivity (dielectric properties) in the microwave region of the spectrum (Wang et al. 1978). Water has two forms in the soil; the bound water and free water. Bound water is a thin layer of water, on the order of a few molecules, surrounding the soil particles. This is tightly held by the soil particles through the matric and osmotic forces, preventing the water molecules from moving freely – hence the name 'bound water'. The matric forces acting on the water molecules reduce rapidly with increasing distance from the soil particle. At a certain distance, the water molecule will have more freedom to move within the soil medium. This type of water is called free water (Hallikainen et al. 1985). Soil is very complex in nature and its physical properties depend mainly on its structural component, which is widely variable. A less complex and variable type of soil is sand. Compared to the complex composition of natural soils, sand is primarily composed of fine granulated silica, and depending on its location, it may also contain crushed rocks, lava fragments, shell or coral. Sand particles are usually characterized as lightweight which makes them easily transportable by water and wind, and thus sand can often be found significant distances from its origin.

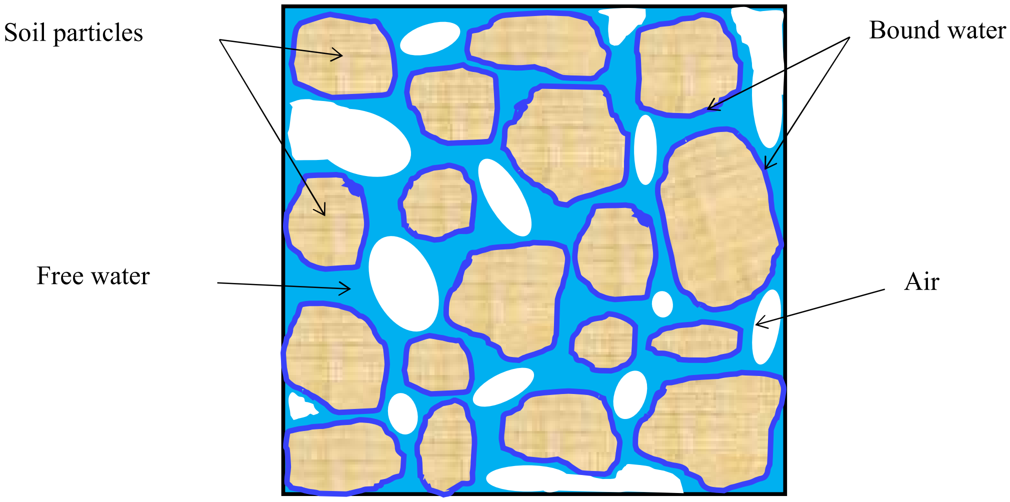

Figure 3.6: Soil is compost of soil particles, air voids and water in two forms

As a natural material, its colour is affected directly by its composition, commonly resulting in gold, pink, green and black colouring. Sand has no, or very little, ability to retain water. Instead, water moves easily through sand, and when sandy soils are irrigated or rain occurs, the water penetrates the sand surface and the sand remains well aerated. Due to the simple composition of sand compared to other soil types, it is selected as the most suitable medium to use in the experiment presented this thesis.

The interaction between sand and a radar signal results in both surface and volume scattering mechanisms (Ulaby et al. 1982). The occurrence of each of these scattering mechanisms depends mainly on the surface and subsurface moisture content, which governs its dielectric constant. The dielectric constant of soil and the effect of moisture on it is discussed in detail below.

3.4.1 Dielectric Constant and Soil Moisture

The dielectric constant of a medium characterises the resistance of that medium to wave penetration (Hoekstra and Delaney 1974). The larger the dielectric constant, the lower the penetration capabilities and the more surface scattering occurs to subsequently produce a brighter pixel in a SAR image. The dielectric constant is expressed as a complex number:

$$\varepsilon = \varepsilon' - j\varepsilon'' \tag{3.9}$$

where the real part, ε', is related to the wave propagation speed in the medium, or how the signal will slow down when transmitted through the medium as a function of the medium refractive index:

$$v = \frac{c}{\sqrt{\varepsilon'}} \tag{3.10}$$

where c is the speed of light in the free space, and v is the speed in the medium. The imaginary part (ε'') of the complex dielectric constant represents the loss of energy described by absorption and attenuation through the medium. The efficiency of penetration depth is inversely related to the attenuation coefficient, given by:

$$\alpha = k_o\sqrt{\varepsilon'}[1 + tan^2\delta]^{1/4} . \sin\left(\frac{\delta}{2}\right) \tag{3.11}$$

where α is the attenuation coefficient, and k_o is the wavenumber, defined as:

$$k_o = \frac{2\pi}{\lambda} \tag{3.12}$$

λ is the microwave signal wavelength, and:

$$\tan\delta = \frac{\varepsilon''}{\varepsilon'} \tag{3.13}$$

The attenuation is proportional to the imaginary part ε'' of the dielectric constant and inversely related to the signal wavelength. Therefore, a signal with a longer wavelength can penetrate deeper into the medium.

The dielectric constant of the soil is important in several different applications related to microwave remote sensing (Ulaby 1974). It has been extensively investigated by field and laboratory measurements (Geiger and Williams 1972, Cihlar and Ulaby 1974, Hoekstra and Delaney 1974, Hallikainen et al. 1985, Vall-Llossera et al. 2005). Hallikainen et al. (1985) measured the dielectric constant for five different soil types at a range of microwave frequencies between 1.4–18 GHz and soil moisture content. An illustration of this is shown in Fig. 3.7 for three soil types at L-band wavelength. It shows the variations in the dielectric constant between the soil types when the water content changed. In general, as the soil moisture increases, the dielectric constant (both the real and imaginary parts) also increases. Theoretically, the dielectric constant should approach that of water (~80) at the specified microwave frequency as the moisture content approaches 100%. For dry soils, the dielectric constant remains relatively constant, independent of the microwave frequency and soil type. However, as water content increases, the dielectric constant becomes more dependent on soil type.

Fig. 3.8 presents the dielectric constant of Sandy Loam soil at different microwave frequencies. It can be seen that the dielectric constant is independent of the frequency at very low water content. However, the dielectric constant becomes frequency dependent for increasing soil moisture. At higher levels of soil moisture, the real part of the dielectric constant increases more for lower frequencies.

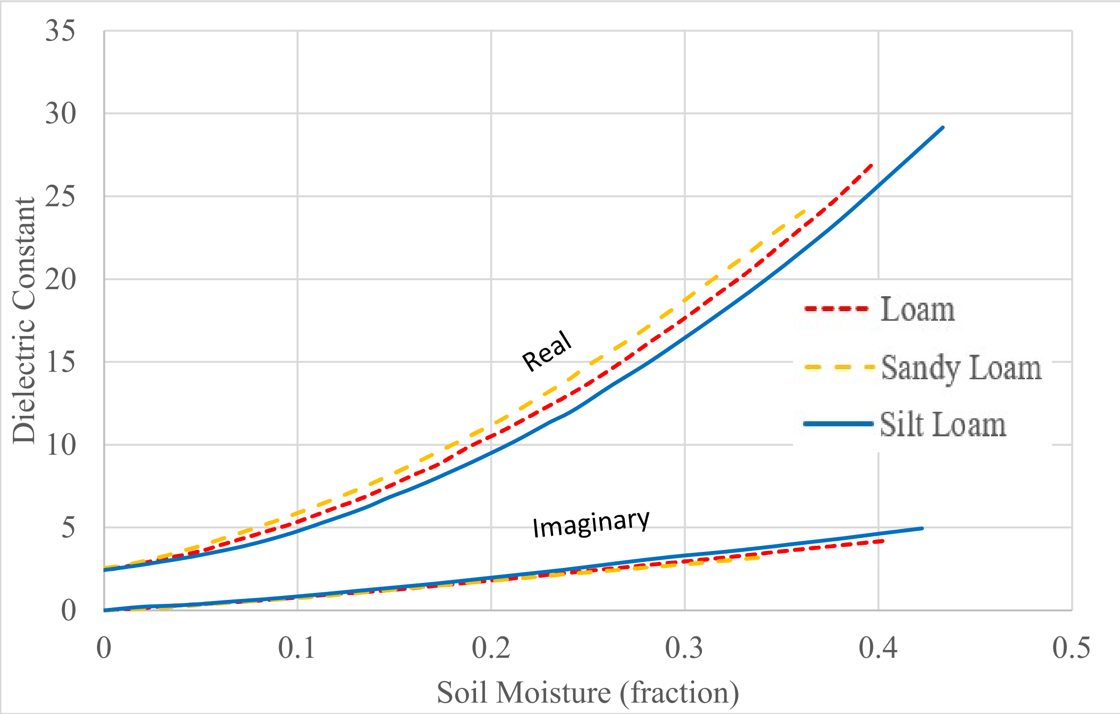

Figure 3.7: Dielectric Constant of three soil types as a function of soil moisture at L-band (after Hallikainen et al. (1985))

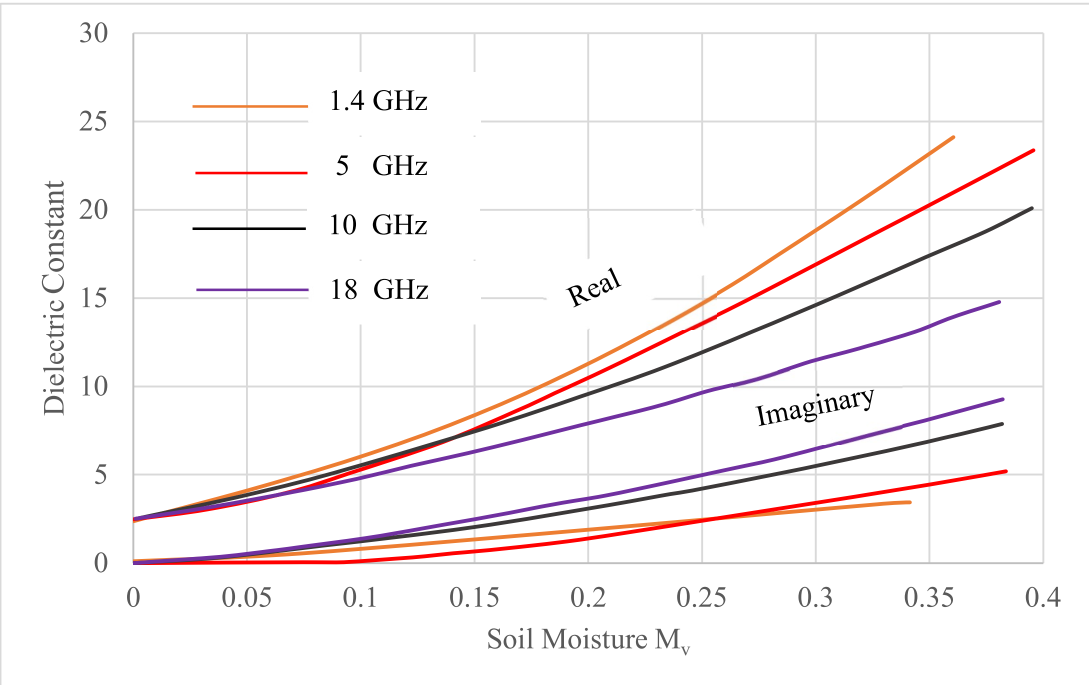

Figure 3.8: Dielectric Constant of Sandy Loam soil as a function of soil moisture at different frequencies

From Fig 3.7 and 3.8, it is clear that there is a positive correlation between the water content and the dielectric constant of different soils at different microwave frequencies, except for those with very low water content. The non-linear relationship between the water content and the dielectric constant is due to the completely different manner in which the free water and bound water interact with the incident radar signal (Dobson et al. 1985).

3.5 Utilising SAR images for soil moisture estimation

Soil moisture is an important hydrological parameter that represents the interaction between the atmosphere and the land surface (Engman 1995). Despite this importance, soil moisture is rarely used as a variable in land process models, such as civil engineering projects and flood planning, due to a lack of sufficient measurements of soil moisture in most parts of the world. Obtaining a dense and reliable set of soil moisture measurements over large regions is not practical using standard manual techniques. This typically involves taking samples of the soil from the field, weighing it, and then drying it in a special oven before weighing the soil sample again after drying. Soil moisture is then estimated as the mass of water lost during the drying process (Evett et al. 2008).

For wide area coverage, remote sensing from space has the potential to be an efficient approach for obtaining routine measurements of soil moisture. Such an approach can exploit the differences in the dielectric constant of water (~80) and dry soil (~ 2–4), and the subsequent relationship between the dielectric constant and soil moisture (shown in Fig 3.7 and Fig 3.8). Furthermore, in Section 3.2 it was shown that the magnitude of the scattered microwave signal is also positively correlated with the dielectric constant of the medium. Thus, measurements of the magnitude of the scattered energy can be used to estimate the soil moisture.

Many studies have used microwave remote sensing to estimate the soil moisture. Most of these are based on using changes in the amplitude of the SAR image as a proxy for variations in the moisture content of the observed land (Karam et al. 1992, Cognard et al. 1995, Dubois et al. 1995, Engman 1995, Quesney et al. 2000). Cognard et al., (1995) investigated the correlation between radar backscatter and the surface water content using both automatic point measurements and ground truth measurements (for soil moisture estimation). For different types of vegetation it was observed that the radar backscatter increases as the surface soil moisture increases (Cognard et al. 1995). The authors also stated that it could be possible to directly link the backscatter signal to soil moisture as long as there is little, or no, vegetation cover on the surface. These results encouraged subsequent research to be conducted to further investigate the relationship between the radar signals and surface soil moisture, in the hope to use the SAR imagery for soil moisture estimation.

Empirical soil moisture inversion models are generally derived by relating in-situ soil moisture measurements with radar backscatter observations. An example of such a model is the simple empirical model of the normalized backscatter moisture index (NBMI) that was proposed by Shoshany et al., (2000):

$$NBMI = \frac{\sigma_{t1}^{o} - \sigma_{t2}^{o}}{\sigma_{t1}^{o} + \sigma_{t2}^{o}} \tag{3.14}$$

$$W_s = a_1\, NBMI + a_2 \tag{3.15}$$

where W_s is the soil water content, σ^{o}_{t1} and σ^{o}_{t1} are the radar backscatter observations over the experiment site at different time points, and a_1 and a_2 are empirical parameters derived from field-based soil moisture observations. This approach of estimating the soil moisture based on change detection minimizes the effects of surface roughness and soil texture, as these tend to remain relatively stable or vary little over time. Therefore, any detected change in the backscatter will be related to the change in the soil moisture content (Shoshany et al. 2000).

3.5.1 Penetration Depth and Soil Moisture

One of the greatest advantages of microwave remote sensing is the capability of the microwave signals to penetrate different mediums, such as dry soil. As discussed in Section 3.2, the magnitude of the transmitted signal is a function of the dielectric constant of the medium. However, when a radar wave crosses the air-soil interface and propagates through the soil, the soil particles will absorb some of the signal energy and as a result there will be an attenuation in the signal strength. The amount of attenuation determines how far the signal can penetrate into the soil. The depth of penetration at which a resolvable signal is still detectable is called the skin depth or penetration depth. The penetration depth (*Pd*) is defined as the depth at which the signal power density is dropped to *1/e* of its surface interface power (Von Hippel 1954), and can be expressed as:

$$P_d = \frac{\lambda}{2\pi} \frac{\sqrt{\varepsilon_r'}}{\varepsilon_r''} \tag{3.16}$$

As seen in Eq. 3.16, the skin depth is a function of the microwave radiation wavelength and the dielectric constant of the medium. The skin depth can be improved by using longer signal wavelengths, along with a reduced imaginary part of the dielectric content of that medium. The imaginary part, which accounts for the signal attenuation, increases with higher water content. Overall, dry soils and longer wavelengths can significantly improve penetration depths.

The skin depth of a pure sand sample as a function of moisture content was analysed by Ulaby (1974) at three different frequencies, namely X- band (10 GHz), C-band (4 GHz) and L-band (1.3 GHz) (Fig. 3.9). For each frequency, the maximum penetration depth is observed at lowest moisture content of the soil sample. As expected from above, increasing the soil moisture decreases the penetration depth. However, at a moisture content <0.1 g/cm^3 the skin depth sharply increases, but only gradually decreases at soil moisture content >0.1 g/cm^3. As also expected from Eq. 3.16, the skin depth is strongly frequency dependent, with L-band (the longest wavelength) having the higher skin depth, approaching infinity for a completely dry homogeneous sand. Nonetheless, the microwave penetration capability is very limited for wet sand at all frequencies, with the signal only penetrating up to a few centimetres even at lower moisture content and a high frequency. From the remote sensing point of view, an L-band signal appears be most promising for subsurface imaging as it can penetrate relatively dry sand by up to several metres.

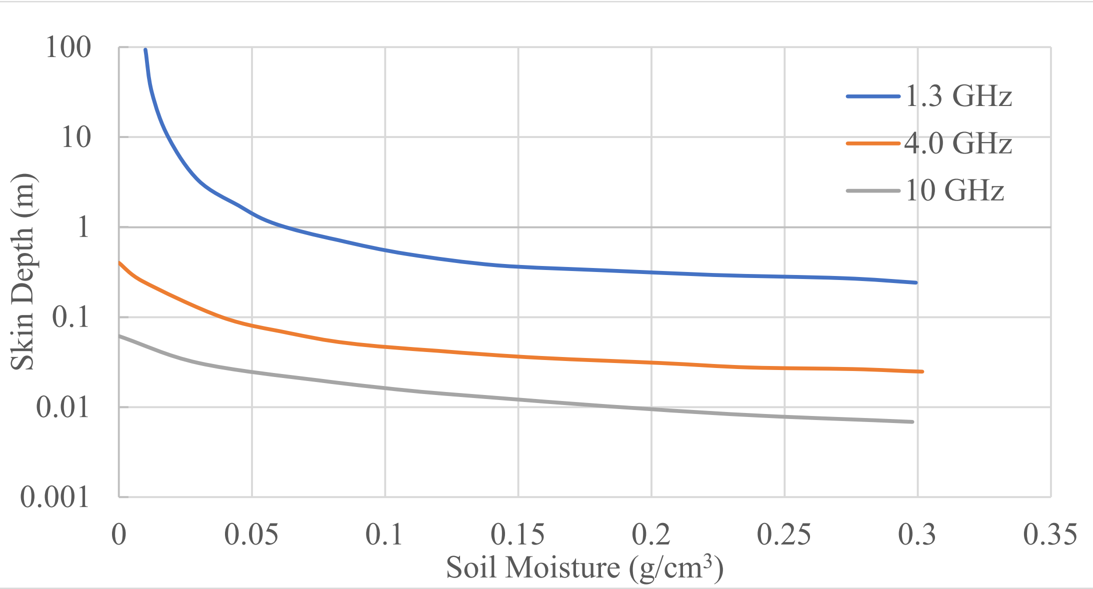

Figure 3.9: Skin Depth of pure sand as a function of soil moisture at different frequencies. Modified after Ulaby (1974)

3.5.2 Utilizing SAR for subsurface imaging

It is now clear that microwave radiation can penetrate the soil surface to a depth that depends on the soil physical characteristics, such as the soil type (Hallekainen et al., 1985) and the dielectric constant (Ulaby et al., 1974). Furthermore, Roth and Elachi (1975) explained that volume scattering losses due to inhomogeneous scatterers in the medium are many times higher than the loss due to that medium conductivity. That means that, in a homogeneous fine-grained material, the penetration depth could be very deep (Roth and Elachi 1975). Findings of the above researches agree with the physical theory of electromagnetic radiation propagation into different media. However, these observations were made from laboratory experiments and their application to data acquired by spaceborne or airborne SAR sensors for subsurface imaging has not been quantitatively verified. Nonetheless, they have been exploited in a largely qualitative manner for shallow subsurface imaging using SAR, which has been particularly vital for geological studies in remote desert environments (McCauley et al. 1982).

The first subsurface imaging discovery was made using Shuttle Imaging Radar (SIR-A) images. These were obtained in November 1981 over the Selima Sand Dunes region, located on the border of Libya, Sudan, and Egypt, and revealed remarkable, previously unknown paleo-drainage channels buried under the desert sands (McCauley et al., 1982). Fig 3.10 shows a comparison between Landsat MSS and SIR-A images over that area, which represents the driest core in the world where rainfall only occurs every 30–50 years. Details of the ancient buried rivers are clearly shown in the SIR-A image, while only the sand layer is visible in the Landsat MSS image. Further field investigations by Schaber et al., (1986) showed that these 'radar-rivers' were buried under a 1.5 m thick sand layer.

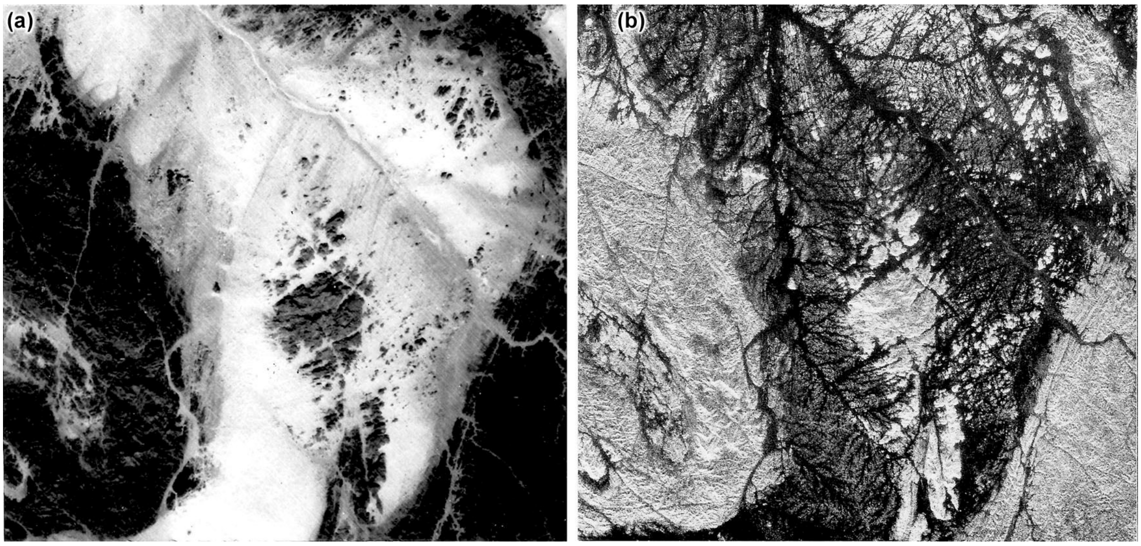

Figure 3.10: Subsurface imaging from Space imaging radar. (a) Landsat MSS band 2 showing white sand cover; (b) SIR-A L-band radar image showing details of what lies beneath thin sand

SIR-A is a SAR system with single HH polarization and the local incidence angle at the surface is 50^{o} with a spatial resolution of 40 m. The skin depth of the SIR-A L-band signals were measured in the lab for sand samples from the area above range from 1.5–6 m depth (Farr et al. 1986). Subsequent analysis showed that the wind-blown sand cover is largely transparent to the L-band radar signals due to its very low moisture content (<1%), which gives it a low dielectric constant that enables the imaging of the dry water courses beneath the sand.

In a separate study, Blom et al (1984) noted some lineaments on SEASAT SAR images over the Mojave Desert in California that did not appear on aerial photos. Field observations confirmed that no surface features could have caused the lineaments in the radar image. Further investigations showed that geological structures buried under 2 m of alluvium cover caused these lineaments in the SAR images. They suggested that, in order to detect subsurface features using radar signals, the covering materials should be homogeneous, fine-grained, and dry. Hence, the desert is the most suitable environment for subsurface imaging research.

Elachi et al (1984) described the radar signal attenuation and refraction while penetrating an extreme dry sand layer in the Sahara Desert. They showed that the subsurface feature echo could substantially increase if the depth of the covering material is less than the skin depth and, under certain conditions, the subsurface feature could yield a stronger echo than if it was on the surface. This is due to the fact that the radar incidence angle is reduced when the signal is refracted at the air-surface interface (Fig. 3.11). This yielded strong backscatter from features buried under 1–2 m thickness of fine-grained sand with water content less than 1%.

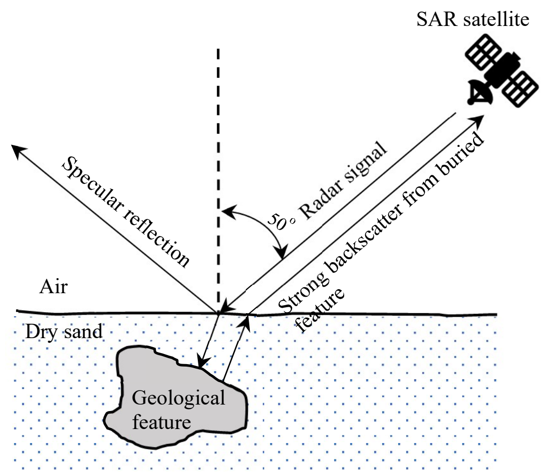

Figure 3.11: The refraction of the transmitted signal might increase the strength of the reflected signal if the buried target was in the right orientation towards the refracted signal

In a novel approach to directly measure the radar signal attenuation in the natural soils, Farr et al. (1986) buried two electronic receivers in the Nevada Desert and measured the signal strength at the surface layer and at two different depths as a function of the soil moisture. Their result closely matched the previous laboratory measurements of signal attenuation, and it was concluded that the SIR-B L-band signal at 1.2 GHz can penetrate between 0.7–1.7 m in the desert soil (Farr et al. 1986). Paillou et al. (2003) investigated the Bir Safsaf region in south central Egypt using combined data from an orbital SAR (C and L bands) and a ground penetrating radar (GPR) at 500 and 900

MHz. The geometrical and dielectric properties of the buried features under the sand, which were measured by GPR, were used as input for the SAR image interpretation and they concluded that over arid areas, low-frequency orbital L-band (1.25 GHz) SAR allows one to investigate the subsurface down to several metres when covered by dry material such as sand (Paillou et al., 2003). In a recent study of a subsurface paleo-drainage system in an arid region, Paillau et al. (2009) reported that long-wavelength SAR images acquired using the PALSAR system could probe the subsurface down to a few metres in the extremely dry sands. This enabled them to map a ~900 km long river system in the Libyan desert (Paillou et al. 2009).

From the above literature, the ability of the radar signal to penetrate the unconsolidated sand of the desert to provide information about the subsurface geological structures is well-documented. However, these examples of subsurface imaging are mainly reliant on a qualitative visual analysis of the SAR images, and it was a set of specific conditions that made this possible. These are the extremely dry sand surface layer (low dielectric constant), the presence of the subsurface scattering object (or surface) within the penetration depth of the radar signal, and the physical characteristics of the soil. Under optimum conditions, it is apparent that an L-band radar signal (1.2 GHz) can penetrate up to 2 m in very dry sand. More generally, some conditions for using SAR imagery for subsurface feature detection can be defined. These conditions can be summarized by: (i) presence of a buried, radar reflective feature, (ii) a covering material that is dry, homogeneous and has a thickness so that the buried feature can receive and reflect enough power so that it would be feasible to detect it using a radar system.

3.5.2.1.1 ***Radar imaging depth***

The ability of a buried feature to backscatter sufficient energy for detection is dependent on the signal attenuation in the overlying medium. The skin depth, previously defined as the depth at which the transmitted signal power is decayed to 1/e of its surface power, accounts for one-way transmission of a signal. However, in subsurface imaging a transmitted radar signal suffers attenuation during its two-way trip within the sand medium. The two-way penetration length for the radar is described by the radar imaging depth (RID). Schaber and Breed (1999) empirically calculated the RID for L-band through dry sand and estimated it to be ¼ of the skin depth.

Williams and Greeley (2001) conducted an experiment to quantify the radar signal attenuation as a function of radar frequency, moisture content and sand thickness in a laboratory experiment. The experiment involved radar frequencies from 0.5–12.6 GHz and three sand moisture levels (0.3, 4.7 and 10.7% by volume). The experiment was conducted in three stages, each stage representing a specific water content of the sand layer. Stage 1 involved nearly dry sand (water content <0.3%), stage 2 used a water content of 4.7% (Fig. 3.12) and in stage 3 the water content was increased to 10.7% (Fig. 3.13). It was found that the dry sand has very little effect on the signal attenuation; adding dry sand slightly decreased the transmission power at most frequencies. Moreover, from examining Fig. 3.12 and 3.13, it can be seen that the attenuation is positively correlated to the signal frequency. When the frequency is increased, the attenuation also increases. However, at lower frequencies, the attenuation is small even at higher moisture content (10.7%), which challenges the initial conclusion that subsurface imaging requires extremely dry sand. The ability of the radar signal to penetrate moist sand is very important for studying subsurface features in regions where the surface soil is not extremely dry.

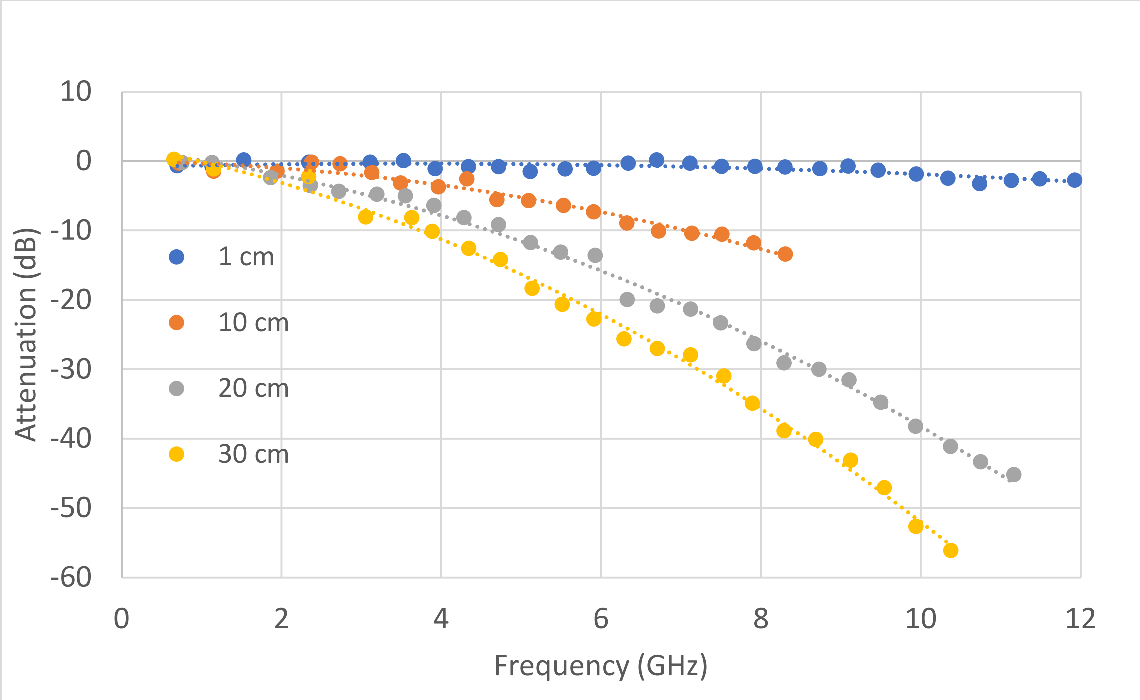

Figure 3.12: Attenuation of the transmitted signal at different depths as a function of frequency for sand soil with 4.7% water content

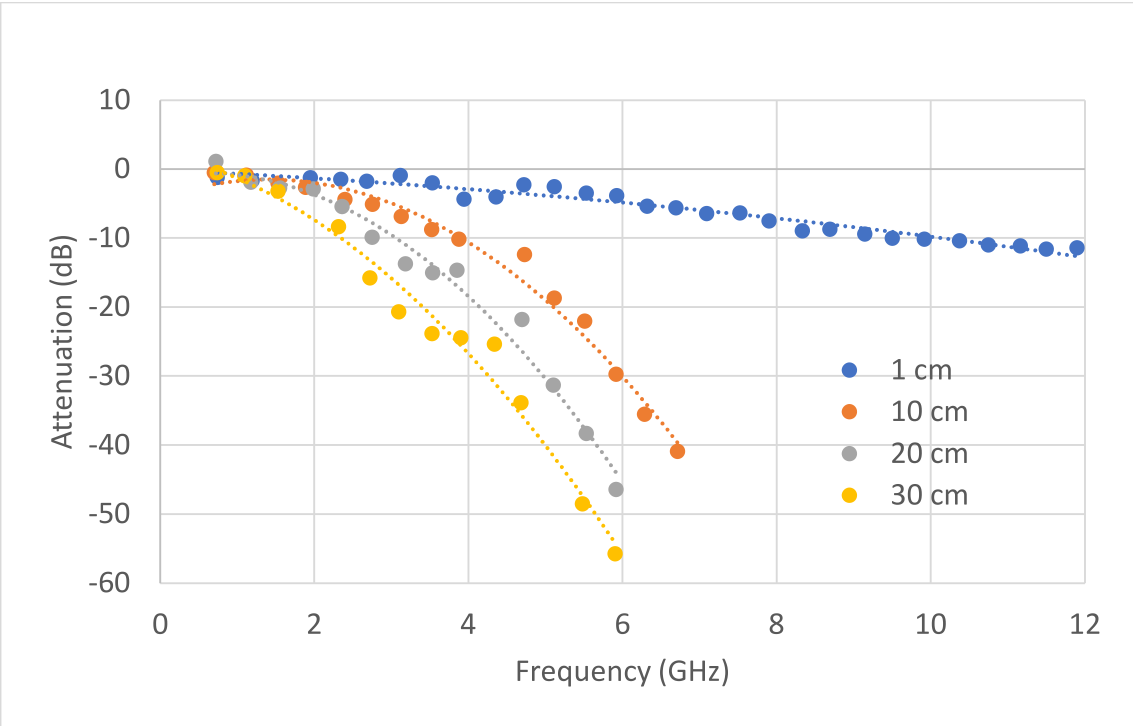

Figure 3.13: Attenuation of the penetrated signal at different depths as a function of frequency for sand soil with 10.7% water content

3.5.2.2 The effects of soil moisture on the differential phase

The potential for soil moisture to affect DInSAR measurements was first described by Gabriel et al. (1989). They analysed L-band SEASAT SAR data using the three-pass DInSAR technique to measure the ground surface change in agricultural fields in California. Over the nine-day interval, the differential interferogram revealed a few centimetres change in the path length. By comparing these changes with the irrigation records of the farms in the study area, they found that most of the phase change was related to the variations in the soil moisture of these fields. They attributed the interferometric phase change to changes in the surface elevation due to the clay swelling-shrinkage as a result of the increase or decrease in the water content (Gabriel et al. 1989). Although it remains untested, this study indicates an indirect soil moisture contribution to the InSAR phase. The limitation of this hypothesis is that not all soil types are known to be expandable upon wetting, and thus it only applies to certain soil types (Mitchell, 1991).

A direct phase change due to the moisture variation in the soil can be attributed to a change in the penetration depth. The water content affects the soil relative permittivity (dielectric constant) which in turns affects the penetration depth. As the soil water content increases, so does the refractive index. This increases the optical path length between the subsurface target and the radar antenna. Consequently, the interferometric phase observed over such area will corresponding to apparent movement away from the radar antenna (or more commonly subsidence) even if the soil surface is static. It is therefore important to understand the moisture dependent interferometric phase variations to correctly model the DInSAR deformation analysis (Zwieback et al. 2017).

Nolan and Farr (2003) attempted to investigate a quantitative relationship between the interferometric phase and soil moisture. They monitored some agricultural land in

Colorado using ERS SAR images and field measurements of soil moisture. A millimetric scale variation in the path length was reported, and this showed a strong correlation with the hydrological features, such as watershed boundaries and stream channels, which were possibly related to the shrink-well of the clay soils. However, they were not able to establish a relationship between the differential phase and the change in the soil moisture content.

The ambiguous presence of a soil moisture phase signal in DInSAR observations was analysed in a robust laboratory experiment by Morrison et al, (2011) using a homogeneous pure sand soil sample. They observed the DInSAR phase for two identical soil samples. Water was added to the first sand sample at the beginning of the experiment to increase its water content from dry to ~25%, while the other sand sample was left dry during the experiment to be used as a reference. The DInSAR phase was measured for the two sand samples over the drying period of the first sand sample. During that time, an optical camera was used to precisely monitor any surface elevation changes. The only variable parameter in the experiment was the water content, which allows precise investigation of the differential phase with respect to the varying moisture content. A large phase variation was observed for the drying soil sample, compared to un-changed phase for the dry sand sample (Morrison et al. 2011), as shown in Fig. 3.14.

The experiment confirmed that the observed DInSAR phase of a soil surface is related to its moisture content, or more specifically the penetration depth. This is important because it suggests that the soil moisture signal of DInSAR phase could be exploited to quantitatively estimate the water content of soil.

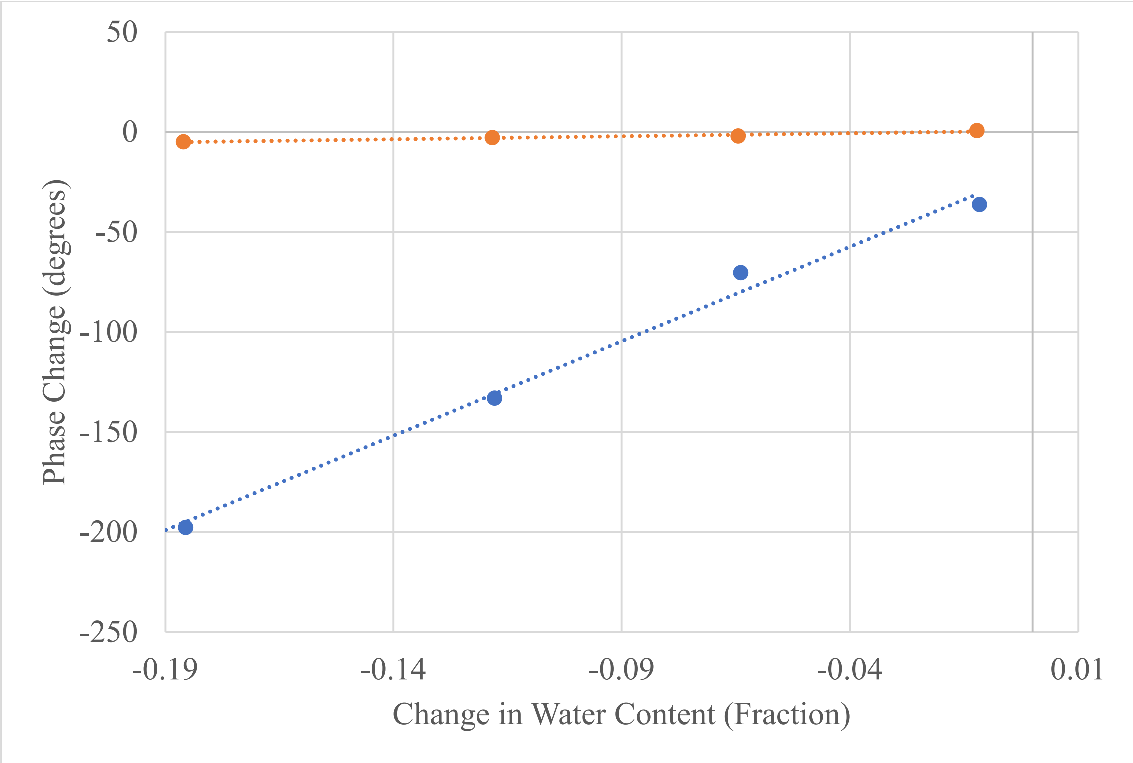

Figure 3.14: Variation in the DInSAR phase for the two sand samples. The blue line is the phase response of the wet sand while drying and the orange line is the phase response of the reference dry sand sample. Modified after Morrison et al., (2011)

3.6 Subsurface feature detection using SubSAR

As outlined in this Chapter, it is apparent that the magnitude of the backscattered signal and the differential phase are both affected by the water content of that soil, and can both be attributed to changes in the penetration depths. Nonetheless, with respect to subsurface imaging, so far only the amplitude component of the backscattered signal has been utilized to distinguish buried targets from surface targets.

Morrison et al. (2013) developed a new approach for utilising the full characteristics of the radar wave for discriminating between surface and buried targets in a laboratory experiment. This approach provides a validation of the microwave propagation theory. Details of this experiment, including the effects of the soil moisture on the penetration depth, and how that affects the backscattered signal, are provided below.

3.6.1 Experimental design

The experiment conducted by Morrison et al. (2013) involved monitoring the DInSAR phase history and the backscatter of a buried target in a drying soil sample. A 100% non-expansive, homogeneous pure sand soil sample is used in this experiment. The sample was divided into two equal halves (Fig 3.15), with a surface area of approximately 1 m^2 and depth of 20 cm. A trihedral corner reflector was buried in the centre of each soil sample at a depth of 10 cm. One section (Area 2) was left dry during the experiment to be used as a reference for the measurements. The water content of the other section (Area 1) was increased to 40% by adding a predetermined amount of water to the soil sample. A ground-based radar was then used to acquire a series of C-band SAR images of the soil samples during the drying period. Again, a high-resolution optical camera was used to monitor the soil sample for any surface movement. The backscatter of thee parts of the experimental soil sample was monitored during the drying time. These were the dry soil sample (Area2), surface reflection of the wet soil in area 1, and the buried trihedral CR in the wet area 1.

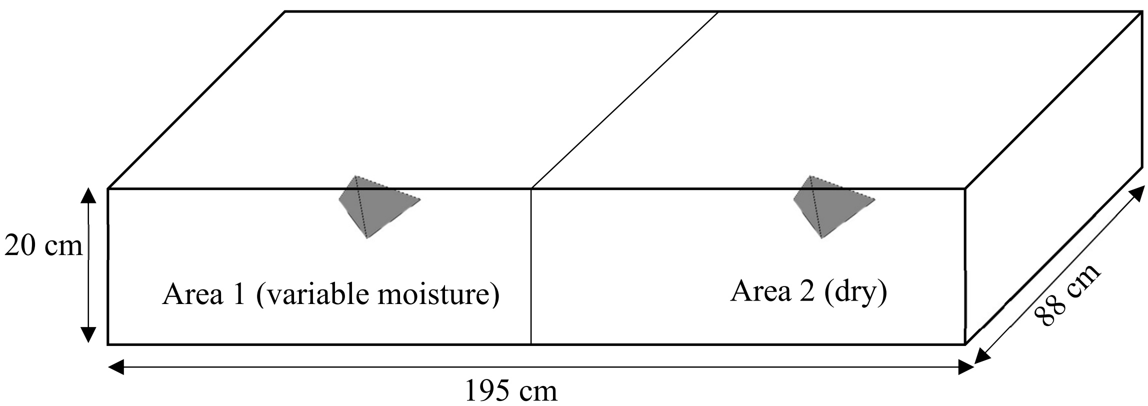

Figure 3.15: SubSAR experiment design where the soil was divided into two equal halves and a trihedral CR was buried in the middle of each area. Sand in Area 2 was left dry during the experiment and water was added to area 1 during the experiment and left to dry. Modified after Morrison et al. (2013)

3.6.2 Amplitude behaviour

When water was added to area 1, some water leaked into area 2, which caused the moisture of area 2 to slightly change. The backscatter of Area 2 (dry sand) was reasonably stable over time (blue solid line in Fig 3.16), with minor reduction in the backscatter of approximately 0.5 dB, largely attributed to drying from the contaminated area. The surface backscatter behaviour of the wet soil of Area 1 (orange sloid line in Fig 3.16) showed a clear reduction upon drying, which was largely attributed to variation in the signal penetration depths at different moisture levels. On the other hand, there was an increase in the backscatter of the buried trihedral CR (grey solid line in Fig 3.16) in area 1 during the drying period, which mirrored the behaviour of the surface reflection of the same area. This represented the increasing signal transmission in the drying soil medium.

During the soil drying period, the reduction in the soil moisture will cause the dielectric constant of the soil to reduce as well, as discussed in section 3.4.1. Furthermore, the magnitude of the reflected signal is proportional to the dielectric constant of the soil (Section 3.2). Therefore, the surface reflection of the drying soil sample (Area 1) shows a reduction in the backscatter. It is also discussed in Section 3.2 that the power of the transmitted (penetrated) signal is inversely proportional to the dielectric constant of the soil. Therefore, the buried trihedral CR at Area 1 shows an increase in the backscatter (increase in the transmitted signal) during the drying period.

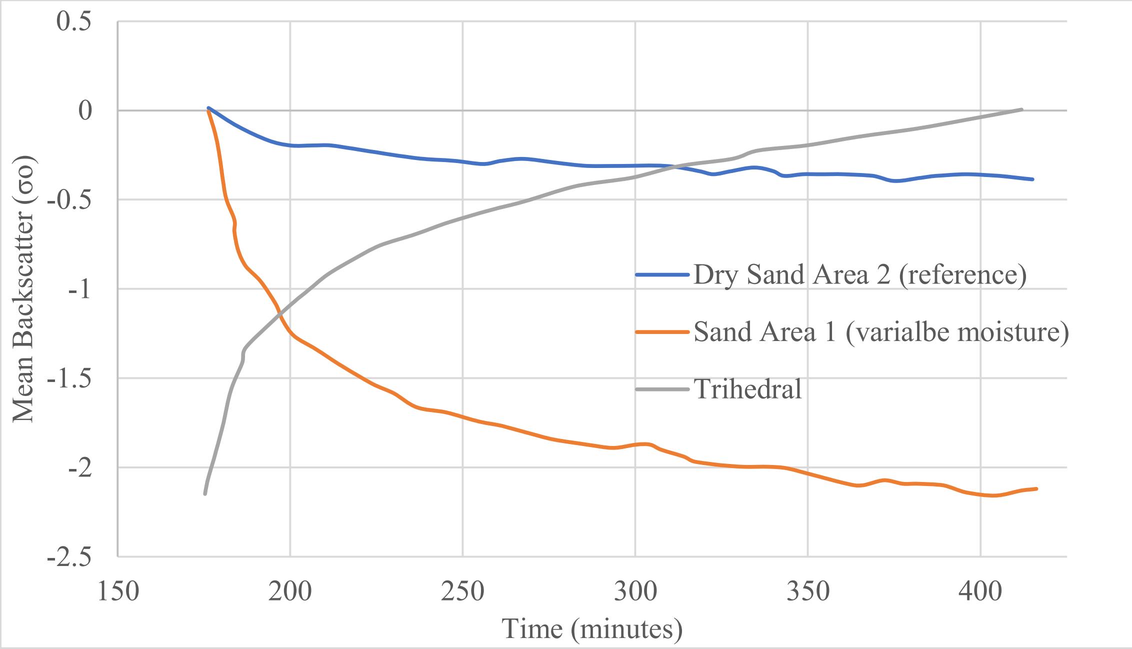

Figure 3.16: Temporal backscatter behaviour of three samples of the experiment: a surface dry soil Area 2 represented by the blue line, surface backscatter of drying soil Area 1 represented by orange line and buried trihedral CR under drying soil in Area 1represented by grey line. The x-axis represents the drying time in minutes

3.6.3 Phase behaviour

From the temporal stack of SAR images, a series of differential interferograms was constructed, with the master image corresponding to that acquired when the sand was at its wettest. The DInSAR phase behaviour was analysed for the buried trihedral reflector in Area 1, sand surface of Area 1, and the dry Area 2 (Fig. 3.17). There is a remarkable distinction in the DInSAR phase behaviour between the buried trihedral and the surface in Area 1. The phase for the surface is relatively stable, in similarity to the dry Area 2, while the buried trihedral reflector in the drying Area 1 shows a phase change during the drying period. This indicates that the optical path distance between the radar antenna and the buried trihedral has changed. The high-resolution camera that was used to monitor the sand surface changes confirms that the sand surface didn't change during the drying period by the amount that causes the indicated phase change. Therefore, the phase change can only be related to the variations in the sand moisture.

In summary, changing the soil moisture of the sand above the buried trihedral alters the DInSAR phase history of that target, and there is a linear relationship between the phase change and the moisture content change, which is in strong contrast with the phase of the surface soil.

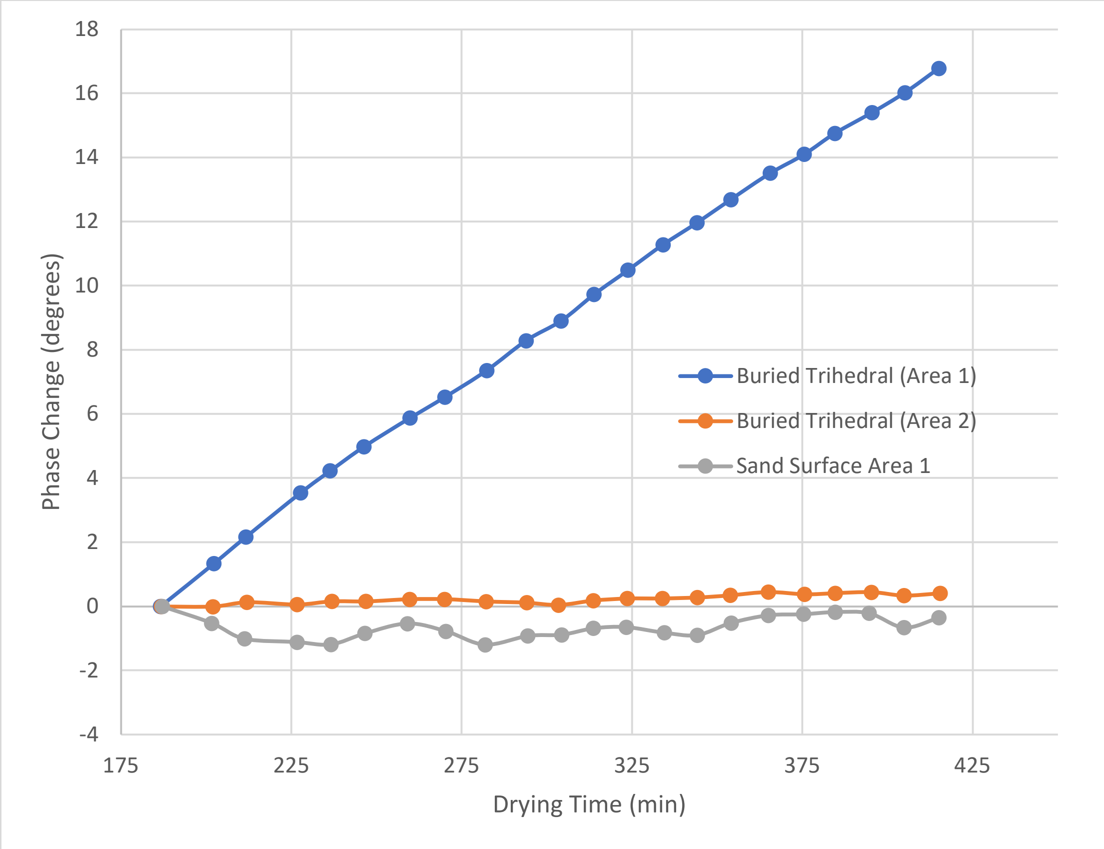

Figure 3.17: DInSAR phase history during the experiment. The phase of the buried trihedral in Area 2 (orange dotted line) is relatively stable as there was no change in the sand moisture. While the phase of the buried trihedral of Area 1 (blue dotted line) is clearly shift with time. It is almost linearly correlated to the sand moisture

The results of the laboratory experiment conducted by Morrison et al. (2013) clearly reveal that changing the soil moisture causes variations in both the backscatter and the DInSAR phase. This has important implications, from the subsurface imaging point of view, because it suggests that these two observed variables can be used to discriminate between a surface return and that from a buried target. This technique for discriminating between surface and subsurface features is referred to as Sub-surface Synthetic Aperture Radar (SubSAR).

For application to wide areas, Morrison et al., (2013) suggested starting with analysing the DInSAR phase for the whole area over a specific time period. If the variation in the soil moisture is known over this area, then it is possible to search for any pixel that shows the same linear correlation between the DInSAR phase and soil moisture change to that shown in the Fig. 3.16. This would be the first indication of a potential buried target. The second indication of the presence of a buried target would be the backscatter response. For those pixels that exhibit the appropriate DInSAR phase behaviour, the observed change in the backscatter should be inversely related to the change in the moisture and in contrast with the surrounding pixels. By utilising these two discriminating factors it should therefore be possible to search large areas for possible buried target signatures, provided that the soil moisture is known. However, the observed phase and the backscatter behaviour of the buried targets dissents all the previous theories of the soil response to the microwave signals. For example, Cognard et al. (1995) reported that that, for different types of soils, the radar backscatter is increased as the surface soil moisture increases (Cognard et al. 1995). Similarly, the phase change of wet soil is inversely related to the moisture content (Morrison et al., 2011). These are both contrary to the behaviour observed for a buried object.

Overall, the SubSAR technique seems to be a promising tool for subsurface imaging as it can discriminate between the surface and buried target responses by monitoring the DInSAR phase and backscatter of a changing soil moisture. The potential benefits of this method are that it can be used to explore remote areas without the need for field investigations or comparison with optical remote sensing imagery. However, despite its significant potential, the SubSAR technique is still limited to laboratory experiments and its application to satellite SAR data remains untested. Once it is validated, it will be widely applicable to many disciplines including, but not limited to, infrastructure management, environmental science, archaeological exploration and most importantly, for humanitarian purposes, such as land mine detection.

3.7 Summary

In this chapter, the main factors that influence the microwave signal's interaction with the soil surface have been discussed. To summarise, part of the signal reflects from the soil surface while the other component penetrates the surface, to a depth depending on the signal wavelength and the dielectric constant of the soil. For a specific soil type, the dielectric constant, which is proportional to the water content, influences both the amplitude and the phase of the backscattered signal.

Subsurface imaging exploits the fact that part of the incident energy penetrates the soil medium and can interact with objects contained within it. To date, it is only the amplitude component of the backscattered signal that has been utilised to analyse buried target signals, which is not sufficient to determine conclusively whether the imaged target is exposed on the surface or buried. However, at the end of this chapter, a recently proposed method for subsurface imaging that depends on analysing both the amplitude and the differential phase of the target was introduced – SubSAR. Using this approach, it is possible to discriminate between surface and buried features without the need for additional sources of information and thus, it is considered to be a promising scheme for buried feature detection in remote areas where ground truth is very difficult to obtain. However, this technique is still limited to laboratory experiments and its application to satellite SAR data has not been evaluated.

In order to evaluate the application of the SubSAR method to spaceborne SAR data, a field-scale equivalent of the SubSAR laboratory experiment is required. The following Chapter addresses this, and provides details of an experiment designed and implemented for the purpose of evaluating the application of SubSAR for satellite-based buried feature detection. This involves covering a trihedral corner reflector with known characteristics under a layer of sand to simulate a buried target. The DinSAR phase and the backscatter of this buried target will then be monitored in conjunction with the moisture content of the overlying sand.

Chapter 4: Experimental Design and Implementation

4.1 Introduction

Chapter Three introduced the different methods of using SAR data for subsurface imaging. Early models involved searching the SAR image for any features that are not visible on the ground or in optical remote sensing imagery. The visual interpretation of the SAR image for this purpose, however, requires additional sources of information regarding the existence of the buried targets. However, a recently developed method for subsurface target detection (SubSAR) was then introduced, that utilises the amplitude information of the SAR image as well as the DInSAR phase history. This has the potential to be a promising method for discriminating between surface and buried features without requiring additional sources of information. The overall aim of this thesis it to validate this SubSAR technique for application to satellite SAR data. Therefore, this chapter discusses the design of field-scale experiments, which are equivalent to the original SubSAR laboratory experiments. This involves creating a set of radar point targets and covering them with a layer of sand to simulate buried targets. A set of measurements are then required to test the validity and the quality of the experiment, involving the analysis of the radiometric and interferometric phase stability of the point targets (i.e., corner reflectors in this study). This is required to ensure that any change in the measured phase and backscatter is due to the variations in the water content of the covering sand and not the instability of the corner reflectors (CRs). Lastly, the SubSAR experiment itself is then presented, which is implemented by monitoring the effect of the covering sand's moisture content on the incident signal.

4.2 Study area

The combination of study area characteristics and radar point targets is essential to the success of the SubSAR field experiment. The radar point targets used in this study are corner reflectors (CRs), and these should exhibit a high signal-to-clutter (STC) ratio in order to be readily identified in a SAR image. In other words, the backscattered signal from the area surrounding the CR (i.e., the background) should be very low compared to that from the CR itself. Specifically, the background backscatter should be at least 20 dB less than the CR radar cross–section (Sarabandi and Chiu 1996). Additionally, the CRs should be located in areas devoid of man-made features, especially in the line of sight direction. This is because – like CRs – buildings, fences and other built structures can also exhibit high radar reflectivity due to double bounce reflection, which can subsequently make it a challenging task to identify CRs in the SAR imagery. For this reason, Bunny Farm (Fig 4.1), located 10 km to the south of Nottingham, England, was selected as the study area to implement the experiment. This arable farm produces a variety of different crops from season to season (Fig. 4.2) and has an area exceeding 100 hectares. No man-made features are located inside the farm, and trees are predominantly confined towards the outer field boundaries.

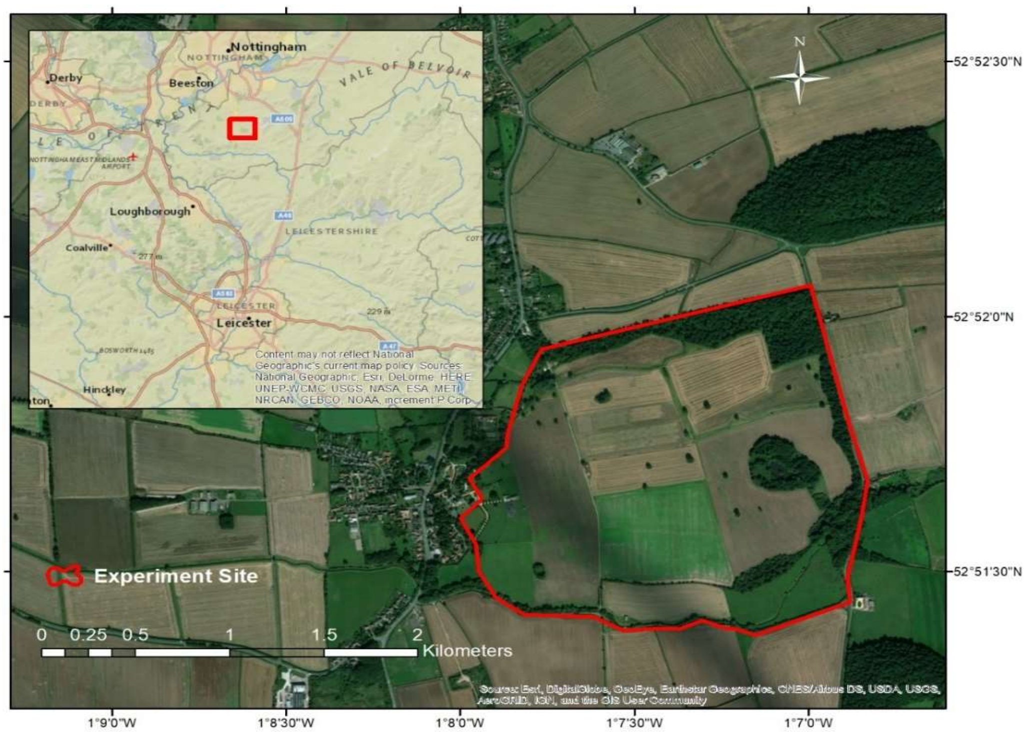

Figure 4.1: Location of the experimental site (Bunny Farm), near the city of Nottingham. The site is clear from man-made features, with little topography that will not cause any distortion to the SAR image.

Figure 4.2: The study area (Bunny Farm). The farm is used to grow a variety of crops.

The farm area is topographically flat, as can be seen from Fig 4.2, with a maximum height variation (relief) of less than 10 m (Fig 4.3). Consequently, there should be no layover, shadow or foreshortening effects present in any of the SAR imagery for this study area. Finally, the site is secure, meaning that the CRs can be installed during the experiment period without risk of them being disturbed. However, there were some farm management restrictions surrounding the use of this site for the experiment. Firstly, it was specified that concrete foundations were not permitted, and secondly, that the CR structures should be removed upon conclusion of the experiment. Accordingly, to satisfy these constraints, it was necessary to design novel CRs that were rigid but also readily removable after the experiment had been completed.

Figure 4.3: Topographic map of the experimental site.

Given the limited budget of this research project and the size of the experimental area, it was proposed to install a total of seven trihedral CRs within this study area for long term monitoring. The distribution of the CRs within the area was another important factor to consider for the successful implementation of the experiment. In terms of separation distance, the CRs needed to be far enough apart so that they are resolved as separate targets in the SAR image, and so that there is no interference in the signal from neighbouring targets. However, to minimize atmospheric effects on the CR measurements, the separation distance between adjacent CRs must also be kept to a minimum (Ferretti et al. 2007). For these reasons, potential CR locations were identified within the experimental site in such a way that the baseline between the CRs was 150–300 m, while also being easily accessible by car for logistical purposes, e.g., to aid the deployment of the CRs and the sand samples. Moreover, these locations were selected in order to avoid potential conflict with the farm machinery. Fig. 4.4 below shows the proposed locations for the CRs within the study area. In order to confirm the suitability of these locations and to determine the appropriate size of the CRs, a clutter analysis was undertaken for a circular area of 50 m radius around each of these proposed locations (see Section 4.4.1).

Figure 4.4: The proposed locations for the CRs. The yellow circles represent a buffer zone of 50m around each CR, which is the area to be analysed for background clutter.

4.3 SAR data

In this study, SAR data acquired by the Sentinel-1 satellite was utilised. Sentinel-1 is the first satellite mission of the Copernicus program – an Earth Observation and monitoring initiative operated by the European Space Agency (ESA) on behalf of the European Union (EU). The Copernicus program aims to provide information that will help to improve the climate change response, environmental management, and civil security within Europe (européenne 2012). Sentinel-1 is a constellation of two identical, near-polar orbiting satellites. The first satellite, Sentinel-1A, was lunched on 3rd April 2014 and the second, Sentinel-1B, was launched two years later (Miranda et al. 2017). Providing medium resolution SAR data for environmental and monitoring research, both Sentinel-1 satellites host a C-band SAR system (5.4 GHz – 5.55 cm) that is intended to complement the previous ESA SAR missions of ERS-1 & 2 and ENVISAT. The Sentinel-1 mission acquires data in both the ascending and descending tracks, offering an improvement in revisit time with respect to ERS and ENVISAT, with a repeat cycle of 6 days over Europe and 12 days for the majority of the remaining global landmass (ESA 2013). Sentinel-1 has many acquisition modes and that one used for interferometric processing is the Single Look Complex (SLC) – Interferometric Wide (IW), which is utilised in this research. The characteristics of this imaging mode are listed in Table 4.1 below (européenne 2012).

Table 4.1: Characteristics of IW imaging mode of Sentinel-1.

Product Type	**Interferometric Wide Swath, Slant-range, Single Look Complex**		
Coordinate System	Slant Range		
Spatial Resolution	20 m (Azimuth) x 5 m (Ground range)		
Pixel sampling	14.1 (Azimuth) x 2.3 (Slant range)		
Polarization	Single (HH or VV) or Dual (HH+HV or VV+VH)		
Beam ID	IW1	IW2	IW3
Ground Range Coverage [km]	251.8		
Slant Range Resolution [m]	2.7	3.1	3.5
Azimuth Resolution [m]	21.7	21.7	21.6
Slant Range Pixel Spacing [m]	2.3	2.3	2.3
Incidence angle [°] (Swath Centre)	32.9	38.3	43.1

The Sentinel-1 IW product is composed of three sub-swaths (Fig. 4.5a), with each sub-swath further consisting of a series of small images, or bursts. There are typically nine bursts in each sub-swath (Fig. 4.5b). The bursts are ordered in the azimuthal acquisition time where each burst has a duration of 2.75 seconds, and the overlap between the bursts is between 50–100 samples. Each of these bursts is provided pre-processed as a separate SLC image. To create a wide IW image from these sub-swaths, the bursts of each sub-swath have to be merged together to create a full sub-swath image, in a process known as de-burst (Sowter et al. 2016). The de-burst operation consists of generating one continuous image using the azimuthal time of each burst, by removing the black demarcation lines between the individual bursts. Then the three de-burst sub-swaths are merged to form the final mosaicked IW product. The de-burst and merge processes are commonly applied within SAR processing software.

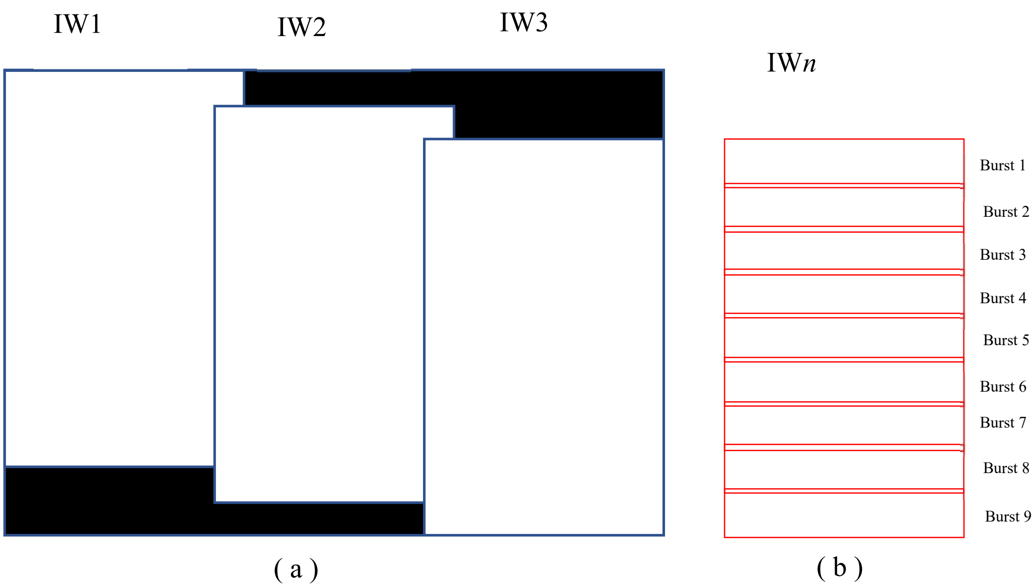

Figure 4.5: Sentinel-1 SLC image structure. (a) the three sub-swaths in the azimuth direction, (b) the bursts in each swath.

4.3.1 **SAR image track selection**

Sentinel-1 acquires data during both the ascending and descending passes, with the experimental study area covered by the ascending track No. 30 and the descending track No. 154 (Fig. 4.6). Since the experiment requires field visits concurrent with the satellite overpass, careful selection of the appropriate track is necessary. The satellite overpass time is at 6:20 AM (GMT) for the descending pass and 5:45 PM for the ascending pass. Due to practicalities, such as suitable lighting conditions throughout the duration of the experiment, the ascending pass (Track 30) was chosen.

For this track, all the data used in this research were downloaded freely from the Copernicus Open Access Hub (https://scihub.copernicus.eu/dhus/). These SAR images are acquired in the VV polarization mode and the incidence angles of each frame vary across the swath width from 29.1° in the near range to 46° in the far range (ESA, 2012).

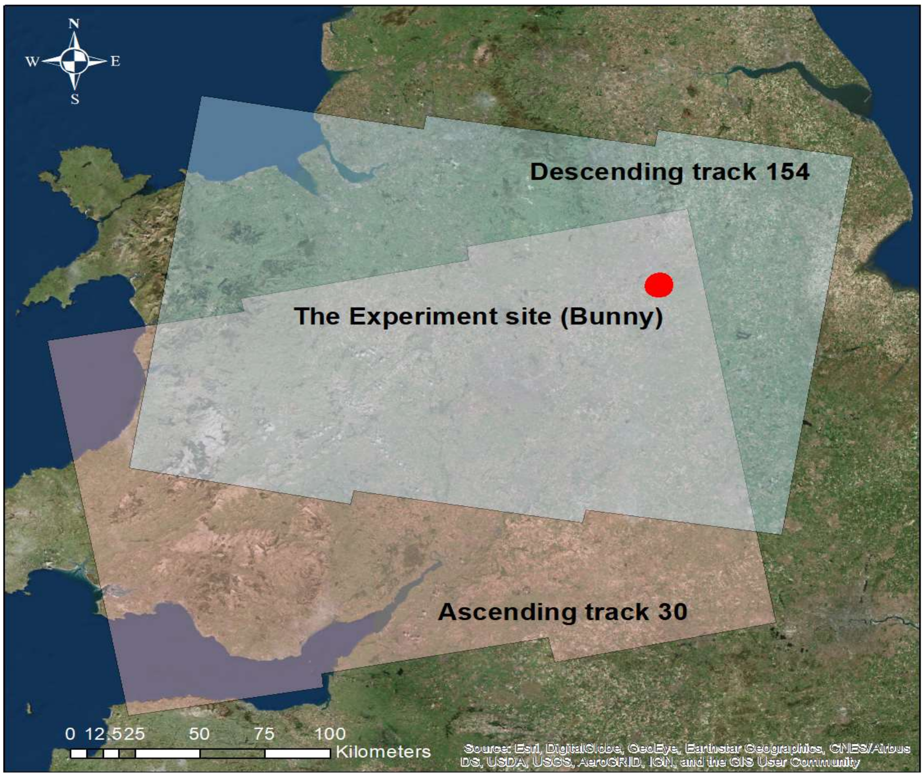

Figure 4.6: The Sentinel-1 tracks over the experimental site.

4.3.2 Image selection

The SAR imagery used in this research project can be categorised into three datasets (Table 4.2). The first dataset was used in the clutter analysis for determining the design of the optimum CR in terms of size and their positioning. This dataset consisted of 12 Sentinel-1 SLC images covering the period 12th March 2015 –22nd July 2015. These images represent all the available Sentinel-1 data for the study area from Track 30 prior to CR installation commencement on 15th August 2016. It is necessary to note that although Sentinel-1A was launched in April 2014, data only became publicly available in March 2015 for the majority of the UK, which is why there was only 12 images used in the background clutter analysis, see section 4.4.1. Data during the CR installation period between 15th August 2016 and 1st October 2016 was not used in any analysis. The second set of data is that used in the stability analysis of the installed CR network in order to determine its suitability for the SubSAR experiment. This will be covered in detail in Section 4.7.1. A total of 19 Sentinel-1 images were used in this analysis for the period 2nd October 2015–19th December 2016. During this period, the CRs are present at proposed locations in the field (Fig 4.4) and were not covered with sand. The third dataset was used in the SubSAR buried feature experiment. This is the most important part of the experiment as it will help to answer the research questions. This experiment is covered in Section 4.8. A stack of 37 Single-Look Complex (SLC) level-1 Sentinel-1 images were acquired over the experimental site between 2nd October 2015 and 19th December 2016. Table 4.2 lists the dates of Sentinel-1 images used in this thesis, along with the status of the CRs at each image acquisition.

Table 4.2: Sentinel-1 images used in this thesis.

Image date	Experiment 1	Experiment 2	CR Status
12/03/2015	clutter analysis		No CRs
24/03/2015	clutter analysis		No CRs
05/04/2015	clutter analysis		No CRs
17/04/2015	clutter analysis		No CRs
29/04/2015	clutter analysis		No CRs
11/05/2015	clutter analysis		No CRs

23/05/2015	clutter analysis		No CRs
04/06/2015	clutter analysis		No CRs
16/06/2015	clutter analysis		No CRs
28/06/2015	clutter analysis		No CRs
10/07/2015	clutter analysis		No CRs
22/07/2015	clutter analysis		No CRs
15/08/2015			CR Installation
27/08/2015			CR Installation
08/09/2015			CR Installation
20/09/2015			CR Installation
02/10/2015	Stability analysis	SubSAR	Un-covered CRs
19/11/2015	Stability analysis	SubSAR	Un-covered CRs
01/12/2015	Stability analysis	SubSAR	Un-covered CRs
13/12/2015	Stability analysis	SubSAR	Un-covered CRs
25/12/2015	Stability analysis	SubSAR	Un-covered CRs
06/01/2016	Stability analysis	SubSAR	Un-covered CRs
18/01/2016	Stability analysis	SubSAR	Un-covered CRs
30/01/2016	Stability analysis	SubSAR	Un-covered CRs
11/02/2016	Stability analysis	SubSAR	Un-covered CRs
23/02/2016	Stability analysis	SubSAR	Un-covered CRs
06/03/2016	Stability analysis	SubSAR	Un-covered CRs
18/03/2016		SubSAR	Buried CRs
30/03/2016		SubSAR	Buried CRs
11/04/2016		SubSAR	Buried CRs
23/04/2016		SubSAR	Buried CRs
05/05/2016		SubSAR	Buried CRs
17/05/2016		SubSAR	Buried CRs
29/05/2016		SubSAR	Buried CRs
10/06/2016		SubSAR	Buried CRs
04/07/2016		SubSAR	Buried CRs
16/07/2016		SubSAR	Buried CRs
28/07/2016		SubSAR	Buried CRs
09/08/2016		SubSAR	Buried CRs
21/08/2016		SubSAR	Buried CRs
02/09/2016		SubSAR	Buried CRs

14/09/2016		SubSAR	Buried CRs
26/09/2016		SubSAR	Buried CRs
08/10/2016		SubSAR	Buried CRs
20/10/2016		SubSAR	Buried CRs
01/11/2016	Stability analysis	SubSAR	Un-covered CRs
07/11/2016	Stability analysis	SubSAR	Un-covered CRs
13/11/2016	Stability analysis	SubSAR	Un-covered CRs
25/11/2016	Stability analysis	SubSAR	Un-covered CRs
01/12/2016	Stability analysis	SubSAR	Un-covered CRs
07/12/2016	Stability analysis	SubSAR	Un-covered CRs
13/12/2016	Stability analysis	SubSAR	Un-covered CRs
19/12/2016	Stability analysis	SubSAR	Un-covered CRs

4.4 Corner reflectors

As described in Chapter Two, the amplitude component of the SAR image is a measure of the backscattered signal from objects on the earth's surface. Brighter image pixels correspond to objects that have a large radar cross-section (RCS) and therefore produce a greater amount of backscatter. Radar point targets, such as corner reflectors (CRs) and transponders, are usually characterised by large a RCS relative to their small size. CRs are the most economical type of radar point target because they are passive devices that do not require a power source to operate, have low maintenance requirements and are simple to construct (Curlander, 1991). A CR is typically characterized as a high brightness target in a SAR image due to its reflectivity for the radar signals, which ensures that the target can be readily identified in the acquired SAR images. Using appropriate CR detection procedures, the phase at the exact location of the reflector can be determined and analysed (Bovenga et al. 2012).

Corner reflectors can be made in various shapes, such as cylinders, dihedral CR, trihedral CR, top hat, and flat plate reflectors (Robertson 1947). Of these, the trihedral CR is the most common and practical device for SAR observations due to its low manufacturing cost, orientation flexibility, long term structural stability and high RCS relative to its small physical size (Freeman, 1992). For trihedral CRs, the triple bounce of the incident signals causes the CR to have a high-constant RCS for a wide range of incidence and azimuth angles (Knott 2012). It is for this reason that high intensity backscatter values can be obtained for pixels containing CRs, regardless of whether the CRs were or were not carefully oriented towards the SAR satellite.

For these reasons, a trihedral CR design was chosen for this study. A trihedral CR (Fig 4.7), consists of three identical, right-angled isosceles triangular faces, which are joined together along their short sides (*la*). Each two joined faces are mutually perpendicular to each other to assure the re-directivity of the incoming signals. The peak RCS for a typical trihedral CR can be calculated as (Robertson 1947):

$$RCS_{trihedral} = \frac{4\ la^4}{3\lambda^2} \tag{4.1}$$

where *la* is the length of the small side of the triangle sheet, and λ is the wavelength of the SAR signal.

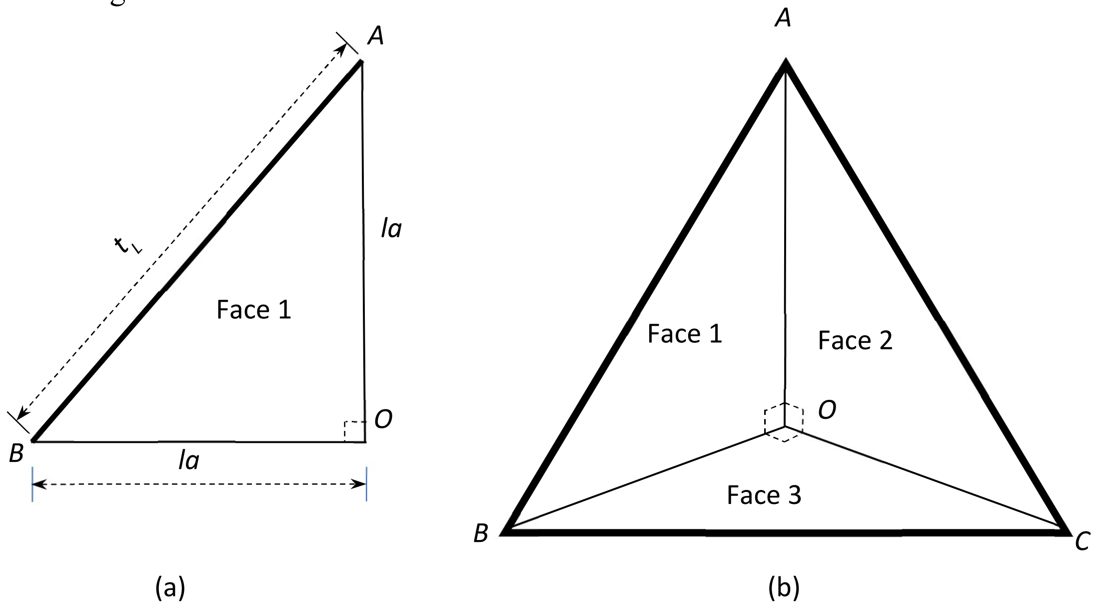

Figure 4.7: Trihedral Corner Reflector Diagram. 4.7a represents a right-angled triangle face which represents the main component of the CR. 4.7.b is an assembled trihedral CR from three right-angled faces.

The maximum RCS can be achieved when the CR boresight line coincides with the radar line of sight (Fig 4.8). The trihedral CR boresight, or symmetry access, is the perpendicular line to the CR aperture that passes through the apex of the reflector. To effectively produce a bright point target in SAR imagery, suitable design, positioning and look direction specifications need to be met (Bovenga et al. 2012). The electromagnetic wave will undergo a triple reflection (triple bounce) when it strikes the reflector's interior face within the operating angle of the trihedral. The final reflection will direct the signal back to the source in the same incident direction. Not all of the interior area of the reflector is involved in the triple reflection mechanism as some of the rays will only be reflected twice before leaving the reflector, depending on the incidence angle and the orientation of the device.

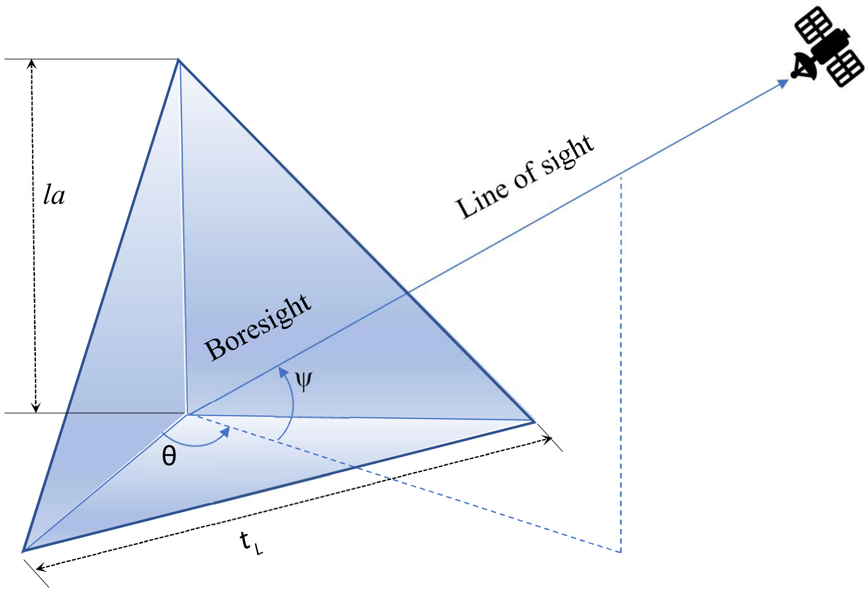

Figure 4.8: Trihedral corner reflector orientation geometry. Maximum RCS is obtained when the CR boresight line coincides with the satellite line of sight.

Thus, the area of the reflector where the three-bounce dominates is called the effective area (Robertson 1947). The shaded area of the CR in Fig 4.9 illustrates the effective area of the reflector where the triple bounce reflection mechanism occurs. The parts of the reflector that do not contribute to the triple bounce constitute 1/3 of the aperture, leaving the effective aperture as a hexagonal shape whose side length is one third of the triangular face's long side length.

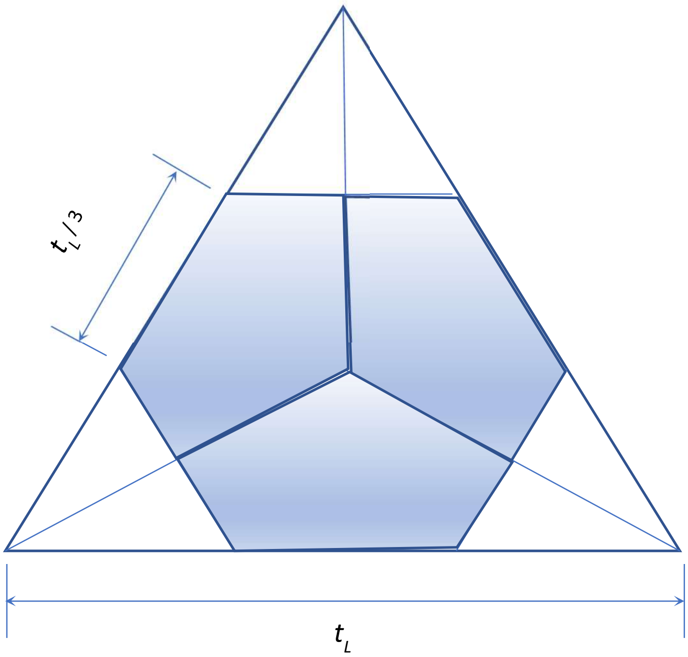

Figure 4.9: The effective area of the trihedral CR aperture (shaded hexagon) that participates in the internal triple bounce reflection. The unshaded tips have no contribution to the triple bounce reflection mechanism in the optimum orientation.

4.4.1 CR size determination

Due to the dynamic nature of the farm, the amplitude level of the background is expected to fluctuate throughout the year. A baseline analysis of multi-temporal Sentinel-1 imagery over the proposed CRs locations is therefore required to precisely determine the optimum size of the CRs. To achieve this, an area of 50 m radius was monitored for each proposed CR location for a period of 6 months covering the different farming seasons. As mentioned in Chapter Two, the raw digital numbers (*DNs*) for the pixels in a SAR amplitude image can only be used for qualitative analysis and are not suitable for quantitative applications. For this reason, pixel *DN* values were converted into backscatter coefficient values to make them suitable for multi-temporal image analysis. The process of converting a SAR image pixel *DN* value into a physical value that is directly related to the scene backscatter measurements is known as radiometric calibration. The following calibration steps are described in detail by

Miranda et al. (2015). For distributed targets, the backscatter coefficient (σ^o) can be derived from the image *DN* as follows:

$$\sigma^o = \frac{DN^2}{A_{dn}^2 . K} \sin(\theta_i) \quad (4.2)$$

Where A_{dn} is the product final scaling from internal SLC to final SLC, θ is the incidence angle and *K* is the calibration constant (provided with each image product). In the case of Sentinel-1 products, data are provided with a calibration Look-Up Table (LUT) to assist the conversion process. The radar cross-section LUT for Sentinel-1 (A_σ), is defined as:

$$A_\sigma = \sqrt{\frac{A_{dn}^2 . K}{\sin(\theta_i)}} \quad (4.3)$$

where A_σ is the LUT interpolated value that contains calibration information about the scene needed to transform the radar *DN* into σ^o. This implies that the calibration LUT essentially contains the calibration constant (*K*), the incidence angle, and the area normalisation factor as explained by Freeman (1992). The LUT is provided as sub-sampled range vectors that can be interpolated for the entire study area. Once it is interpolated, the LUT can then be used directly to convert the *DN* into σ^o using the following formula:

$$\sigma^o = \frac{DN^2}{A_\sigma^2} \quad (4.4)$$

where *DN* for SLC products can be derived as:

$$DN = \sqrt{I^2 + Q^2} \quad (4.5)$$

where *I* and *Q* are the real and imaginary parts of the complex number, respectively. The σ^o calculated from this step are provided as a natural value, which can then be converted into the logarithmic scale (*dB*) using:

$$\sigma_{db}^o = 10. log_{10} \sigma^o \quad (4.6)$$

Using this procedure, the *DNs* within the 12 Sentinel-1 images shown in Table 4.2 (labelled as Clutter analysis) were converted to backscatter coefficient (σ_{db}^{o}) values. The images used in the clutter analysis cover a period of six months (12th March 2015 to 22nd July 2015) prior to deploying the CRs in the field. The earliest image in this analysis is the first ever Sentinel-1 image acquired over the study area and thus, this analysis could not be extended before this time. After August 2015, the CR installation campaign started in preparation for the main experimental phase, so it was no longer possible to analyse the clutter after that date. Clutter analysis is an important design step that aims to investigate the backscatter behaviour of the proposed CR installation area at different periods to help determine the optimum CR size that will maintain visibility at all times. For each proposed CR location (Fig 4.4), a buffer area of 50 m radius was analysed within the Sentinel-1 images to find the maximum clutter value, as determined by the maximum σ_{db}^{o} value in each buffer zone. The results of the clutter analysis are shown in Table 4.3 and illustrated in Fig 4.10.

Table 4.3: The maximum σ_{db}^{o} value in each proposed CR buffer zone in dB values.

Image No.	Image date	CR1	CR2	CR3	CR4	CR5	CR6	CR7
1	12/03/2015	-8.19	-5.87	-7.32	-5.88	-6.00	-6.91	-8.67
2	24/03/2015	-4.27	-0.98	-3.65	-3.38	-4.03	-4.54	-5.30
3	05/04/2015	-3.39	-4.79	-7.43	-6.67	-6.11	-2.73	-9.96
4	17/04/2015	-6.36	-4.96	-3.68	-5.12	-4.01	-2.89	-9.44
5	29/04/2015	-3.85	-4.21	-5.46	-6.86	-6.41	-1.79	-10.11
6	11/05/2015	-4.01	-2.28	-4.89	-7.02	-4.67	-6.29	-7.97
7	23/05/2015	-2.50	-1.71	-0.14	0.50	-1.43	0.59	-6.06
8	04/06/2015	-2.28	-2.78	3.31	1.09	-1.78	0.95	3.50
9	16/06/2015	1.74	-5.41	1.35	-1.46	-1.11	0.29	-6.82
10	28/06/2015	-2.32	-5.73	1.56	0.54	-0.73	3.00	-6.18
11	10/07/2015	-4.87	-6.27	-3.69	-3.37	-2.17	-3.60	-3.15
12	22/07/2015	-2.03	-0.66	-3.81	-6.72	-6.06	-9.45	-5.78

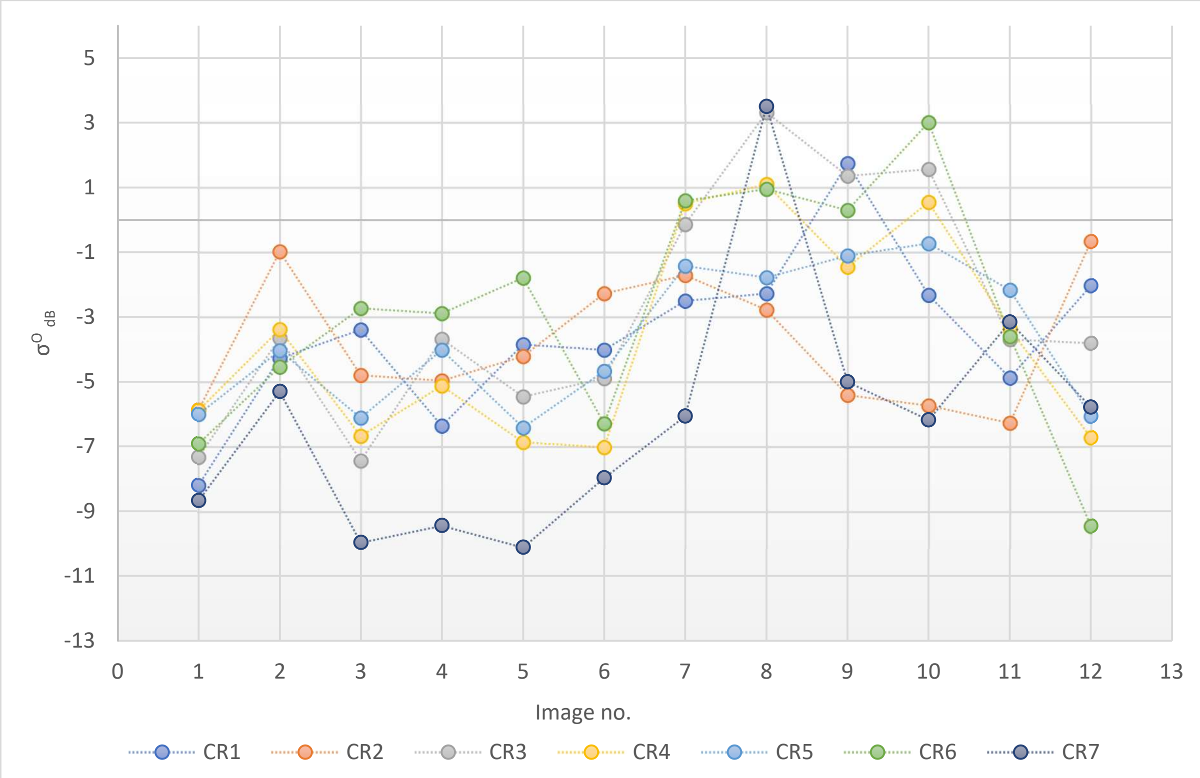

Figure 4.10: Maximum σ^o_{db} for each CR buffer zone

From the observations above, the maximum σº (dB) for each proposed CR buffer zone was found to be variable over time. This was mainly caused by the dynamic changes in the vegetation cover (crop growth) over the monitoring period. Overall, it ranged between -11 dB and +3 dB. The average peak σº for all the CR buffer zones was about -4 dB, which is relatively low. According to Sarandibi et al. (1996), the RCS of a CR has to be 20 dB more than the background to be accurately identified in the SAR image. Thus, the minimum RCS for each reflector has to be the maximum observed σº value plus 20 dB. This corresponded to RCS of 21.7 dB, 19.3 dB, 23.3 dB, 21 dB, 19.3 dB, 23 dB and 23.5 dB for CR1 through to CR7, respectively. The different RCS values relate to different reflectors sizes, however, for practical purposes during CR manufacture it is easier to have them all the same size. Therefore, a CR with a minimum RCS of 23.5 dB will maintain visibility in the SAR images at all times and at all proposed locations. Considering the experiment of the buried target simulation and the attenuation that could affect the signal when transmitted through the sand layer (as explained in Chapter Three), a 1 m triangle face length (side *la* in Fig. 4.7) was chosen for the construction of the CRs. A CR of such size will theoretically produce a RCS of ~31 dB, which is at least 7 dB greater than the minimum required RCS. Accordingly, when deployed at the locations shown in Fig. 4.4, the CRs were expected to produce very bright points in the SAR images as the contrast in brightness between the background and the CRs is significant.

4.4.2 CR manufacture

In order to achieve the desired RCS, several factors must be considered in the CR design and manufacturing processes. Firstly, this experiment is designed to last for a year's worth of SAR observations. Therefore, the CRs need to be sturdy, rigid and weather resistant. The main factor in achieving this is the material. Aluminium is the most commonly used material to manufacture CRs, and while it is more expensive than other materials such as steel, it is typically less susceptible to corrosion and oxidation. Also, aluminium is typically not as strong as steel, but it is also almost one-third of its weight. As well as the material, other factors that may affect the performance of the CRs need to be considered. These are the curvature of the triangle plates, plates irregularities, and the inter-plate orthogonality (Garthwaite M. 2017). Plate curvature is the deformation of the plate along its entire length relative to a perfectly flat plane, such as gradual bending across the plate. Plate irregularities are the presence of any small-scale anomalies or non-uniformities that cause a deviation from a perfect flat plate. These factors could significantly reduce the RCS of the CRs if they are not carefully and precisely manufactured.

The design of the trihedral CR consists of three faces, where each face is an isosceles, right-angled triangular plate of *la* = 1 m (Fig 4.11b). For the reasons explained above, aluminium was chosen as the construction material for the triangular faces because it is lightweight and weather resistant. Aluminium sheets of 3 mm thickness were used to overcome the surface irregularities problem. Furthermore, 2.5 cm of the long side of each face (t_L) is bent by 90° to the outside (Fig 4.11a), in order to strengthen the CR faces and to prevent the deformation and curvature during construction and installation. The prefabricated aluminium faces to this specification were purchased from metals4U Ltd.

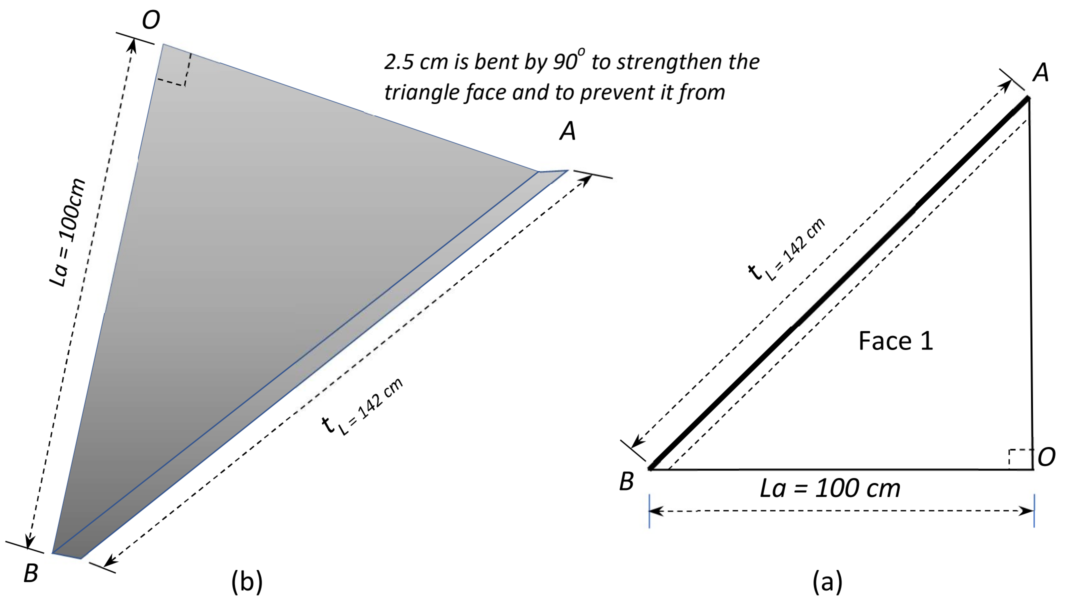

Figure 4.11: The aluminium triangular face. (a) dimensions of a CR face, (b) perspective view of the face, where 2.5cm of the long side (t_L) is bent at 90 degrees to the outside direction.

The last factor to consider during the manufacturing is the inter-plate orthogonality, which is the extent to which the three triangle plates form right angles at their intersection. To this extent, a precise digital angle finder was used to measure the inter-plate angles, and extra care was taken to maintain a right-angle between each two plates. This comprised fixing the three faces together using angle brackets, nut and bolts. Additionally, several holes were drilled close to the CR apex to prevent flooding by allowing precipitation to drain away. The fully assembled CR is too big and the transportation will be very costly. Furthermore, transporting large structures may cause them to be damaged or deformed during the transportation. Therefore, all the materials were transported to the field, where the CRs were assembled (Fig 4.12). The CRs were assembled and install in the study area by myself, at a rate of one CR per day.

Figure 4.12: Assembled CR. The angle brackets are used to support the faces and maintain the inter-plate orthogonality.

4.4.3 Installation

As previously explained, there some constraints were placed on the use of the CRs at the experimental field site. To reiterate, these were that concrete foundations are not permitted and that the CRs must be completely removed upon the conclusion of the experiment. With concrete foundations being the common and most rigid way to install the CR in the field, an alternative solution was required. To overcome this, steel barrels were utilised as temporary rigid bases for the CRs (Fig. 4.13a). The barrels were fixed to the ground using three iron stakes of 1 m length, with the top 30 cm screwed to the barrels and the lower 70 cm of each stake embedded in the ground (Fig 4.13b). Each barrel was filled with 270 kg of crushed stones to provide sufficient stability and rigidity for the CR throughout the duration of the experiment. This simple structure can also be removed easily from the field once the experiment is complete. This represents a novel method of installing the CRs, with the added benefit of being low cost, easy to implement and not labour intensive.

Given the weight of the filled barrels it was necessary to allow sufficient time before commencing the experiment undergo load-settlement at each CR location. Therefore, the experiment started more than six months after installation, where it was presumed that no more settlement was occurring, and these structures are completely stable.

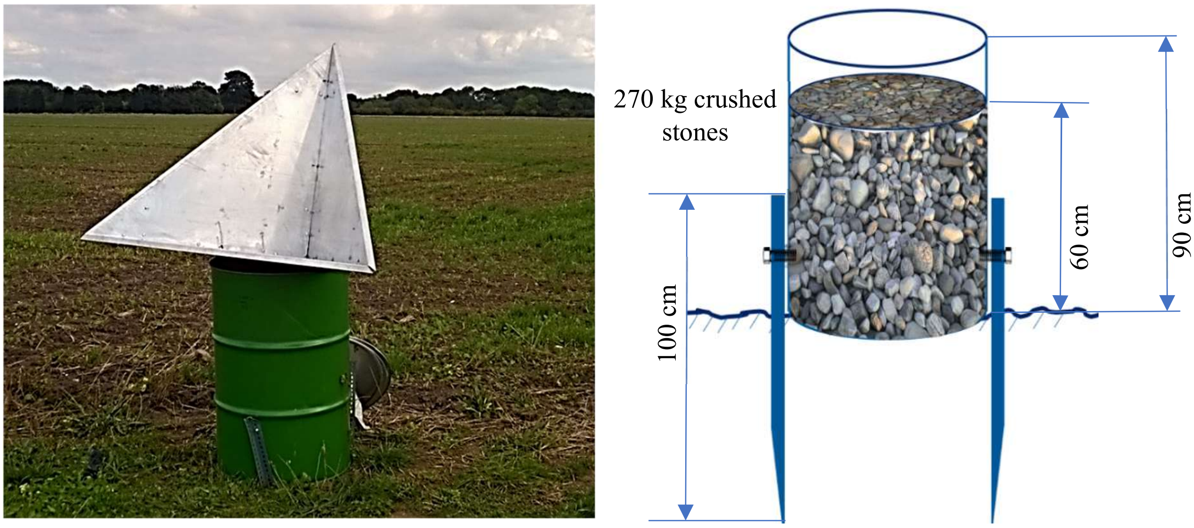

(a) (b)

Figure 4.13: (a) The trihedral CR installed over the steel barrel, (b) schematic of the steel barrel foundation.

The exact locations at which the CRs were installed are provided in Table 4.4. In most CR experiments, the mounting of the CRs on top of the base is one of the most complex and expensive aspects. This is mainly because of the motion screws that are used to orientate the CR to the correct direction and to re-orientate the CR to different satellite passes. In this experiment, the CRs were designed to be fixed to a single satellite pass and so only a single orientation procedure is required.

Table 4.4: Coordinates of the CRs as observed by handheld GPS.

CR	Latitude (N)	Longitude (E)	Elevation (m)
CR1	52.86384°	-1.12822°	38.84
CR2	52.86282°	-1.12779°	40.07
CR3	52.86129°	-1.12713°	40.01
CR4	52.86003°	-1.12662°	38.33
CR5	52.85847°	-1.12653°	40.55
CR6	52.86253°	-1.12204°	43.46
CR7	52.86342°	-1.11804°	42.13

Consequently, it is not necessary to use a complex mounting mechanism and each CR can instead be fastened securely to the barrel by three screws. Fig. 4.14 shows the steps for fixing the CR on top of the foundation barrel and securing it with screws.

Figure 4.14: The CR is securely fixed on the barrel using screws. The location and orientation of the CR is fixed and cannot be re-oriented.

4.4.4 Alignment of the corner reflectors

As mentioned previously, trihedral CRs can be oriented in any direction within the satellite field of view and still be visible to the radar. This is because the re-entering structure of the CR produces a broad RCS pattern. Accordingly, the orientation of each CR is not absolute and a pointing error of a few degrees is acceptable (Xia 2008; Knott 2012). Nonetheless, in order to maximise the observed RCS of each CR it is necessary to carefully determine and measure the orientation of each CR relative to the satellite path. To align the corner reflector towards the SAR satellite, the alignment vector (or the boresight in Fig. 4.7) from the reflector's centre perpendicular to the reflector's aperture plane has to be pointing directly towards the satellite (Ge et al. 2011). This vector is equidistant from all of the reflector's axes and can be identified by two angles, the tilt and azimuth angles, as explained below.

4.4.4.1 Tilt angle

To align the CR towards the satellite it has to be tilted by an angle proportional to the radar signal incidence angle at that location. The reflector's boresight angle, normal to the front face (Ψ) is:

$$\psi = tan^{-1}\left(\frac{1}{\sqrt{2}}\right) \approx 35.26^{o} \qquad (4.7)$$

This angle is constant for all trihedral CRs. In order to obtain the maximum RCS for the reflector, the optimum tilt angle for each CR is given as:

$$tilt\ angle = Satellite\ altitude - \psi \qquad (4.8)$$

where the satellite altitude is the maximum elevation angle during the satellite pass over the study area, and can be estimated by using the information provided by the following website (this is specifically for Nottingham and Sentinel-1A):

http://www.heavens-above.com/PassSummary.aspx?satid=39634&lat=52.9548&lng=-1.1581&loc=Nottingham&alt=69&tz=GMT

Using this website, the appropriate the relative orbit number of Sentinel-1 (i.e. Track 30) is selected and the details related to this track are then displayed alongside the track sky plot (Fig. 4.15). This reveals a maximum latitude of the selected satellite pass to be 45°, which results in a tilt angle of ~10°. This angle was set using a digital clinometer with accuracy of 0.1°. Fig 4.16 below is a schematic diagram that illustrates the required angle for the optimum tilt orientation of the CRs.

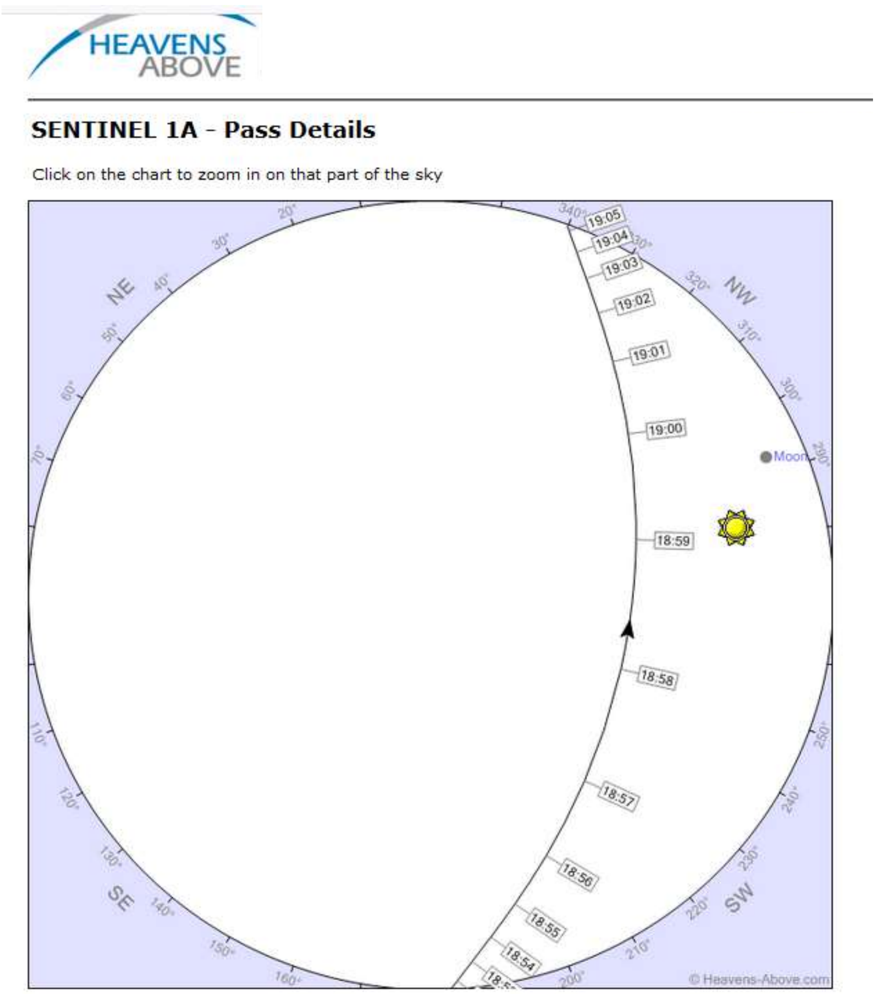

Chart size 650 (500 - 1600)

Date: 01 July 2019
Orbit: 695 x 696 km, 98.2° (Epoch: 01 July)

Event	Time	Altitude	Azimuth	Distance (km)	Brightness	Sun altitude
Rises	18:51:29	0°	181° (S)	3,063	8.8	20.7°
Reaches altitude 10°	18:53:49	10°	188° (S)	2,150	8.2	20.4°
Maximum altitude	18:58:20	45°	261° (W)	947	7.5	19.7°
Drops below altitude 10°	19:02:53	10°	335° (NNW)	2,166	8.8	19.1°
Sets	19:05:15	0°	341° (NNW)	3,088	9.4	18.7°

Figure 4.55: Sentinel-1 orbital parameters of track 30 over the experimental site.

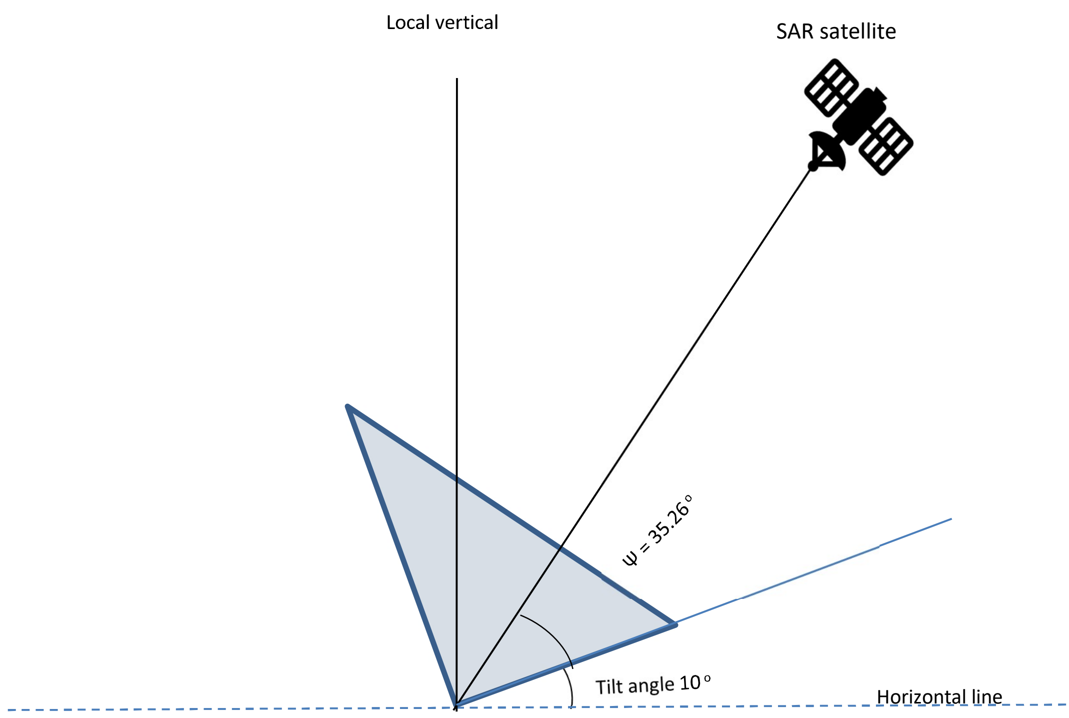

Figure 4.16: CR tilt angle orientation.

4.4.4.2 Azimuth angle

To maximise the RCS, the aperture of the CR must also be pointing perpendicular to the satellite pass. To do so, the azimuth angle (*Az*) of the satellite pass is required:

$$Az = sin^{-1}\left(\frac{\cos\left(inclination\ of\ satellite\ orbit\right)}{\cos\varphi_{geodetic}}\right) \tag{4.9}$$

where the orbit inclination angle for the Sentinel-1 ascending pass is 98.18° (ESA, 2013) and $\varphi_{geodetic}$ is the latitude of the CRs at the study area (i.e., 52.86°). Thus, the azimuth of the satellite pass at that location is -13° 37’ 52" (-13.63°). This azimuth angle was then used to orient the CR perpendicular to the satellite pass (Fig. 4.17). Since high accuracy orientation is not mandatory, this angle was set using a magnetic compass. All seven CRs were oriented towards Sentinel-1 ascending track 30 in this manner. To confirm the visibility of the CRs, an average amplitude image of the study area is generated (Fig. 4.18), using the 19 SAR images listed in Table 4.2 and labelled with Stability analysis. The CRs in these images are un-covered. It is worth noting that this image is in the full Sentinel-1 resolution without multi-looking, where the pixel spacing in the range (horizontal axis) is 2.3 m and the azimuth pixel spacing (vertical axis) is approximately 14.1 m.

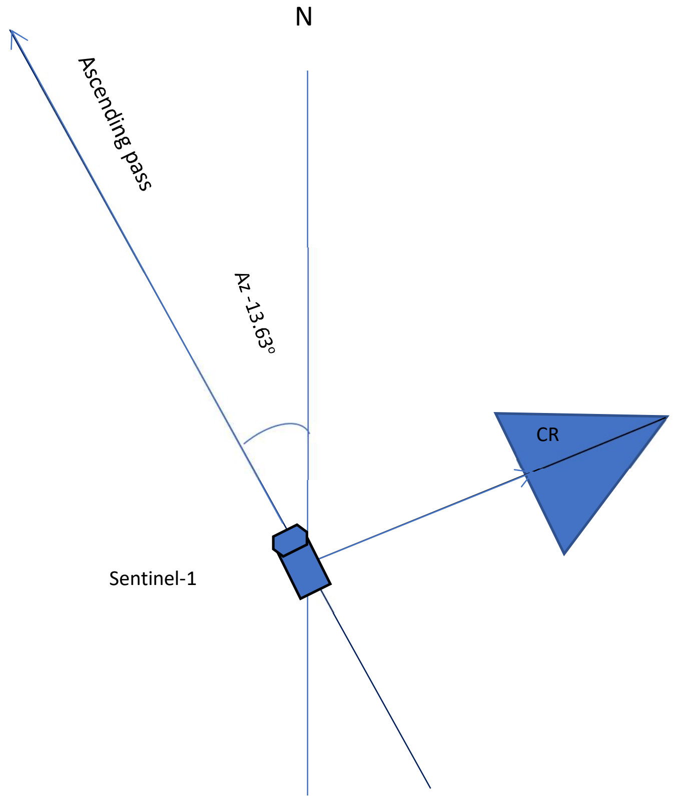

Figure 4.17: Azimuth of Sentinel-1 ascending pass over the experimental site.

Averaging the amplitudes of 19 SAR images will significantly reduce the speckle of the radar images and improves the visibility of the point targets, such as the CRs in this case. The CRs are clearly identified as bright points in the average amplitude image and each CR is labelled with its name for referencing. The visibility of all the CR in this image confirms the efficacy of the CR design and installation campaign. Further quantitative analysis is to be implemented to determine the RCS of each CR and its deviation from the theoretical value. This would provide an additional measure of the accuracy of the design and manufacturing process.

Figure 4.18: Average amplitude image from 19 Sentinel-1 SLC images over the experimental site. The CRs are clearly visible and labelled in the image.

4.4.5 Buried target simulation

Once all CRs are installed in the field, the next stage is to devise a method for using them to simulate buried features for the main SubSAR experiment. This comprised covering the aperture of the CR with a layer of sand that was contained within a plastic bag (see Section 4.8 for more information). To obtain accurate SAR observations from the covered CR, this layer should be placed in a flat position on top of the CR so that the SAR signal is transmitted perpendicularly to the sand layer (Fig 4.19). If the sand layer surface is not flat, then the SAR signal will backscatter from the top surface of the sand layer. A frame was required to hold the layer of sand in position, however, it needed to be constructed of materials that allow the SAR signal to penetrate to the CR and then be reflected back to the SAR antenna (see Fig. 4.18).

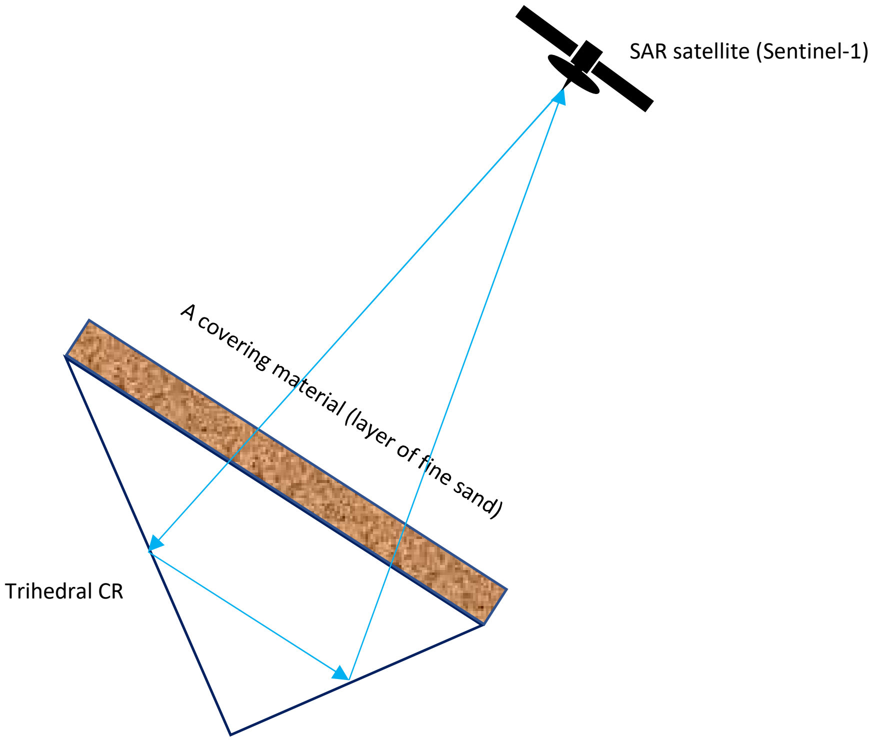

Figure 4.19: The buried target simulation concept.

For this purpose, wooden frames were fitted to the CRs to support the 14 kg mass of the sand layer. The wooden frame was made from 2.5 cm x 5 cm wooden planks, separated by 25 cm to allow as much of the radar signal as possible to be transmitted. The wooden frame was fastened to the CR body by screws, and thus remain fixed for the entire experimental period. Polystyrene sheets of 2.5 cm thickness were used to fill the open spaces in the frame and produce a flat surface on which the sand layer could be overlain (Fig. 4.20). The polystyrene has been approved as a transparent material for the radar signal, so it can be used to without the loss of the signal strength.

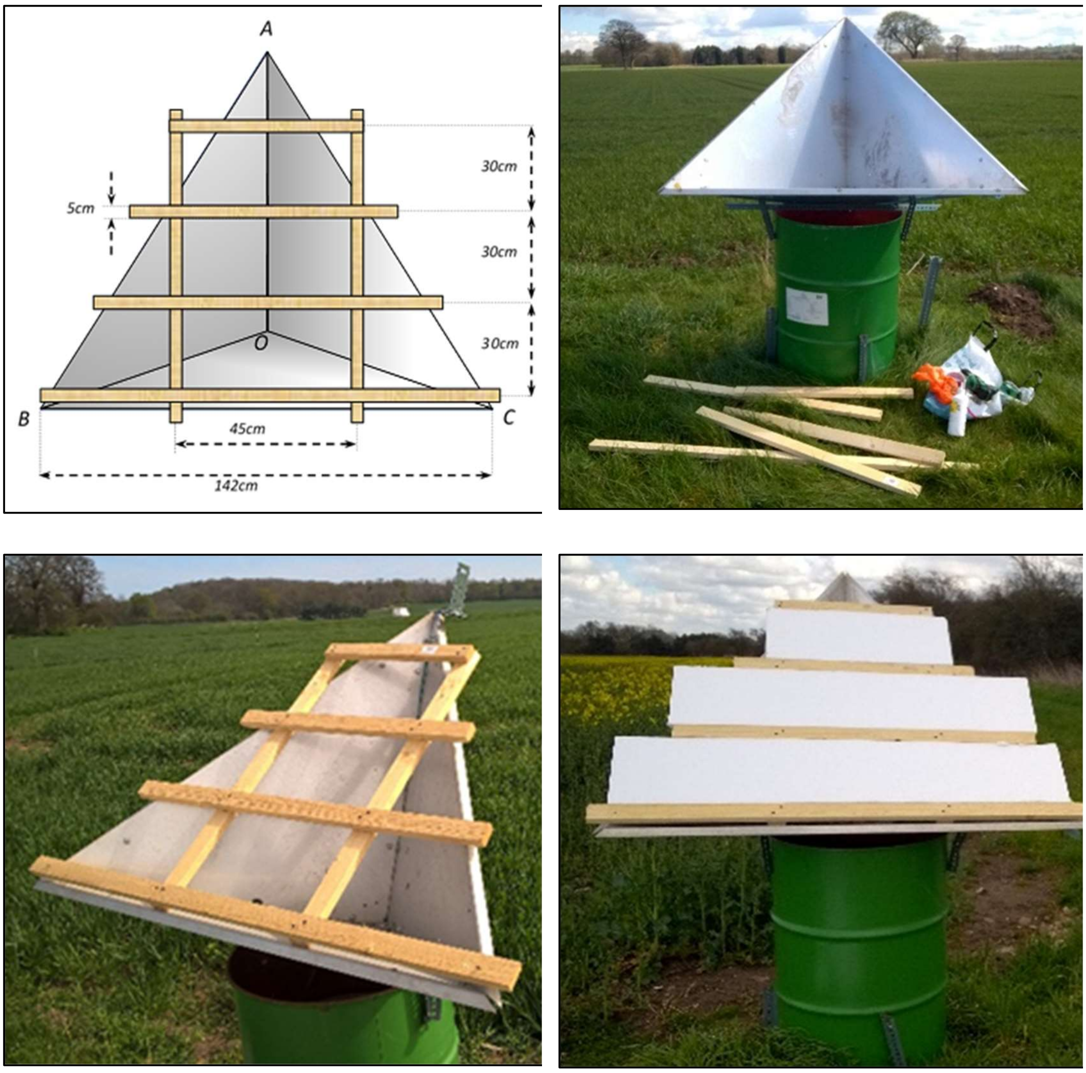

Figure 4.20: A wooden frame is fixed to the CR aperture to support the heavy weight of the sandbags. The spacing between the wooden sticks is not less than 25cm, which is sufficient to allow the SAR signal to pass through. The polystyrene sheets that are used to fill the gabs, are transparent to the SAR signals.

Similar to the plastic bags used to hold the sand, these wooden frames are used in all the observations throughout the experiment. Therefore, their influence on the SAR signal over time will be consistent and can be considered negligible. In summary, the outlined experimental configuration enables control of various parameters that can affect the use of SAR for subsurface feature detection, including the buried target scatting properties, the characteristics of the cover material, penetration depth and moisture content. The final CR when it covered by a sand layer is presented in Fig. 4.21.

Figure 4.61: The complete layout of the CR with sand cover.

4.5 CR detection in the SAR imagery

In order to retrieve accurate amplitude and phase information for the CRs for quantitative analysis, it is first necessary to be able to precisely identify their locations in the SAR imagery. Over-sampling is required to identify the location to within sub-pixel accuracy (Hanssen, 2001). There are slight differences in the procedure required to extract the amplitude and phase information for the CRs. In the following two sub-sections, the amplitude and phase retrieval for the CRs are discussed separately.

4.5.1 CR detection for amplitude extraction

The extraction of amplitude information for the CRs requires them to first be accurately located in the SAR amplitude image. The CRs usually appear as very bright points in the SAR amplitude image, such that on many occasions its brightness can extend to several pixels, rather than only a single pixel. This makes the identification of the exact location of the CR in the SAR amplitude image a very difficult task, and in turn accurate amplitude information cannot be retrieved directly. In order to retrieve accurate amplitude information for the CRs, over-sampling is required to identify the location of the CR in the SAR amplitude image to within sub-pixel accuracy (Hanssen, 2001). Starting from the GPS coordinates (Table 4.4), the CR locations are estimated in the SAR image geometry (azimuth, range) using the Range-Doppler algorithm (Curlander, 1982). Next, a subset of 256 × 256 pixels is clipped from the image around the approximate location of each CR. These subsets are oversampled by a factor of 8 using the zero-padding method in the spectral domain. The CRs are then located at the peak power of the interpolated subset amplitude image. The following steps describe this process in more detail:

1- Locate the position of the required CR in the image and subset an area of 256 × 256 pixels around that CR. Fig. 4.22 shows the subset around CR6, which can be clearly identified as a bright point in the middle of this subset.
2- Oversample this subset by factor of 8 in the spectral domain using the zero-padded method. This involves creating a zero padded matrix of 2048 × 2048 pixels (Fig 4.23). Then interpolate the image subset into the zero-padded matrix in the spectral domain (Fig 4.24).

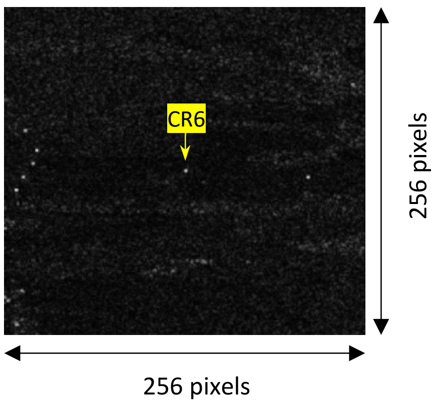

Figure 4.22: A subset of 256 × 256 is clipped around each CR. This is an example subset around CR6, where we can clearly see CR6 at the middle of this image.

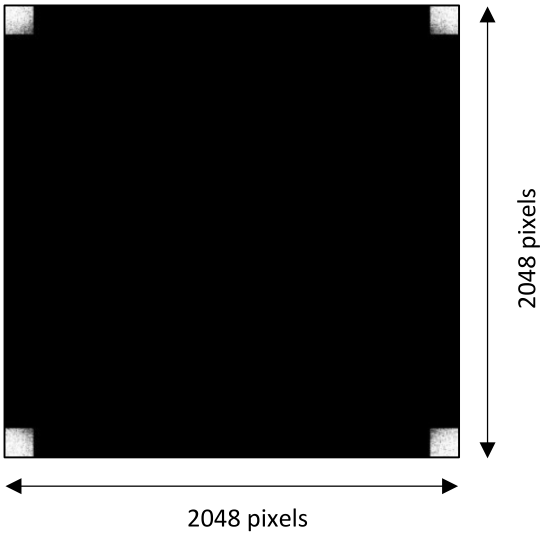

Figure 4.23: Zero-padded matrix 2048 × 2048 pixels, which is 8 times the original subset area.

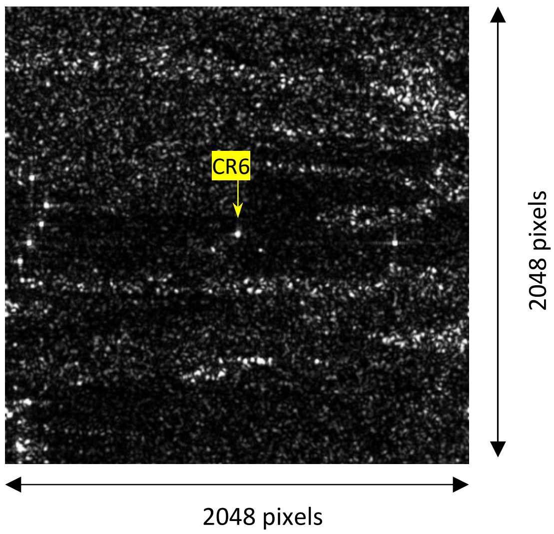

Figure 4.24: Oversampled image of the 256 x 256 subset.

From the oversampled image (Fig 4.24), the Impulse Response Function (IRF) of the point target (CR6 in this example) can be derived. The IRF represents the SAR system response to the point target, also known as the point spread function. It is a two-dimensional profile of the image brightness pattern corresponding to the exact location of the corner reflector in the oversampled image. A typical IFR is illustrated in Fig. 4.25, which shows how the fundamental characteristics of the SAR system can be derived, as well as providing the necessary information for deriving the RCS of the CR under investigation. The most important characteristic of the IRF is the width of the central peak (mainlobe). The SAR resolution can be calculated by measuring the -

3dB width of the mainlobe from the IRF. This can be calculated for both the range and the azimuth directions. The IRF is used to accurately identify the location of the CR within the oversampled image, where the peak value of the IRF in both the range and azimuth directions represent the best estimation of the CR location. The amplitude value of this peak is the amplitude value of the corresponding CR that will be used for further calculations. Analysis of the IRF for each CR will be presented in the next chapter.

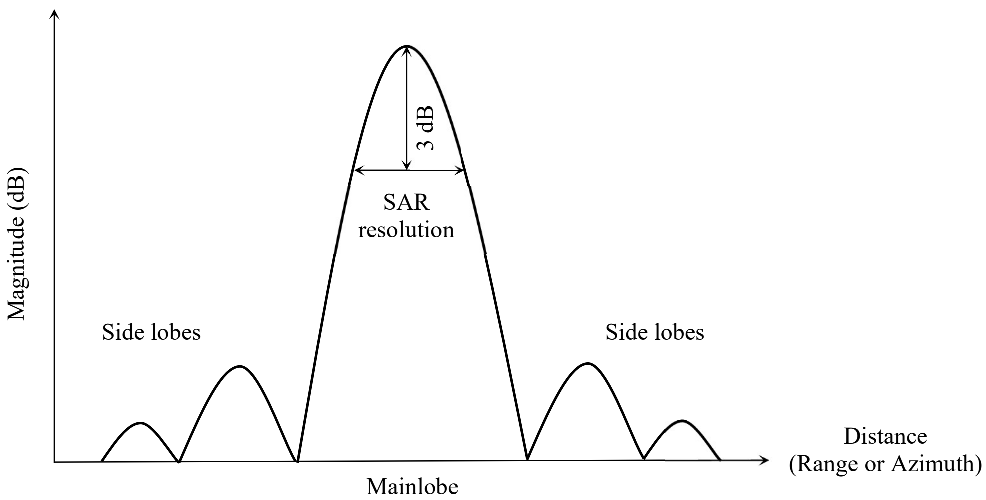

Figure 4.25: A typical IRF for a point target. The width of the -3dB distance of the mainlobe peak represents the system resolution. The Peak mainlobe represents the exact location of the point target (e.g., the CR).

4.5.2 CR detection for phase extraction

The extraction of accurate phase information for the CRs requires the precise identification of each CR in the complex differential interferograms. The CR location in a differential interferogram can be identified by finding the corresponding peak location of the CR from the co-registered amplitude image. As stated above, it is difficult to identify this location from the co-registered image and over-sampling is required to identify the location of the CR in the SAR image to within sub-pixel accuracy (Hanssen, 2001). The GPS coordinates provided in Table 4.6 do not represent the precise locations of the CRs in the image, although they can be used to identify the zero-padding patch location around the 'approximate' CR location (Marinkovic et al., 2004). To obtain sub-pixel location accuracy for the CRs, analysis of the IRF of each CR location is required to identify the peak amplitude location of that specific CR. This is similar to the amplitude extraction described in Section 4.5.1, but it requires a higher level of precision. This is performed by clipping an area of 32 × 32 complex pixels around each CR location in both the amplitude image and the unwrapped differential interferogram and then interpolating these subsets by a factor of 1/16 using the zero-padding method in the spectral domain (Hanssen 2001; Kadlečík et al. 2015). The accurate location of the CR is located at the peak power of the interpolated subset of the amplitude image. The corresponding location from the interpolated differential interferograms patch corresponds to the desired phase value for the precise CR location. These phase values are extracted for each CR from the generated differential interferograms. This CR detection procedure is summarised in Fig 4.26.

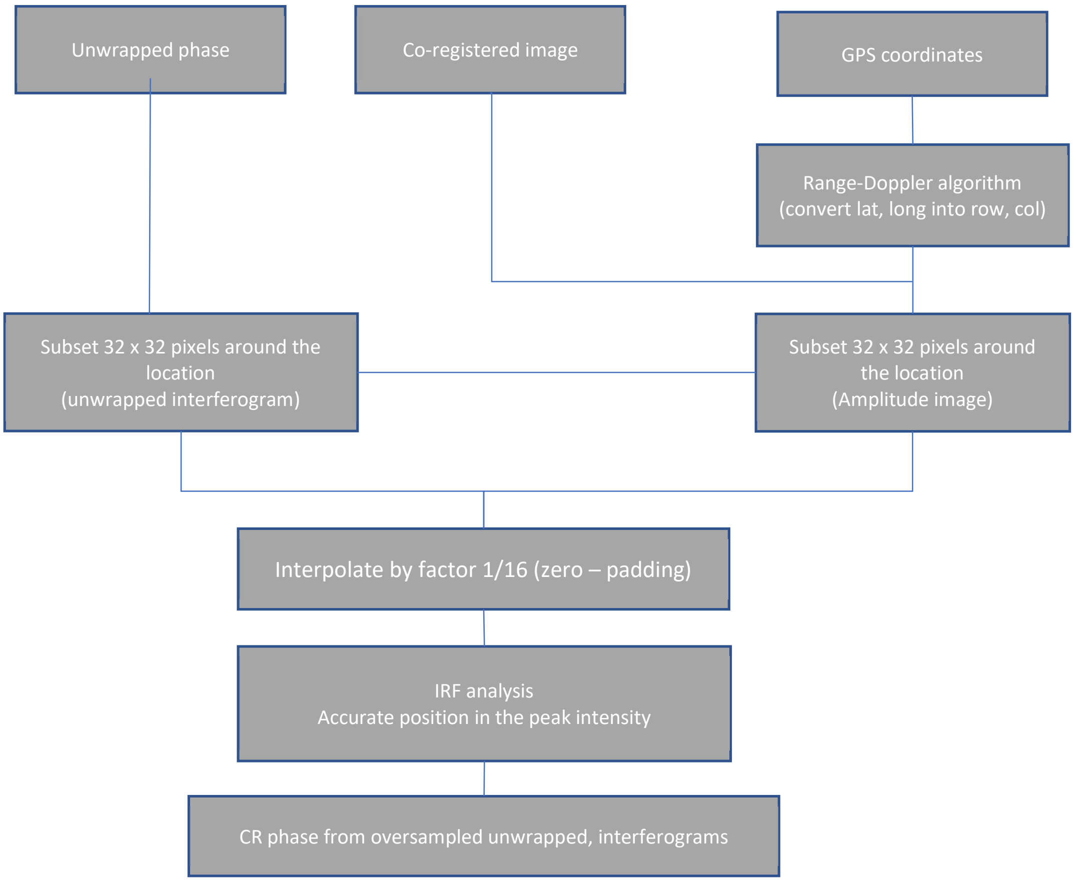

Figure 4.26: Flowchart of the CR phase extraction procedure, after Hansson (2001).

4.6 DInSAR processing

The SAR images listed in Table 4.2 are used to generate a series of differential interferograms that ae used to calculate the phase of each CR. The processing flowchart is shown in Fig 4.27, which primarily utilises the Punnet InSAR processing software (Sowter et al. 2016) of Geomatic Ventures Ltd ®. In summary, the stack of SLC Sentinel-1 images is first co-registered with respect to a common master image. In this case, the master image was selected as the first image in which all the CRs were in-situ (i.e., the image acquired on the 2nd October 2015). From the co-registered stack of Sentinel-1 images, complex differential interferograms are constructed by point-wise complex multiplication of corresponding pixels in the master and each slave image in the stack, resulting in 36 pairs (differential interferograms). During the differential interferogram phase unwrapping, CR6 was used as the reference point. This point lies in the middle of the experiment field a reasonable distance from all other reflectors. Phase unwrapping was implemented using a statistical-cost network-flow phase unwrapping algorithm (Chen & Zebker, 2001). The data were processed in full resolution, and no multi-looking was performed.

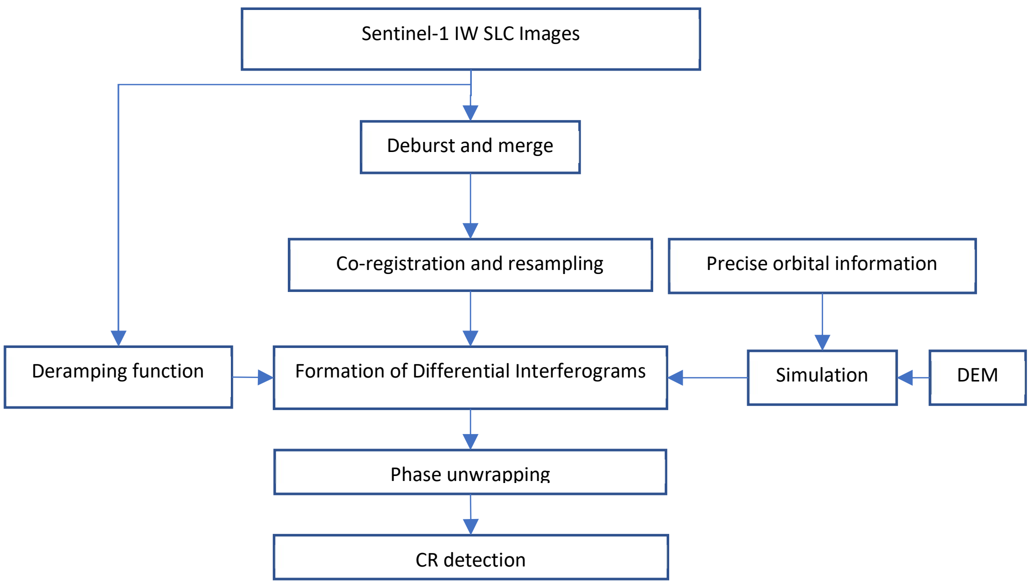

Figure 4.27: Flow chart of the DInSAR processing chain using Punnet ®, after Sowter et al. (2016).

4.7 Experimental test

To test the validity and the quality of the experiment, some tests were conducted involving the radiometric and phase stability of the CRs, as well as an accuracy assessment of the InSAR phase calculation. This was essential for ensuring that any change in the measured phase and backscatter in the main SubSAR buried target experiment is due to the variations in the water content of the covering sand and not the instability of the CRs.

4.7.1 CR stability monitoring

CRs are typically characterised by their stable phase and amplitude over time, making them ideal targets for temporal monitoring. The main experiment is designed to determine the effect of the moisture content of the covering material on buried feature detection, by observing the variations in the phase and amplitude of the covered reflectors. Therefore, an important first step is to check how stable the CRs are over time to determine whether the observed variations in these two signal components are related to the instability of the CRs or the moisture content.

4.7.1.1 CR radiometric stability

Once in situ, the radiometric stability of the CRs was monitored using a time-series of Sentinel-1 imagery for occasions when the CRs were not covered with sand. The dates of the images used in the radiometric stability analysis are listed in Table 4.2. The aim of this analysis is to evaluate the radiometric stability of the CRs to determine their reliability for measuring the signal attenuation in the buried feature experiment. To evaluate the radiometric stability of the CRs, the RCS (σ) for each CR is computed from each of the Sentinel-1 SAR images using the following equation (Miranda & Meadows, 2015):

$$\sigma = \frac{I_P}{A_{dn}^2 C_F} \frac{P_A}{K} \quad (4.10)$$

where I_P is the total power in the mainlobe and C_F is the relative power in the sidelobe, which are derived from the IRF for each CR as explained below. P_A is the pixel area, and is calculated as:

$$P_A = \Delta_r \times \Delta_a \quad (4.11)$$

where Δ_r is the pixel spacing in the range (3.2396 m), and Δ_a is the pixel spacing in the azimuth (13.9258 m); these values are calculated as the -3dB width of the impulse response function of the CR in both range and azimuth directions. K is the calibration constant, and A_{dn} is the product final scaling from internal SLC to final SLC, provided in the image LUT.

4.7.1.1.1 Total power in the mainlobe (I_p)

To calculate the total power in the mainlobe, the background radar cross-section from distributed targets contribution must be removed from the image where the radar point target is superimposed. Meaning that the background correction needs to implement for each CR in all the images. The following steps are used to remove this effect from the image and to calculate the I_P:

- Subset an area of 256 x 256 pixels around each CR.
- Convert the pixel values into intensities by squaring the *DN* values of each pixel in the subset.
- Select four areas of equal size (10 x 10 pixels each) located around the point target location in such a way that they exclude pixels attributable to CR response. These areas will be representative to the background, dashed black squares in Fig 4.28.

- Square the pixel values for the background sample areas, sum them, and divide by the total number of pixels in these areas (i.e. 400 pixels) to derive the mean background pixel intensity.
- Correct the intensity image for background clutter by subtracting from the mean background pixel intensity calculated above.
- Interpolate the intensity background corrected sub-image by factor of 8 in the spectral domain using zero-padded method
- Correct the interpolated image for background by subtracting the pixel values from the background mean intensity value calculated above.
- The total power in the mainlobe area (red square in Fig. 4.28) is then calculated as the sum of the intensity values of all pixels within 2x2 resolution cells.

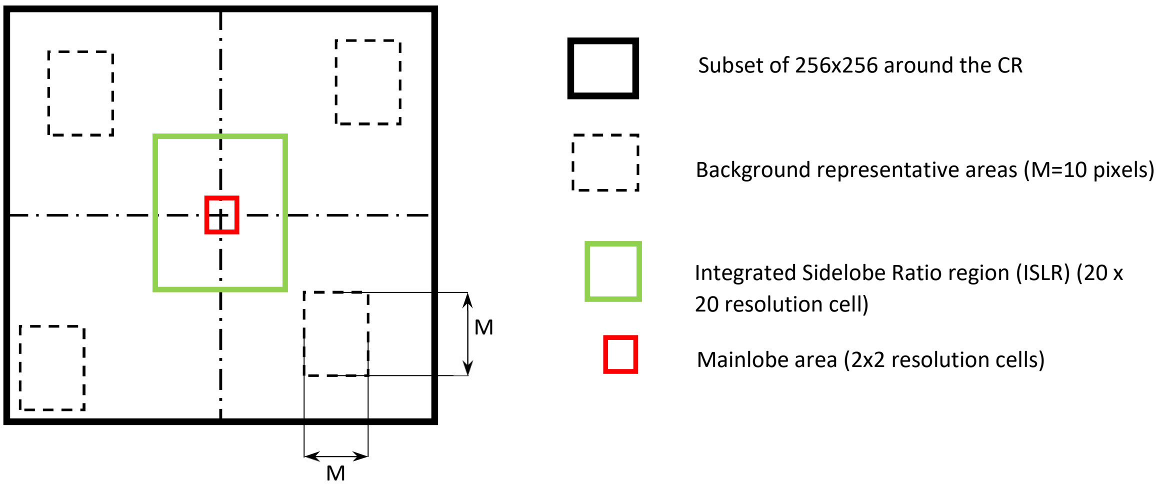

Figure 4.28: Definition of point target response area and background areas.

4.7.1.1.2 Relative power in sidelobe (C_F)

The relative power in the sidelobe is defined as:

$$C_F = \frac{1}{(1+ISL\ \ )} \tag{4.12}$$

where the integrated sidelobe ratio (ISLR) is the proportion of the energy of the sidelobes (E_2), within an area of 20 by 20 resolution cells excluding the mainlobe, relative to the energy of the mainlobe (E_1) (2 by 2 resolution cells):

$$ISLR = \frac{(E_2 - E_1)}{E_1} \qquad (4.13)$$

The calculated radar cross-sections (RCSs) were subsequently converted to units of dB using Eq. 4.6.

4.7.1.1.3 Radiometric stability test

The variation in σ for each CR in the network during the time period covered by the specified SAR images is shown in Fig 4.2. It is apparent that CR4 is clearly the most unstable of the CRs over time, exhibiting a mean σ of 15.46 ± 11.46 dB. Such a low mean and large variation in σ could be an indication that this particular CR was accidentally damaged during installation or at some point during the experiment. Owing to this high instability, CR4 is not deemed suitable to be used in the main buried target experiment because of the difficulty in isolating the contribution of the CR instability from the effects of moisture content on the observed RCS. CR4 is therefore excluded from any further analysis.

The remaining CRs are relatively stable in time, with means ranging between 23.97 dB (CR2) and 27.46 dB (CR5) and standard deviations ranging between ±0.87 dB (CR1) and ±2.33 dB (CR2). The minor variation in σ for each CR is likely caused by variations in the background conditions such as vegetation cover or atmospheric effects, which might cause the backscatter values of the background to increase or decrease. The mean σ values are ~15% less than the theoretical value calculated for the trihedral CRs, which is potentially due to small orientation and manufacturing errors. Importantly, however, σ is consistent over time which reflects a good level of radiometric stability, therefore making these CRs suitable for use in the main the experiment.

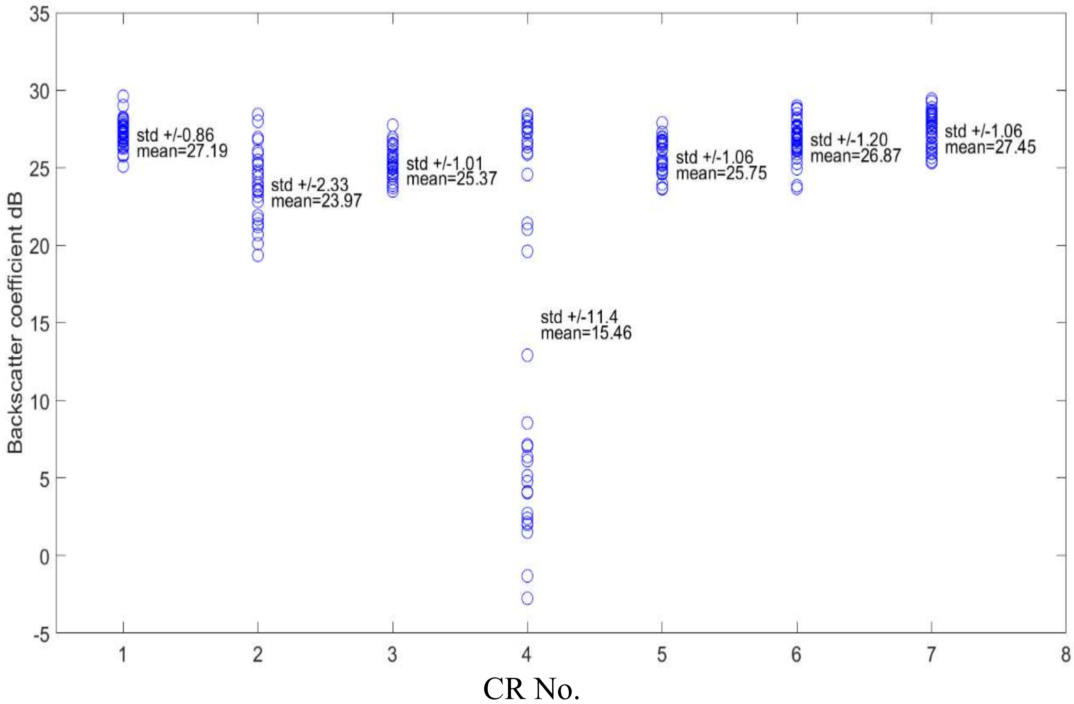

Figure 4.29: The radiometric analysis of the CRs throughout the experiment period, where the number in the x-axis represent the CRs.

4.7.1.2 CR phase stability

Analysing the stability of the CRs and the quality of Sentinel-1 interferometric phase is also vital to ensure that it is possible to detect, with high precision, any change in the phase due to the sand moisture content in the buried feature detection experiment.

The temporal phase stability of the CRs can be evaluated by analysing the DInSAR phase for each individual CR with respect to a reference point. From Chapter Two, the differential phase equation (Eq. 2.22) has four components; the displacement component, atmospheric component, DEM errors and noise:

$$\Delta\phi_{diff} = \frac{4\pi}{\lambda}\, d + \varphi_{atmo} + \varphi_{DEM} + \varphi_{noise} \tag{4.14}$$

CR6 is used as the reference point in this analysis as this point is located in the middle of the field with intra-distance to each of the six other CRs of 250–450 m. Such short distances help to minimise atmospheric effects on the phase observations (Hanssen, 2001). Moreover, the DEM error component can be reduced by using a high quality digital elevation model for the site, and in this case, a GPS was used to measure the CR elevations. The other limiting factor in the DInSAR processing is the noise, which is predominantly related to decorrelation between two observations. Since CRs are being used, these points will remain correlated in all observations and hence, the noise term is negligible. The remaining observable phase is the target displacement component, which is caused by the relative motion of one CR with respect to the

reference point.

Table 4.5: Statistical parameters for the DInSAR phase for each CR.

CR	Mean (rad)	SD (rad)
CR1	0.6802	0.6425
CR2	-0.6643	0.6566
CR3	-0.3955	0.5651
CR5	-0.7076	0.7482
CR7	1.3631	0.6464

Phase stability analysis is implemented for all the images where the CRs are un-covered (Table 4.2). Using the image acquired on 2nd October 2015 as the master, the successive 18 slave images, which were acquired both before (19/11/2015–11/3/2016) and after (1/11/216–19/12/2016) the main buried feature experiment, are co-registered to the master image and a set of 18 differential interferogram is constructed using the procedure explained in Section 4.6. The phase history of each CR from these differential interferogram is extracted as explained in Section 4.5.2. The mean interferometric phase and the standard deviation (SD) for the CRs are calculated to analyse their stability with respect to the reference point (CR6). Table 4.5 below details these phase statistics for the CRs that are used in this experiment, excluding the reference point (CR6) and the discarded CR4. The results in Table 4.5 show that all the CRs are reasonably stable. The average relative motion of any CR is less than 1.4 rad for this period, which is equivalent to 6 mm in the line of sight (LOS). The variation of the phase is less than 0.8 rad for all the reflectors, which confirms the relative stability of the CRs and their suitability for investigating the effect of soil moisture in the buried feature experiment.

4.7.2 Interferometric phase accuracy

To assess the quality of Sentinel-1 interferometric phase observations for measuring relative displacement between the CRs, InSAR-derived displacements were compared with the measurement made using a total station. This involved manually altering the location of the most stable CR in the network, CR1, by a few centimetres and validating this movement using a total station. CR1 was moved twice during this experiment, on 25th November 2015 and 13th December 2015. A Leica TC405 total station was set-up over the same occupation point each time, which was situated a short distance from CR1 (5.30 m). A surveying benchmark located only 5 m from CR1 was then used as reference for accurately measuring the CR's displacement. Each time the CR was moved, the new position of the CR apex measured relative to the benchmark to find the exact relative displacement that occurred. The observed displacement was then projected to the satellite LOS to enable a direct comparison with the interferometric observations. The dates and corresponding displacement of CR1 are listed in Table 4.6. It was ensured that each displacement would not exceed a full wavelength of Sentinel-1 signal (5.55 cm), so no ambiguity was introduced to the measurements. The mean difference between the two sets of measurements (the total station and InSAR) is -1.95 mm. This close agreement between the two sets of observations clearly indicates that the InSAR observations are very sensitive to the displacement of the CR.

Table 4.6: Sentinel-1 LOS displacements in comparison with the true displacement of CR1 as measured by the total station.

Image date	LOS (DInSAR) (mm)	LOS (total station) (mm)	Discrepancy (mm)
25/11/2016	12	13.3	-1.3
13/12/2016	-13.5	-10.9	-2.6

This result is similar to that from an equivalent experiment using ERS and ENVISAT data, which was 1.6 mm and 2.6 mm (vertical), respectively (Marinkovic et al. 2007). Therefore, this experiment has demonstrated that Sentinel-1 interferometric observations can be used with confidence to detect millimetric ground deformations.

4.8 Buried feature detection experiment

As previously explained, the main experiment is to test the application of the SubSAR technique for buried feature detection from satellite SAR data. The overall concept of the experiment is that the Sentinel-1 C-band signal is incident upon a sand layer, which acts as a medium through which the signal will propagate and be reflected by the CR back through the sand layer to the SAR antenna, as shown in Fig 4.19. The CRs described above were utilised as the buried targets because they have been shown to be stable in time, with respect to the interferometric phase and amplitude. Also, they have known scattering characteristics, meaning that their scattering behaviour can be monitored throughout the experiment and compared with their theoretical RCS to ascertain how various factors, such as the moisture and thickness of covering material, affect the capability of using Sentinel-1 SAR for buried feature detection.

To simulate buried targets, each CR was buried beneath a 1 cm layer of pure fine sand at a specific time period during the experiment. Pure sand is used as is conventional for most soil moisture investigations (Farr et al., 1986; Nolan & Fatland, 2003; Morrison et al., 2012). With an open base area of ~0.85 m^2, a volume of 8500 cm^3 of sand (with a mass of 14 kg) was required to cover each CR with a 1 cm thick layer of sand (as eluded to in Section 4.4.5). A thickness of 1 cm was chosen based on the ability of the structure of the CRs to withstand the associated weight of the sand. A thicker layer of sand was decided against due to concerns that this could damage the CRs over the duration of the experiment and subsequently affect the amplitude and phase measurements. In order to ensure the CRs remained fully covered during the experiment, domestic vacuum plastic bags (130 cm × 90 cm air-tight bags) were used to secure the unconsolidated sand. As can be seen in Fig. 4.30, the sand is spread evenly inside the plastic bag by laying it on a flat table. Before vacuuming the air out, it was necessary to that the surface of the sand layer was flat, which was achieved by rolling a wooden pin across the entire bag. Air is vacuumed out of the bag and the cap is tightly fastened to secure it. As discussed above, given that identical plastic bags are used throughout the experiment, its effect on the radar signal will be consistent over time – no matter how subtle – and can be considered negligible.

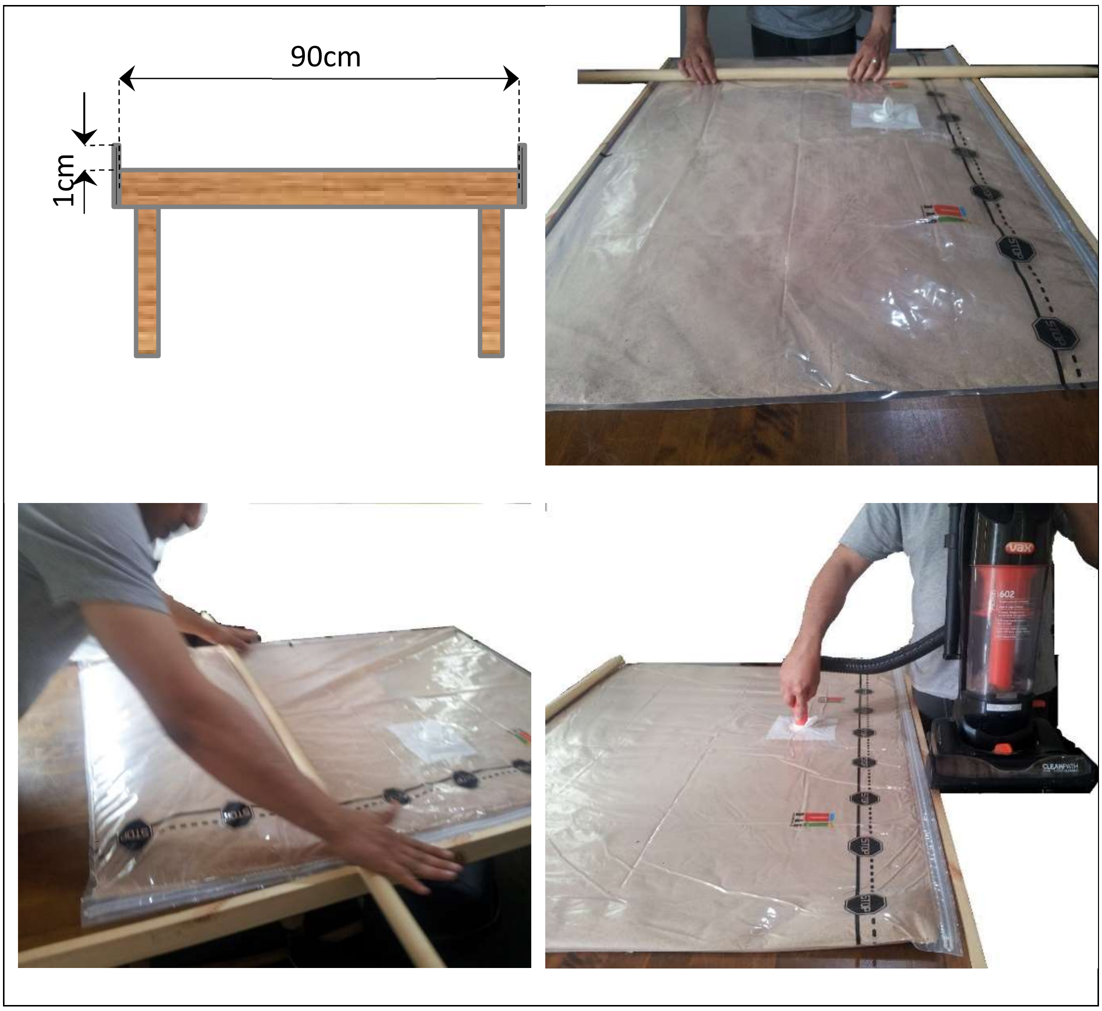

Figure 4.30: Sand sample preparations steps.

4.8.1 Moisture content

The main premise of the SubSAR buried feature experiment is to determine the effect of the moisture content of the sand layer on the Sentinel-1 C-band signal – both the amplitude and phase. This therefore requires the moisture content of the sand layer to be varied between Sentinel-1 image acquisitions over the study area. This was achieved by adding varying volumes of water to the sand layer and then measuring the resulting moisture content using a ML3 ThetaProbe soil measuring kit (±0.1% accuracy). The sand sample for each CR was prepared in a plastic container (48 cm length × 29 cm width × 40 cm height), within which the sand-water mixture was mixed thoroughly to obtain a homogeneous medium. The moisture content was recorded at

15 regularly spaced locations within the container using a 3 × 5 grid as illustrated in Fig. 4.31.

Figure 7.31: Measuring the moisture content of the sand sample over a virtual grid of 3x5, using ML3 ThetaProbe kit.

The sand was then mixed again, levelled and another set of soil moisture measurements were taken. The final moisture content was calculated as the mean of these two sets of measurements.

Using knowledge of the satellite orbit, the desired moisture content of the sand layer for each CR was established just prior to each Sentinel-1 overpass of the site, varying from dry sand (0.01%) to a 10% moisture level. The sand layers were prepared just prior to each field visit, however, some of these layers were damaged as the plastic bags tear easily during transit to the experimental site or during installation at the CRs. Consequently, the same number of observations were not obtained for all CRs. The results of the experiment are presented and discussed in the following chapter.

4.9 Summary

This chapter has outlined the buried feature experimental design that represents a field-scale equivalent of the SubSAR experiment. A crucial aspect of the experiment is the optimum design, precise manufacturing, and accurate positioning of the CRs that are to be used as buried features. Temporal analysis of the backscatter coefficient of the experimental site was required to define the size of the CRs to ensure that they are readily identifiable in the Sentinel-1 SAR imagery. This type of imagery was chosen as it is freely available and is regularly acquired over the study area, in both ascending and descending acquisitions. The criteria of selecting the suitable image track is explained, as is the process for orienting the CRs and detecting them in the Sentinel-1 imagery. The experimental design was tested in terms of radiometric and interferometric phase stability of the CRs and, with the exception of CR4, the CR network was found to be suitable for the buried feature experiment. Finally, the SubSAR equivalent field-scale experiment was described, which involves covering the CRs with layer of sand with varying water content and then observing the backscatter and the phase of the covered targets. In the next chapter, the results of the buried feature detection experiment will be presented and discussed.

Chapter 5: Field Observations and Experimental Results

5.1 Introduction

The previous chapter described the design and implementation of the experiment that will be used to validate the SubSAR technique for buried feature detection using Sentinel-1 data. After conducting the initial tests on the suitability of the experiment, observations were obtained by covering some of the CRs with sand layers concurrent with each satellite overpass. The moisture content of the sand layers was varied between passes and between CRs to obtain a range of moisture levels, from nearly dry sand (~0.1%) to 10% moisture content. The aim of the experiment is to investigate the effect of the water content of the sand cover on the SAR signal and how this can be used to detect buried features from Sentinel-1 images. This involves analysing both the backscatter and interferometric phase of the buried CRs. In this chapter, the results obtained from this experiment are presented. Based on these results, the possible relationships between the sand water content and both the backscatter and the interferometric phase are investigated.

5.2 Buried CR observations

Four CRs (CR1, CR2, CR3 and CR5) were covered with a layer of sand during Sentinel-1 overpasses and, in each case, the moisture content of the sand layer was precisely measured. Table 5.1 lists the Sentinel-1 image dates and corresponding moisture content for each CR covering layer. CR6 and CR7 remained exposed (i.e., un-covered) throughout the experiment to be used as references for comparison with the buried CRs. Due to its instability (as explained in Section 4.9.1), measurements obtained from CR4 were discarded to leave only those measurements made for the stable CRs. All remaining observations are used to analyse the effect of the sand moisture on the SAR signal components, as will be discussed in this chapter.

Table 5.1: The soil moisture (%), for each CR sand cover during the experiment. Shaded cell means exposed and V is Void observation.

Date	CR1	CR2	CR3	CR4	CR5	CR6	CR7
30-Mar-16			2.0	V			
11-Apr-16		3.1	4.3	V	1.8		
23-Apr-16		0.1	1.0	V	0.1		
05-May-16		1.9	2.2	V	0.2		
17-May-16		2.5	7.0	V	1.2		
29-May-16		1.0	6.3	V	2.1		
10-Jun-16	7	2.5	6.5	V	3.5		
04-Jul-16		2.2	6.5	V	5.8		
16-Jul-16	9.5	2.0	7.2	V	7.0		
28-Jul-16		8.0	8.5	V	2.5		
09-Aug-16		2.5	10.0	V	3.5		
21-Aug-16		3.1	9.2	V	3.0		
02-Sep-16		0.1	2.1	V	1.5		
14-Sep-16		0.1	2.8	V	2.0		
26-Sep-16		0.1	7	V	1.7		
08-Oct-16		0.1	3.0	V	2.5		
20-Oct-16			2.1	V	3.0		

In total, 50 successful field observations were made between 30th March 2016 and 20th October 2016. It was not possible to obtain observations before and after these two dates primarily due to poor lighting conditions in the field at the time of the satellite overpass. The moisture levels used in this experiment ranged between dry sand (~0.1% moisture) and wet sand (10% moisture). A histogram showing the distribution of the measured sand moisture content can be seen in Fig 5.1. This shows that the number of observations at each sand moisture level was variable and ranged between a single observation for the 4-5% moisture level to 14 observations for 2–3% water content.

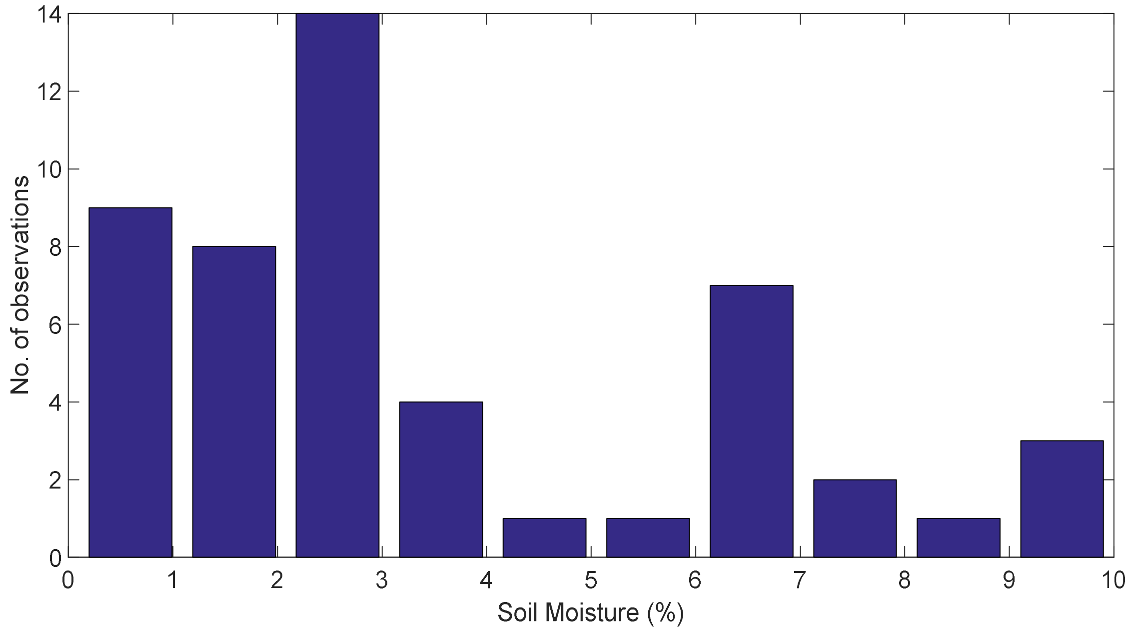

Figure 5.1: Histogram of moisture levels distribution used in the experiment

Similarly, the number of observations obtained for each CR was variable, ranging from 2 observations for CR1 to 17 observations for CR3. As discussed in Chapter 3, this was due to some difficulty in installing some of the prepared sand layer bags at the CRs. Likewise, the moisture content measured for each CR is somewhat varied, as presented in table 5.1.

5.3 Backscatter analysis

To investigate the effect of the sand layer on the backscatter of the buried CRs, the RCS of the CRs were monitored throughout the experiment for both buried and un-covered observations. As explained earlier, CR6 and CR7 were left un-covered for the entire experiment to be used as a reference for the other CRs. Backscatter observations from these reference CRs therefore provided a baseline against which the behaviour of the other CRs could be compared.

5.3.1 Reference CRs

The backscatter of CR6 and CR7, which were both left un-covered throughout the experiment, was monitored using the procedure explained in Section 4.7.1. CR6 and CR7 were both easily identified in all the Setinel-1 SAR images due to the high contrast between the CRs and the background as can be seen in Fig 5.2 and 5.3. This enabled the backscatter of CR6 and CR7 to be extracted precisely. The time-series analysis of the backscatter of these two CRs is presented in Fig 5.4 and 5.5, indicating a reasonable level of radiometric stability throughout the duration of the experiment. The mean backscatter are 26.9 dB and 27.5 dB for CR6 and CR7, respectively, with standard deviations of 1.2 dB and 1.1 dB. This relatively minor variation observed around the mean backscatter is likely due to background clutter. The background where the CRs are installed, is a farm area. The height and density of the vegetation cover is changing all the time. When calibrating the image to calculate the RCS of the CR, the average background is considered in the calculations (Miranda et al. 2015), and that affect the calculated RCS of the CR. The calculated RCS for the reference CRs is slightly below the theoretical one (~31 dB for a 1 m trihedral CR). This is most likely due to imperfection in the fabrication and orientation of the CRs.

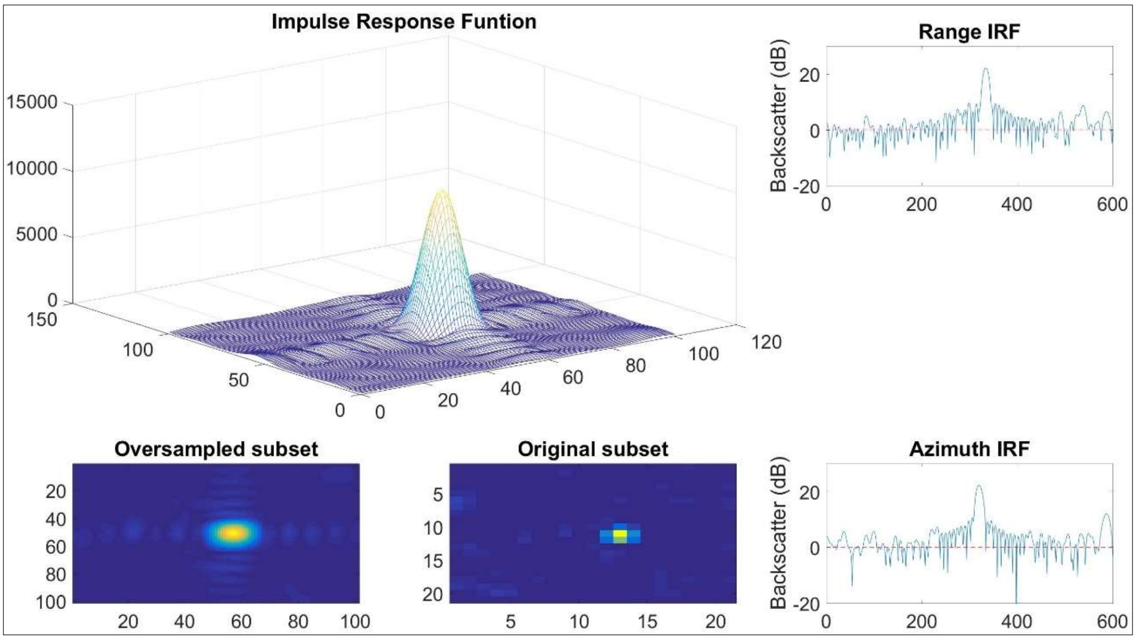

Figure 5.2: Backscatter analysis of CR6 that was implemented as part of calculating the RCS of the CR

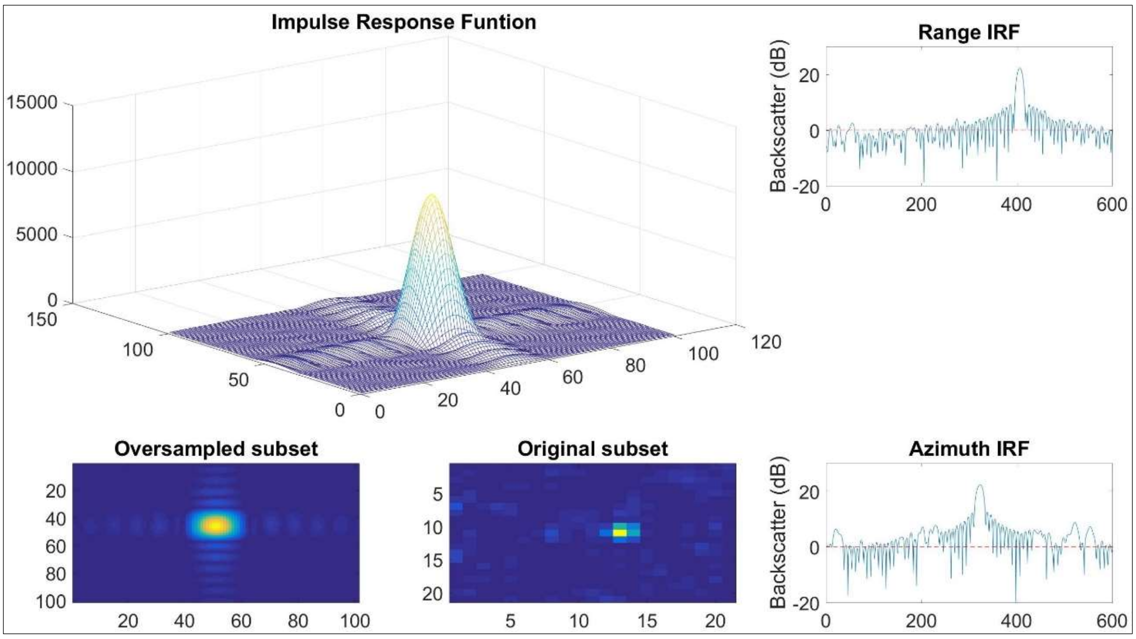

Figure 5.3: Backscatter analysis of CR7 that was implemented as part of calculating the RCS of the CR

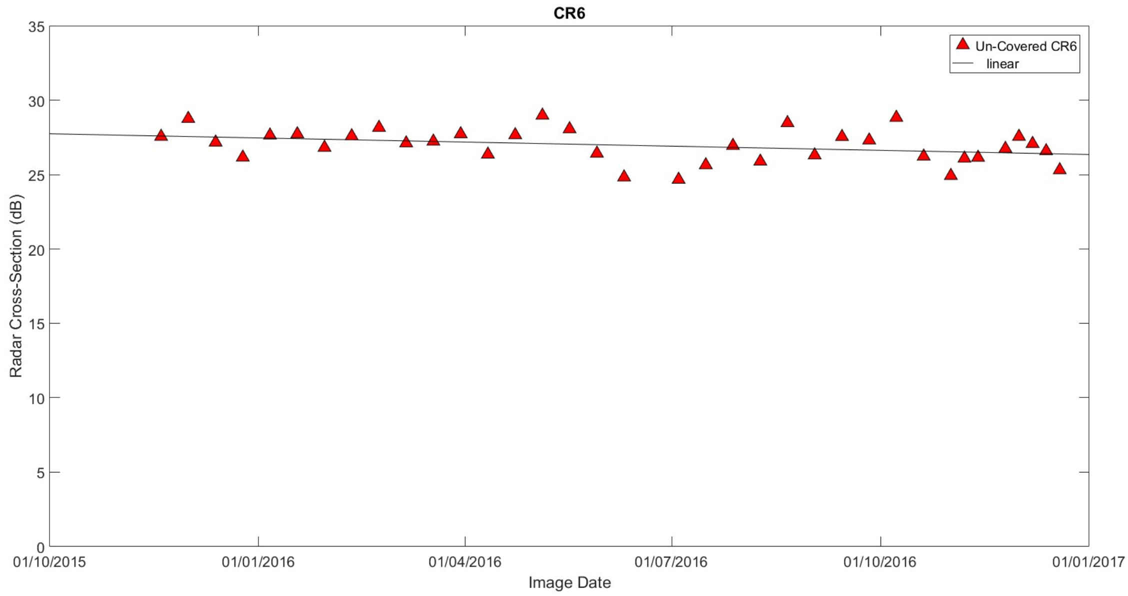

Figure 5.4: Backscatter history of CR6

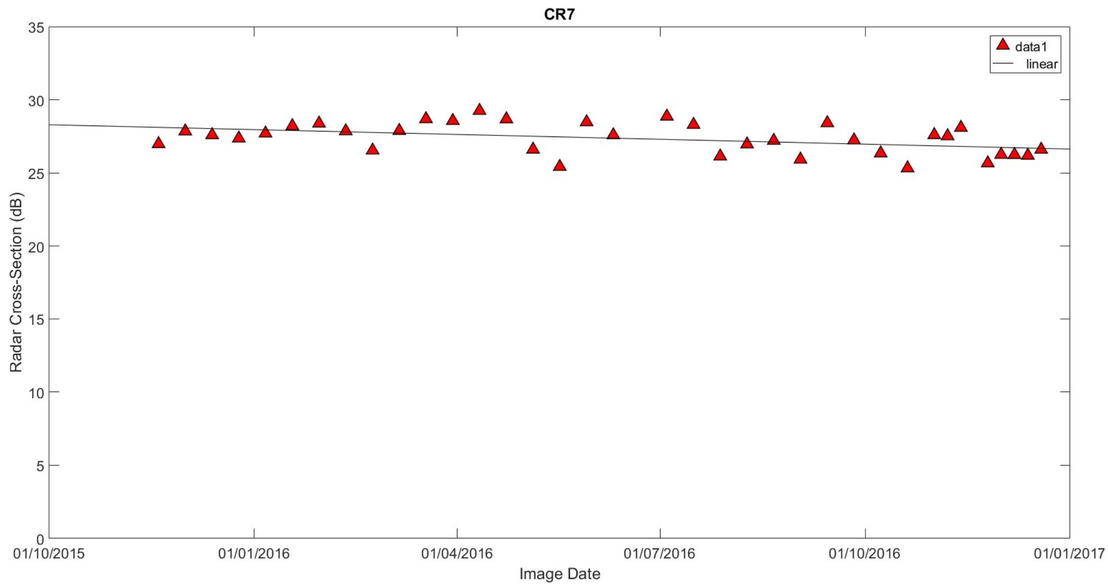

Figure 5.5: Backscatter history of CR7

Over the period of the experiment (approximately 1 year), the mean backscatter of the reference CRs slightly reduced. This is expected as a result of the degradation of the CRs structure and the contamination of different debris after being left in the field for a long period, which will reduce the reflectivity of the aluminium sheets that form the CR.

5.3.2 Buried targets

The remaining CRs of the network (CR1, CR2, CR3 and CR5) were involved in the buried target detection experiment. Each of these CRs was observed while buried by a sand layer and during the time when un-covered. When buried, the backscatter signal will be attenuated upon passing through the sand layer. The attenuation can be measured by comparing the post-burial backscatter response with the mean pre-burial response of each CR. The following sub-sections will discuss the backscatter results for each CR separately.

5.3.2.1 CR1

As with the reference CRs, CR1 was easily identified in the SAR image during the un-covered observations. Fig. 5.6 shows a high contrast between the CR backscatter and the background (~25 dB difference), which makes the identification of the CR in the SAR imagery a straightforward task. Out of the 17 field visits, which is the total number of field observations, CR1 was only covered with sand twice; on the 10th June 2016 and 16th July 2016. The water content of the sand layer was 7% and 9.5%, respectively. The backscatter history of CR1 is represented by Fig 5.7 for both the buried and un-covered observations. The mean and the standard deviation of CR1 backscatter for the un-covered case were 27.2 dB and 0.87 dB, respectively. The backscatter history of CR1 for the un-covered observations shows a similar trend to the reference CRs. The overall mean is 26.7 dB and standard deviation 0.8 dB. The mean RCS is 13% less than the theoretical RCS. As is the case with the reference CRs, this is most likely due to imperfection in the CR fabrication and orientation. The backscatter gradually reduced with time, from ~27.5 dB at the beginning of the experiment to 26 dB towards the end of the experiment. Again, this is due to the degradation in the CR structure.

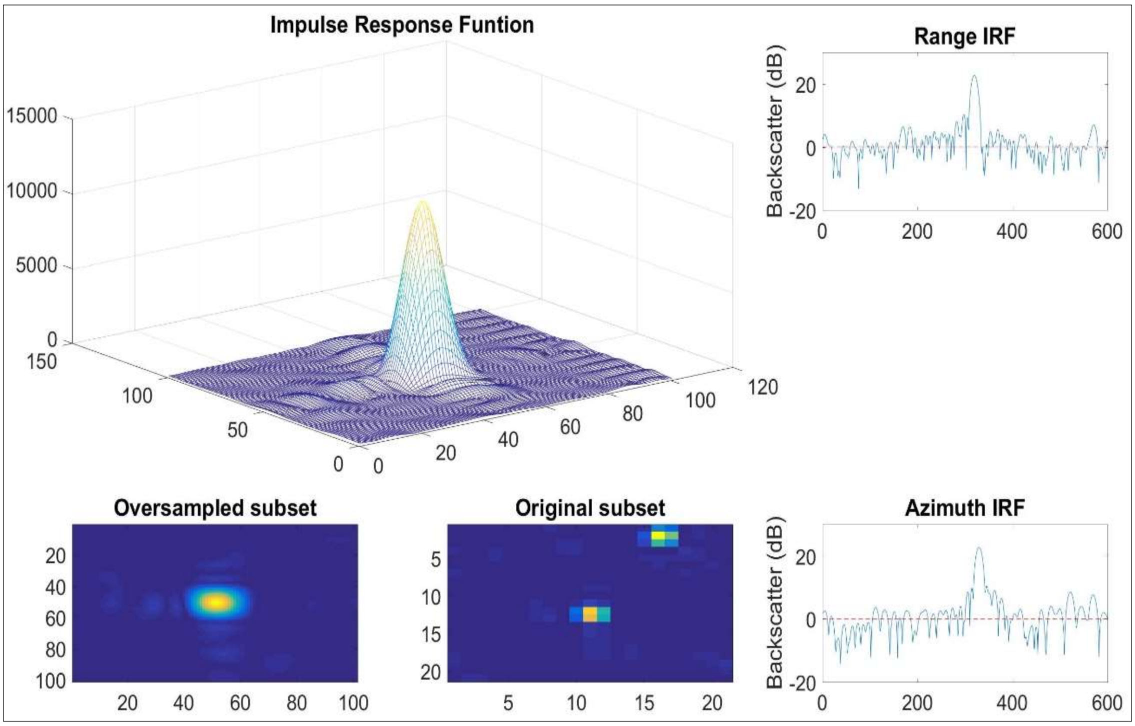

Figure 5.6: Backscatter analysis of CR1 (un-covered observation).

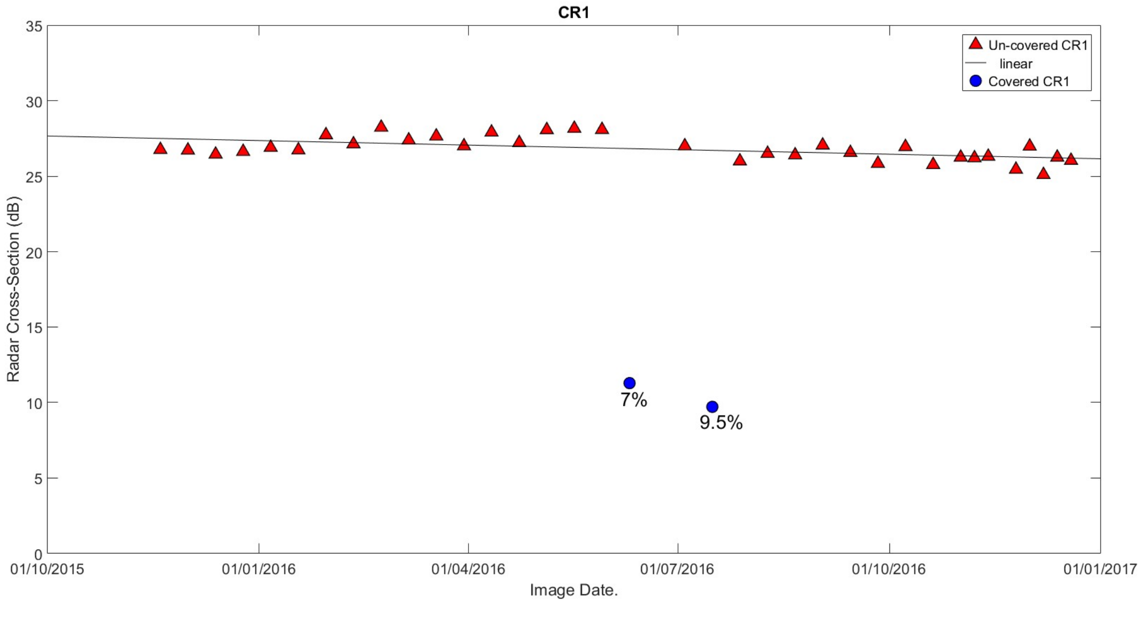

Figure 5.7: Backscatter history of CR1. Red triangles represent the un-covered observations and the blue circles represent the covered observations, where the numbers represent the sand moisture used in that observation.

When CR1 was covered with a moist sand layer, the signal is severely attenuated as there was a striking reduction in the backscatter. For the two field observations, the attenuation was -15.5 and -17 dB, respectively. The backscatter analysis of the buried observation for CR1 with sand of 9.5% water content is represented in Fig 5.8, where the peak of the backscatter of CR1 is significantly reduced by -17 dB, approaching the background scattering value making the detection of the CR in the SAR image a more challenging task, but it is still possible to recognise it. As explained in Chapter 3, the signal transmission depends on the dielectric constant of the medium. For the un-covered observations, the dielectric constant of air is approximately 1, therefore there is no attenuation in the observed backscatter of the un-covered CR. When the CR is covered with a sand layer, the sand-water mix in that layer has a dielectric constant higher than the air. Therefore, there will be a reduction in the transmitted signal power, which explains the observed attenuation in the buried CR signal.

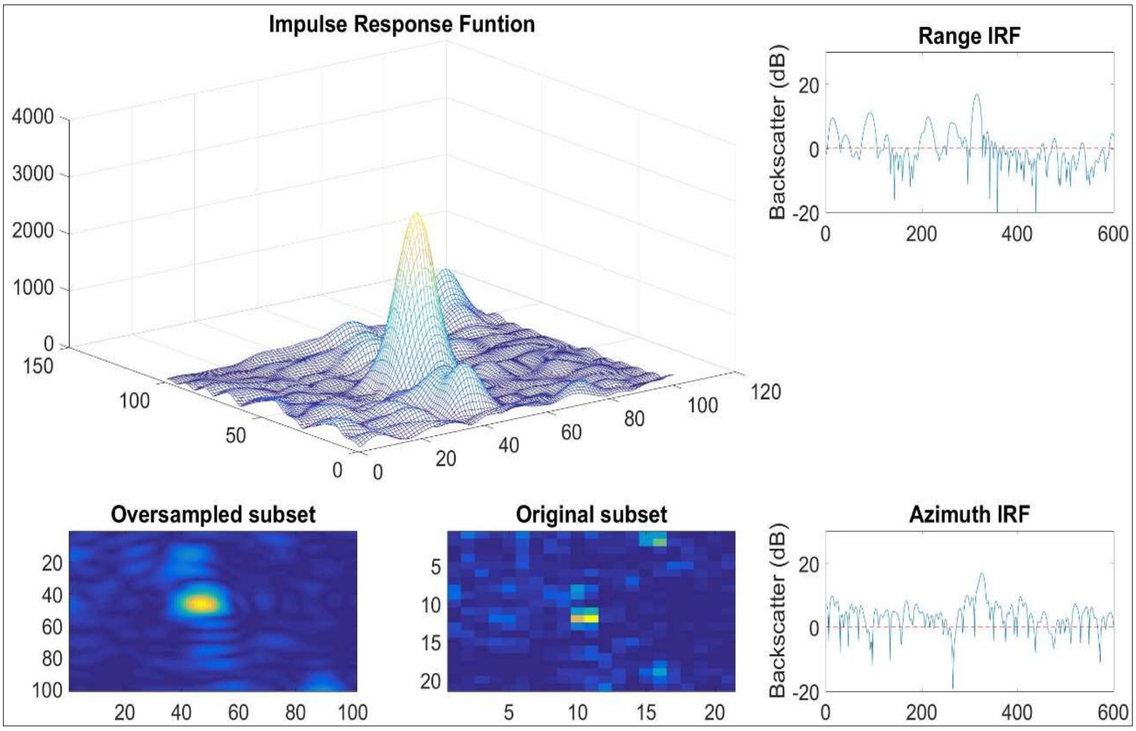

Figure 5.8: Backscatter analysis of CR1 (covered with 9.5% sand moisture)

5.3.2.2 *CR2*

The overall mean backscatter of CR2 from the un-covered observations was 24 dB. The backscatter history (Fig 5.9) shows a temporal reduction in CR2 backscatter of -5 dB over the experimental time, which is higher than that for CR1 and for the reference CRs. The backscatter of CR2 is 27 dB at the beginning of the experiment and was reduced to 22 dB towards the end of the experiment. Nonetheless, CR2 still exhibited a high backscatter value compared to the background. Analysing the IRF of CR2 for the un-covered observations, Fig 5.10, shows that the backscatter of CR2 is higher than the background, with a difference about 25dB, which regardless of the temporal reduction in the backscatter, can still be easily identified in the SAR image.

Again, when the CR is covered with a sand layer, the SAR signal is attenuated, and the backscatter is reduced, as can be seen in Fig 5.9. There are 15 field observations for CR2 in which it was covered with a sand layer. During the 17 field visits, the sand layers of CR2 failed at two occasions (March 30th, 2016 and October 20th 2016). Thus, CR2 couldn't be covered on these two dates.

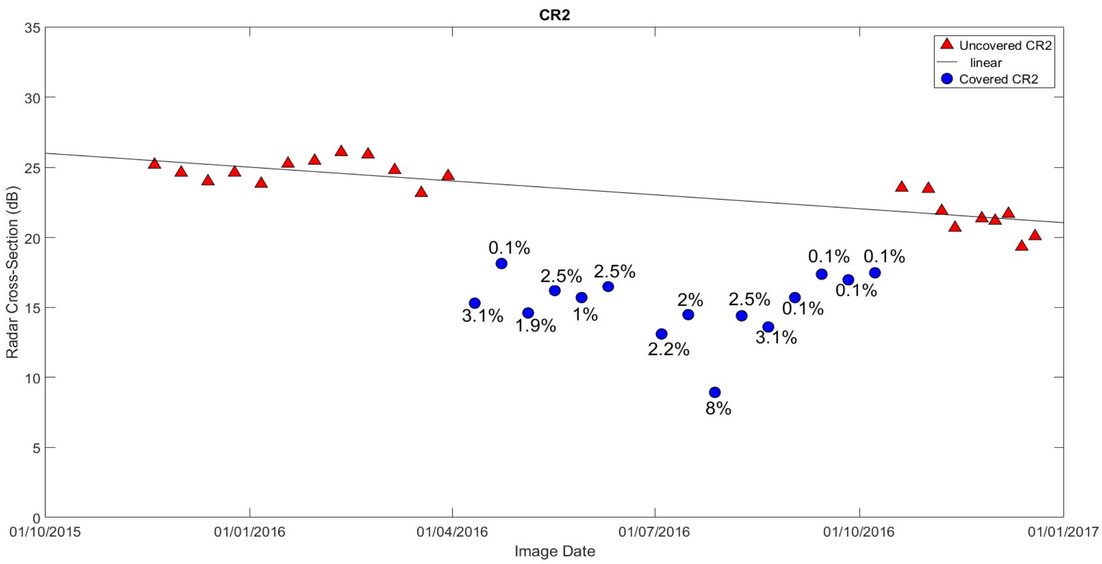

Figure 5.9: Backscatter history of CR2. Red triangles represent the un-covered observations and the blue circles represent the buried observations. Numbers next to the buried observations represent the percentage of water content in the sand layer.

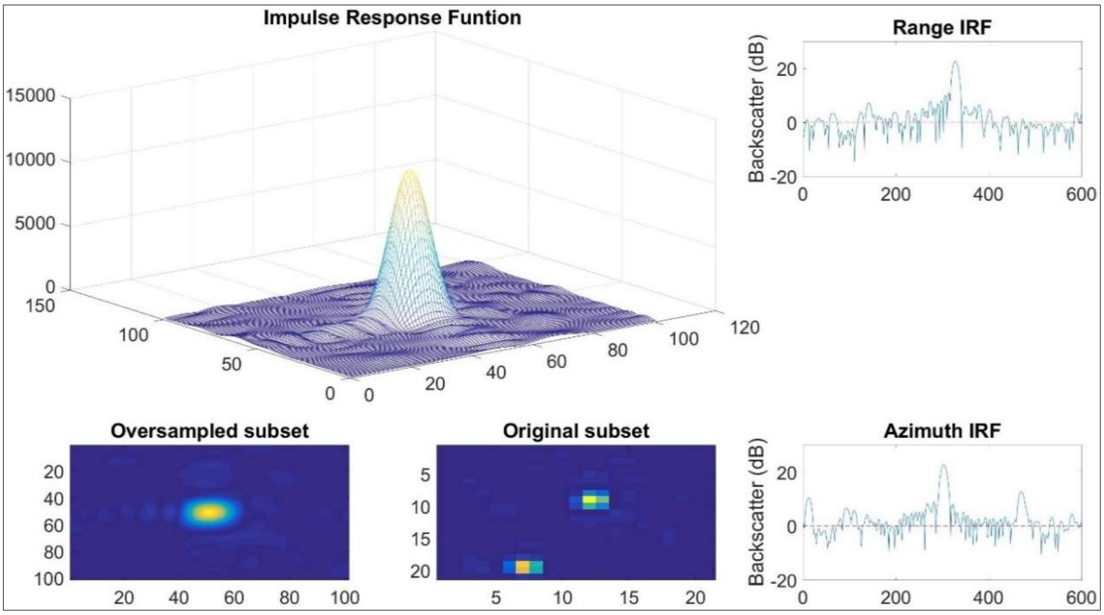

Figure 5.10: Backscatter analysis of CR2 (un-covered observation)

The moisture levels of the sand layer covered by CR2 ranged from dry sand (0.1 %), to 8%. For the higher moisture level, the backscatter signal was attenuated by more than -14 dB. This reduction in the backscattered signal made the IRF peak come close to the background value (Fig 5.11), which in turn makes the identification of the CR more difficult.

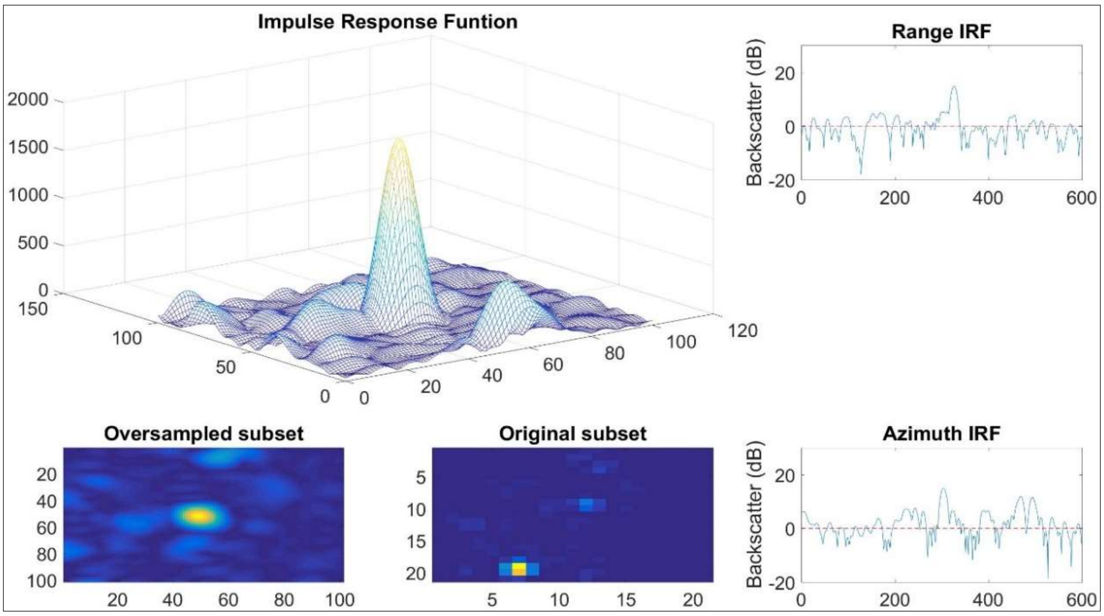

Figure 5.11: Backscatter analysis of CR2 (covered with sand of 8% moisture)

5.3.2.3 CR3

CR3 was the first CR to be installed at the experimental site. Similar to CR1 and CR2, the backscatter of un-covered CR3 shows a high contrast between the CR and the background (Fig 5.12). Consequently, the identification of CR3 in the SAR image is straightforward and precise. CR3 was relatively stable in time as can be seen from the analysis of the un-covered observations of CR3 in Fig 5.13, with only a minor temporal reduction of less than -1 dB over the experimental period. The mean and standard deviation for these observations are 25.4 dB and 1.1 dB, respectively.

For the buried observations, CR3 has the biggest number of successful field observations, with 17 buried observations (out of the 17 field visits). The moisture levels associated with CR3 ranged from 0.1% to 10%. The buried observations show a clear attenuation in the backscatter of CR3, as in the case of CR1 and CR2. Unlike the other CRs, CR3 was tested with a high level of sand moisture (10%) where the SAR signal was significantly attenuated. As a result, the backscatter was close to that of the background (Fig 5.14). The reduction in the backscatter is estimated to be more than -18 dB, and the identification of the buried CR from the background was very difficult, if not impossible. Therefore, it was deemed that the buried CR could no longer be identified in the SAR image at 10% sand moisture content.

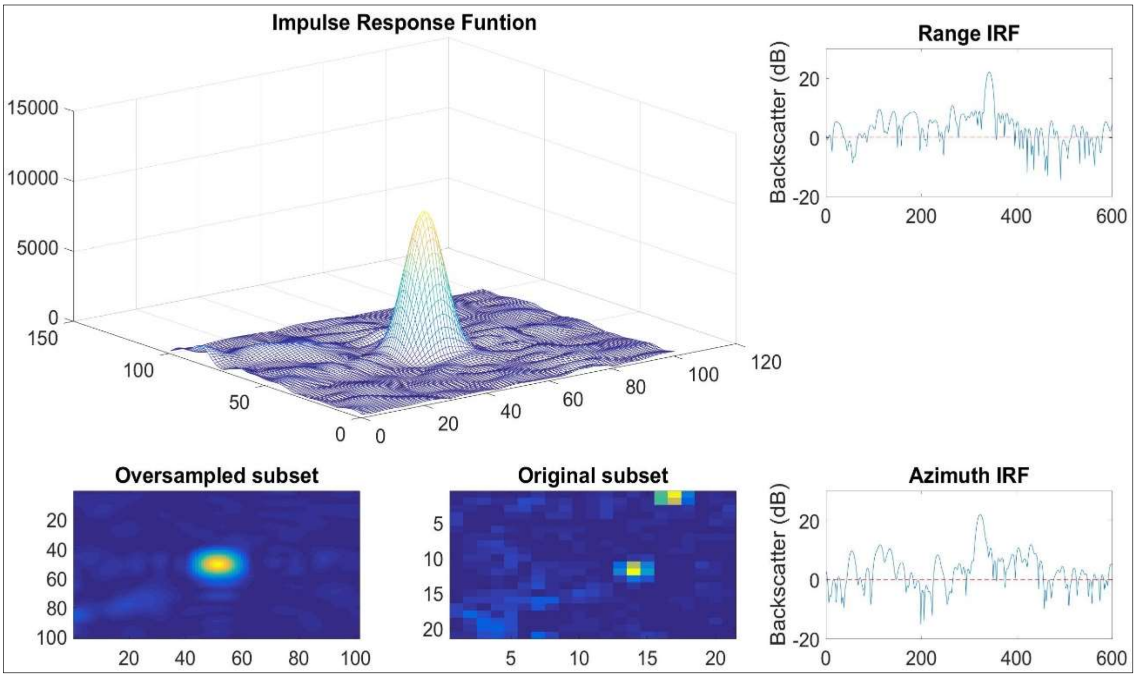

Figure 5.12: Backscatter analysis of CR3 (un-covered observation).

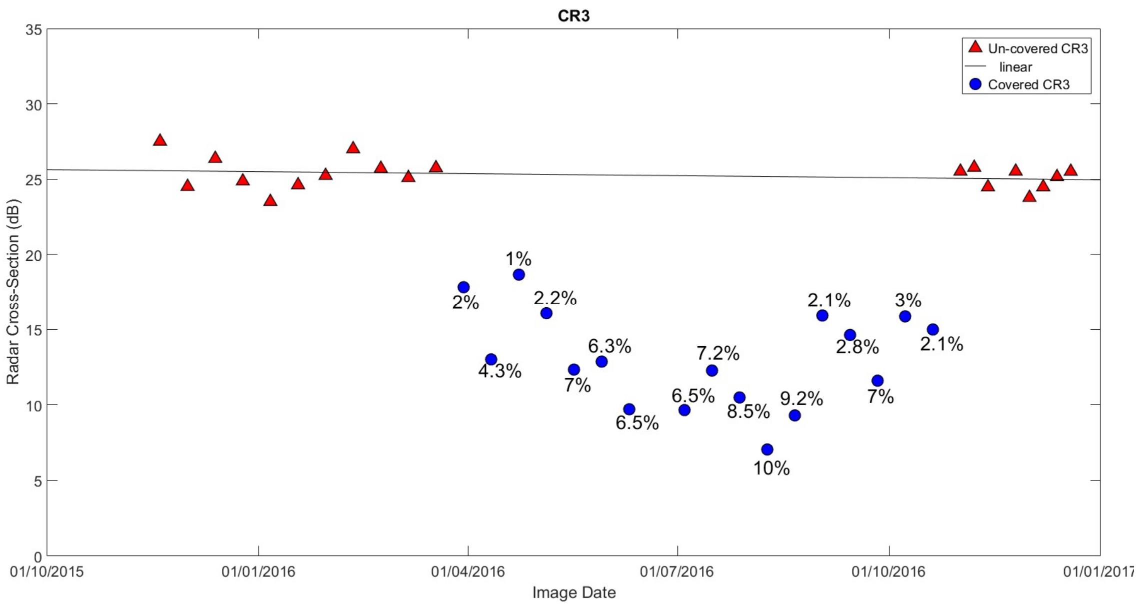

Figure 5.13: Backscatter history of CR3. Red triangles represent the un-covered observations and the blue circles represent the covered observations, where the numbers represent the percentage of the sand moisture of each observation.

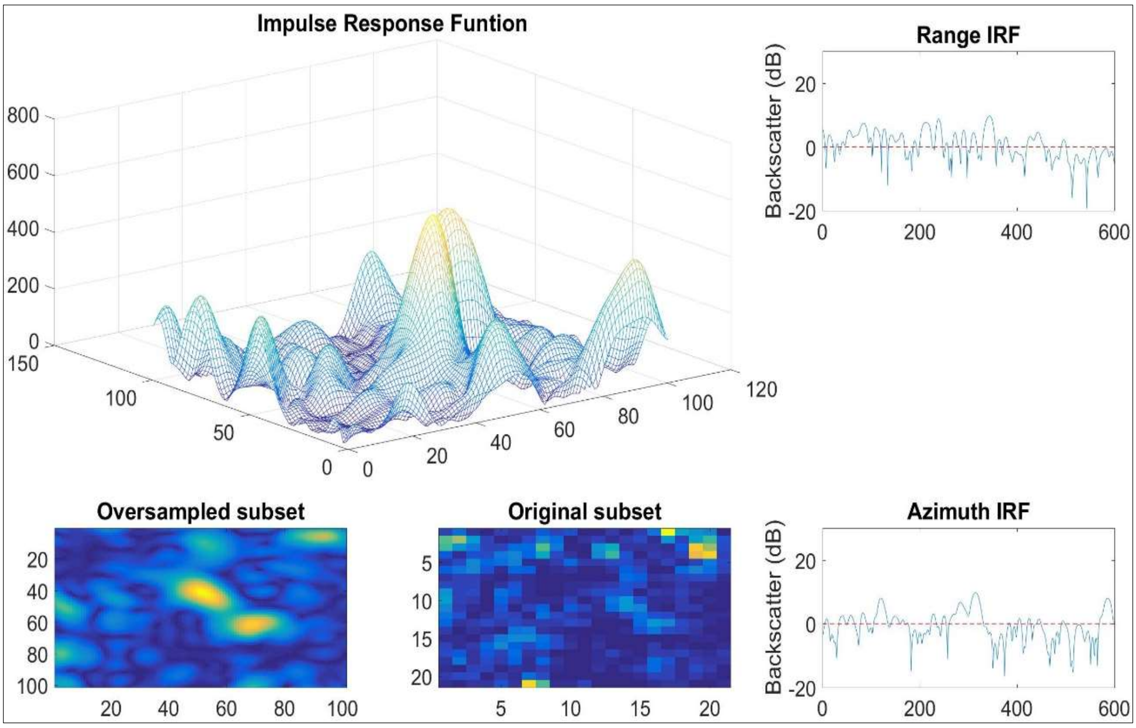

Figure 5.14: Backscatter analysis of CR3 (covered with sand of 10% moisture). CR3 cannot be identified at such moisture level and the IRF analysis has double peaks with very low values. These are most likely representing some surrounding objects in the vicinity of CR3.

5.3.2.4 CR5

The last CR that was used in buried feature experiment is CR5. There were 16 successful buried field observations for CR5, from the 11th April until 20th of October 2016. Like the pre-burial observed backscatter for CR3, the backscatter of CR5 also remains relatively constant over time, Fig 5.15, with mean 25.7 dB and standard deviation 0.7 dB. There is a sharp contrast between CR5 (un-covered) and the background of more than 25 dB (Fig 5.16). As a result, the detection of CR5 in the SAR image was straight forward. However, upon burial with sand of variable moisture content, there is a clear reduction in the backscatter for CR5. The moisture levels covered by CR5 ranged between dry sand (0.1%) and 7%. Fig 5.17 is the backscatter analysis of CR5 while it is covered by a sand layer of 7% moisture content. The peak IRF is highly reduced by the sand cover, compared to the un-covered observation of Fig 5.16.

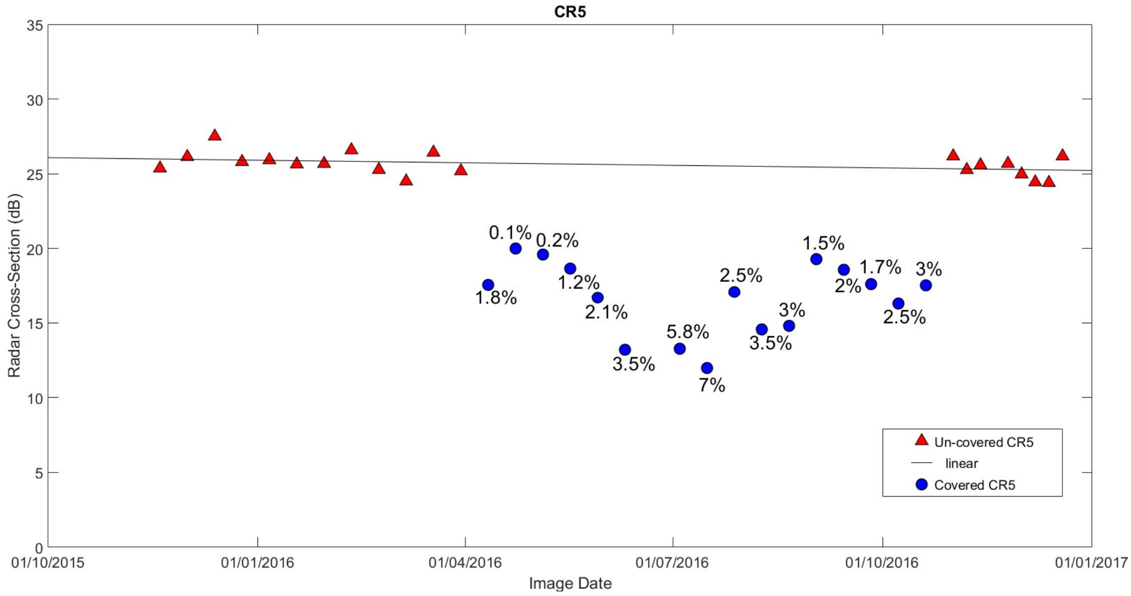

Figure 5.15: Backscatter history of CR5. Red triangles represent the un-covered observations and the blue circles represent the covered observations. Numbers represent the percentage of water content in the sand layer.

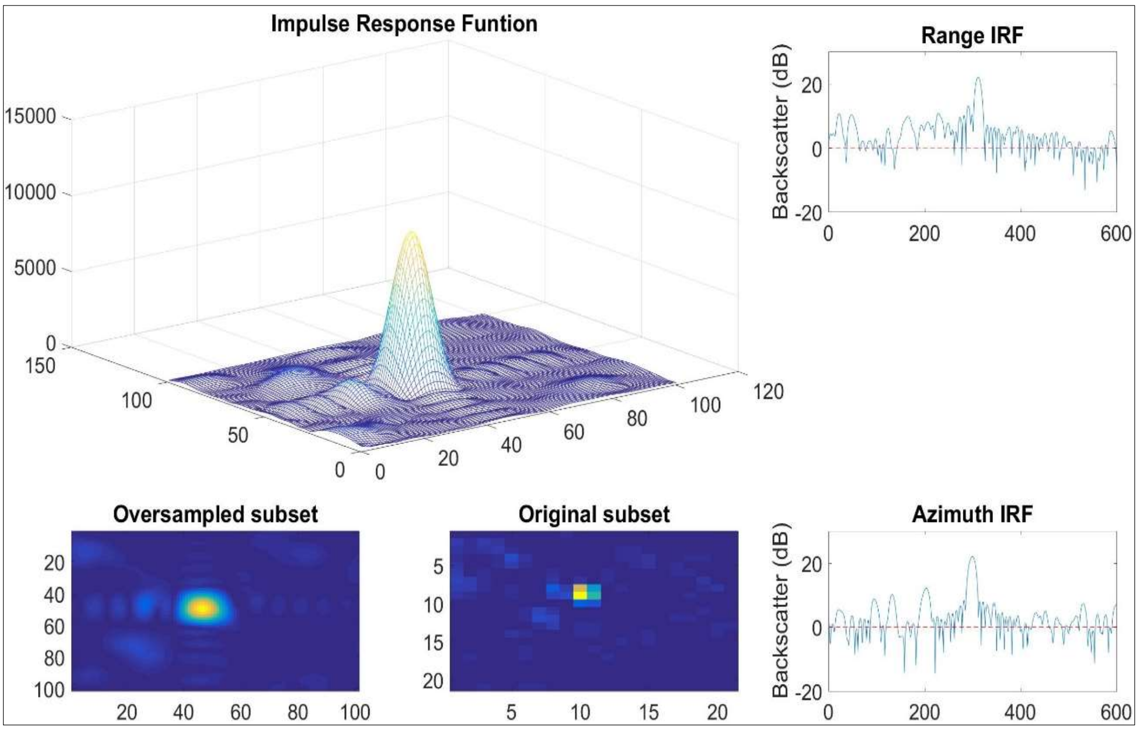

Figure 5.16: Backscatter analysis of CR5 (un-covered observation) where CR5 can be easily identified

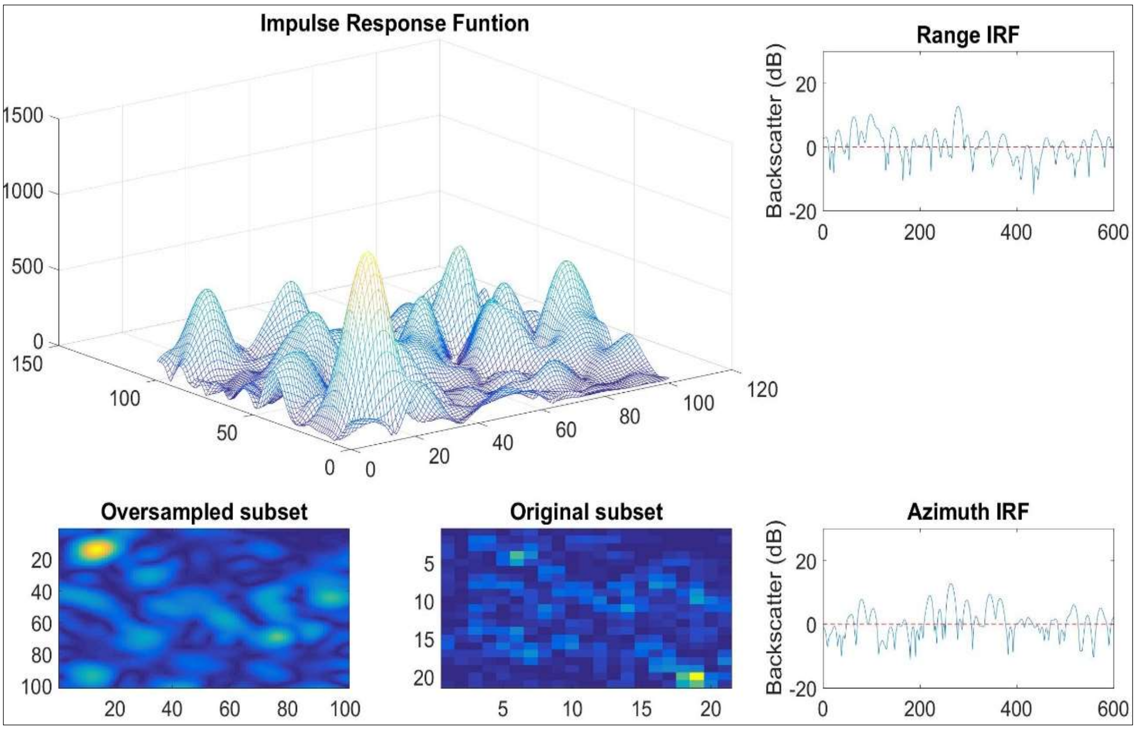

Figure 5.17: Backscatter analysis of CR5 while buried under sand layer of 7% water content.

5.3.3 Discussion

The first part of the buried feature detection experiment involves analysing the backscatter of the CRs. The backscatter of the four CRs involved in this experiment are analysed in both the buried and un-covered observations. Analysis of all un-covered CRs observations (excluding the discarded CR4) revealed that there is a high contrast between the CRs backscatter and the background. Generally, the mean backscatter of all the CRs was above 24 dB, which is much higher than the background. However, this is lower than the theoretical RCS of the CRs, which is 31 dB for the 1m trihedral CR. This is primarily due to orientation errors during the CRs installation. Possible fabrication imperfection could also have such implications on the observed RCS for the CRs. These are usually caused by curvature in the triangle sheets that formed the CRs, or that the triangle sheets were not precisely aligned perpendicularly to each other. Fig 5.18 is the backscatter history of all the CRs. The RCS for all the CRs tended to gradually reduce over time. This is most likely caused by debris accumulation over time in the CR aperture, which reduced the reflection capability of the aluminium sheets, as well as the degradation in the CR structures.

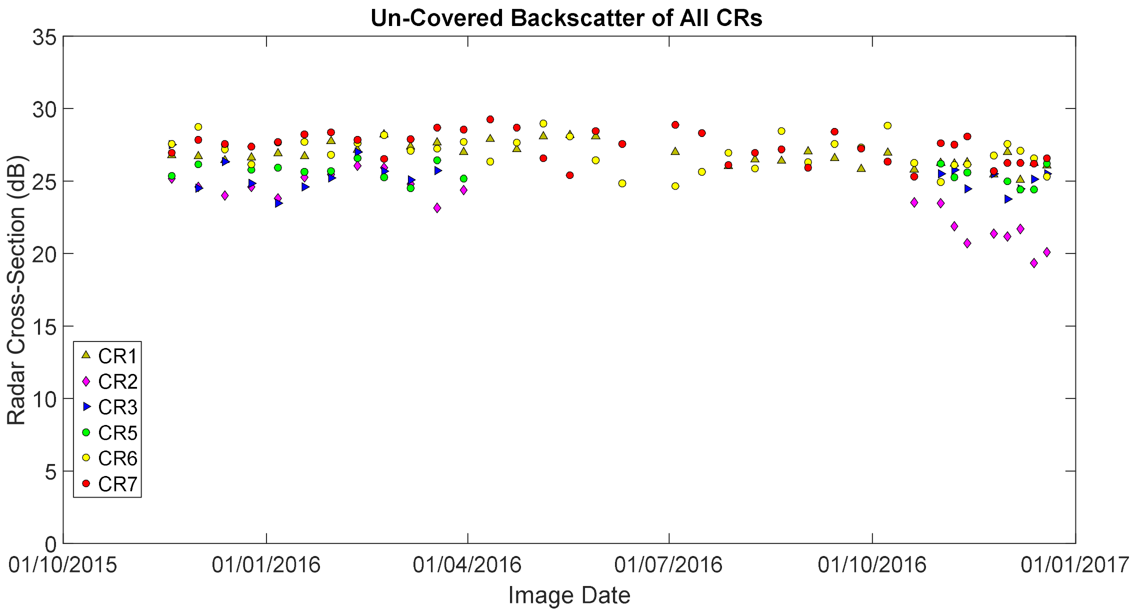

Figure 5.18: Backscatter history of all the CRs

Post-burial, there was a reduction in the observed backscatter due to signal attenuation when passing through the sand layer overlying the CRs. The attenuation is estimated by measuring the reduction of the buried CR backscatter observation from the general regression line of the un-covered observations of that CR. The relationship between the backscatter reduction (attenuation) and the corresponding sand moisture is presented in Fig 5.19. Although there is some noise in the observations, there is a strong linear correlation between moisture content and the signal attenuation with a coefficient of determination (R^2) of 0.91. This implies that for a 1 cm sand cover, 90% of Sentinel-1 backscatter signal attenuation can be predicted by an increase in sand moisture. As explained in Section 3.2, the magnitude of the reflected energy is a function of the Fresnel reflection coefficient (ρ). It was also explained that the later is further a function of the dielectric constant. Therefore, the backscatter should increase when using higher soil moisture levels. This is the opposite of the results presented here. This is an indication that all the buried observations were indeed from the beneath CRs, and not from the surface sand layer, and the attenuation in the signal results from penetrating the sand layers.

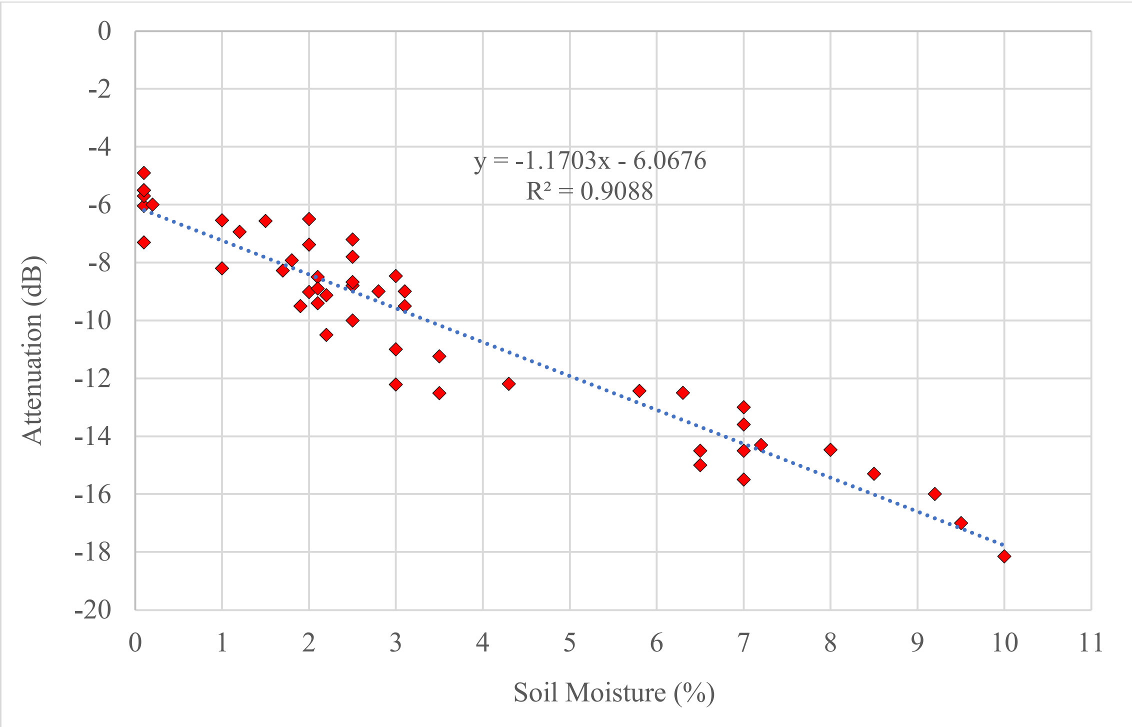

Figure 5.19: The relationship between the moisture content and the attenuation in the backscatter.

An average decrease in the backscatter signal of approximately -6 dB is expected when the CRs are buried under dry sand (moisture content <0.1%). Such level of attenuation is higher than observed in laboratory investigations (Williams & Greeley, 2001), which have suggested that the transmitted signal attenuation is about 6 dB for a 1 cm thick sand with water content of 10%. Williams and Greeley (2001) reported that at C-band, the signal attenuation of 1 cm dry sand is less than 2 dB. This discrepancy from the SubSAR experiment results is most likely caused by the additional plastic bag that was used to hold the sand-water mix, and the wooden frame with the polystyrene pad. Instead of sand-water mix as used in the laboratory experiments, the signal in the field experiment has to pass through the sand-water mix, as well as the plastic bag, wooden frame, and the polystyrene pad. However, since the same combination are used for all the buried observations, the effects of these additional component will be constant in all the observations. With increased sand moisture content, the signal is further attenuated, and identification of the buried CRs in the SAR imagery becomes a challenging task. For sand moisture content of 10%, the signal is attenuated by -18 dB to approach background levels, meaning that the buried CR can no longer be identified from Sentinel-1 image. Thus, the maximum soil moisture at which a buried CR could be detected is 9.5%.

The backscatter analysis results contradict the information presented in Section 3.2, where it was explained that magnitude of the reflected and transmitted energy from a dielectric medium both depend on the dielectric constant of that medium. For soil surface reflection, the backscatter increases as the soil moisture increases. Therefore, the reduction in the observed backscatter in response to increased soil moisture can only be explained by volume scattering from a subsurface feature where the signal attenuation is proportional to the dielectric constant of the soil medium.

5.4 DInSAR analysis

The second part of the experiment involves analysing the DInSAR phase of the covered CRs to retrieve the information about the effects of sand moisture content on the phase of the transmitted signal. Using the first image where all the CRs are installed in the field as the master image (October 2nd, 2015), a series of 36 differential interferogram was generated from the co-registered stack with respect to the master image, by subtracting the phase of the slave from the phase of the master. Mathematically, this is implemented by multiplying the phase of the slave image by the complex conjugate of the master image. The procedure of DInSAR analysis (explained in Section 2.7.2) and the phase extraction process for the CRs in the experiment (discussed in Section 4.7.2) was followed. The DInSAR phase history for all the CRs was then calculated with respect to a reference point (CR6).

Similar to the backscatter analysis, the phase of the CRs is analysed for both the buried and un-covered observations. The phase behaviour of the un-covered observations for the CRs generally shows relative stability over time, but with an oscillation of approximately ± 1 rad (Fig 5.20). There is a comparable temporal oscillation in the phase of the 5 CRs that could be related to atmospheric effects. Although appearing relatively stable, there is a gradual displacement in the location of most CRs with respect to the reference point over the duration of the experiment. This displacement is of the order of 1–2 rad, which corresponds to approximately 0.5–1 cm change in the LOS.

Field surveys were not implemented to measure the precise position of each CRs at each field visit for practical reasons. Assuming that the CR structure itself remained stable, this apparent displacement likely reflects ground motion, which could potentially be due to groundwater level change or soil dynamics, but there is no available information to confirm this.

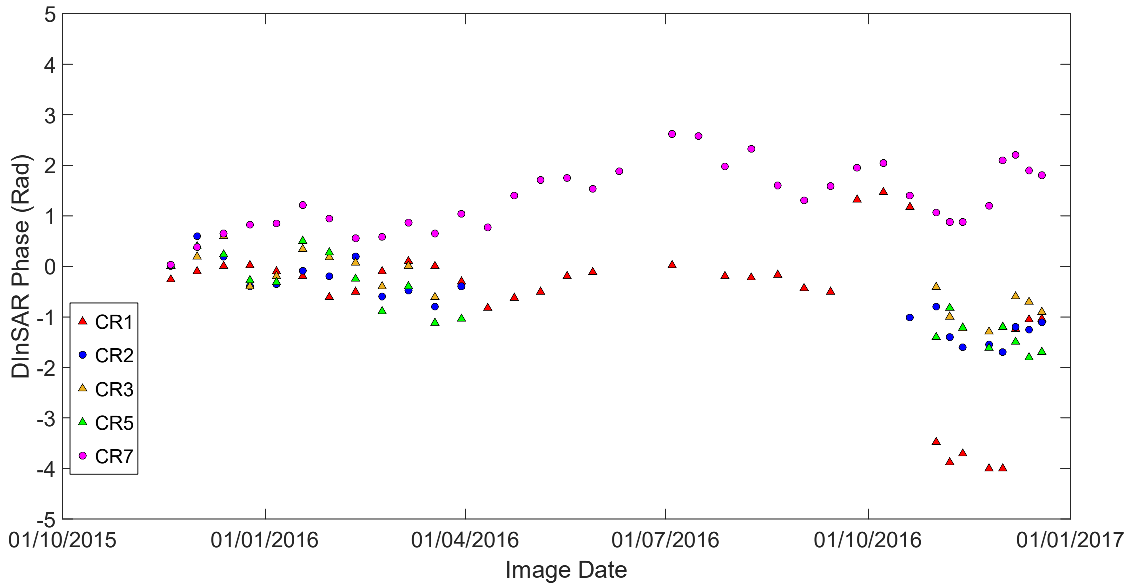

Figure 5.20: DInSAR Phase history of the CRs from the un-covered observations

For the buried observations, the experiment was set up in a way to try to ensure that the only variable parameter is the sand moisture content. Therefore, any differences in the phase between the buried and un-covered observations can be assumed to correspond to variations in the sand moisture. However, because this is a field experiment, other 'un-controlled' parameters could affect the phase observations. Again, these can mainly be attributed to atmospheric effects. The un-covered phase observations are plotted alongside the buried phase observations for each CR in order to calculate the phase shift caused by the sand cover.

Fig 5.21 represents the phase history of CR1. The general trend of the uncovered observations shows some oscillation of the phase, on the order of ± 1rad,with an average displacement of -1 rad in the LOS over the experimental period. This corresponds to less than 0.5 cm change in the CR position, with respect to the reference point, in the satellite LOS. The phase change in the buried observations, on the other hand, is higher than the temporal oscillation of the phase, with an increase in the phase of approximately 5 and 6 rad corresponding to sand moisture of 7% and 9.5%, respectively.

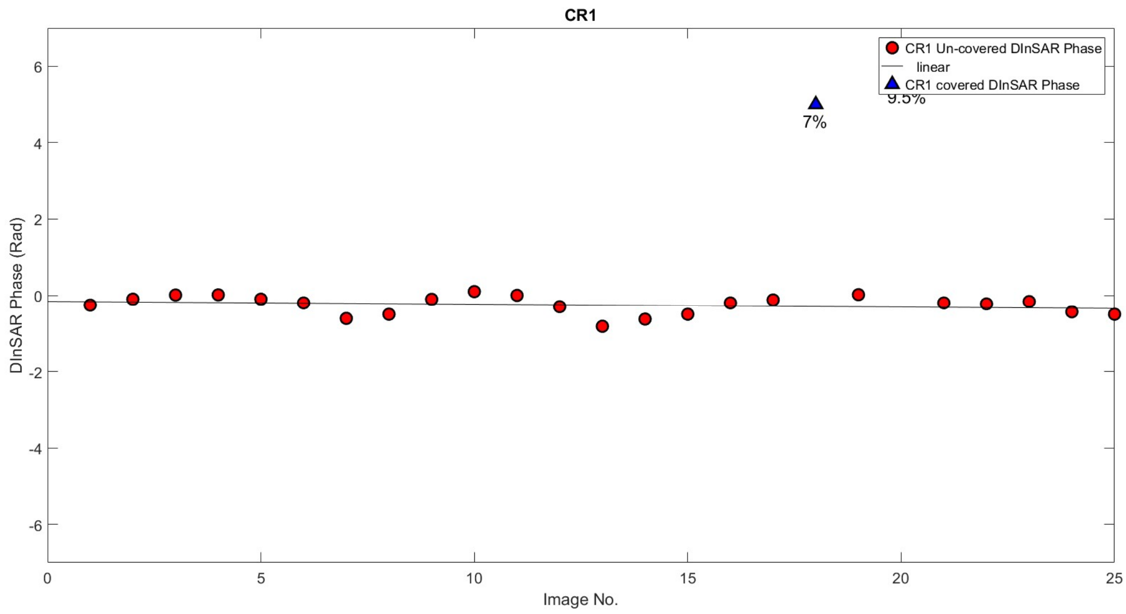

Figure 5.21: DInSAR Phase history of CR1 including the buried and un-covered observations. Numbers next to the buried observations represent the percentage of the sand moisture

Similarly, the phase history of CR2, CR3 and CR5 are represented by Fig 5.22, 5.23, and 5.24, respectively. For the un-covered observations, the CRs have a similar trend to CR1, where there is an apparent motion in the CR position of 1.5, 1.2, and 1.6 rad for CR2, CR3 and CR5, respectively, over the experimental period. These motions are related to 7mm, 5mm, and 7mm, respectively, in the satellite LOS, which indicate that the ground is gradually moving, but again, no ground truth is available to confirm this motion. For the buried observations, there is a phase change related to the amount of water in the sand cover.

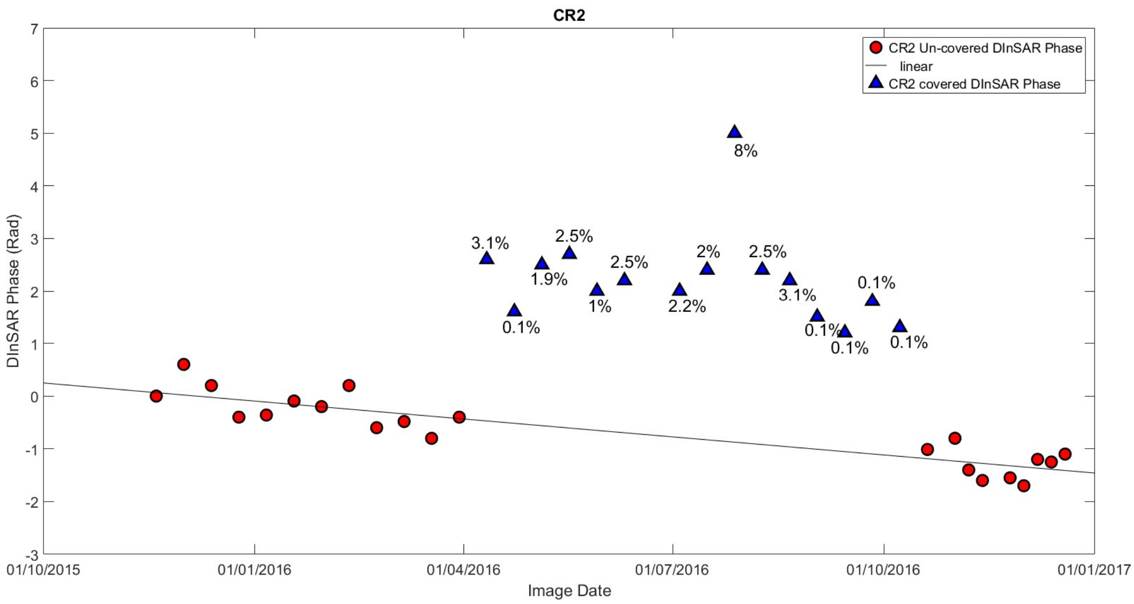

Figure 5.22: DInSAR Phase history of CR2 including the buried and un-covered observations. Numbers next to the buried observations represent the percentage of the sand moisture

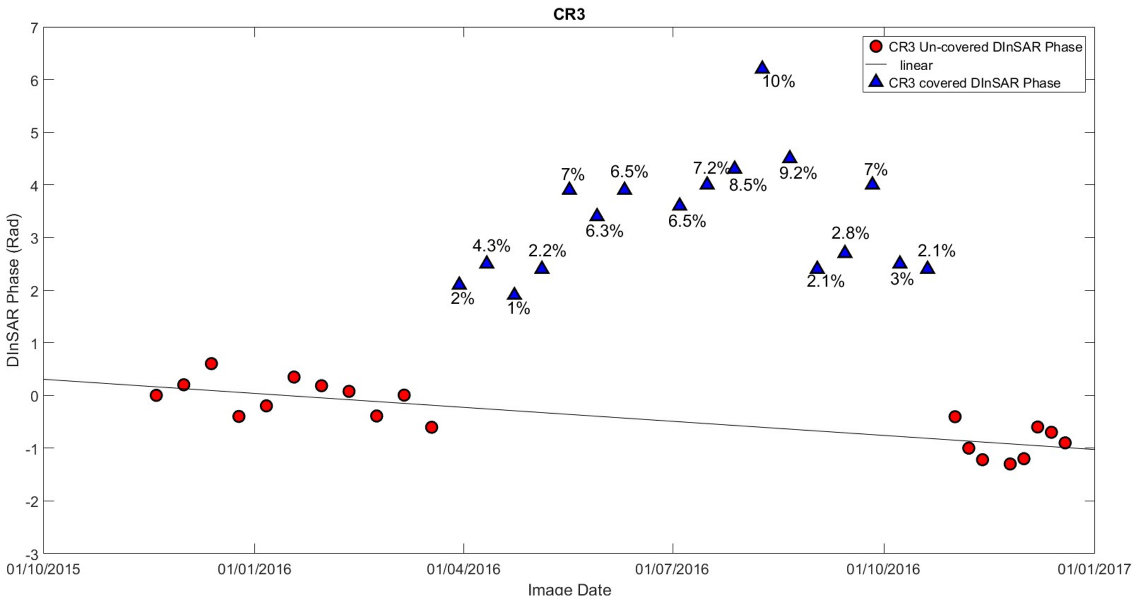

Figure 5.23: DInSAR Phase history of CR3 including the buried and un-covered observations. Numbers next to the buried observations represent the percentage of the sand moisture

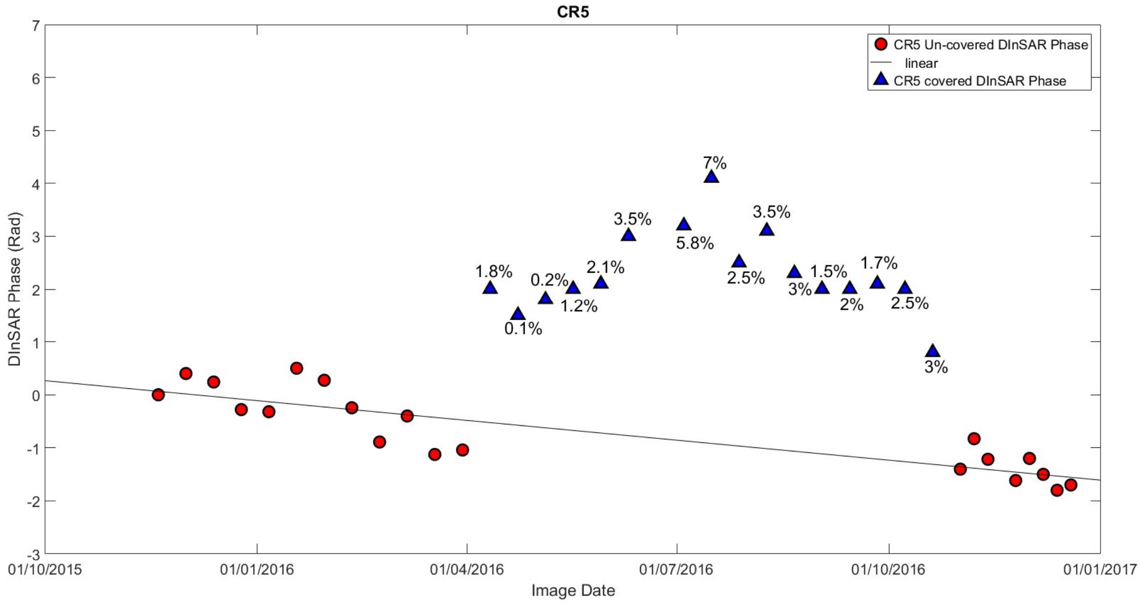

Figure 5.24: DInSAR Phase history of CR5 including the buried and un-covered observations. Numbers next to the buried observations represent the percentage of the sand moisture

In comparison, the phase history of CR7 is presented in Fig 5.25. the general trend the phase of this CR is opposite to the rest of the network with an increase in the phase between the start and end of the experiment of 1.5 rad. This is corresponding to 7mm decrease in the LOS distance. The ground motion near CR7 is different than the other CRs, as this CR appears to be sinking, rather than uplifting. Once again, there is no ground truth to validate the displacement.

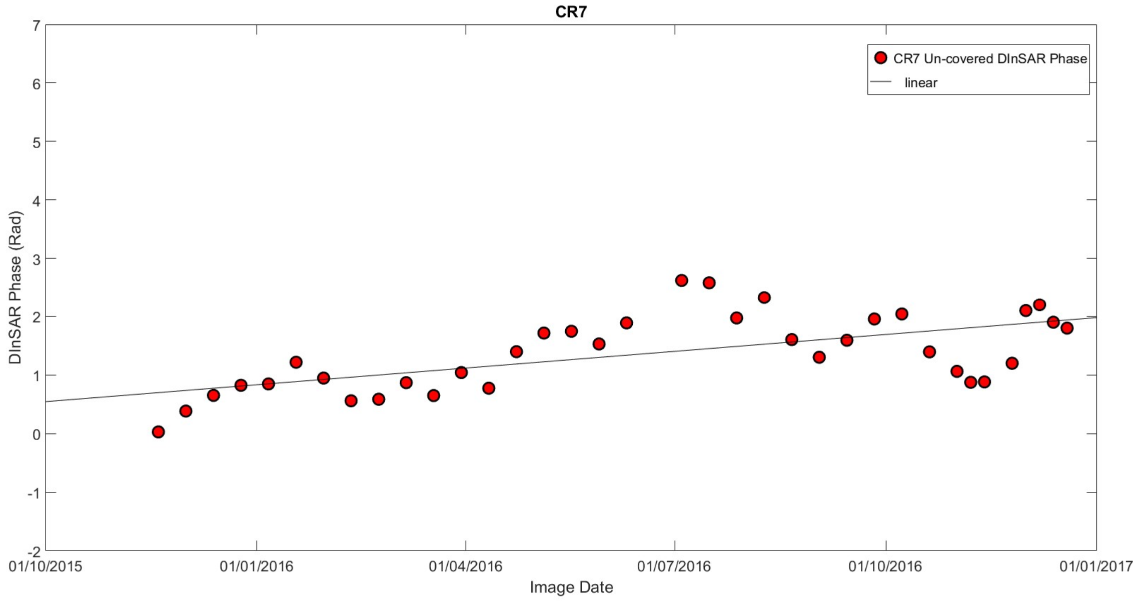

Figure 5.25: DInSAR Phase history of CR7

5.4.1 Discussion

The second part of the experiment involves analysing how the DInSAR phase of the CRs changes in response to being buried under a sand layer of varying moisture content. The un-covered observations for each CR enable the spatio-temporal behaviour of that CR to be characterised. In general, all the CRs used in this experiment show relative stability, with a small LOS displacement over time, on the order of ±2 rad (less than 1cm).

These displacements indicate that the ground is not stable and slightly moving with time, which reflects the soil dynamics, but there is no ground truth for validation. However, upon burial, there is a clear change in the observed phase. The sand layer thickness remained constant at 1 cm for the buried observation so that the only variable parameter was the water content. The result of the buried feature experiment revealed a phase change with magnitudes varying according to the amount of the water content in the sand layer. In contrast, the phase observations of the un-covered CRs has no obvious changes. The dielectric constant for a given soil type is directly controlled by the moisture content (Hallikainen et al., 1985). The refractive index, according to Eq. 3.3, is a function of the dielectric properties of the medium. When the soil becomes wet, the refractive index increases as well. The transmitted signal will then travel at lower speed within the wet sand layer. This in turn will be translated into an increase in the path length, and hence the change in the observed differential phase. The observed interferometric phase is therefore appears moving away from the satellite antenna, or an apparent subsidence of the surface, even when the surface is not moving. The trihedral CRs used in this experiment are radar point targets, and it is their backscatter that dominates the signal return. Therefore, the observed phase change is associated solely with the variations in the sand moisture content, and not to speckle behaviour of the background. Quantitative analysis of the phase change was implemented to establish a relationship between the phase change and the sand moisture content. For each CR involved in the experiment, the phase change due to the sand-water mix was estimated by comparing the phase of the buried observations with that of the un-covered observations. Computationally, this was achieved by subtracting the buried phase from the un-covered phase regression line. By calculating the phase change for all the buried observations, it was possible to model the phase change caused by the sand-water cover mix. This relationship is presented by Fig 5.26. There is a positive linear correlation between the two variables, with coefficient of determination (R^2) of 0.87, which means 87% of the phase change can be predicted by changes in the sand water content.

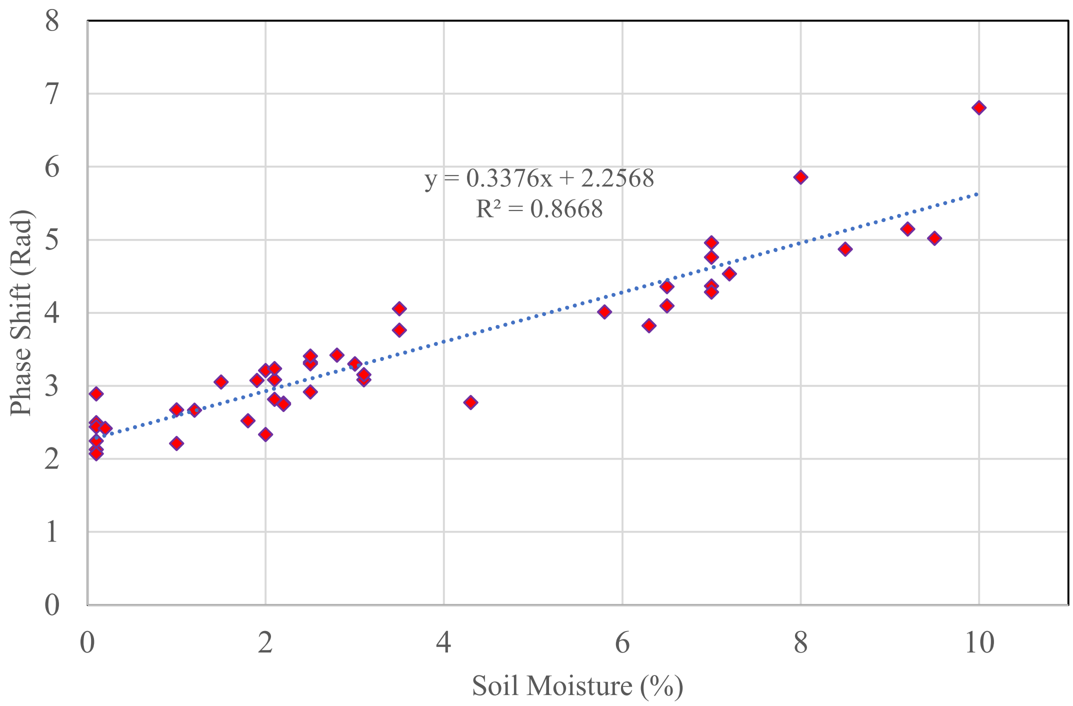

Figure 5.26: The relationship between the sand moisture and the corresponding phase change

Differential interferometric phase is well known as responsive to soil moisture changes (Gabriel et al., 1989; Nolan and Fatland, 2003; Nolan, 2003). The soil moisture affects the observed differential phase either directly through changing the volume scattering in the soil, affecting the refractive index (Nolan and Fatland, 2003; Nolan, 2003). Or indirectly through changing the soil surface via shrink-swelling of clay soils (Gabriel et al., 1989). Both these explanations (path length change and clay shrink-swelling) have the same effect on the observed differential phase direction and magnitude. As the moisture increases, an apparent uplift could be observed, while subsiding is observed when the soil moisture decreases (Rabus et al., 2010).

The result obtained from this experiment shows that the interferometric phase shifts positively as the soil moisture increases. That means a subsidence is observed as the soil moisture increases and uplift is observed as the soil dries. This is the opposite of the above-mentioned findings and can only be explained by subsurface scattering mechanism. For dry soil, the radar signal can penetrate easily as the refractive index is low and most of the power received by the radar antenna comes from dielectric contrasts in the soil medium (Ulaby et al., 1981), which is the subsurface feature. As the soil moisture increases, the refractive index increases as well and the signal travels at lower speed in the wet medium and the target appears to be subsiding. As the soil dries again, the target appears moving upwards (uplifting).

The backscatter-phase information obtained from this experiment can be exploited for wide-scale subsurface feature detection campaigns that have wide range of applications, such as geological studies, buried pipeline monitoring, civil engineering, archaeological explorations, and so on. However, certain conditions need to be met for successful SubSAR applications, such as the type of features that could be detected by this method, the suitable measurement platform, and geographical and seasonal considerations. All these details and the implications of applying SubSAR scheme in the real world will explained in detail in Chapter 6.

5.5 Summary

The aim of this research is to investigate the possibility of using Sentinel-1 data to detect buried features using the SubSAR technique. This was achieved by designing a field-scale experiment that involved burying a network of trihedral CRs with a layer of sand. The water content of the sand was then varied for each satellite overpass. This enabled the effects of changing the water content of the sand layer to be investigated for both the backscatter and DInSAR phase of the buried CRs.

With respect to the backscatter, when the Sentinel-1 signal is transmitted through the sand layer, a reduction in the backscatter is clearly detected from the buried CR. Signal attenuation is estimated from all the buried observations and a relationship is derived between the change in the sand moisture content and the signal attenuation. The attenuation is found to increase linearly in response to sand with increasing moisture content. This is in contrary to the general rule of thumb that the backscatter of the soil surface is increased when the soil moisture increased as well, as explained in Chapter 3.

This is an indication that the observed backscatter is not from the soil surface (sand layer surface), but from the buried CR beneath. Therefore, monitoring the backscatter behaviour, with the knowledge of the sand moisture, can be utilised in detecting buried features.

At 10% sand moisture content, the observed backscatter signal was reduced to the background level and thus the CRs could no longer be identified from Sentinel-1 images. This result is in close agreement with a laboratory simulation experiment using similar parameters (1 cm sand layer and C-band). Overall, the backscatter analysis revealed that it is possible to use Sentinel-1 C-band to penetrate sand to at least 1 cm thickness for a maximum moisture content of 9.5%.

The second part of the experiment involved analysing the phase history of each CR. For the un-covered observations, the phase history of the CRs indicate relative stability over time, with minor oscillation that is attributed to atmospheric effects. When the CRs are covered with a sand layer to simulate buried targets, there is a clear shift in the observed phase which is variable for different moisture levels. The phase shift is usually an indication of a moving CR. However, in this case the significant phase shifts are associated with the sand cover. The observed phase shift signal is equivalent to a subsiding target. When the sand moisture increased, the target appears to be further from the satellite due to the extra time that the signal travelled within the sand layer. This is in contrast to surface soil observations, where for increased soil moisture, the soil appears uplifting due to swallow effects (Gabriel et al. 1989). Consequently, the results present here provide confirmation of the SubSAR technique, in that the phase can be used to discriminate between buried and surface targets.

The final conclusion is that the results of this field-scale experiment reviled that the DInSAR phase and the backscatter of a buried features both exhibit an inverse behaviour to the surface soil scattering properties, which verifies the SubSAR experimental results. Therefore, it is possible to use the SubSAR technique on a wide scale, using satellite SAR data, for buried feature detection.

Chapter 6: SubSAR Implications

6.1 **Introduction**

In the previous chapters, the validity of the SubSAR scheme for subsurface feature detection using satellite SAR data has been tested in field-scale experiments. It has been demonstrated that the C-band radar signal is responsive to variations in the moisture of the sand layer overlying a buried corner reflector. Many factors in this field experiment were controlled, including the soil type, target characteristics and depth, and soil moisture. Moreover, the buried target (i.e., corner reflector) appears as a very bright object in the SAR images and its signal dominates the associated resolution cell of a Sentinel-1 image. Accordingly, the controlled field-scale experiments that have been conducted represent an optimum set of conditions for testing the SubSAR scheme. However, the ability to exploit the SubSAR on a wider scale is dependent on a complex combination of factors (e.g., radar system characteristics, environmental conditions) and ultimately, the availability of the SAR data. Currently, there are many satellite SAR systems, both in orbit and planned for future missions, such as TerraSAR-X and COSMO-SkyMed (X-band), Sentinel-1 and RadarSAT-2 operating in the C-band, and ALOS-2 in the L-band, as well as the planned P-band SAR mission, Biomass. If the SubSAR scheme can be applied successfully using data from all of these SAR satellites, it could offer huge potential for detecting buried targets globally, which has many benefits in the fields of geological exploration, archaeological studies, infrastructure monitoring, and ordinance detection. However, the SubSAR scheme is not yet fully tested for representative real-life scenarios, such as a target buried at a different depth, in different soil types and in a different climate to those tested in this study. Ultimately, they key questions are how does a target react to the different radar wavelengths and where are the possible sites that the SubSAR scheme can be successfully implemented? This chapter discusses the various challenges that could influence the performance of the SubSAR scheme. This involves the use of simulations to help to understand how SubSAR could be applied in real-world scenarios.

6.2 **Measurement platform**

The ability to exploit the SubSAR on a wider scale is underpinned by the availability of SAR data. There are currently many operational SAR satellites in orbit that vary in their characteristics, such as the wavelength, spatial resolution and revisit period. Table 6.1 summarises the current operational SAR satellite missions, along with their characteristics. Current spaceborne SAR systems operate in the three main radar bands (X-, C-, and L-bands). Every satellite has its own characteristics that could be exploited in different ways to perform subsurface imaging, which will determine where and when the SubSAR scheme can be successfully exploited. For subsurface imaging, the penetration capability of each systems depends mainly on the radar wavelength and the soil dielectric properties (Hallikainen et al. 1985). Additionally, the resolution of the SAR system significantly influences the buried target detection capability using the SubSAR scheme as it is directly affects the signal-to-clutter ratio (SCR) of the buried target (Freeman, 1992). In addition to the listed SAR systems in Table 6.1, there are future planned missions that could offer additional opportunities to exploit SubSAR for subsurface feature detection. For example, the European Space Agency (ESA) is planning to launch Biomass SAR satellite, a P-band (70 cm) SAR system for comprehensive measurements of global forest biomass. Another future spaceborne SAR system is ICEYE, a constellation of small SAR satellites that, together, offer daily to hourly revisit frequency, which aims to provide interferometric SAR observations globally every few hours. In addition to the spaceborne SAR systems, airborne SAR systems are also used for a variety of purposes, such as forest and ecosystem classification, soil moisture measurements, land use classification, geological mapping and natural hazard monitoring (Wanpiyarat *et al.* 1997). Airborne SAR system specifications vary significantly from spaceborne systems, in terms of frequency used, the revisit period and spatial resolution. This chapter will focus on spaceborne SAR systems as the data is regularly acquired and readily available from each satellite data provider, therefore, facilitating the application of the SubSAR on a wide scale. In contrast, the operational cost is high for airborne SAR systems and the data is much less accessible. In principle, the entire Earth surface can be imaged with these different satellite SAR systems. If the SubSAR scheme can be applied successfully using data from all of these SAR satellites, it could offer huge potential for detecting buried targets globally, which has many benefits in the fields of geological and archaeological exploration, infrastructure monitoring, and other humanitarian applications such as ordinance detection (demining). However, as stated before, SubSAR has only been tested in the lab and in a controlled field experiments, under optimised circumstances. The following sections will explore the different factors, with respect to the SAR system, that could limit the use of the SubSAR scheme on a wider scale.

Table 6.3: Current operational satellite SAR missions

Band	**Sensor**	**Image Mode**	**Resolution (m)**		**Revisit Period**
			Azimuth	Range	
X-Band	TerraSAR-X	Starting Spotlight	0.24	0.6	11 days
		High Res Spotlight	1.1	1.2	
		Stripmap	3.3	1.2	
		ScanSAR	18.5	1.2	
	COSMO-SkyMed	Spotlight	1.0	1.2	16 days for a single satellite and 1-day
		Stripmap	3.0	3.5	
		ScanSAR	16.0	8.1	

					revisit achieved by the tandem configuration.
	PAZ	Stripmap	3	3	11 days when works individually, but can woks as a constellation with TerraSAR-X
		ScanSAR	16	6	
		Spotlight	1	1	
		HR Spotlight	<1	<1	
C-Band	Sentinel-1	Stripmap	5.0	5.0	6 days with constellation of 2 satellites
		Interferometric Wide Swath	20.0	5.0	
		Extra Wide Swath	40.0	20.0	
	RADARSAT-2	Spotlight	0.8	1.6	4 days with constellation of 3 satellites
		Ultra-Fine	2.8	1.6	
		Multi-Look Fine	4.6	3.1	
		Fine	7.7	5.2	
L-Band	ALOS-2	Spotlight	1.0	3.0	14 days
		Stripmap Ultra-Fine	3.0	3.0	
		High-sensitive	4.3	6.0	
		Stripmap Fine	5.3	9.1	
		ScanSAR	77.7	47.5	

6.3 **Real-world considerations**

This thesis has demonstrated that SubSAR is a promising method for detecting subsurface targets in field experiments. However, this scheme can only be applied under certain conditions and many factors could affect, or limit, its wider use. This section will discuss some of the main factors that affect the SubSAR applications. In summary, these are the soil, climatic zone and the SAR system-target characteristics.

6.3.1 **The soil medium**

The soil medium, as explained in Chapter Three (Section 3.4), is a mixture of variable natural particles, like minerals and organic matter, that vary in size from the smallest clay particles to large gravels. The soil matrix is also composed of air voids, water and organisms, and is considered to be a very complex natural system to support life on Earth. The interaction of microwaves with a soil medium can be characterised by surface and volume scattering, as previously explained in Section 3.3. The surface scattering depends on the dielectric constant of the soil medium, surface roughness and the vegetation cover, whereas volume scattering depends on the soil texture and moisture content, in addition to the radar wavelength being the key factor in the occurrence of any of these scattering phenomena (Engheta and Elachi, 1982). The soil dielectric constant (ε) is a function of its textural composition and volumetric water content (Hallikainen *et al.* 1985). So far, in this study only a homogeneous sandy soil has been considered, with a smooth surface and devoid of any vegetation cover. However, a typical 'real' soil could affect subsurface imaging through both the surface and volume scattering mechanisms. The main implications of each of these soil characteristics are highlighted in the following subsections.

6.3.1.1 **Surface scattering**

The concept of surface roughness was introduced in Section 3.3.1. The magnitude of the reflected signal is proportional to the dielectric constant of the soil, while the scattering direction depends on the surface roughness. Specular reflection occurs at a perfectly smooth surface, where most of the incident radar signal is forward scattered at the same angle of the incident wave, but on the opposite direction, with a very small backscattered signal towards the radar (Carver and Elachi, 1985), which results in little clutter in the SAR image. Surface clutter could significantly reduce the ability to detect a buried target by overwhelming the resolution cell signal (Morrison and Bennett, 2015). Therefore, areas characterised by smooth surface represent ideal locations for the SubSAR application where the surface clutter is low, and the buried target signal can be easily detected. This is in contrast to a rough soil surface interaction, where the radar signal is backscattered in all directions (i.e., diffuse scattering) (Ulaby *et al.* 1978). Surface roughness is a function of the radar signal wavelength (Roger and Ulaby, 1994). Longer radar wavelengths, such as ALOS-2 L-band, could mitigate the rough-surface scattering effect (the clutter) and improve the signal-to-clutter ratio (SCR) of the buried target. Therefore, buried targets in regions characterised by rough soil surfaces could potentially be detected by exploiting long radar wavelength.

6.3.1.2 **Volume scattering**

A medium is electromagnetically heterogeneous if it contains inclusions whose dielectric constant are different from the host medium material and their sizes are comparable to the radar signal wavelength (Carver *et al.* 1985). Unlike the pure sand used in this study, typical soils are heterogeneous, such that the soil structure is a composite mixture of sand, silt and clay with aggregates and grains of different sizes. When a radar signal is transmitted into such a medium, then the signal will be scattered off the soil aggregates in different directions and cause volume scattering. Volume scattering is caused mainly by dielectric discontinuities within the soil medium (Kozlov *et al.* 2007). Figure 6.1 shows a schematic model of volume scattering from an uneven soil with particles of different sizes. The backscattered signal received by the radar antenna for this area is the sum of surface scattering at the air-soil interface and subsurface volume scattering from the aggregates and other large grains within the soil volume. In general, both surface and volume scattering contributions are present in SAR images. Surface scattering increases as the soil dielectric constant (water content) increases, as stated in Chapter Three. Whereas volume scattering decreases when the soil moisture increases, in part because the signal attenuation within the soil medium increases rapidly with moisture content, and because the air-soil transmission decreases with increasing moisture content. The volume scattering contribution in wet soil is therefore very small and, at short radar wavelengths, such as X-bands, this could be negligible, while in dry soil conditions volume scattering becomes comparable to, or greater than, the surface scattering component (Nashashibi *et al.* 1996).

In conclusion, the implementation of the SubSAR scheme in non-uniform soil could be difficult as the clutter of the volume scattering could have the same characteristics as the buried target, which makes it a challenging task to separate the target signal from the volume clutter signal. In contrast, there is no, or very little, volume scattering from a radar signal propagating a uniform soil with consistent small grain sizes (compared to the radar wavelength). Sandy soil, such as most of the hot-desert lands, is a good example of a uniform medium where both surface and volume scattering are generally very low, as will be shown later in this chapter, which could support the detection of subsurface features. In the simulation section we consider an aggregated soil surface and volume return, which constitutes the clutter signal.

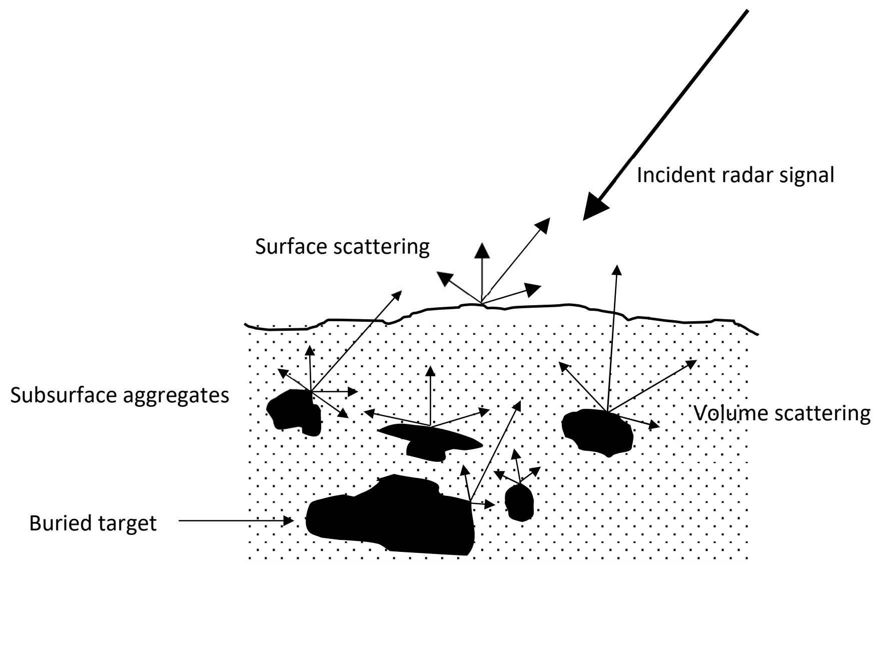

Figure 6.8: Volume scattering within a soil medium. Large soil particles contribute to the overall radar scattering of this area and prevents the detection of buried targets.

6.3.1.3 **Vegetation cover**

In this study, the surface of the soil layer above the target was kept bare during the field experiment. However, approximately 67% of the land surface is covered with vegetation (World Bank, 2016), therefore it is essential to consider the effect of vegetation cover on the wider exploitation of the SubSAR scheme. The vegetation canopy interaction with the microwave signal mitigates the strength of the soil backscattered signal through its stems and leaves. The radar signal suffers two-way absorption, as well as volume scattering, when passing through a vegetation layer (Mo *et al*. 1983). This signal loss is known as vegetation attenuation and its magnitude depends on the density of the vegetation layer and the vegetation volume scattering depends on the geometry and the dielectric constant of the vegetation cover. Therefore, the general presence of vegetation complicates the retrieval of accurate subsurface scattering information (i.e. the phase and amplitude of the buried target), as the signal suffers multi-layer attenuation in comparison to that from just the bare soil alone.

The SubSAR scheme presented here with C-band SAR cannot be directly applied in vegetated areas because of the complex combination of attenuation and scattering of part of the radar signal from the vegetation canopy and the two-way attenuation of the transmitted radar signal within the soil medium beneath the vegetation canopy. However, longer radar wavelengths (i.e., L-band) are less susceptible to the scattering effects of vegetation (Ulaby *et al*. 1981), so satellites such as ALOS-2 could offer more promise for successfully implementing SubSAR in vegetation terrain.

This section has highlighted the key ways in which the soil medium can affect the application of the SubSAR scheme in non-optimal land surface conditions such as those typically faced in many areas around the world. From this, it can be concluded that homogeneous soils that are devoid of vegetation are clearly most preferential for subsurface imaging using SubSAR. This likely restricts the use of the SubSAR to arid regions, particularly deserts, where the vegetation cover is very sparse, and the soil medium is predominantly comprised of relatively homogeneous sand.

6.3.2 **Geographical settings**

Arid regions cover more than one-third of the global land surface and are characterised by a severe lack of water, with annual rainfall typically less than 250 mm (Gamo *et al.* 2013). This lack of water hinders the growth and development of vegetation, and so vegetation cover is very sparse. Arid regions represent ideal locations to utilise radar subsurface imaging because the large extent of the barren sand sheets provide the optimum condition for the radar signal to penetrate into the surface by a few centimetres to a few metres, depending on the radar wavelength and the dielectric constant of the sand. Geographically, the majority of the arid regions (Figure 6.2) are located in North Africa, Australia, North and South America, and the near east and middle Asia (Gaur *et al*. 2018). Additionally, cold arid regions can be found close to the poles, such as the polar deserts in the Antarctic continent (Hogg and Wall, 2012). A well-known example of a sandy desert is the Sahara Desert in North Africa, which is the largest hot desert in the world with an area of more than 9 million km^2 (Salem, 1989). It is characterised by excessive heat and extreme aridity, with very low humidity and mean annual precipitation of less than 100 mm. Sand sheets occupies approximately 15% of the Sahara Desert (Laity, 2009). To further investigate the suitability of arid regions for subsurface imaging in terms of surface and subsurface (volume) scattering effects, a Sentinel-1 image over part of the Sahara Desert in Southern Egypt is considered (Figure 6.3). The image was acquired from the ascending track number 131 on 10/1/2020.

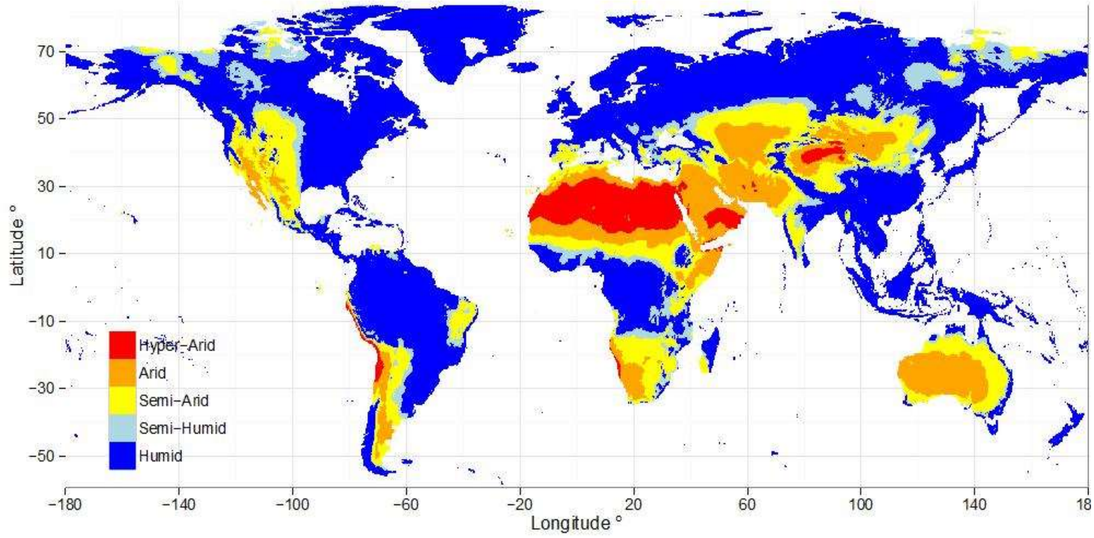

Figure 6.2: Global distribution of climate zones. For radar subsurface imaging, the hyper-arid (red) and arid (orange) are of particular importance as they are characterised by lack of vegetation cover, and large extent of sand sheets. Ref: http://ozewex.org/semi-arid-ecosystems-particularly-sensitive-to-mega-droughts/

It was processed to perform radiometric calibration, geometric corrections, speckle filtering and orthorectification using the ESA SNAP Sentinel toolbox software. Finally, the σ^o values were converted into logarithmic dB values and the image was visualised in a GIS. An inspection of an optical satellite image confirms that this area is predominantly sand. The backscatter values in the selected scene ranges between -30 dB in the western part of the image, to up to 1 dB in some locations in the north-east part of the image. The mean backscatter of the whole scene is estimated to be less than -23.9 dB with a standard deviation of 4.1 dB. The very low backscatter values could be an indication of a smooth surface, where the specular reflection causes the radar signal to reflect away from the satellite direction. However, it is most likely that the sand is very dry and homogeneous and therefore much of the signal penetrates into the subsurface. Without the presence of subsurface scatterers such as rocks of suitable size and depth, the volume scattering is very low which results in a low backscattering coefficient for this area.

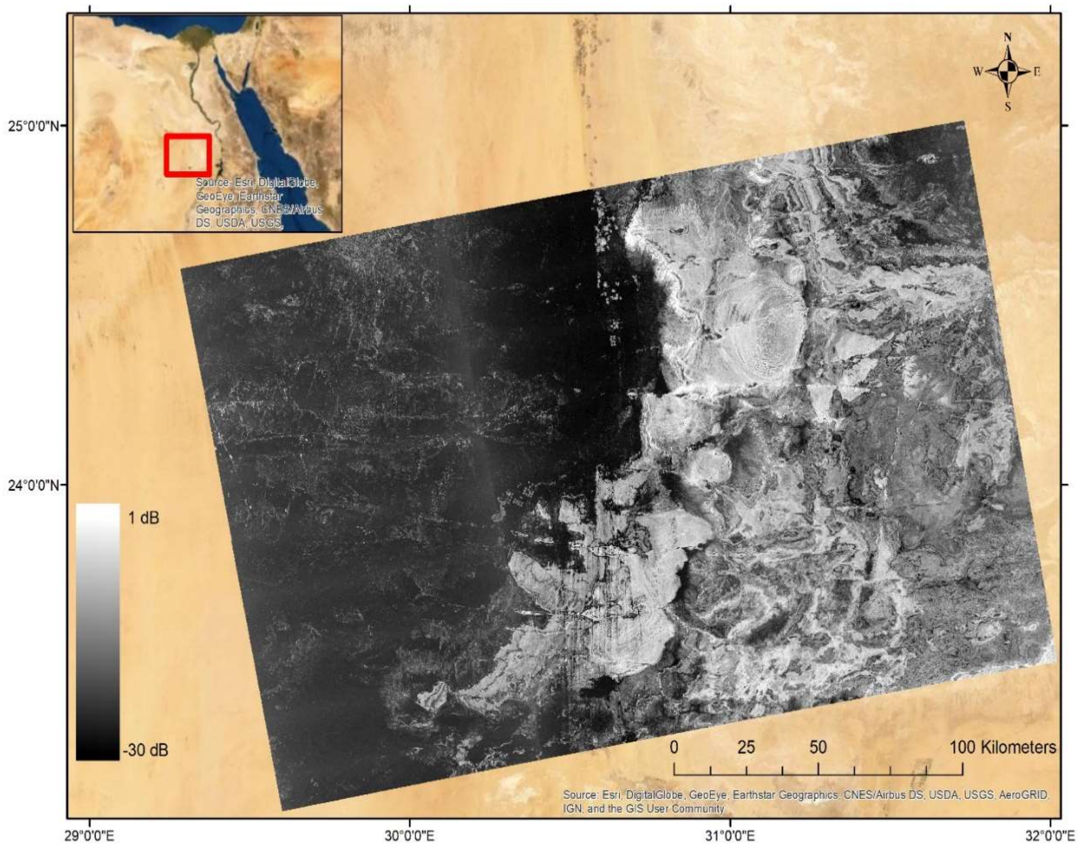

Figure 6.3: Sentinel-1 image over south Egypt. Date of acquisition 10/1/2020. The image is radiometrically corrected and ortho-rectified using ESA SNAP Sentinel-1 toolbox. The image was acquired from the ascending track number 131.

The area of higher backscatter within the scene likely reflects rock outcrop with moderate surface roughness where the surface reflection component is higher. In general, the very low backscatter in the western part of the image reflects very little surface and subsurface (volume) scattering. The area is very dry and therefore, the sand surface backscatter is very low and most of the radar signal penetrated the surface into the soil medium. In the absence of dielectric discontinuities within the soil medium, volume scattering is therefore, very low. As a result, clutter associated with surface and volume scattering is low, which offers the potential to achieve a high SCR if a subsurface feature is present here. Therefore, detection of buried targets in such a region is highly possible. Based on this, the Sahara Desert – and deserts with similar characteristics – appears to be an ideal candidate location for subsurface imaging using the SubSAR scheme, provided other conditions (e.g., moisture) are met. The characteristics of this desert region will be exploited for the real-world scenario that will be presented in Section 6.4.

6.3.2.1 **Signal propagation in desert soils**

In order to further evaluate the exploitation of SubSAR in desert regions, it is necessary to understand the behaviour of the radar signal propagation through the sandy soil. The process by which the radar signal propagates through the sand layer was previously explained in Chapter Three. To summarize, at the point of incidence between the radar wave and the soil surface, part of the signal will reflect (i.e., backscatter), while the remaining signal will penetrate into the soil. The amount of signal transmitted and reflected depends on the dielectric constant of the soil and the surface roughness. For simplicity, we will assume that the surface is smooth, and the reflected signal only depends on its dielectric constant. Then, according to Hallikainen *et al*. (1985), the dielectric constant of a soil depends on the soil moisture and radar wavelength. Accordingly, the combination of the moisture content of the sand and the radar wavelength are additional critical factors that can affect the detection of a buried feature using the SubSAR scheme. The behaviour of the two components of the radar signal – the amplitude and phase – in response to both soil moisture and wavelength therefore requires consideration.

a) Amplitude behaviour

The radar signal reflects from the surface of a bare soil through specular reflection or diffuse scattering. As above, we will consider the smooth surface case here for simplicity. The magnitude of the reflected signal was previously explained in Section 3.2 by the Fresnel reflection coefficient, which is characterised by the dielectric constant of the soil. As shown in Figure 3.2, the magnitude of the reflected energy increases as the dielectric constant of the soil increases. The reflected energy at low moisture content (low dielectric constant) is very low and hence the magnitude of the transmitted signal is high. The efficiency of the signal penetration is inversely related to the attenuation coefficient, as explained in Section 3.4.1. The attenuation is directly proportional to the dielectric constant of the soil and the target depth, and inversely related to the signal wavelength, as illustrated in Figures 3.12 and 3.13 (Section 3.5.2). Therefore, a signal with a longer wavelength can penetrate deeper into the medium with less attenuation. For example, a strong backscatter could be yielded from a target buried at depth 2 metres in a dry sand using L-band radar signal Elachi *et al.* (1984). Similarly, attenuation for targets at shallow depths is less than for deeper targets at the same moisture level and radar wavelength. Morrison *et al.* (2013) suggested that the attenuation increases linearly with increased soil moisture over a small moisture range, and this was confirmed by the results of the field experiment presented in Chapter Five.

b) Phase behaviour

The phase behaviour of the transmitted signal was previously explained in Section 3.4.1, and it was shown that the speed of the signal is reduced by a factor inversely related to the square root of the dielectric constant of the medium. The phase change of the two-way path between two dates, as represented by Morrison et al. (2012) is:

$$\Delta\phi = 2kd\{\sqrt{|\varepsilon_m|} - \sqrt{|\varepsilon_n|}\} \tag{6.1}$$

where $\Delta\phi$ is the two-way phase change of the transmitted signal, k represents the wavenumber, d is the subsurface target depth and ε_m, ε_n are the soil dielectric constant values at the two different times where the radar signal is transmitted into the soil. The phase change of a target buried in a sandy soil at depth = 5 cm is illustrated in Fig 6.4 for X-, C- and L-bands. Figure 6.4 illustrates that a small change in the soil moisture level over a buried target will lead to significant phase jumps when observed using a high frequency radar system. Without sufficiently frequent observations there is a risk of under-sampling and a 2π phase ambiguity problem will arise that could make the phase unwrapping a difficult task (Zebker *et al*. 1992). The phase of the longer radar wavelengths, such as C- and L-bands, is less sensitive to the soil moisture and the phase gradually changes in response to variations in the soil water contents. Ultimately, the preferential observation sampling frequency depends on the rate of soil moisture change and the SAR frequency. Nonetheless, the phase changes slowly with respect to the soil moisture at low radar frequency, meaning that less frequently observations can still be used to accurately characterise the phase change. This is particularly important with spaceborne SAR systems, where the number of observations is limited to the revisit period on the order of several days for current SAR satellites, as explained in Table 6.1.

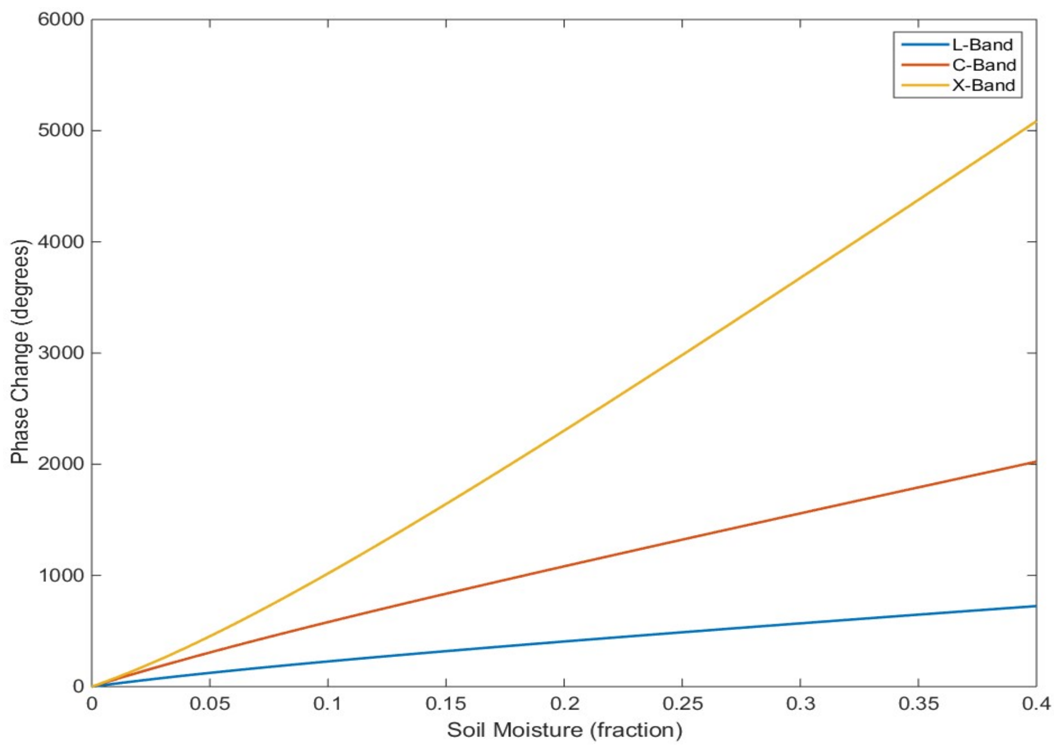

Figure 6.4: Phase change of a target buried in a sandy soil at depth = 5cm, as observed at three radar frequencies; X-, C-, and L-bands.

6.3.3 **Resolution and clutter**

The resolution of the SAR system is an essential factor in the subsurface imaging using the SubSAR scheme. The magnitude of the clutter received by the SAR system depends on the size of the resolution cell with respect to the size of the target. Low resolution systems have large resolution cells and therefore contain more sources of clutter than small resolution cells (i.e., high resolution systems). To illustrate this, the concept of SCR is typified in Figure 6.5. In the first case (Fig 6.5a), the point target (black square) occupies 25% of the resolution cell area, whereas the same target occupies only 0.25% of the other resolution cell (Fig 6.5b). The average background clutter in both resolution cells is similar. The SCR in this case can be estimated as (Freeman, 1992):

$$SCR = \frac{\sigma_T}{\langle \sigma_C^o \rangle \, . \, A_c} \tag{6.2}$$

where σ_T is the RCS of the point target, and σ^o_C is the ensembled average of clutter backscatter, and A_C is the illuminated area projected on the ground (the clutter area).

The SCR for a small-size resolution cell is typically many times higher than the SCR of the large-size resolution cell. For example, a metal structure which has the RCS of a metal plate with dimensions 0.5 x 0.5 m (could be part of a subsurface industrial structure that represents a flat plate reflector), has an RCS of 25 dBm^{-2}. The SCR is approximately 47 dB when observed with a high-resolution SAR system (1 x 1 m). However, the same target SCR would be decreased to 27 dB when observed with a low-resolution SAR system (10 x 10 m). Whereas the SCR for a distributed target is independent of the SAR resolution, as both the target and the clutter will fully occupy the resolution cell area.

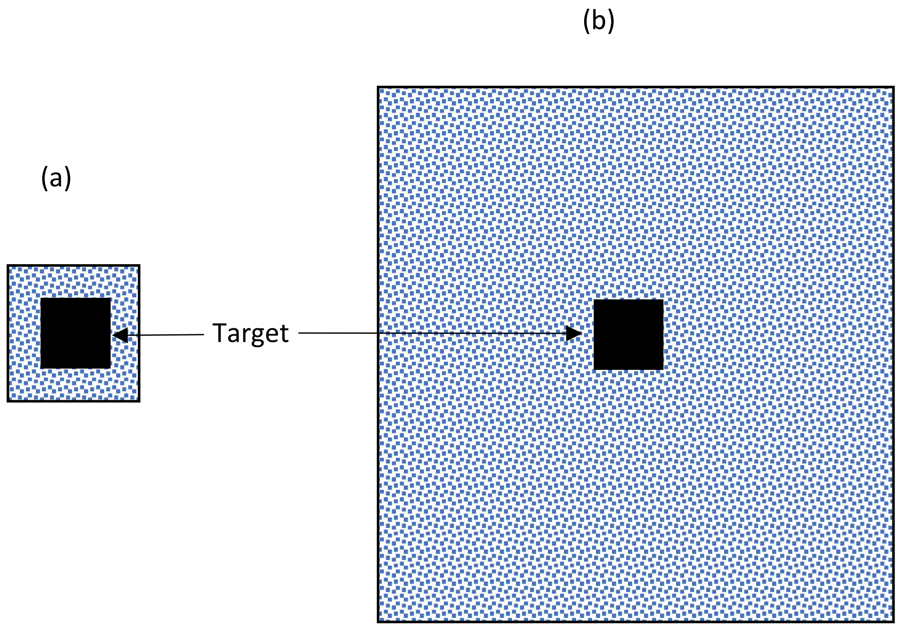

Figure 6.5: A point target (black square) occupies 25% of the resolution cell area of a high-resolution system (a) and the same target occupies 0.25% of the resolution cell of a low-resolution system (b). The blue dots in both cells represent the background clutter, where its average in both resolution cell is the same.

6.4 Implications for the real-world application of SubSAR

Considering all the information presented so far, this section discusses the key aspects of implementing the SubSAR scheme for a simulated real-world scenario. Before doing so, it is necessary to reiterate that SubSAR relies on a measuring the temporal phase and amplitude changes in response to variations in soil moisture across a temporal stack of co-registered DInSAR imagery.

This scenario considers two different buried targets, a point target and a distributed target. The point target is some undefined structure which has the equivalent RCS of a metal flat plate reflector of 25 dBm^{-2}. Whereas the distributed target is represented by a subsurface rocky layer, with a backscatter coefficient of 0 dBm^{-2}. Each of these targets is buried under a 5cm layer of homogeneous sandy soil, where the surface backscatter coefficient at dry soil condition is -22 dBm^{-2}. A C-band SAR satellite is observing the area at daily basis and acquiring data at an incidence angle of 35°. The spatial resolution of the SAR system is 20m (azimuth) x 5m (range). A theoretical soil moisture model is used in this simulation that provides daily measurements of the soil moisture over a period of 100 days.

As explained in Chapter 2, the radar signal return is the coherent addition of all the scatterers within the resolution cell. This would include the soil surface, and any subsurface return. For the proposed scenario, the surface is represented by a homogeneous sandy soil and the subsurface return is related to the buried target. If we assume the signal is entirely attributed to the surface return, and no subsurface targets are existing, then the intensity of the backscattered signal will be related to the dielectric constant of the soil (the water content). Whereas the surface phase of a non-expansive soil (such as the sandy soil) is not affected by the moisture and will remain stable at different moisture levels. The signal intensity is independent from the phase in this case and no meaningful information could be derived from analysing the phase-intensity relationship. In the following sections, two target types will be considered, a point target, representing an ideal case for subsurface imaging, and a distributed target, which would be the general case in most real-world applications.

a) *The buried target is a point target.*

An undefined structure which has the equivalent RCS of a metal flat plate reflector of 25 dBm^{-2} is assumed to be a buried target, that could be part of a subsurface industrial metal structure. Figure 6.7 illustrates the observations scenario of the buried point target.

The first plot represents the soil moisture measurements along the 100 days. The components of the target signal (the phase and intensity) are represented by the second plot from top. This signal is assumed to be driven solely from the buried target, excluding any surface return effects. Both the phase and the intensity of the subsurface target are responsive to the soil moisture variations and they are related to each other linearly. The third plot represents the surface signal excluding any subsurface return. The magnitude of the surface scattering increases linearly with soil moisture, whereas the phase is not affected by the moisture variations as the sand is non-expansive soil. In this case, the surface phase is assumed to remain zero at different moisture levels.

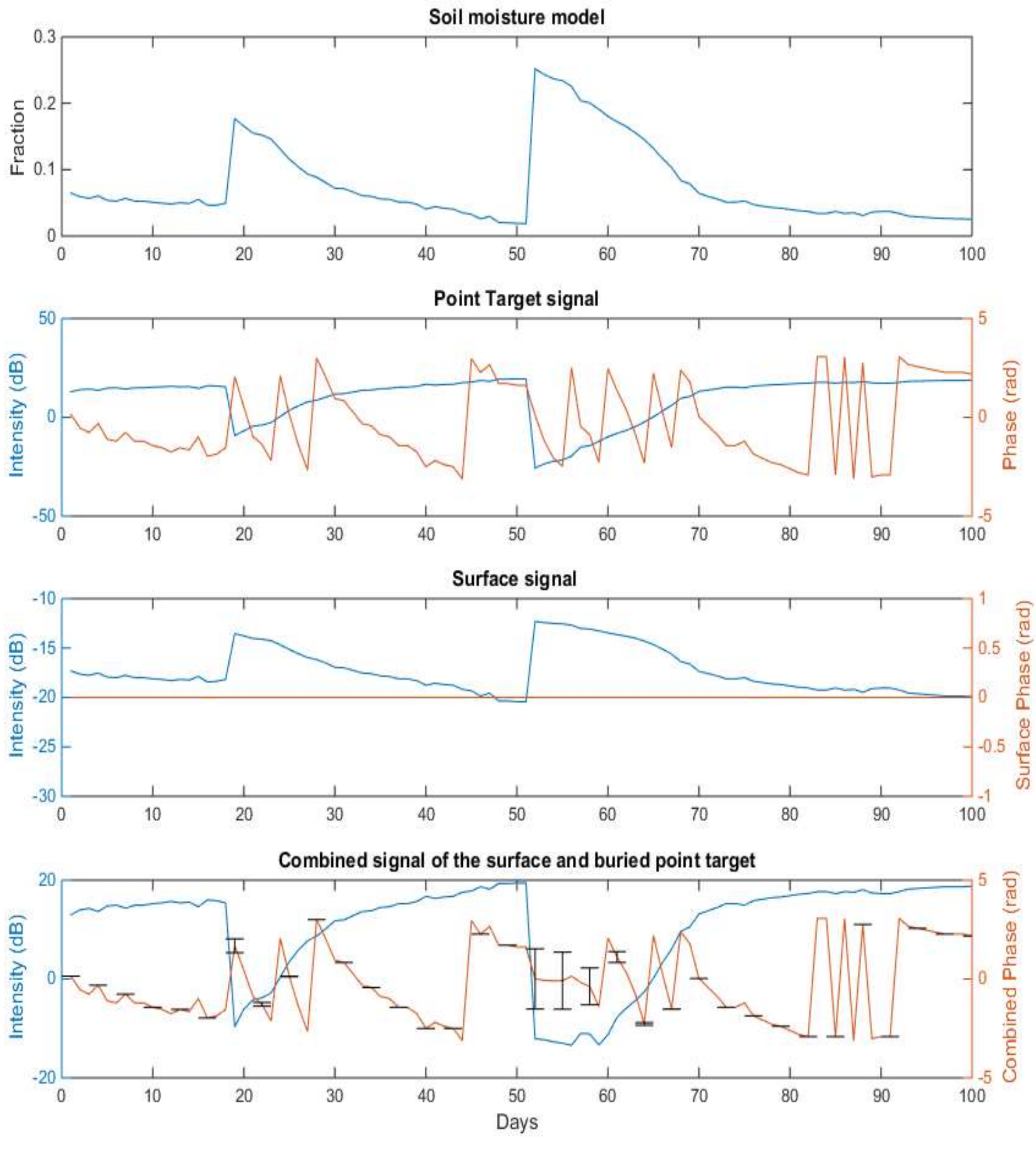

Figure 6.6: Real-world simulation scenario of a buried point target. The first graph from top represents a theoretical soil moisture model over a period of 100 days. The second graph from top represents the buried target signal, excluding any clutter effects form the surface. Third graph is the surface signal, excluding the subsurface target. The last graph is the coherent addition of the target and the surface signals, which represents the combined signal that will be observed by the SAR system. The phase error in the combined signal was estimated from the target and the surface signals and represented as black error bars.

The target and the surface signals are coherently added to obtain the combined signal, which represents the signal that will be observed by the satellite for the scene. This is represented by the last graph in Figure 6.6, and the error in the phase is represented by the vertical extent of the black bars. It can be noticed in this graph that the phase for the period between days 52 and 59 is close to zero, which corresponds to the same period of high soil moisture, indicating that the radar return is dominated by the surface signal, rather than the subsurface target. The error in the phase of the combined signal is proportional to the soil moisture, where the error increases as the soil moisture increases as well. Conversely, the combined phase for the periods between days 28 – 44 and 68 – 82 is gradually decreasing in response to drying soil in these periods, while the combined intensity for the same periods is gradually increasing. This is an indication that the signal is dominated by the subsurface return, rather than the soil surface.

Analysing the relationship between the phase and intensity of the observed signal could reveal important information about the origin of the signal. To understand that more, let us assume the observed signal is only originated from the buried target, and no surface return is included with the signal. The intensity – phase relationship in this case is linearly related to each other at different moisture levels (Figure 6.7). This graph will be called the SubSAR curve and will be used as an indicator to detect whether the signal is a subsurface target signal or not. This is an ideal graph derived merely from the target signal and will be used as a model for the phase unwrapping process that will be discussed later. In reality, however, that relationship will be derived from the combined signal where the surface signal will degrade the target influence in the overall signal, making the application of the SubSAR scheme a challenging task, as will be explained later. Figure 6.8 below illustrates three different observations scenario for the buried point target, assuming 1, 6, and 12 days revisit periods.

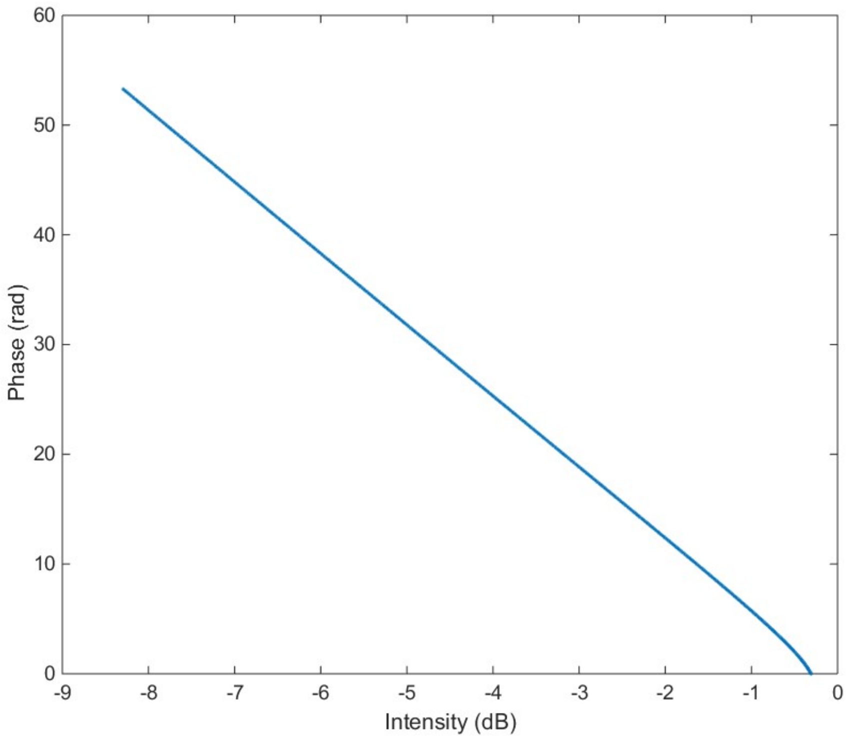

Figure 6.7: Intensity-Phase curve representing the SubSAR indicator. The phase of the subsurface target is increasing linearly with moisture, whereas the amplitude is decreasing with increasing moisture. Together, they can indicate whether the signal is a surface, or subsurface signal.

Each column in the figure below represents the observations at different revisit period, where the first column (left), represents the revisit period of 1 day, the second column (middle), represents the 6 days revisit scenario, and the last column (right), is the 12 days revisit period. The first figure in each column illustrates the observed phase of the scene, which is the phase of the combined (target and surface) signal. The second figure represents the observed intensity of the scene. While the last figure in each column represents the intensity – phase curve described above. The phase in this figure is the observed phase that represents the combined signal, which is a wrapped phase (modulo-2π) that needs to be unwrapped. The phase unwrapping can help to remove the existing phase ambiguities an it enables a meaningful interpretation of the data.

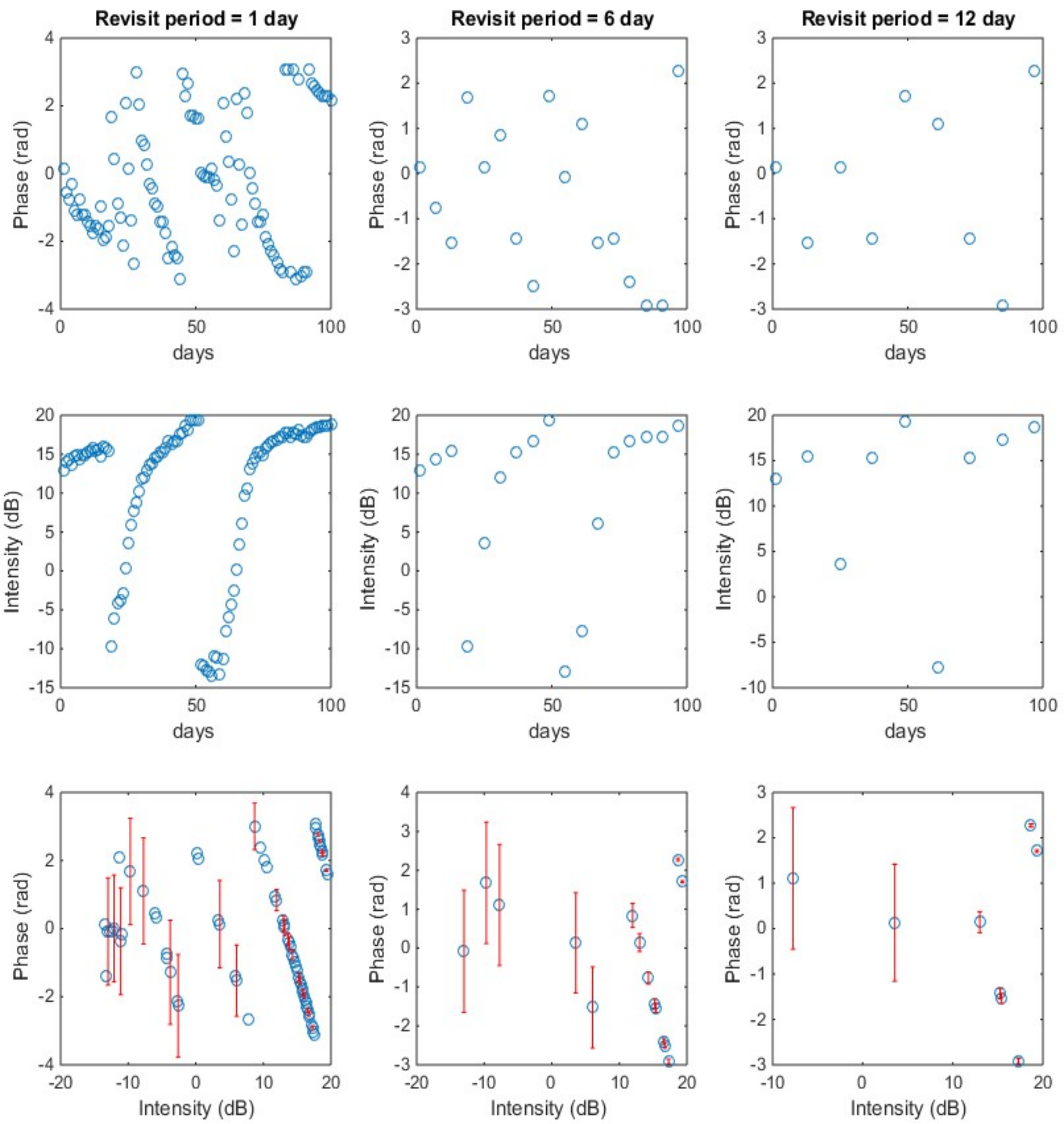

Figure 6.8: Observations at three different revisit periods. The first column from left represents a revisit period of 1 day, the second and third columns represent revisit periods of 6 and 12 days, respectively. The first and second rows from top represent the observed phase and intensity at different revisit periods, respectively. The last row is the intensity-phase curve.

The wrapped phases of the observed phase samples represented by the last row in Figure 6.8 can be unwrapped using the ideal amplitude -phase curve in figure 6.7 as a reference model. The intensity gradient from the ideal intensity-phase curve can be used to estimate the phase difference between each two successive measurements. This method can estimate phase jumps that are multiples of ±2π. If the observations are sparse, such as the case of 12 days revisit period (third column), phase aliasing problem occurs (Spagnolini, 1993), and the unwrapping could not be implemented correctly even with the help of the ideal intensity-phase curve.

b) The buried target is a distributed target.

The other types of target in this scenario is a distributed target which is represented by a subsurface rocky layer, with a backscatter coefficient of 0 dBm^{-2}. All the observations parameters are similar to that of the point target. Figure 6.9 represents the model observation scenario of the distributed target. The first graph in the figure represents the theoretical soil moisture model over the 100 days interval. The second graph represents the subsurface rocky layer signal, excluding any surface return. The third graph is the surface return, excluding any subsurface effects. While the last figure represents the combined signal of the surface and subsurface target. The phase error represented by the black error bars in the last graph, where it can be noticed that these error bars are larger at periods associated with high moisture levels, indicating the domination of the surface return on the overall signal. Figure 6.10 below illustrates the observations scenario at three different revisit periods, namely 1, 6, and 12 days. The structure of this figure is similar to Figure 6.8 above, where each column represents different revisit period, and the rows represent the intensity, phase, and the intensity-phase curve, respectively. For the daily revisit period, it is possible to reconstruct the full phase history by correctly unwrapping the combined phase, using the intensity-phase curve to estimate the phase jumps depending on the intensity-phase gradient. The phase unwrapping becomes a problem at sparse observations associated with the long revisit periods. In this case, acquiring data over a long period, such as a year or more worth of data, could provide sufficient phase observations and help the phase unwrapping problem.

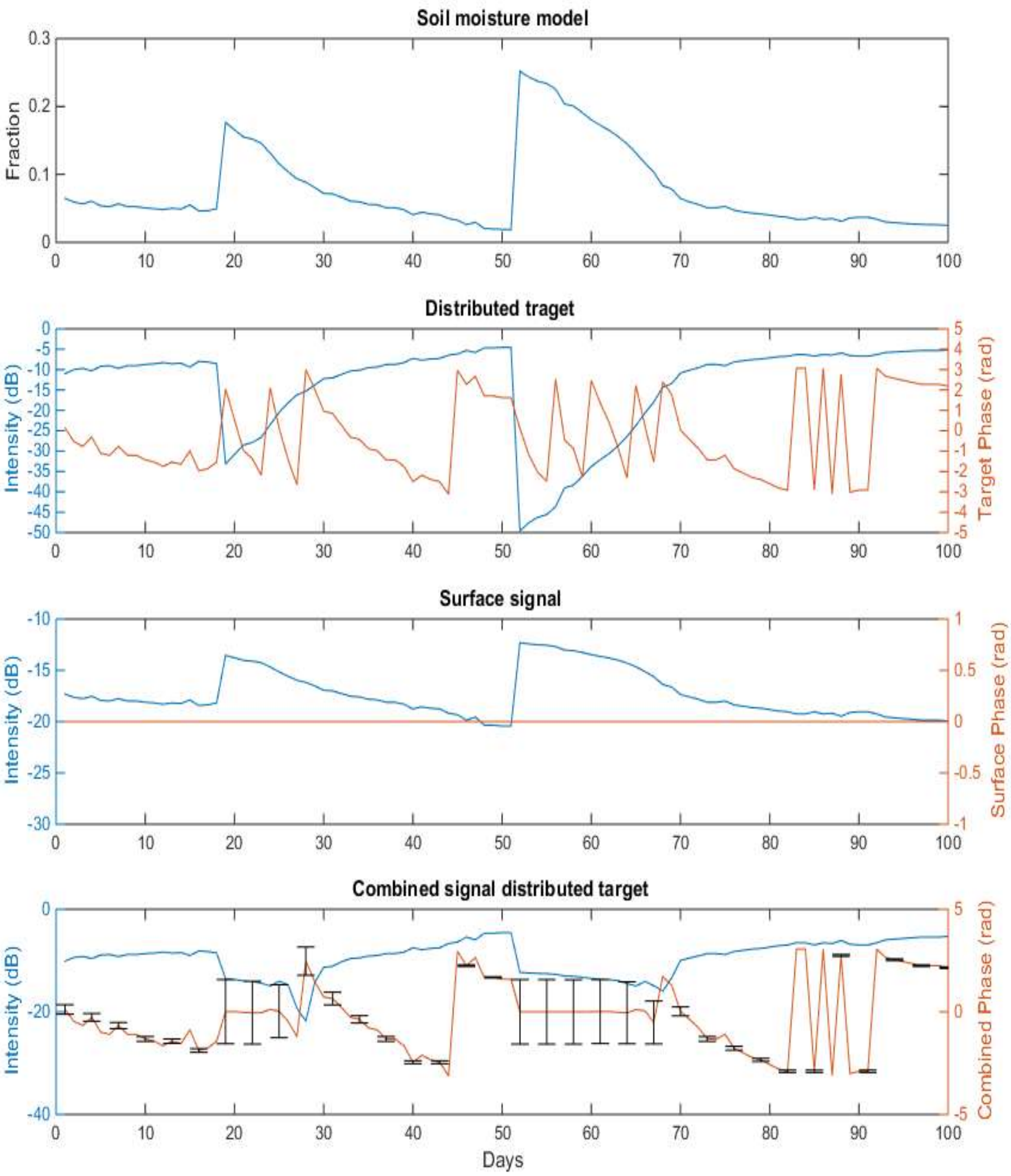

Figure 6.9: Real-world simulation scenario of a buried distributed target. The first graph from top represents a theoretical soil moisture model over a period of 100 days. The second graph from top represents the buried target signal, excluding any clutter effects form the surface. Third graph is the surface signal, excluding the subsurface target. The last graph is the coherent addition of the target and the surface signals, which represents the combined signal that will be observed by the SAR system. The phase error in the combined signal was estimated from the target and the surface signals and represented as black error bars.

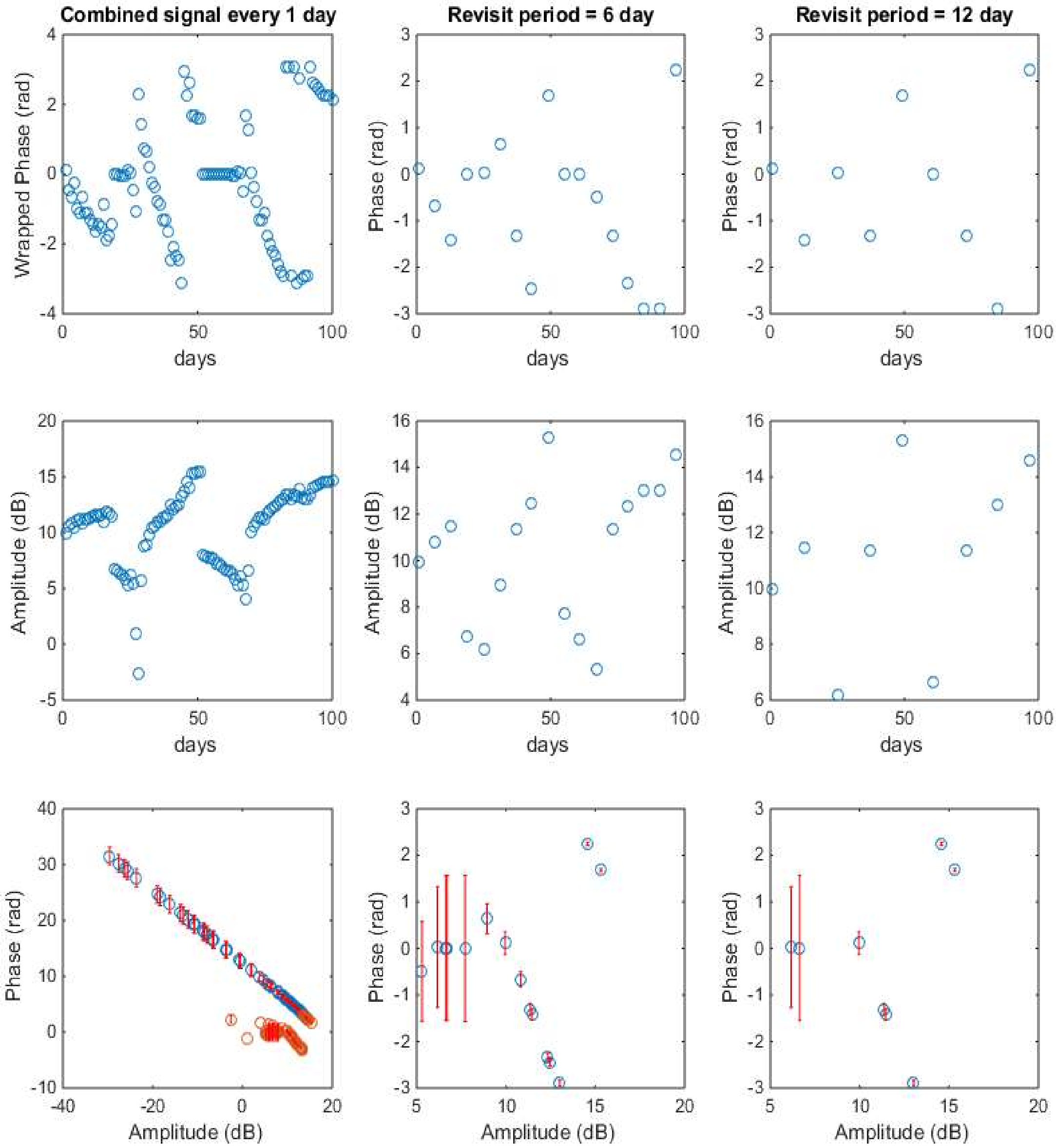

Figure 6.10: Real-world simulation scenario of a buried distributed target. The first graph from top represents a theoretical soil moisture model over a period of 100 days. The second graph from top represents the buried target signal, excluding any clutter effects form the surface. Third graph is the surface signal, excluding the subsurface target. The last graph is the coherent addition of the target and the surface signals, which represents the combined signal that will be observed by the SAR system. The phase error in the combined signal was estimated from the target and the surface signals and represented as black error bars.

This is the first step towards a practical SubSAR application that provides an initial discrimination between surface and subsurface signals, without the knowledge of the soil moisture. For this simulation, a theoretical soil moisture model is proposed, which in the real life could be obtained from field observations using a soil moisture sensor or can be obtained from weather data. Further investigations could be implemented to estimate the depth of the buried target if the soil moisture was precisely measured.

From the soil moisture, and with the knowledge of the soil type, the dielectric constant can be calculated from Hallikainen et al. (1985), and Equation 6.1 can be used to calculate the depth of the target. Similarly, the target depth can be estimated from the attenuation of the target signal, as the attenuation is a function of the soil moisture, radar frequency and target depth. The change in the attenuation between two observations (i.e., wet and dry measurements) can be used to estimate the target depth by reversing the attenuation equation. More advanced and accurate methods will depend on deriving the virtual bandwidth of the radar frequency shift as it passes through different moisture layers (Morrison et al., 2015). In most cases, especially for remote areas, soil moisture measurements are not available. In this case, the model can be implemented as discussed above by observing the intensity - phase relationship. For locations that do not include a subsurface target, this intensity - phase curve would be just a horizontal straight line where the phase is nearly stable, and the intensity varies whenever there is a change in the soil moisture. Otherwise, if the area contains a subsurface target, both the phase and intensity are responsive to the soil moisture changes and therefore, this curve will be comparable to the ideal curve of Figure 6.7.

6.3 Conclusions

This chapter considers primary factors that could affect the performance of the SubSAR scheme in the real-world. SubSAR is a promising scheme that has the potential to aid geological and archaeological explorations and for monitoring infrastructure such as buried pipelines and other man-made structures. A review of the current operational SAR satellites reveals that the entire globe is covered at regular periods from the three major radar bands (X-, C-, and L-bands). These satellites offer huge potential to detect buried targets globally. Ultimately, the selection of the SAR system for subsurface imaging depends on the characteristics of the buried target and the study area.

This chapter presented a real-world simulation scenario using two different buried targets, a point and distributed targets. This model described how the SubSAR scheme can be applied in the real world for subsurface feature detection. Three different revisit periods were considered to show how the sampling rate could affect the results. The main problem with the application of the SubSAR scheme is the phase unwrapping. For sparse observations, associated with long revisit period, there is only few phase samples that could prevent accurate phase unwrapping. Acquiring data over longer period in this case could mitigate this problem by providing more phase samples. An understanding of the backscatter-phase behaviour for subsurface targets provides a scheme for correctly unwrapping phase for sparse measurement scenarios.

No doubt, L-band SAR systems, such as ALOS-2, have many unique capabilities that could be successfully utilized for subsurface imaging in specific circumstances. For example, the penetration depth is the higher than the other two radar bands and L-band is less sensitive to the soil moisture variations (Hallikainen *et al.* 1985), which helps to reduce the 2π phase ambiguity. However, the revisit period for ALOS-2 is only 14 days and this may not be frequent enough to capture any variations in the phase and amplitude of the proposed buried target during a period of varying moisture conditions, such that spanning a rainfall event.

There are currently two satellite systems operating in the C-band, these are RADARSAT-2 and Sentinel-1. RADARSAT-2 offers high-resolution imagery of up to 1 m in Spotlight mode, which can reduce the clutter effects and improve the SCR of small targets. In contrast, the best Sentinel-1 resolution is 5 m in Stripmap mode, while in its usual Interferometric Wide Swath operating mode is it has a nominal resolution of 20 m x 5m. Nevertheless, Sentinel-1 offers an improved revisit period of 6 days using a constellation of the two satellites. Additionally, Sentinel-1 is the only operational satellite that offers regular global observations and the data is free of charge, which makes it readily accessibility for potential utilisation with the SubSAR approach.

Higher frequency SAR systems operating in the X-band usually have a higher spatial resolution. For example, TerraSAR-X and COSMO-SkyMed both have a spatial resolution of up to 1 m in specific imaging modes. This is very important for maintaining a high SCR, which is essential for image interpretation and subsurface target detection. However, the phase sensitivity of the X-band to the soil moisture is very high and frequent observations are required to capture the accurate phase change for different moisture levels.

Airborne SAR systems are of growing importance, in particular UAV systems. They can be operated anytime depending on the weather conditions and at different radar bands. They can be operated at daily or hourly rates to provide the desired temporal sampling to capture the detailed phase changes at different moisture levels. With the high-resolution capability and the very low NESZ, small targets such as buried mines and ordnance can be realistically detected, which could save human lives. Future spaceborne SAR systems could also offer daily to hourly revisit frequencies through constellations of SAR satellites such as ICEYE SAR constellation, which is planned to provide interferometric SAR observations globally every few hours.

With regards to environmental considerations, it is concluded that subsurface target detection using the SubSAR scheme is primarily restricted to arid areas that are devoid of vegetation. Therefore, sandy deserts soil represent ideal locations for the SubSAR, provided that SAR observations are acquired whenever there is a change in the soil moisture.

In keeping with the experiments conducted within this thesis, only point targets have been considered in this chapter. Further work is needed to test the applicability of the SubSAR scheme to detect buried distributed targets. In particular, this would include understanding how the distributed target affects the SCR under different soil moisture conditions and for different resolution and frequency SAR systems. This would help to understand the possibilities, constraints, and limits of the SubSAR scheme for buried distributed target detection. Future work can be extended to explore the different SAR platforms that are not covered in this thesis, such as airborne and UAV SAR systems which offer a higher spatial resolution, different acquisition frequency, and can be operated in different wavelengths that are not covered by the spaceborne SAR systems.

Chapter 7: Conclusions and Recommendations for Future Work

7.1 Summary

This thesis has tested the validity of the SubSAR laboratory technique for subsurface feature detection at field-scale using satellite SAR data. This chapter highlights the main elements of this thesis, beginning with a reflection of the aims and objectives of the research that were defined in Chapter One. Each objective is reviewed in turn, explaining how it was achieved and the main outcomes. The limitations of the study are also discussed, as are recommendations for future work to enhance the research.

7.2 Review of aims and objectives

The overall aim of this thesis was to implement the SubSAR technique for buried feature detection using satellite SAR data. Three specific research questions were then identified based on this aim:

4- Is it possible to use SubSAR to detect objects buried under a layer of sand from satellite SAR data?

5- What is the effect of the moisture content of the covering layer on the SAR signal?

6- What is the maximum soil moisture content that allows a measurable SAR signal to be detected from the buried target?

To answer the above research questions and achieve the overall thesis aim, several objectives were defined. Each of these is reviewed below.

Objective 1: *Design and implement a field-scale equivalent of the SubSAR laboratory experiment, which uses a network of corner reflectors as buried features during the satellite SAR overpass.*

The design of a field-scale equivalent to SubSAR laboratory experiments involved creating a set of radar point targets and covering them with a layer of sand to simulate buried targets. The following steps were implemented in sequence to achieve this particular objective:

A. Point target selection

CRs are typical radar point targets that are used for different applications. In this research, a trihedral CR design was selected to be used in the buried feature detection experiment. A trihedral CR was selected as it is the most practical device for SAR observations due to its low manufacturing cost, orientation flexibility, long term structural stability and high RCS relative to its small physical size. To ensure the accurate identification of the CR in the SAR image, the CR needed to have a high RCS with respect to the background. The RCS is defined by the size of the CR and the signal wavelength. However, the visibility of the CR in the SAR image is not only determined by its RCS, but is also affected by the background clutter level. Thus, for optimum results, the study area should be analysed before deciding the size of the reflector.

B. Study area selection

Bunny farm, located to the south east of Nottingham, was selected as the study site at which to implement the experiment. This experiment was planned to last for one year of observations and the CRs needed to maintain visibility in the SAR images throughout the entire experimental period. For this reason, this site was analysed for background clutter before constructing the CRs to determine the optimum size that will be used to maintain visibility in-situ. Variations in the backscatter of the study area were monitored for several months. Then, a set of CRs that have a RCS above the maximum observed background backscatter were designed in order to maintain the visibility at different times.

There were some restrictions associated with the use of this site for the experiment. Firstly, the CRs had to be installed in locations that do not disturb the farm machinery work. Additionally, concrete foundations were not permitted in the site, which were initially intended to be used to provide rigid base to support the CRs. Furthermore, the CR structures need to be removed upon conclusion of the experiment. Overcoming the first restriction required the identification of a suitable location for each CR with the help of the farm manager. When designing the CRs, a rigid and low-cost alternative for a concrete base was used to support the CR frame during the experiment, while ensuring that they were also readily removable afterwards. Steel barrels that are fixed to the ground with iron sticks, filled with crushed stones, are used as the bases for supporting the CRs to the ground. A total of 7 CRs were installed in the field and some of them were covered with a layer of sand to simulate buried targets during the Sentinel-1 SAR satellite overpasses.

Objective 2: *Test the quality and the validity of the experiment (radiometric stability, phase stability and accuracy). This is required to ensure that any change in the measured phase and backscatter is due to the variations in the soil moisture and not related to the stability of the CRs.*

The buried feature detection field experiment was designed to determine the effect of the covering sand moisture content on the visibility of the CRs from the SAR image. This requires analysing the behaviour of the phase and amplitude of the covered reflectors, with respect to the sand moisture. Therefore, an important quality check is to determine how stable are the CRs over time to identify whether the observed variations in these two components are associated with the buried simulation experiment or are due to the instability of the CRs.

Determining the radiometric stability of the CRs involved monitoring the backscatter of each CR on the occasions when the CR is un-covered. The aim of this analysis was to evaluate the radiometric quality of the CRs to determine their reliability for measuring the signal attenuation in the buried feature experiment. This analysis revealed that one of the CRs in the network (CR4) was clearly radiometrically unstable, with mean σ of 15.46 ± 11.46 dB. Such a low mean and large variation in σ is an indication that this particular CR was accidentally damaged during installation or at some point during the experiment. Owing to this high instability, CR4 was not deemed suitable to be used in the buried target experiment and was therefore excluded from any further analysis. This is because of the difficulty in isolating the contribution of the CR instability from the effects of moisture content on the RCS. The other 6 CRs were found to be relatively stable in time, with mean backscatter of >24 dB.

The second part of the check conducted prior to starting the experiment was that of the quality of Sentinel-1 interferometric phase. This is vital to ensure that any detected change in the phase is due to the sand moisture content of the buried feature. Analysing the DInSAR phase of the CR network showed that all the CRs were reasonably stable. The average relative motion of any CR was less than 1.4 rad for the test period, which is equivalent to 6 mm in the LOS. The oscillation of the phase was less than 0.8 rad for all the reflectors, which confirms the relative stability of the CRs.

Results of the radiometric and interferometric stability tests confirmed the validity of the designed experiment for the SubSAR field experiment, and any observed variations in the backscatter or the DInSAR phase can be solely related to changes in the water content of the sand layer in the buried feature detection experiment.

Objective 3: *Investigate the variations of both the backscatter and phase of the buried features while the water content of the sand layer is varied, to be able to derive a* *relationship between these two factors and the amount of the water content change.*

After testing the validity of the experiment, field observations were made by covering some of the CRs with sand layers of known water content during each satellite overpass. Variable water content levels were used in the experiment to cover the broadest possible range of moisture levels, which were between dry sand (~0%) and 10%. The total number of observations was 50 from four CRs used in the experiment. As the only variable in these buried observations was the sand moisture, any change in the backscattered and phase was related to the variations in the sand moisture. Both the amplitude and the phase of the buried CRs were analysed to find how they are affected by varying water content. The results are summarised below:

A. Amplitude analysis

The backscatter of the CRs was analysed for both the un-covered and buried observations. There was a clear reduction in the observed backscatter of the buried CRs, due to signal attenuation when passing through the sand layer. Quantitative analysis of the backscatter attenuation with the corresponding soil moisture enabled a relationship to be established between the two variables. This was in the form of a linear relationship with coefficient of determination (R^2) of 0.9. This is in good agreement with the laboratory simulation results where a linear relationship between the sand cover moisture content and the backscatter attenuation is found to be linear as well.

B. DInSAR phase analysis

The DInSAR phase of the CRs was also monitored throughout the experimental period for the un-covered and buried observations. For the un-covered observations, the DInSAR phase was fairly stable over time with minor oscillations of less than 1 rad. However, upon burial, there was a clear shift in the phase of each buried CR. In general, the LOS distance between the buried CR and the SAR satellite appeared longer by the amount of the signal delay caused by passing through the sand-water mixture. Thus, the CR appeared to be subsiding with respect to the reference point. In other words, as the sand moisture increases, the phase shift increases. The phase shifts with respect to the corresponding sand moisture were quantified and a linear relationship was clearly observed between the two variables, with an R^2 of 0.87. The DInSAR phase results come to an agreement with the SubSAR experimental results by Morrison et al. (2013).

7.3 Limitations and recommendations

From the results presented here, it can be concluded that SubSAR is a valid technique for detecting features buried under a thin layer of sand using Sentinel-1 SAR data. In summary, if the water content of the sand cover is known, a buried feature can be detected by monitoring the behaviour of one of the SAR image components – backscatter or the DInSAR phase history – in relation to changes in the sand moisture content. Nonetheless, it is also important to consider the limitations associated with the key stages of the experiment approach implemented in this study.

7.3.1 Background clutter analysis

As part of the CR design stage, it was necessary to design a CR that maintains visibility throughout the experimental period. Therefore, the backscatter of the study area was monitored to find the maximum backscatter value in each proposed CR location. Once the maximum value was identified, the CR was designed to have an RCS that is higher than that value by a specific threshold. A limitation in this study concerns the length of monitoring period.

Due to the limited time in the field experiment period, it was only possible to monitor the study area for six months, which may not be sufficient to fully characterise the annual scattering behaviour of some study areas. Therefore, in any future experiment, it is recommended to monitor the site for a whole year for a better insight of the seasonal changes in the backscatter of a chosen study area. This will subsequently help to achieve a CR design that maintains visibility in the SAR image at any time of the year.

7.3.2 CR stability monitoring

Three tests were implemented to ensure the validity of the experiment; these are the radiometric and interferometric stability monitoring, and interferometric phase accuracy. These three tests are crucial in ensuring that the observed changes in the phase and backscatter of the buried CRs in the buried feature experiment result from covering the CRs with the sand layers, and are not due to instability in the CRs.

7.3.2.1 Radiometric stability

For the radiometric stability evaluation, the RCS for each CR was computed from each Sentinel-1 SAR image acquired when the CRs were not covered with sand layers. Analysing the backscatter variation for each CR enabled the identification the one CR (i.e. CR4) that was unstable during the experiment. This CR was not used in the later experiments due to the difficulties in isolating the contribution of the CR instability from the effects of moisture content on the RCS. Accordingly, for this purpose an evaluation of the radiometric stability should be considered essential for any future experiments of this kind.

7.3.2.2 Interferometric stability

Monitoring the interferometric phase of the CRs for the images where the CRs were un-covered is vital to ensure that it is possible to detect, with high precision, any change in the phase due to the sand cover in the buried feature detection experiment. The results obtained here showed that all CRs were reasonably stable, with average motion of less than 1.4 rad (< 6mm). Unfortunately, it was not possible to verify this through surveying campaigns due to difficulties related to the experimental site and the localities of the CRs within the site. For future work, it is highly recommend to conduct precise levelling campaigns at regular intervals. Installing a network of levelling bench marks in the field would help the surveying campaigns.

7.3.2.3 Interferometric phase accuracy

Interferometric phase monitoring provided a measure of the stability of the CRs. Since regular and precise field surveying was not possible for all the CRs, the validity of the processing methods and sensitivity of Sentinel-1 to detect the relative displacement between the CRs was tested and validated using a total station. The position of CR1 was altered by a few centimetres twice during the experiment. These displacements were precisely measured by a total station and were projected to the satellite LOS. The displacements are then estimated from the interferometric processing and compared with the total station measurements. It was found that the two sets of observations (InSAR and total station) are agreeable with mean discrepancy of -1.95 mm. This is a confirmation that Sentinel-1 interferometric observations can be used with confidence to detect millimetric displacement in the CR positions. This means that the observed phase changes in the buried target detection are indeed related to the sand cover and not the CR instability. This test is very important to estimate the accuracy of Sentinel-1 InSAR observations. However, it is recommended that such a test is implement over the whole network and for multiple displacements instead of only two as undertaken in this study.

7.4 Buried feature detection using satellite SAR

The main experiment in this thesis involved the field-scale application of SubSAR technique. The overall concept of the experiment was that a Sentinel-1 C-band signal is incident upon a sand layer, which acts as a medium through which the signal will propagate and be reflected by the CR back through the sand layer to the SAR antenna. The interferometric phase and the backscatter of the CRs were monitored for the buried and un-covered observations. Using the known scattering characteristics of the CRs, the backscatter for the buried observations were compared with the mean backscatter of the un-covered observations for each CR, and the change in the backscatter (attenuation) was quantified with respect to the moisture content of the sand layer. A linear relationship was estimated between the sand moisture and the attenuation, which confirms the laboratory experiment results (Morrison et al. 2013). The CR could not be identified in the SAR image at 10% sand moisture, whereas it was still possible to measure the attenuation in the laboratory for a moisture content up to 20%. With respect to the phase change, a linear relationship between the sand moisture and the phase change also confirmed the results of the SubSAR laboratory experiments.

Overall, the results of the backscatter and the DInSAR analysis confirm the validity of the SubSAR technique for application satellite SAR-based subsurface feature detection. If the moisture content of the sand cover is known, then either of the two SAR components (backscatter and phase) can be used to detect the buried feature, along with the moisture content. For the backscatter component, if a negative relationship between the backscatter and the soil moisture is present, then this is an indication of a signal from a buried feature. In contrast, for surface scattering signal, there is a positive relationship between the soil moisture and the backscatter. Similarly, a positive relationship between the sand moisture and the DInSAR phase is an indication of a buried feature, in converse to a negative relationship for surface reflection.

The two indicators for buried feature detection each rely upon soil moisture being measured concurrently with the SAR observations. This means an external source of information is required for the subsurface imaging, which can be impractical as it is difficult to obtain soil moisture measurements, concurrent with the SAR satellite overpass in remote areas for real life applications. However, it is possible to detect buried features without the need for soil moisture measurements if both the backscatter and the DInSAR phase observations are used together. For surface reflection from sandy soil, there is a negative relationship between the backscatter and the phase. That is as the sand moisture increases, the backscatter also increases while the DInSAR phase decreases. Conversely, if the relationship between the backscatter and DInSAR phase is reversed (i.e. a positive relationship), then this is an indication of a buried feature signal. Although not required, if moisture content measurements are available, these can be used to confirm the observations made using SubSAR.

The possibility of detecting buried features from satellite SAR data only – without the need for ancillary information such as soil moisture content – is valuable for analysing wide areas for anomalies in the phase-backscatter relationship. Such anomalies may indicate the presence of a buried features. This potentially has significant implications for real world applications of buried feature detection, such as identifying landmines and pipeline routing. However, SubSAR has some limitations in terms of the soil type, water content levels, and depth to feature. Currently, the technique is only tested for pure sand soil in both laboratory and field experiments, which is only applicable to certain parts of the world, i.e., deserts. With respect to the soil moisture, it was found that at 10% moisture content, Sentinel-1 signal cannot penetrate 1cm sand layer. Therefore, lower soil moisture levels are preferred to detect buried features, which means that this method is suitable to areas of low moisture content. Additional experiments are recommended to test the possibility to detect buried features at different depths.

7.5 Suggested future work

Following the above discussion, the current research could be enhanced in the future by focussing on the following aspects:

1- Testing variable depths of sand and a wider range of moisture content to gain a better understanding of the signal-depth relationship.

2- Using more CRs; the data availability of both Sentinel-1 A and B, means that a greater number of observations, even with the same period of the current experiment, can be achieved.

3- Testing the SubSAR technique using different SAR wavelengths, i.e. L-band, which has a better penetration capabilities and more practical uses.

Summary

This thesis has tested the validity of the SubSAR technique of buried feature detection using Sentinel-1 SAR data. A field-scale experiment, equivalent to the SubSAR laboratory experiment, was designed. The experiment involved establishing a network of seven CRs, and cover some of them with a 1-cm layer of sand to simulate buried targets. The sand moisture was variable with each satellite overpass and the effect of the sand layer on the satellite signal is analysed. It was found that Sentinel-1 can penetrate the sand layer and detect the buried CRs at different moisture levels. As the sand moisture change between the observations, the variations in the backscatter and the DInSAR phase were monitored. A linear relationship between the backscatter attenuation and the sand moisture is derived and a similar relationship between the phase and the sand moisture is derived as well. SubSAR is concluded to be a valid technique for buried feature detection using satellite SAR data. This technique can be easily applied in real-life applications by monitoring the phase-backscatter relationship only, without the need for soil moisture measurements. For surface observations (i.e. desert sand surface), there is a positive relationship between these two observables. While if there is a buried feature, this relationship is negative. Therefore, monitoring wide-area for any anomalies in the phase-backscatter relationship is an easy way to detect possible buried features.

References

Atwood, W. C. (1952). Dielectric horn, Google Patents.

Bovenga, F., et al. (2012). Using corner reflectors and X-band SAR interferometry for slope instability monitoring. Advances in Radar and Remote Sensing (TyWRRS), 2012 Tyrrhenian Workshop on, IEEE.

Brown, W. M. and L. J. Porcello (1969). "An introduction to synthetic-aperture radar." IEEE spectrum **6**(9): 52-62.

Bussey, H. E. (1960). "Standards and measurements of microwave surface impedance, skin depth, conductivity and Q." IRE Transactions on Instrumentation **1**(2): 171-175.

Carver, K.R., Elachi, C. and Ulaby, F.T., 1985. Microwave remote sensing from space. *Proceedings of the IEEE*, *73*(6), pp.970-996.

Cihlar, J. and F. T. Ulaby (1974). "Dielectric properties of soils as a function of moisture content."

Cognard, A. L., et al. (1995). "Evaluation of the Ers-1 Synthetic Aperture Radar Capacity to Estimate Surface Soil-Moisture - 2-Year Results over the Naizin Watershed." Water Resources Research **31**(4): 975-982.

Cohen, I. B. (1940). "The First Explanation of Interference." American Journal of Physics **8**(2): 99-106.

Curlander, J. C. (1982). "Location of spaceborne SAR imagery." IEEE Transactions on Geoscience and Remote Sensing(3): 359-364.

Curlander, J. C. and R. N. McDonough (1991). Synthetic aperture radar, John Wiley & Sons New York, NY, USA.

Cutrona, L. J., et al. (1961). "A high-resolution radar combat-surveillance system." IRE Transactions on Military Electronics **1051**(2): 127-131.

De Leeuw, M. R. and L. M. T. de Carvalho (2009). "Performance evaluation of several adaptive speckle filters for SAR imaging." Anais XIV Simpósio Brasileiro de Sensoriamento Remoto: 7299-7305.

Dobson, M. C., et al. (1985). "Microwave dielectric behavior of wet soil-Part II: Dielectric mixing models." IEEE Transactions on Geoscience and Remote Sensing(1): 35-46.

Dubois, P. C., et al. (1995). "Measuring soil moisture with imaging radars." IEEE Transactions on Geoscience and Remote Sensing **33**(4): 915-926.

Elachi, C. (1987). "Spaceborne imaging radar research in the 1990 s: An overview." Johns Hopkins APL Technical Digest **8**(1): 60-64.

Elachi, C., et al. (1982). "Spaceborne synthetic-aperture imaging radars: Applications, techniques, and technology." Proceedings of the IEEE **70**(10): 1174-1209.

Elachi, C., Brown, W.E., Cimino, J.B., Dixon, T., Evans, D.L., Ford, J.P., Saunders, R.S., Breed, C., Masursky, H., McCauley, J.F. and Schaber, G. (1982). "Shuttle imaging radar experiment. Science." Science **218**(4576): 996-1003.

Engheta, N. and Elachi, C., 1982. Radar scattering from a diffuse vegetation layer over a smooth surface. *IEEE Transactions on Geoscience and Remote Sensing*, (2), pp.212-216.

Engman, E. T. (1995). "Microwave remote sensing of soil moisture, progress, potential and problems." **1**: 489-491.

ESA (2013). Sentinel-1 User Handbook.

Européenne, A. s. (2012). Sentinel-1: ESA's Radar Observatory Mission for GMES Operational Services, ESA communications production.

Evans, D. L., et al. (1992). "Radar interferometry studies of the Earth's topography." Eos, Transactions American Geophysical Union **73**(52): 553-558.

Evett, S., et al. (2008). "Field estimation of soil water content: A practical guide to methods, instrumentation and sensor technology. IAEA-TCS-30. Int." Atomic Energy Agency p **131**.

Farr, T. G., et al. (1986). "Microwave penetration and attenuation in desert soil: a field experiment with the Shuttle Imaging Radar." IEEE Transactions on Geoscience and Remote Sensing(4): 590-594.

Farr, T. G. and M. Kobrick (2000). "Shuttle Radar Topography Mission produces a wealth of data." Eos, Transactions American Geophysical Union **81**(48): 583-585.

Ferretti, A. (2014). Satellite InSAR data: reservoir monitoring from space, EAGE publications.

Ferretti, A., et al. (2007). "InSAR Principles: Guidelines for SAR Interferometry Processing and Interpretation." TM 19 A, B, C.

Ferretti, A., et al. (2007). "Submillimeter accuracy of InSAR time series: Experimental validation." IEEE Transactions on Geoscience and Remote Sensing **45**(5): 1142-1153.

Franz Leberl, et al. (1976). "Side-looking radar mosaicking experiment." Photogrammetric Engineering and Remote Sensing **42**(8).

Frey, O., Magnard, C., Ruegg, M. and Meier, E., 2009. Focusing of airborne synthetic aperture radar data from highly nonlinear flight tracks. IEEE transactions on geoscience and remote sensing, 47(6), pp.1844-1858.

Frost, V. S., et al. (1982). "A model for radar images and its application to adaptive digital filtering of multiplicative noise." IEEE Transactions on pattern analysis and machine intelligence(2): 157-166.

Gabriel, A. and R. Goldstein (1988). Crossed orbit interferometry. Geoscience and Remote Sensing Symposium, 1988. IGARSS'88. Remote Sensing: Moving Toward the 21st Century., International, IEEE.

Gabriel, A. K. and R. M. Goldstein (1988). "Crossed orbit interferometry: theory and experimental results from SIR-B." International Journal of Remote Sensing **9**(5): 857-872.

Gabriel, A. K., et al. (1989). "Mapping small elevation changes over large areas: differential radar interferometry." Journal of Geophysical Research: Solid Earth **94**(B7): 9183-9191.

Gamo, M., Shinoda, M. and Maeda, T., 2013. Classification of arid lands, including soil degradation and irrigated areas, based on vegetation and aridity indices. *International journal of remote sensing*, *34*(19), pp.6701-6722.

Gaur, M.K. and Squires, V.R., 2018. Geographic extent and characteristics of the world's arid zones and their peoples. In *Climate variability impacts on land use and livelihoods in drylands* (pp. 3-20). Springer, Cham.

Ge, D. Q., et al. (2011). "Integrating Corner Reflector and Psinsar Technique to Monitor Regional Land Subsidence." 2011 Ieee International Geoscience and Remote Sensing Symposium (Igarss): 1619-1622.

Gee, D., Sowter, A., Novellino, A., Marsh, S. and Gluyas, J., 2016. Monitoring land motion due to natural gas extraction: Validation of the Intermittent SBAS (ISBAS) DInSAR algorithm over gas fields of North Holland, the Netherlands. Marine and Petroleum Geology, 77, pp.1338-1354.

Geiger, F. and D. Williams (1972). "Dielectric constants of soils at microwave frequencies."

Ghiglia, D. C. and M. D. Pritt (1998). Two-dimensional phase unwrapping: theory, algorithms, and software, Wiley New York.

Goldstein, G., et al. (1988). "Satellite radar interferometry: Two-dimensional phase unwrapping." Radio science **23**(4): 713-720.

Goodman, J. W. (1976). "Some fundamental properties of speckle." JOSA **66**(11): 1145-1150.

Graham, L. C. (1974). "Synthetic interferometer radar for topographic mapping." Proceedings of the IEEE **62**(6): 763-768.

Gray, A. L. and P. J. Farris-Manning (1993). "Repeat-pass interferometry with airborne synthetic aperture radar." IEEE Transactions on Geoscience and Remote Sensing **31**(1): 180-191.

Grebby, S., Orynbassarova, E., Sowter, A., Gee, D. and Athab, A., 2019. Delineating ground deformation over the Tengiz oil field, Kazakhstan, using the Intermittent SBAS (ISBAS) DInSAR algorithm. International Journal of Applied Earth Observation and Geoinformation, 81, pp.37-46.

Griffiths, H., et al. (2014). Stimson's introduction to airborne radar, Scitech Pub Incorporated.

Hallikainen, M. T., et al. (1985). "Microwave dielectric behavior of wet soil-part 1: Empirical models and experimental observations." IEEE Transactions on Geoscience and Remote Sensing(1): 25-34.

Hanssen, R. F. (2001). Radar interferometry: data interpretation and error analysis, Springer Science & Business Media.

Hertz, H. (1893). Electric waves: being researches on the propagation of electric action with finite velocity through space, Dover Publications.

Hoekstra, P. and A. Delaney (1974). "Dielectric properties of soils at UHF and microwave frequencies." Journal of geophysical research **79**(11): 1699-1708.

Hogg, I.D. and Wall, D.H., 2012. Polar deserts. *Life at extremes: environments, organisms and strategies for survival*, pp.176-195.

Holtzman, J. C., et al. (1978). "Radar image simulation." IEEE Transactions on Geoscience Electronics **16**(4): 296-303.

Horn, R., Nottensteiner, A. and Scheiber, R., 2008, June. F-SAR-DLR's advanced airborne SAR system onboard DO228. In 7th European Conference on Synthetic Aperture Radar (pp. 1-4). VDE.
Hulsmeyer, C. (1904). "The Telemobiloscope." Electrical Magazine **2**: 388.

Jordan, R. L. (1980). "The Seasat-A synthetic aperture radar system." IEEE Journal of Oceanic Engineering **5**(2): 154-164.

Just, D. and R. Bamler (1994). "Phase statistics of interferograms with applications to synthetic aperture radar." Applied optics **33**(20): 4361-4368.

Kadlečík, P., et al. (2015). "Evaluation of the subsidence based on dInSAR and GPS measurements near Karvina, Czech Republic." AUC Geographica **50**(1): 51-61.

Karam, M. A., et al. (1992). "A microwave scattering model for layered vegetation."

King, D. (1949). "The measurement and interpretation of antenna scattering." Proceedings of the IRE **37**(7): 770-777.

Knott, E. F. (2012). Radar cross section measurements, Springer Science & Business Media.

Kozlov, A.I., Ligthart, L.P. and Logvin, A.I., 2007. *Mathematical and physical modelling of microwave scattering and polarimetric remote sensing: monitoring the Earth's environment using polarimetric radar: formulation and potential applications* (Vol. 3). Springer Science & Business Media.

Laity, J.J., 2009. *Deserts and desert environments* (Vol. 3). John Wiley & Sons.

Lal, R. (1990). Soil erosion in the tropics: principles and management, McGraw-Hill Inc.

Lewis, A. J. and H. C. Macdonald (1970). "Interpretive and mosaicking problems of SLAR imagery." Remote Sensing of Environment **1**(4): 231-236.

Li, F. K. and R. M. Goldstein (1990). "Studies of multibaseline spaceborne interferometric synthetic aperture radars." IEEE Transactions on Geoscience and Remote Sensing **28**(1): 88-97.

Lillesand, T., et al. (2014). Remote sensing and image interpretation, John Wiley & Sons.

Lockhart, J. A. R. and A. J. L. Wiseman (2012). Introduction to crop husbandry: including grassland, Elsevier.

Nolan, M. and Fatland, D.R., 2003. Penetration depth as a DInSAR observable and proxy for soil moisture. *IEEE Transactions on Geoscience and Remote Sensing*, *41*(3), pp.532-537.

MacDonald, H. and A. Lewis (1976). "Operation and characteristics of imaging radar systems." Remote Sensing Electro Magnetic Spectrum **3**: 23-45.

Marinkovic, P., et al. (2007). InSAR quality control: Analysis of five years of corner reflector time series. Proceedings of Fringe 2007 Workshop (ESA SP-649), Frascati, Italy.

Marshall, C., Large, D.J., Athab, A., Evers, S.L., Sowter, A., Marsh, S. and Sjögersten, S., 2018. Monitoring tropical peat related settlement using ISBAS InSAR, Kuala Lumpur International Airport (KLIA). Engineering Geology, 244, pp.57-65.

Massonnet, D. and K. L. Feigl (1998). "Radar interferometry and its application to changes in the Earth's surface." Reviews of geophysics **36**(4): 441-500.

Massonnet, D., et al. (1993). "The displacement field of the Landers earthquake mapped by radar interferometry." Nature **364**(6433): 138.

McCauley, J. F., et al. (1982). "Subsurface valleys and geoarcheology of the eastern Sahara revealed by shuttle radar." Science **218**(4576): 1004-1020.

Merrill, I. S. (1990). "Radar handbook." John Wiely.

Merrill, I. S. (1990). Radar handbook.

Merrill, I. S. (2001). "Introduction to radar systems." Mc Grow-Hill: 607-609.

Miranda, N., et al. (2017). The Sentinel-1 constellation mission performance. Geoscience and Remote Sensing Symposium (IGARSS), 2017 IEEE International, IEEE.

Miranda, N., et al. (2015). "Radiometric Calibration of S-1 Level-1 Products Generated by the S-1 IPF." Viewed at https://sentinel. esa. int/documents/247904/685163/S1-Radiometric-Calibration-V1. 0. pdf.

Mo, T., Schmugge, T.J. and Jackson, T.J., 1983. Calculations of radar backscattering coefficient of vegetation-covered soils.

Moore, R. and G. Thomann (1971). "Imaging radars for geoscience use." IEEE Transactions on Geoscience Electronics **9**(3): 155-164.

Morrison, K., et al. (2013). "Using DInSAR to separate surface and subsurface features." IEEE Transactions on Geoscience and Remote Sensing **51**(6): 3424-3430.

Morrison, K., et al. (2011). "Laboratory measurement of the DInSAR response to spatiotemporal variations in soil moisture." IEEE Transactions on Geoscience and Remote Sensing **49**(10): 3815-3823.

Morrison, K., 2013. Mapping subsurface archaeology with SAR. *Archaeological Prospection*, *20*(2), pp.149-160.

Nashashibi, A., Ulaby, F.T. and Sarabandi, K., 1996. Measurement and modeling of the millimeter-wave backscatter response of soil surfaces. *IEEE Transactions on Geoscience and Remote Sensing*, *34*(2), pp.561-572.

Nolan, M. and Fatland, D.R., 2003. Penetration depth as a DInSAR observable and proxy for soil moisture. *IEEE Transactions on Geoscience and Remote Sensing*, *41*(3), pp.532-537.

Orfanidis, S. J. (2002). "Electromagnetic waves and antennas."

Paillou, P., et al. (2009). "Mapping of a major paleodrainage system in eastern Libya using orbital imaging radar: the Kufrah River." Earth and Planetary Science Letters **277**(3-4): 327-333.

Quesney, A., et al. (2000). "Estimation of watershed soil moisture index from ERS/SAR data." Remote Sensing of Environment **72**(3): 290-303.

Rabus, B., Wehn, H. and Nolan, M., 2010. The importance of soil moisture and soil structure for InSAR phase and backscatter, as determined by FDTD modeling. IEEE Transactions on Geoscience and Remote Sensing, 48(5), pp.2421-2429.

Robertson, S. D. (1947). "Targets for microwave radar navigation." Bell System Technical Journal **26**(4): 852-869.

Roth, L. and C. Elachi (1975). "Coherent electromagnetic losses by scattering from volume inhomogeneities." IEEE Transactions on Antennas and propagation **23**(5): 674-675.

Salem, B.B., 1989. *Arid zone forestry: a guide for field technicians* (No. 20). Food and Agriculture Organization (FAO).

Sarabandi, K. and T.-C. Chiu (1996). "Optimum corner reflectors for calibration of imaging radars." IEEE Transactions on Antennas and propagation **44**(10): 1348-1361.

Schaber, G. G., et al. (1986). "Shuttle imaging radar: physical controls on signal penetration and subsurface scattenng in the eastern sahara." IEEE Transactions on Geoscience and Remote Sensing(4): 603-623.

Shoshany, M., et al. (2000). "The relationship between ERS-2 SAR backscatter and soil moisture: generalization from a humid to semi-arid transect." International Journal of Remote Sensing **21**(11): 2337-2343.

Skolnik, M. (1990). Radar Handbook , Chapter 2, McGraw-Hill (New York).

Skolnik, M. I. (1962). "Introduction to radar." Radar Handbook **2**.

Sowter, A., et al. (2016). "Mexico City land subsidence in 2014–2015 with Sentinel-1 IW TOPS: Results using the Intermittent SBAS (ISBAS) technique." International journal of applied earth observation and geoinformation **52**: 230-242.

Stimson, G. W. (1983). "Introduction to Airborne Radar Hughes Aircraft Company, El." Segundo, CA.

Ulaby, F. (1974). "Radar measurement of soil moisture content." IEEE Transactions on Antennas and propagation **22**(2): 257-265.

Ulaby, F. T., et al. (1978). "Microwave backscatter dependence on surface roughness, soil moisture, and soil texture: Part I-bare soil." IEEE Transactions on Geoscience Electronics **16**(4): 286-295.

Ulaby, F. T., et al. (1981). "Microwave Remote Sensing-Active and Passive-Volume I-Microwave Remote Sensing Fundamentals and Radiometry (v. 1)."

Ulaby, F. T., et al. (1982). Microwave remote sensing: active and passive. Vol. 2, Radar remote sensing and surface scattering and emission theory, Addison-Wesley Reading, MA.

UMEHARA, T., Uratsuka, S., Kobayashi, T., Satake, M., Nadai, A., Maeno, H., Masuko, H. and Shimada, M., 2002. 3-5 Development of Airborne high-resolution multi-parameter imaging radar SAR, Pi-SAR. Journal of the Communications Research Laboratory, 49(2).

Vall-Llossera, M., et al. (2005). L-band dielectric properties of different soil types collected during the MOUSE 2004 field experiment. INTERNATIONAL GEOSCIENCE AND REMOTE SENSING SYMPOSIUM.

Von Hippel, A. R. (1954). "Dielectrics and waves."

Wang, J., et al. (1978). "Dielectric constants of soils at microwave frequencies-2."

Wanpiyarat, V., Buapradupkul, D. and Chutirattanaphan, S., 1997. Potential use of airborne synthetic aperture radar to monitor agricultural land uses–a case study in Thailand. *Office of Soil Survey and Land Use Planning, Department of Land Development, Bangkok, Thailand*.

World Bank Group, 2016. *World development report 2016: digital dividends*. World Bank Publications.

Xia, Y. (2008). CR-Based SAR-Interferometry for landslide monitoring. Geoscience and Remote Sensing Symposium, 2008. IGARSS 2008. IEEE International, IEEE.

Zebker, H. A. and R. M. Goldstein (1986). "Topographic mapping from interferometric synthetic aperture radar observations." Journal of Geophysical Research: Solid Earth **91**(B5): 4993-4999.

Zebker, H. A. and J. Villasenor (1992). "Decorrelation in interferometric radar echoes." IEEE Transactions on Geoscience and Remote Sensing **30**(5): 950-959.

Zebker, H. A., et al. (1994). "Accuracy of topographic maps derived from ERS-1 interferometric radar." IEEE Transactions on Geoscience and Remote Sensing **32**(4): 823-836.

Zwieback, S., et al. (2017). "Depth-resolved backscatter and differential interferometric radar imaging of soil moisture profiles: observations and models of subsurface volume scattering." IEEE Journal of Selected Topics in Applied Earth Observations and Remote Sensing **10**(7): 3281-3296.

Appendix A: Computer Programs

The following scripts are used in this PhD research to process, calibrate, and analyse the data. These scripts are imbedded within Punnet software from Geomatic Ventures Ltd. However, other parts of Punnet cannot be included in this appendix as they are restricted by Geomatic Ventures Ltd.

```
%this script will read all the calibration parameters of a Sentinel
1 image
%stored in the annotation\calibration directory
%Ahmed Dhahir Athab
%31/3/2015
%
%First: specify the full name and path for the required xml file
%this part to read the path of each image
%
fcd = fopen('calibration_parameters.txt', 'wt' );%the calibration
files sequences
fid=fopen('sarfiles.txt','r');
d=textscan(fid,'%s','Delimiter','\n');
%dataset_m=d{1,1}{nn+2,1};
no_img=length(d{1,1});
kl=0;
for ng=1:3:no_img
    kl=kl+1;
    sarimg=d{1,1}{ng,1};%saving the path of each image into this
array
    sar_img{kl,:}=sarimg;%I changed this into cell array to be able
to include all the characters in the SAR iamge file location
end
%
for ii=1:kl;%this is the number of images
    cal_path=strcat(sar_img{ii,:},'\annotation\calibration\');

cal_files=strcat(sar_img{ii,:},'\annotation\calibration\calibration*
');
    av=dir(cal_files);%list all the calibration files of a single
image
    L={av.name};%names of the calibration files
    C = L';%transposing the names
    for j=1:length(C);%reading the calibration parameters from each
swath
        cal_fil=strcat(cal_path,C{j,:});%this is the full path and
file name of a calibration file
        tx_cal=xml2struct(cal_fil);
        data_lines=length(tx_cal.calibrationVectorList);

cols=tx_cal.calibrationVectorList(1).calibrationVector.sigmaNought;
        cols=str2num(cols);
        data_cols=length(cols);
        %initializing the data matrecis
```

```
        linesN=zeros(data_lines,1);%transposing the lines vector to
get a column vector
        SigmaN=zeros(data_lines,data_cols);
        betaN=zeros(data_lines,data_cols);
        pixels=zeros(data_lines,data_cols);
        gamma=zeros(data_lines,data_cols);
        DN=zeros(data_lines,data_cols);
        for i=1:data_lines %this is the number of the data given for
each image

llnn=tx_cal.calibrationVectorList(i).calibrationVector.line;
            linesN(i)=str2num(llnn);

pxl=tx_cal.calibrationVectorList(i).calibrationVector.pixel;
            pixels(i,:)=str2num(pxl);

sgmn=tx_cal.calibrationVectorList(i).calibrationVector.sigmaNought;
            SigmaN(i,:)=str2num(sgmn);

btan=tx_cal.calibrationVectorList(i).calibrationVector.betaNought;
            betaN(i,:)=str2num(btan);

gman=tx_cal.calibrationVectorList(i).calibrationVector.gamma;
            gamma(i,:)=str2num(gman);

dnn=tx_cal.calibrationVectorList(i).calibrationVector.dn;
            DN(i,:)=str2num(dnn);
        end
        %saving the workspace into a mat file with the same image
swath
        %name
        nm=length(C{j,:});%length of the calibration file name
        kkll=C{j,:};
        pp1=kkll(1,1:nm-4);%to remove the last part of the file name
(.xml)
        ws=strcat(pp1,'_iw_',num2str(j));
       %
       %
       %writing the calibration annotation file names into text
files like
       %sareditor

       %zz=pwd;% path for the current working directory
       %kk=numel(C(:,1)); %calculating the number of elements in the
array C
       %for x=1:kk;
         %  fcd = fopen( 'Parameters\sarfiles.txt', 'at' );
           %fprintf( fcd, '%s', zz,'\Dataset\');
           fprintf( fcd, '%s\n', ws);% for envisat images, the file
name must be duplicated

       %end
       %
       %
        save (ws)
    end
end
fclose('all');
```

```
%CR's calibration as point targets.
%date: 19 - Feb - 2016
%Inputs: C3CR_sub_1000.mat files subtracted from the slave.raw files
during
%the punnet create interferogram processing.
%outputs: Sigma_dB for each CR
%Ahmed Athab
%
load no_files n_files;
load m_hdr_path
nlin=master.no_lines;
ncol=master.no_pixels;

crrows=[500 500 500 500 500 500 500];
crcols=[500 500 500 500 500 500 500];
%
%PEAK APPROXIMATE LOCATION FROM THE ZINV
load peak_location_zinv;
%Pz_crrows=[1029 1002 1023 1019 1000 1019 1027];
%Pz_crcols=[1018 1027 1041 1032 1015 1027 1105];

%location of the background representative areas selected manually
for each
%reflector (raw and col)
M1_r=[40 33 20 15 29 22 15];
M1_c=[18 13 10 14 24 11 20];
M2_r=[43 38 23 21 36 20 21];
M2_c=[89 86 91 94 102 104 108];
M3_r=[104 102 110 98 111 116 105];
M3_c=[98 92 93 101 96 89 91];
M4_r=[114 104 96 87 120 114 119];
M4_c=[16 14 14 13 10 14 13];
%
%peak power location from the interpolated subsets
% rr_Xamp=[512 512 514 513 513 512 513];
% cc_Xamp=[515 514 510 512 512 512 517];
%
%Pixel area from the annotation file of that image, should be read
%automatically
            dr=2.33;%range_pixel_spacing
            da=13.86;%azimuth_pixel_spacing
            Pa=dr*da;%pixel area
for i=5:n_files
    file_nam=strcat('C',num2str(i),'CR_sub_1000 ');
    load (file_nam,'CR_sub_1000');
    for k=1:7
        %image_nam=CR_sub_1000';
        cr_sub_256{k}=CR_sub_1000{k}(crrows(k)-
128:crrows(k)+127,crcols(k)-128:crcols(k)+127);
    end
    %converting pixel values into intensities by squaring
    for n=1:7
       W=cr_sub_256{n};
       cr_sub_256_int{n}=W.^2;
    end
    % cr_sub_256_int_bgr=abs(cr_sub_256_int)-B;%this is the
background corrected intensity%Background to Peak (BP) ratio
    %because there is a difference in the power of the output image
from the
    %fft interpolation,
    %
```

```
    for j=1:7;%the reflectors
        %background calculations
        BG=cr_sub_256{j};
        M1=abs(BG(M1_r(j)-5:M1_r(j)+4,M1_c(j)-5:M1_c(j)+4));
        M2=abs(BG(M2_r(j)-5:M2_r(j)+4,M2_c(j)-5:M2_c(j)+4));
        M3=abs(BG(M3_r(j)-5:M3_r(j)+4,M3_c(j)-5:M3_c(j)+4));
        M4=abs(BG(M4_r(j)-5:M4_r(j)+4,M4_c(j)-5:M4_c(j)+4));
        %
        %average background intensity value,
        M=(M1.^2+M2.^2+M3.^2+M4.^2);
        MM=sum(sum(M));
        %B=MM/400;%mean background intensity
        B=(MM/400);%check the effect of background values
        %B=5000;
        B_mean(i,j)=B;
        CR=cr_sub_256_int{j};%handeling one corner reflector at a
time
        %
        %the zero-padded FFT interpolation
        zdash=zeros(2048,2048); %zero matrix 8 times the 256 subset
area
        fz1=fft2(CR);
        for k=1:128 % distribute corners of FFT in padded array
            for m=1:128
                zdash(k,m)=fz1(k,m);
                zdash(1920+k,m)=fz1(128+k,m);
                zdash(k,1920+m)=fz1(k,128+m);
                zdash(1920+k,1920+m)=fz1(128+k,128+m);
            end
        end
        zdash=zdash;%scale factor, see ppt for more details. this
affecting both real and imaginary parts
        zinv=ifft2(zdash); % this is the interpolated corner
reflectors in one image
        Xamp=abs(zinv)/64;%converting the complex into absolute
        %Xamp_bgr=Xamp-B;%corrected for background
        AA=Xamp(Pz_crrows(j)-50:Pz_crrows(j)+50,Pz_crcols(j)-
50:Pz_crcols(j)+50);%matrix approximately centred on the CR to find
the exact location of the CR (peak or max)
        [Val,Indx]=max(AA(:));%the value and the index of the
maximum in the central subset
        [rr cc] = ind2sub(size(AA),Indx);%the row and column of the
maximum in the central subset
        rr_Xamp=Pz_crrows(j)-50+rr-1;%row of the maximum in the
original subset
        cc_Xamp=Pz_crcols(j)-50+cc-1;%col of the maximum in the
original subset
        %
        %plotting the mesh of AA, range and azimuth IRF, and the amp
of
        %AA
      %  fig_nam=strcat('CR',num2str(7),'_image_',num2str(7));
        %figure('units','normalized','outerposition',[0 0 1 1])
        fig_nam=figure('units','normalized','outerposition',[0 0 1
1]);%maximizing the figure size to the screen size
        subplot(3,3,[1:2,4:5]);% see my documentations for the size
of plots
        %AA=Xamp(1024-75:1025+75,1024-75:1025+75);%for displying
purposes only in order to remove the effects of the other nearby
CR's
```

```
        mesh(AA);
        %now we have the value and the location of the peak value of
the
        %point target;
        %firstly:spatial resolution
        %1- range resolution
        K=Xamp(rr_Xamp,:);%one line across the point target (dB)
        subplot(3,3,[7,8])
   plot(10*log10(K(700:1300)));
   hold on
   %plotting the zero dashed line
   plot([0 600],[0 0],'r--')
%      plot((K(500:1500)));
    ax=gca;
    ax.YLim=[-40,30];
    ax.XLim=[0,600];
    ylabel('Backscatter (dB)')

    %subplot(3,3,9);
    %imtool(AA);
    %
    k_rang=K;
    K=10*log10(K);
    PdB=K(cc_Xamp);%peak intensity value in dB
    K_3dB=PdB-3;%-3dB value to which the with of the IRF will be
calculated
    %lft=zeros(1,cc_Xamp);%left part of the vector
   % rit=zeros(1,length(K)-cc_Xamp);%right part of the vector
    lft=K(1:cc_Xamp);%left par of the peak power line
    rit=K(cc_Xamp+1:2048);%right part of the peak power line
    [lft_3 indx_L] = min(abs(lft(800:end)-K_3dB));%value and
location of the closest value in the left part to the peak -3dB
    [lft_3 indx_R] = min(abs(rit(1:50)-K_3dB));
    indx_L=indx_L+799;
     Range_resolu=length(lft)+indx_R-indx_L;%range resolution
     %SS=strcat('Range resolution =',num2str(Range_resolu/8*dr),'
m');
     %text(950,70,SS);

     %2- azimuth resolution
     K=(Xamp(:,cc_Xamp))';%one line across the point target (dB)
     subplot(3,3,[3,6,9]);
    plot(10*log10(K(700:1300)));
    hold on
    plot([0 600],[0 0],'r--')
    %     plot((K(500:1500)));
    camroll(-90);
    ax=gca;
    ax.YLim=[-40,30];
    ax.XLim=[0,600];
    ylabel('Backscatter (dB)')

     %
    % k_az=K;
     K=10*log10(K);
     PdB=K(rr_Xamp);%peak intensity value in dB
     K_3dB=PdB-3;%-3dB value to which the with of the IRF will be
calculated

     up_s=K(1:rr_Xamp);
     dw_s=K(rr_Xamp+1:2048);
```

```
      [up_s_3 indx_U] = min(abs(up_s(900:end)-K_3dB));%value and
location of the closest value in the left part to the peak -3dB
      [dw_s_3 indx_D] = min(abs(dw_s(1:50)-K_3dB));
      indx_U=indx_U+899;
      Azimuth_resolu=length(up_s)+indx_D-indx_U;%azimuth resolution
     % SS2=strcat('Azimuth resolution
=',num2str(Azimuth_resolu/8*da),' m');
     % text(990,-28,SS2);
      %the resolution in range and azimuth, which is the half power
width
      %of the peak value
      rang_res(i,j)=Range_resolu;
      az_res(i,j)=Azimuth_resolu;
      %range_res=Range_resolu;
      %azimuth_res=Azimuth_resolu;
      %%

      %there is a problem with calculating the resolution, the method
I am
      %using is not enough and not accurate. I need to interpolate
the K
      %values to find the exact location of the -3dB values
      range_res=12;
      azimuth_res=12;
      %range_res=3.46;%this is the resolution in metres from Peter
excel sheet
      %azimuth_res=21;
      %Step 2: calculating the mean background intensity
      %background sample areas, manually selected for each CR
      %%
     % Xamp_bgr=Xamp-B;
     % DN_peak=abs(Xamp_bgr(rr_Xamp,cc_Xamp));
    %  p_zinv=Xamp_bgr;
      DN_peak=abs(zinv(rr_Xamp,cc_Xamp));%this is the max value in
which the CR is located

             BP=10*log10(B/DN_peak);%background to peak ratio image
             BP_ratio(i,j)=BP;
             p_zinv=abs(zinv);%the intensity of the interpolated
image
             %Step 5: ISLR calculation (Integrated Sidelobe Ratio)
             %the resolution cell was measured manually and is equal
to 16 pixels in
             %range and 8 azimuth in the oversampled image (fft)
             %
             %
             E1=sum(sum(p_zinv(rr_Xamp-
azimuth_res:rr_Xamp+azimuth_res,cc_Xamp-
range_res:cc_Xamp+range_res)));%power within two resolution cells
             %this area was reduced in size, according to Peter, this
will ensures that
             %nearby point targets will not included in the analysis
             %ISLR for BAE is 10x10 resolution cells for the outer
box,
             %according to Peter Meadows
             E2=sum(sum(p_zinv(rr_Xamp-
(5*azimuth_res):rr_Xamp+(5*azimuth_res-1),cc_Xamp-
(5*range_res):cc_Xamp+(5*range_res-1))));%power within 10 recolution
cells
            % E1=E1/64;%corrected for interpolation
           %  E2=E2/64;%corrected for interpolation
```

```
            ISLR_dB(i,j)=10*log10((E2-E1)/E1);%Andy approch for ISLR
            islr=(E2-E1)/E1;
            ISLR(i,j)=islr;
            %relative power in sidelobe
            %this equation assumes the ISLR NOT in dB
            cf=1/(1+islr);
            Cf(i,j)=cf;


            %Total power in the mainlobe IP
            ip=sum(sum(p_zinv(rr_Xamp-
azimuth_res:rr_Xamp+azimuth_res,cc_Xamp-
range_res:cc_Xamp+range_res)));
           % ip=ip/64;%correction the mainlobe power for
interpolation
           ip=ip-B;%the background used here to modify the total
power in the mainlobe before calculating the
           %RCS and after all the previous steps, ref: Peter Meadows
           %explained in his email
            IP(i,j)=ip;

            Adn=237;%from the calibration annotation files

            K=1;%the absolute calibration factor
            Sigma(i,j)=(ip/Adn^2*cf)*(Pa/K);
            sigma_dB(i,j)=10*log10(ip) - 10*log10(Adn^2)-
10*log10(cf)+10*log10(Pa) -10*log10(K);
            %
            % SS3=strcat('RCS =',num2str(sigma_dB),' dB');
            %text(1030,-28,SS3);

out_fig_nam=strcat('CR',num2str(j),'_image_',num2str(i));
            saveas(fig_nam,out_fig_nam,'jpg');
            close all
    end
     close all

end





function calibration_Sigma_N(image_id,totnlin,nocols);
%this script will use the output of the follwoing two programs:
%1-swath_reader
%2-interpolating_SigmaN
%then applying the equation XX1 from
sentinel1_calibration_annotations.docx
%Value(i)=abs(amplitude(i))^2 / (sigmaN(i)
s1=['famp=fopen(''swath' num2str(image_id) 'amp.dat'',''r'');'];
s2=['fsig=fopen(''SigmaN_swath' num2str(image_id) '.dat'',''r'');'];
s3=['fout=fopen(''Swath' num2str(image_id)
'_sigma_calibrated.dat'',''w'');'];
eval(s1);
eval(s2);
eval(s3);

%
```

```
percent_NN=floor(totnlin/100); % the percentage
GG=percent_NN;
lcount_NN=1;% percentage counter
reverseStr = '';
disp('Calculating the sigma nought for each pixel... ')
for i=1:totnlin
     if i > percent_NN
        msg = sprintf('Completed %d/%d', lcount_NN, 100);
        fprintf([reverseStr, msg]);
        reverseStr = repmat(sprintf('\b'), 1, length(msg));
        %disp([num2str(lcount),'% complete...']);
        lcount_NN=lcount_NN+1;
        percent_NN=percent_NN+GG;
     end
    Ampl(1,:)=fread(famp,nocols,'int16');%one line of the amplitude
image
    Sigm(1,:)=fread(fsig,nocols,'single');%one line of sigmaN values
    AA1=abs(Ampl.^2);
    AA2=(Sigm.^2);
    Value=AA1./AA2;
    %Value=abs(Ampl.^2)/(Sigm.^2);
    fwrite(fout,Value,'single');
end
fclose('all')
disp('...done')
```

```
function [nlin,ncol,master]=deburst_sentinel_slave(image_id)
%
load deburstfiles mleader mdataset;
load ref_img;
consts;
%
% open output file
%
% read in bursts
%
I=1;
master.burst=I;
read_master_sentinel;
no_bursts=master.no_bursts;
first_line_time=zeros(1,no_bursts,'double');
nolines=zeros(1,no_bursts);
nocols=zeros(1,no_bursts);
first_line_time(I)=master.burst_azimuth_time;
[nolines(I),nocols(I)]=TIFF_burstread_slave(master,mdataset);
for I=2:no_bursts
    master.burst=I;
    read_master_sentinel;
    first_line_time(I)=master.burst_azimuth_time;
    [nolines(I),nocols(I)]=TIFF_burstread_slave(master,mdataset);
end
%
% calculate overlaps
%
dt=master.line_time_spacing;
dlines=zeros(1,no_bursts-1);
overlap_lines=dlines;
```

```
for I=1:no_bursts-1
    dlines(I)=round((first_line_time(I+1)-first_line_time(I))/dt);
    overlap_lines(I)=nolines(I)-dlines(I);
end
%
% calculate dimensions of de-burst array
%
total_lines=nolines(no_bursts)+sum(dlines);
%
% initialise file
%
s=['fid_out=fopen(''swath' num2str(image_id) '.dat'',''w'');'];
eval(s);
s=['fid_deramp=fopen(''swath_deramp' num2str(image_id)
'.dat'',''w'');'];
eval(s);
dummyline=zeros(1,2*nocols(1),'int16');
dummyline2=zeros(1,nocols(1),'single');
for i=1:total_lines
    fwrite(fid_out,dummyline,'int16');
    fwrite(fid_deramp,dummyline2,'single');
end
%
% write bursts to file
%
id=0;
for I=no_bursts-1:-1:1
    s=['fid_in=fopen(''burst' num2str(I+1) '.dat'',''r'');'];
    eval(s);
    s=['fid_deramp_in=fopen(''deramp' num2str(I+1)
'.dat'',''r'');'];
    eval(s);
    offset=4*(sum(dlines(1:I))*nocols(1));
    fseek(fid_out,offset,'bof');
    offset2=4*(sum(dlines(1:I))*nocols(1));
    fseek(fid_deramp,offset2,'bof');
    nlin=nolines(I+1);
    if id==1
        nlin=nlin-round(overlap_lines(I+1)/2);
    end
    for j=1:nlin
        data=fread(fid_in,2*nocols(1),'int16');
        data2=fread(fid_deramp_in,nocols(1),'single');
        fwrite(fid_out,data,'int16');
        fwrite(fid_deramp,data2,'single');
    end
    fclose(fid_in);
    fclose(fid_deramp_in);
    id=1;
end
%
fid_in=fopen('burst1.dat','r');
fid_deramp_in=fopen('deramp1.dat','r');
nlin=nolines(1)-round(overlap_lines(1)/2);
fseek(fid_out,0,'bof');
fseek(fid_deramp,0,'bof');
for j=1:nlin
    data=fread(fid_in,2*nocols(1),'int16');
    data2=fread(fid_deramp_in,nocols(1),'single');
    fwrite(fid_out,data,'int16');
```

```
    fwrite(fid_deramp,data2,'single');%the deramp is only about
phase, nothing to do with amplitude
end
fclose('all');
%
col_no=nocols(1);
swath_reader(image_id,total_lines,col_no);%calling the function and
providing the swath number with the dimensoins
%
interpolating_SigmaN(ref_img,image_id,total_lines,col_no);%ref_img
is the SAR imamge reference number and image_id is the swath number
of that image
%
calibration_Sigma_N(image_id,total_lines,col_no);%calculating the
calibrated sigma nought values
%
sigma_to_cmplx_amp(image_id,total_lines,col_no);%re-write complex
swath file from the calibrated amplitude and the original phase
%
%
master.burst_azimuth_time=first_line_time(1);
nlin=total_lines;
ncol=nocols(1);
```

```
"""
@author: Ahmed Athab
"""
import scipy.io
import numpy as np
from scipy import stats
from sklearn.linear_model import LinearRegression
import random# to generate a unique integer list in a range
import matplotlib.pyplot as plt
import operator
#
mat_1 = 'SubSAR_observations.mat'
mat_cont = scipy.io.loadmat(mat_1)
DInSAR = mat_cont['DInSAR']
sigma = mat_cont['sigma']
sm_range_sample = mat_cont['sm_range_sample']

#model = LinearRegression()
#model.fit(x, y)
sm = sigma[:,0]#.reshape((-1,1))
sigma_att = sigma[:,1]#.reshape((-1,1))
#
sm2 = DInSAR[:,0]#.reshape((-1,1))
phase = DInSAR[:,1]#.reshape((-1,1))
#
#sm3 = sm_range_sample[:,0]#.reshape((-1,1))
#sigma_att3 = sm_range_sample[:,1]#.reshape((-1,1))
#phase3 = sm_range_sample[:,2]#.reshape((-1,1))
```

```
slope_sigma_a, intercept_sigma_a, r_value_sigma_a,
p_value_sigma_a, std_err_sigma_a = stats.linregress(sm,
sigma_att)
slope_phase_a,intercept_phase_a, r_value_phase_a,
p_value_phase_a, std_err_phase_a = stats.linregress(sm2,
phase)



#ssmm2 = sm2
#phase2 = phase
#the linear regression model values match  Matlab, Excel, and
Minitab
# analysing the backscatter attenuation
pt_stat = 2
pt_end = 50
stp = 1
no_iter = 10000
#
# initializing empty arrays
################################################
slope_sigma = np.empty([no_iter, pt_end])
slope_sigma[:] = np.nan
#
intercept_sigma = np.empty([no_iter, pt_end])
intercept_sigma[:] = np.nan
#
r_value_sigma = np.empty([no_iter, pt_end])
r_value_sigma[:] = np.nan
#
p_value_sigma = np.empty([no_iter, pt_end])
r_value_sigma[:] = np.nan
#
std_err_sigma = np.empty([no_iter, pt_end])
std_err_sigma[:] = np.nan
###############################################
slope_phase = np.empty([no_iter, pt_end])
slope_phase[:] = np.nan
#
intercept_phase = np.empty([no_iter, pt_end])
intercept_phase[:] = np.nan
#
r_value_phase = np.empty([no_iter, pt_end])
r_value_phase[:] = np.nan
#
p_value_phase = np.empty([no_iter, pt_end])
p_value_phase[:] = np.nan
#
std_err_phase = np.empty([no_iter, pt_end])
std_err_phase[:] = np.nan
##############################################
range_sm = np.empty([no_iter, pt_end])
range_sm[:] = np.nan
#
```

```
for j in range(no_iter):
    random_dist = random.sample(range(0,50), 50)
    ssmm = sm[random_dist]
    #ssmm = sm
    sigma_att2 = sigma_att[random_dist]
    #sigma_att2 = sigma_att
    #
    ssmm2 = sm2[random_dist]
    phase2 = phase[random_dist]

    print('iteration ' + str(j + 1) + ' of ' + str(no_iter))
    for i in range(pt_stat,  pt_end, stp):
        slope,intercept, r_value, p_value, std_err =
stats.linregress(ssmm[0:i], sigma_att2[0:i])
        slope_sigma[j, i] = slope
        intercept_sigma[j, i] = intercept
        r_value_sigma[j, i] = r_value
        p_value_sigma[j, i] = p_value
        std_err_sigma[j, i] = std_err
        # must calculate the sm range for each sample
        rng = max(ssmm[0:i]) - min(ssmm[0:i])
        range_sm[j, i] = rng
        #
        slope2,intercept2, r_value2, p_value2, std_err2 =
stats.linregress(ssmm2[0:i], phase2[0:i])
        slope_phase[j, i] = slope2
        intercept_phase[j, i] = intercept2
        r_value_phase[j, i] = r_value2
        p_value_phase[j, i] = p_value2
        std_err_phase[j, i] = std_err2
    #

#
# averaging the iterations into a single value and calculating
the standard deviation of each point
slope_sigma_avg = slope_sigma.mean(axis=0)   # average each
column
slope_sigma_avg_std = np.nanstd(slope_sigma[:,:], axis=0)
#
intercept_sigma_avg = intercept_sigma.mean(axis=0)
intercept_sigma_avg_std = np.nanstd(intercept_sigma[:,:],
axis=0)
#
r_value_sigma_avg = r_value_sigma.mean(axis=0)
r_value_sigma_avg_std = np.nanstd(r_value_sigma[:,:], axis=0)
#
p_value_sigma_avg = p_value_sigma.mean(axis=0)
p_value_sigma_avg_std = np.nanstd(p_value_sigma[:,:], axis=0)
#
std_err_sigma_avg = std_err_sigma.mean(axis=0)
std_err_sigma_avg_std = np.nanstd(std_err_sigma[:,:], axis=0)
#
slope_phase_avg = slope_phase.mean(axis=0)
slope_phase_avg_std = np.nanstd(slope_phase[:,:], axis=0)
#
intercept_phase_avg = intercept_phase.mean(axis=0)
```

```
intercept_phase_avg_std = np.nanstd(intercept_phase[:,:],
axis=0)
#
r_value_phase_avg = r_value_phase.mean(axis=0)
r_value_phase_avg_std = np.nanstd(r_value_phase[:,:], axis=0)
#
p_value_phase_avg = p_value_phase.mean(axis=0)
p_value_phase_avg_std = np.nanstd(p_value_phase[:,:], axis=0)
#
std_err_phase_avg = std_err_phase.mean(axis=0)
std_err_phase_avg_std = np.nanstd(std_err_phase[:,:], axis=0)
#
range_sm_avg = range_sm.mean(axis=0)
range_sm_avg_std = np.nanstd(range_sm[:,:], axis=0)




x_ax = np.arange(pt_stat, pt_end)
x_ax2 = np.arange(0, 50)

fig1 = plt.figure()
#fig1.suptitle('Statistical Analysis of Backscatter
Attenuation average of ' + str(no_iter) + ' runs' ,
fontsize=16)
#
plt.subplot(2, 2, 1)
plt.plot(x_ax, intercept_sigma_avg[pt_stat:pt_end])
plt.plot([pt_stat, pt_end], [intercept_sigma_a,
intercept_sigma_a], ':m')
#plt.errorbar(x_ax2, intercept_sigma_avg,
yerr=intercept_sigma_avg_std, fmt='.k')
#plt.plot([pt_stat, pt_end], [intercept_sigma_a -
std_err_sigma_a, intercept_sigma_a - std_err_sigma_a], 'r:')
#plt.plot([pt_stat, pt_end], [intercept_sigma_a +
std_err_sigma_a, intercept_sigma_a + std_err_sigma_a], 'r:')
plt.title('Y - Intercept')
plt.grid(linestyle=':')
#plt.xlabel('No. of Observations').set_color("red")

#
plt.subplot(2, 2, 2)
plt.plot(x_ax, slope_sigma_avg[pt_stat:pt_end])
plt.plot([pt_stat, pt_end], [slope_sigma_a, slope_sigma_a],
'm:')
#
#plt.errorbar(x_ax2, slope_sigma_avg,
yerr=slope_sigma_avg_std, fmt='.k')

#plt.plot([pt_stat, pt_end], [slope_sigma_a - std_err_sigma_a,
slope_sigma_a - std_err_sigma_a], 'r:')
#plt.plot([pt_stat, pt_end], [slope_sigma_a + std_err_sigma_a,
slope_sigma_a + std_err_sigma_a], 'r:')
plt.title('Slope')
plt.grid(linestyle=':')
#plt.xlabel('No. of Observations').set_color("red")
```

```
#
"""
plt.subplot(2, 2, 3)
plt.plot(x_ax, std_err_sigma_avg[pt_stat:pt_end])
plt.plot([pt_stat, pt_end], [std_err_sigma_a,
std_err_sigma_a], 'm:')
#plt.plot([pt_stat, pt_end], [std_err_sigma_a -
std_err_sigma_a, std_err_sigma_a - std_err_sigma_a], 'r:')
#plt.plot([pt_stat, pt_end], [std_err_sigma_a +
std_err_sigma_a, std_err_sigma_a + std_err_sigma_a], 'r:')
plt.title('Standard Error')
plt.grid(linestyle=':')
plt.xlabel('No. of Observations').set_color("red")
"""
#
plt.subplot(2, 2, 3)
plt.plot(x_ax, r_value_sigma_avg[pt_stat:pt_end])
plt.plot([pt_stat, pt_end], [r_value_sigma_a,
r_value_sigma_a], 'm:')
#plt.plot([pt_stat, pt_end], [r_value_sigma_a -
std_err_sigma_a, r_value_sigma_a - std_err_sigma_a], 'r:')
#plt.plot([pt_stat, pt_end], [r_value_sigma_a +
std_err_sigma_a, r_value_sigma_a + std_err_sigma_a], 'r:')
plt.title('Correlation Coefficient')
plt.grid(linestyle=':')
plt.xlabel('No. of Observations')#.set_color("red")
#
plt.subplot(2, 2, 4)
plt.plot(x_ax, range_sm_avg[pt_stat:pt_end])
#plt.plot([pt_stat, pt_end], [r_value_sigma_a,
r_value_sigma_a], 'r:')
plt.title('SM range')
plt.grid(linestyle=':')
plt.xlabel('No. of Observations')#.set_color("red")
plt.ylabel('Water Content (%)')#.set_color("red")

#DInSAR
fig2 = plt.figure()
#fig2.suptitle('Statistical Analysis of DInSAR Phase average
of ' + str(no_iter) + ' runs', fontsize=16)
#
plt.subplot(2, 2, 1)
plt.plot(x_ax, intercept_phase_avg[pt_stat:pt_end])
plt.plot([pt_stat, pt_end], [intercept_phase_a,
intercept_phase_a], 'm:')
#plt.plot([pt_stat, pt_end], [intercept_phase_a -
std_err_sigma_a, intercept_phase_a - std_err_sigma_a], 'r:')
#plt.plot([pt_stat, pt_end], [intercept_phase_a +
std_err_sigma_a, intercept_phase_a + std_err_sigma_a], 'r:')
plt.title('Y - Intercept')
plt.grid(linestyle=':')
#plt.xlabel('No. of Observations').set_color("red")
#
plt.subplot(2, 2, 2)
plt.plot(x_ax, slope_phase_avg[pt_stat:pt_end])
```

```
plt.plot([pt_stat, pt_end], [slope_phase_a, slope_phase_a],
'm:')
#plt.plot([pt_stat, pt_end], [slope_phase_a - std_err_sigma_a,
slope_phase_a - std_err_sigma_a], 'r:')
#plt.plot([pt_stat, pt_end], [slope_phase_a + std_err_sigma_a,
slope_phase_a + std_err_sigma_a], 'r:')
plt.title('Slope')
plt.grid(linestyle=':')
#plt.xlabel('No. of Observations').set_color("red")
#
"""
plt.subplot(2, 2, 3)
plt.plot(x_ax, std_err_phase_avg[pt_stat:pt_end])
plt.plot([pt_stat, pt_end], [std_err_phase_a,
std_err_phase_a], 'm:')
#plt.plot([pt_stat, pt_end], [std_err_phase_a -
std_err_sigma_a, std_err_phase_a - std_err_sigma_a], 'r:')
#plt.plot([pt_stat, pt_end], [std_err_phase_a +
std_err_sigma_a, std_err_phase_a + std_err_sigma_a], 'r:')
plt.title('Standard Error')
plt.grid(linestyle=':')
plt.xlabel('No. of Observations').set_color("red")
"""
#
plt.subplot(2, 2, 3)
plt.plot(x_ax, r_value_phase_avg[pt_stat:pt_end])
plt.plot([pt_stat, pt_end], [r_value_phase_a,
r_value_phase_a], 'm:')
#plt.plot([pt_stat, pt_end], [r_value_phase_a -
std_err_sigma_a, r_value_phase_a - std_err_sigma_a], 'r:')
#plt.plot([pt_stat, pt_end], [r_value_phase_a +
std_err_sigma_a, r_value_phase_a + std_err_sigma_a], 'r:')
plt.title('Correlation Coefficient')
plt.grid(linestyle=':')
plt.xlabel('No. of Observations')#.set_color("red")
#
plt.subplot(2, 2, 4)
plt.plot(x_ax, range_sm_avg[pt_stat:pt_end])
#plt.plot([pt_stat, pt_end], [r_value_sigma_a,
r_value_sigma_a], 'r:')
plt.title('SM range')
plt.grid(linestyle=':')
plt.xlabel('No. of Observations')#.set_color("red")
plt.ylabel('Water Content (%)')#.set_color("red")
plt.show()

#
```